University of Antwerp

Faculty of Science

Department of Bioscience Engineering

Synthesis and electron microscopy characterization of novel core-shell and self-assembled nanostructures for plasmon-enhanced photocatalysis

PhD thesis submitted to obtain the degree of doctorate in Bioscience Engineering at the University of Antwerp to be defended by

Rajeshreddy Ninakanti

Promotors:
Prof. Sammy W. Verbruggen
Prof. Sara Bals
Jury members:
Prof. Milorad Milosevic (Chair), University of Antwerp
Prof. Pegie Cool, University of Antwerp
Prof. Pascal Van Der Voort, Ghent University
Prof. Wiebke Albrecht, AMOLF

Antwerp, 27/06/2024

Faculteit Wetenschappen

Department Bio-ingenieurswetenschappen

Synthese en elektronenmicroscopie karakterisering van nieuwe core-shell en zelf-geassembleerde nanostructuren voor plasmon-verbeterde fotokatalyse

Proefschrift voorgelegd tot het behalen van de graad van doctor in de bio-ingenieurswetenschappen aan de Universiteit Antwerpen door

Rajeshreddy Ninakanti

Promotoren:
Prof. Sammy W. Verbruggen
Prof. Sara Bals
Juryleden:
Prof. Milorad Milosevic (Voorzitter), University of Antwerp
Prof. Pegie Cool, University of Antwerp
Prof. Pascal Van Der Voort, Ghent University
Prof. Wiebke Albrecht, AMOLF

Antwerp, 27/06/2024

Abstract

The global challenge posed by increasing levels of greenhouse gases and the associated detrimental impacts of global warming necessitate a strategic shift from traditional fossil fuel-based energy systems to more sustainable, renewable, and circular energy and material solutions. Consequently, the potential of photoactive nanoparticles, particularly those that harness light-driven processes, has captured extensive scientific interest as a viable approach to mitigating energy and environmental challenges on a global scale. Photovoltaics has emerged to be one such widely applied solution the last decade to generate electricity. Although, the adoption of solar light based solutions in the chemical industry has been very less due to sluggish reaction rates and its cascading effects on its economics.

The primary focus of this dissertation is the study of plasmonic metal nanoparticles and metal oxide nanoparticles, emphasizing their applications in light-driven energy conversion. The distinctive properties of plasmonic materials, especially surface plasmon resonance (SPR), are pivotal in these applications. SPR involves the oscillation of electron clouds at the surface of nanoparticles when resonating with incident electromagnetic radiation, significantly enhancing solar radiation absorption. This feature is crucial for addressing the limitations of semiconductor photocatalysts like TiO_2, which typically exhibit restricted absorption of solar irradiation.

Extensive research over the past decade has highlighted the potential of plasmon-enhanced semiconductor photocatalysis, particularly for its unique ability to enhance charge separation and transfer processes and increase absorption across the visible light spectrum. The mechanisms responsible for enhancement of photocatalytic efficiency by plasmonic nanoparticles are near-electric field, electron transfer and enhanced photon absorption which are the major ones depending on the design of nanoscale systems. The objective of this dissertation is to further optimize these plasmonic enhancement mechanisms by strategically tuning the interactions between plasmonic nanoparticles and TiO_2. This is achieved through the development of core-shell nanostructures and the self-assembly of supraparticles, designed to enhance plasmonic photocatalytic systems.

The dissertation begins by elucidating the basic concepts and ideations behind the construction of these nanostructures and their roles in enhancing plasmonic photocatalysis, focusing on mechanisms such as near-electric field enhancement, electron transfer, and enhanced photon absorption. To achieve these objectives, modified synthesis techniques were developed to fabricate novel Au@TiO_2 core-shell structures with precisely controlled TiO_2 shell thickness and self-assembled Au-TiO_2 supraparticles with variable sizes. To understand the structure property relationship, first the structure of the synthesized nanoparticles needs to be accurately established. Consequently, the thesis further delves into the structural characterization of these synthesized nanoparticles, introducing both basic and advanced electron microscopy techniques.

Core-shell structures with significant differences in atomic number complicate the characterization of 2D and 3D electron microscopy. To address these complications, techniques such as multimodal

tomography, exit wave reconstruction, and innovative reconstruction methods are employed, complemented by advanced sample preparation techniques. Subsequent experimental investigations correlate the structural characteristics of the Au@TiO_2 core-shell structures and Au-TiO_2 supraparticles with their experimental and simulated optical properties, utilizing UV-Vis spectroscopy, electron energy loss spectroscopy, and electromagnetic modeling via COMSOL Multiphysics software. This electromagnetic modeling is crucial for simulating and validating the near-field enhancements in core-shell nanostructures through surface-enhanced Raman spectroscopy experiments. For the specific applications of these structures, it was found that Au@TiO_2 core-shell nanoparticles with an optimal 4nm TiO_2 shell thickness show significant enhancement in the hydrogen evolution reaction. Additionally, the largest Au-TiO_2 supraparticles demonstrate superior efficacy in hydrogen peroxide generation. Insights from radical trapping experiments provide a mechanistic understanding, suggesting that the primary mode of plasmonic enhancement involves electron-mediated reactions.

In the concluding section of the thesis, inspired by the comprehensive theoretical knowledge and experimental results accumulated throughout the PhD program, novel hollow and core-shell nanostructures are proposed. These proposals include new catalytic methods and more dynamic ways to characterize these structures such as in-situ electron microscopy techniques, setting the stage for further advancements in the field of renewable energy research. This work not only deepens the scientific understanding of plasmonic materials but also contributes to the development of renewable energy materials.

Samenvatting

De globale uitdaging die veroorzaakt wordt door de toenemende niveaus van broeikasgassen en de daarmee gepaard gaande schadelijke gevolgen van de opwarming van de aarde, maakt een strategische verschuiving noodzakelijk van traditionele, op fossiele brandstoffen gebaseerde energiesystemen naar duurzamere, hernieuwbare en circulaire energie- en materiaaloplossingen. Bijgevolg heeft het potentieel van fotoactieve nanodeeltjes, vooral dewelke door licht aangedreven processen benutten, uitgebreid wetenschappelijke belangstelling gekregen als mogelijke strategie om energie- en milieu-uitdagingen op mondiale schaal aan te pakken. Fotovoltaïsche zonne-energie is in het voorbije decennium een van de breed toegepaste oplossingen gebleken om elektriciteit op te wekken. Hoewel de toepassing van op zonne-licht gebaseerde oplossingen in de chemische industrie veel minder frequent is als gevolg van trage reactiesnelheden en de trapsgewijze effecten ervan op haar economie.

De primaire focus van dit proefschrift ligt op de studie van plasmonische metaalnanodeeltjes en metaaloxidenanodeeltjes, waarbij de nadruk wordt gelegd op hun toepassingen in door licht aangedreven energieconversie. De onderscheidende eigenschappen van plasmonische materialen, vooral oppervlakte-plasmonresonantie (SPR), zijn cruciaal in deze toepassingen. SPR omvat de oscillatie van elektronenwolken aan het oppervlak van nanodeeltjes wanneer deze resoneren met invallende elektromagnetische straling, waardoor de absorptie van zonnestraling aanzienlijk wordt verbeterd. Deze eigenschap is cruciaal voor het aanpakken van de beperkingen van halfgeleiderfotokatalysatoren zoals TiO_2, die doorgaans een beperkte absorptie van zonnestraling vertonen.

In de afgelopen tien jaar heeft uitgebreid onderzoek het potentieel van plasmon-versterkte halfgeleiderfotokatalyse benadrukt, vooral vanwege het unieke vermogen om ladingsscheidings- en overdrachtsprocessen te verbeteren, en de absorptie over het zichtbare lichtspectrum te vergroten. De mechanismen die verantwoordelijk zijn voor het verbeteren van de fotokatalytische efficiëntie door plasmonische nanodeeltjes zijn het nabije-elektrisch veld, de elektronenoverdracht en de verbeterde fotonenabsorptie, waarvan de belangrijkste afhankelijk zijn van het ontwerp van de nanoschaal systemen. Het doel van dit proefschrift is om deze plasmonische versterkingsmechanismen verder te optimaliseren door de interacties tussen plasmonische nanodeeltjes en TiO_2 strategisch af te stemmen. Dit wordt bereikt door middel van de ontwikkeling van core-shell nanostructuren en de zelfassemblage van supradeeltjes, ontworpen om plasmonische fotokatalytische systemen te verbeteren.

Het proefschrift begint met het ophelderen van de basisconcepten en ideeën achter de constructie van deze nanostructuren en hun rol bij het verbeteren van plasmonische fotokatalyse, waarbij de nadruk ligt op mechanismen zoals versterking van het bijna-elektrische veld, elektronenoverdracht en verbeterde fotonabsorptie. Om deze doelstellingen te bereiken, werden gemodificeerde synthesetechnieken ontwikkeld om nieuwe $Au@TiO_2$ kern-schilstructuren te fabriceren met nauwkeurig gecontroleerde TiO_2-schildikte en zelf-geassembleerde $Au\text{-}TiO_2$-supradeeltjes met variabele afmetingen. Om de relatie tussen structuureigenschappen te begrijpen, moet eerst de structuur van de gesynthetiseerde nanodeeltjes nauwkeurig worden vastgesteld. Daarom gaat het proefschrift dieper in op de structurele karakterisering van deze gesynthetiseerde nanodeeltjes,

waarbij zowel eenvoudige als geavanceerde elektronenmicroscopietechnieken worden geïntroduceerd.
Kern-schilstructuren met significante verschillen in atoomnummer compliceren de karakterisering van 2D en 3D elektronenmicroscopie. Om deze complicaties aan te pakken, worden technieken zoals multimodale tomografie, exit-golfreconstructie en innovatieve reconstructiemethoden gebruikt, aangevuld met geavanceerde monstervoorbereidingstechnieken. Daaropvolgende experimentele onderzoeken correleren de structurele kenmerken van de Au@TiO_2-kern-schilstructuren en Au-TiO_2-supradeeltjes met hun experimentele en gesimuleerde optische eigenschappen, waarbij gebruik wordt gemaakt van UV-Vis-spectroscopie, elektronenenergieverliesspectroscopie en elektromagnetische modellering via COMSOL Multiphysics-software. Deze elektromagnetische modellering is cruciaal voor het simuleren en valideren van de verbeteringen in het nabije veld in core-shell nanostructuren door middel van oppervlakte-verbeterde Raman-spectroscopie-experimenten. Voor de specifieke toepassingen van deze structuren werd gevonden dat Au@TiO_2 kern-schil nanodeeltjes met een optimale TiO2-schildikte van 4 nm een significante verbetering vertonen in de waterstofontwikkelingsreactie. Bovendien vertonen de grootste Au-TiO_2-supradeeltjes een superieure werkzaamheid bij het genereren van waterstofperoxide. Inzichten uit radicaal vangexperimenten bieden een mechanistisch inzicht, wat suggereert dat de primaire wijze van plasmonische versterking elektronengemedieerde reacties omvat.
In het afsluitende deel van het proefschrift worden, geïnspireerd door de uitgebreide theoretische kennis en experimentele resultaten die tijdens het PhD-programma zijn verzameld, nieuwe holle en kern-schil nanostructuren voorgesteld. Deze voorstellen omvatten nieuwe katalytische methoden en meer dynamische manieren om deze structuren te karakteriseren, zoals in-situ elektronenmicroscopietechnieken, waarmee de weg wordt geëffend voor verdere vooruitgang op het gebied van onderzoek naar hernieuwbare energie. Dit werk verdiept niet alleen het wetenschappelijke inzicht in plasmonische materialen, maar draagt ook bij aan de ontwikkeling van hernieuwbare energiematerialen.

Acknowledgements

My PhD journey over the past four and a half years has been an extraordinary learning experience, one that I would gladly embrace for a lifetime. I have been fortunate to meet and collaborate with many remarkable individuals, to whom I owe a great deal of gratitude.

I begin by acknowledging this journey and every element that has shaped it—people, laboratory experiences, presentations, proposals, and manuscripts. Let's begin with where the journey began. Thank you Prof. Dr. Sammy W. and Prof. Dr Sara for choosing me to work on a collaborative project with two wonderful teams. I got to experience two different scientific worlds and learned a lot from both the research groups. This opportunity allowed me to explore two distinct scientific realms, and I gained invaluable knowledge from both research groups. Your dynamic support, feedback, and guidance, always just a message or email away, have been immensely appreciated. Thank you for your understanding and patience during my difficult times and for listening to my unconventional research ideas.

I extend my gratitude to all the jury members for reading my thesis, engaging in thoughtful discussions during the pre-defense, and providing invaluable feedback. I am deeply thankful to my master's thesis supervisor, Prof. Dr. Saravanan Pichiah, for introducing me to the world of research and encouraging my exploration of photocatalysis, which led me to this position. The contributions from my collaborators have been essential in enriching this thesis. I am grateful to Dr. Radu-George Ciocarlan, Prof. Dr. Pegie Cool, Dr. Joris Koek, Prof. Dr. Bert Weckhuysen, Dr. Kimberley Elbrink, Prof. Dr. Filip Kiekens, Andrea Guidetti, Prof. Dr. Sabine Van Doorslaer, Prof. Dr. Marlies Van Bael, and Prof. Dr. Saim Emin. I look forward to future collaborations with you all.

The people in both research groups have been the essence of expanding my knowledge and wisdom both scientific and non-scientific. I cannot imagine how the synthesis lab and administration would have worked without you Hilde, Annelize, Lydia and Miek. Armand, Lars, Alexander and Saeid receive a special acknowledgement for all the times I have had a problem at the microscope and one of you have bailed me out of the situation. Ritu, collaborating with you on self-assemblies and discussing plasmonics, fundamental and applied science, life in general, and beyond has been a pleasure. A big thanks to Kellie for the wonderful discussions, all the scientific guidance and showing me the path to being creative in research. Thank you Natan and Dani for helping me out in my initial PhD days. Thank you Tim for time and again helping me out with the reconstructions. Robin DM, collaborating and conversing with you has always been delightful. Another special thanks to Adrian and Thomas for teaching me a great deal about the electron microscope in the short time I could reach out to you. All the fruitful talks with Wouter, Evgenii, Saskia, Deema, Safiyye, Misha, Irina, Brend, Miulena, Wiebke, Hans, Alex, Ece, Proloy, Proloy, Sven, Robin G and Tine have helped me being comfortable with electron microscopy, a subject I knew very little at the start of my PhD. I

have had very useful discussions and fun after work events with everyone in both the research groups and also all my students.

A short lived ‘trying to make an’ entrepreneur journey with Jenthe has taught me lot. Hopefully we make it out there one day 😉 Thank you Christine for the energy boost you give all of us. Gabriele, I hope I can make it to Sicily for the delicious food. Thanks to my regular diabetes supplier - big man Tony. Thank you for the stressbuster dart games and all the fun discussions Arno (and Ritu). Fons, remember the money slogan and thanks for time to time ‘coach pain’ verses. A big thanks to the desi boyz Shahid, Ritu, Nithin and Karthick for the evening/weekend technical, political and social gossip. Thank you to the diversity team for all the fruitful discussions. My hiking adventures in Belgium and Europe is incomplete without mentioning Tom Lauriks, our love for nature, food and wild camping has been a beautiful experience. Thank you everyone for the hallway laughs/talks, tennis experience, climbing experience, barbeques, laughs over Benny Lava, dancing at Unifiesta, love for food and sleepovers at the University with people mentioned above and including Myrthe, Tess, Griet, Weichuang, Linus, Nick, Lore, Laurens, Hesam, Vincent, Allan, Donja, Marjan, Kobe, Marijn, Enrico, Naim, Luis, Julia, Hanson, Iris, Patricia, Gert and Abbas,. A thank you to all the people I have met from outside the research group and have had a nice discussion with.

I cannot leave out the great moral support I have received from my non-work related friends. Thank you to all my close friends from Pune, Lucknow, Portugal and Sweden. A big personal loss in passing away of my grandmother Radhamma during PhD has kept me humble. My father Sarotham, mother Pushpalatha and especially my brother Vinod have been a pillar supporting me all the way since my childhood and I cannot thank them enough for everything. Most of all, I thank my lovely wife Megha for being with me in all the ups and downs, the troubled time, the fun and love filled long distance destressing chats, the celebrations, our marriage, my failures and success.

BEDANKT IEDEREEN!!!

Table of contents

List of abbreviations

LSPR	Localized surface plasmon resonance
1D	One-dimensional
2D	Two-dimensional
3D	Three-dimensional
4D	Four-dimensional
NPs	Nanoparticles
CB	Conduction band
VB	Valence band
UV	Ultraviolet
VIS	Visible
NIR	Near-infrared
SERS	Surface enhanced Raman Spectroscopy
SPs	Supraparticles
M	Metal
SC	Semiconductor
EDS	Energy dispersive x-ray spectroscopy
NRs	Nanorods
PVP	Poly(vinyl pyrrolidone)
PAH	Poly(allylamine) hydrochloride
PSS	Poly(sodium 4-styrenesulfonate)
PAA	Polyacrylic acid
PANI	Poly(aniline)
SDS	Sodium dodecyl sulfate
PMAA	Poly(methacrylic acid)
LUMO	Lowest unoccupied molecular orbital
HOMO	Highest occupied molecular orbital
ROS	Reactive oxygen species
TEM	Transmission electron microscope
STEM	Scanning transmission electron microscope
SEM	Scanning electron microscope
BF	Bright field
ADF	Annular dark field
HAADF	High angle annular dark field
MAADF	Medium angle annular dark field
NFE	Near-field enhancement
ORR	Oxygen reduction reaction
WOR	Water oxidation reaction
DFT	Density function theory
FDTD	Finite-difference time-domain
CCD	Charged coupled device
SAD	Selected area diffraction
EWR	Exit wave reconstruction
WBP	Weighted back-projection

EELS	Electron Energy Loss Spectroscopy
ZLP	Zero-loss peak
ET	Electron tomography
CAT	Computed axial tomography
FIB	Focused ion beam
SNR	Signal to noise ration
EM	Expectation Maximization
SIRT	Simultaneous Iterative Reconstruction Tomography
DART	Discrete Algebraic Reconstruction Technique
TVM	Total Variation Minimization
iDPC	Integrated differential phase contrast
CS	Core-shell
SHINERS	Shell isolated nanoparticle enhanced Raman spectroscopy
TTEAIP	Titanium triethanolaminato isopropoxide
XTT	2,3-bis-(2-methoxy-4-nitro-5-sulphenyl)-(2H)-tetrazolium-5-carboxanilide
TA	Terephthalic acid
FEM	Finite element method
HER	Hydrogen evolution reaction
SA	Stearic acid
DRS	Diffused reflectance spectroscopy
PDD	Pulsed discharge detector
DMSO	Dimethyl sulfoxide
TALH	Titanium bis(ammonium lactato) dihydroxide
EPR	Electron paramagnetic resonance
riCOM	Real-time integration center of mass
SHE	Standard hydrogen electrode
TOF	Turn over frequency
MW	Molecular weight

Chapter 1: Introduction to plasmonic hybrid nanostructures for photocatalytic applications

Based on:

Rajeshreddy Ninakanti, Fons Dingenen, Rituraj Borah, Hannelore Peeters, Sammy W. Verbruggen. *Plasmonic Hybrid Nanostructures in Photocatalysis: Structures, Mechanisms, and Applications*. Top Curr Chem (2022) 380:40. https://doi.org/10.1007/s41061-022-00390-w.

Author contribution:

R.N.,F.D., R.B. and H.P. conceived the study, performed the formal analysis and wrote the paper.

S.W.V. conceived the study, supervised the work, wrote and edited the paper.

1.1 Introduction

Already for a few hundreds of years, alchemists have been coloring glass [1, 2] and other objects (*e.g.* the Lycurgus cup from the 4th century AD (Fig. 1.1) [3, 4]) with specific metal nanoparticles (NPs), yielding beautiful bright colors upon illumination. It took until the 20th century, before scientists brought the origin of these colors to light, attributing the effect to the (localized) surface plasmon resonance of plasmonic NPs [4]. Incident light with a frequency matching the natural frequency of the oscillating CB electrons of a metal NP, is strongly absorbed by these NPs. The CB electrons oscillate against the restoring force of the positive nuclei [5]. Due to this unique optical characteristic, plasmonic NPs like Au, Ag and Cu gained enormous interest over the past decades. Due to their strong interaction with UV, VIS and even near infrared (NIR) light, plasmonic NPs are envisaged as a promising light-harvesting and light-intensification structures in many important light-driven processes such as photovoltaics [6], biosensing [7], surface-enhanced Raman spectroscopy (SERS) [8] and photocatalysis [5, 9]. In view of the growing concerns over climate change, solar light mediated photocatalysis stands out as a crucial research area for sustainable energy generation. In 2019 alone, more than 43 billion metric tonnes of CO_2 were emitted [10]. Furthermore, it is believed that deep decarbonization (> 80%) is impossible without the wide use of H_2 as fuel [11]. Yet, the large-scale application of photocatalysis even with widely investigated materials, as for instance TiO_2, is still hindered by the fact that only a small portion of the solar spectrum is sufficiently energetic to drive the photocatalytic reactions using these pristine materials. Thus, the fairly large band gaps of most semiconductors only allow UV light for photoexcitation (< 5% of sunlight), while the remaining energy of the solar spectrum remains unused [4]. In this regard, plasmonic NPs provide a viable solution for more efficient utilization of the solar spectrum. The energetic coupling of their oscillating free electrons to the broad spectral incident light, results in strong enhancements in several photocatalytic processes such as water splitting [5].

1.1.1 Hybrid plasmonic nanostructures

Over the years, the field of plasmonics has been growing in different directions for improving the light-matter interaction, application-targeted functionality, chemical stability and so on. One such progressively developing field is that of hybrid plasmonic nanostructures, in which different materials with different functionalities are combined in one hybrid composite. The activity, selectivity, and stability of photoinduced processes may thus be improved by the appropriate design of such nanostructures. In this chapter, the term 'hybrid' implies nanomaterials that consist of multiple plasmonic or non-plasmonic materials, forming complex configurations in the geometry and/or at the atomic level (Fig. 1.1c). These can be broadly classified into three main categories, each with its specific structural properties. The first category deals with alloys, where the constituting elements are distributed homogeneously over the nanostructure, leading to a new set of characteristics. The combination of plasmonic with either another plasmonic or a non-plasmonic metal (with other functionalities) will be discussed in this regard. The second category includes the configurations where a plasmonic core is covered by a shell consisting of either another metal, a semiconductor or a polymer. The third category includes configurations of plasmonic self-assembled structures in both 3 dimensional assembly and 2 dimensional array in the form of films.

In the experimental part of this thesis the focus will be upon hybrid plasmonic structures using Au and TiO_2 NPs with varying configurations of core-shell, alloy, hollow and self-assembled supraparticles (SPs). In contrast to other existing reviews based on the synthesis of a certain class of bimetallic NPs [12, 13] or on the use of single or purely metallic plasmonic NPs for a certain application [5, 9, 14–16], this chapter covers the synthesis and consequent properties of plasmonic hybrids and their impact on water splitting and hydrogen peroxide generation.

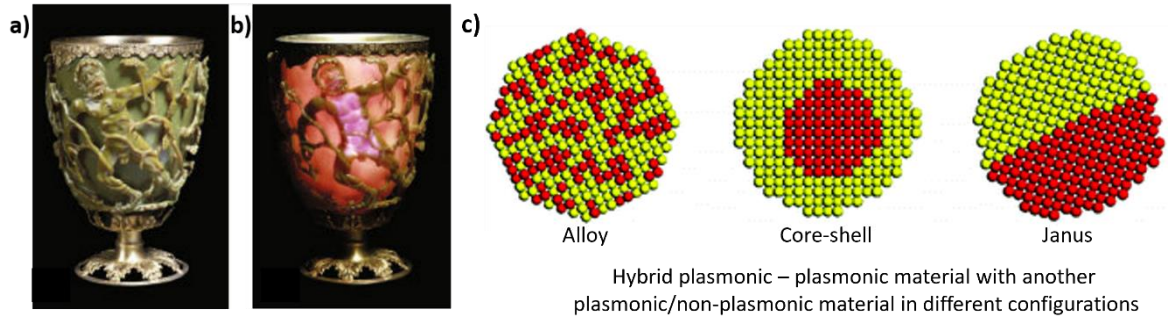

Figure 1.1: Lycurgus cup from the British Museum with illumination from a) the outside and b) the inside. The dichroism is caused by the presence of Ag (66.2%), Au (31.2%) and Cu (2.6%) NPs. The green color originates from the scattering by Ag NPs, while the red-purple is a result of the absorption by Au NPs when light is passing through the cup [17]. c) Scheme representing the different hybrid plasmonic nanostructures. Adapted with permission from [3]. CC BY-NC 2.0

In the next sections the synthesis and subsequent properties of multi metallic alloys, metal@metal, metal@SC, metal@polymer core-shell and self-assembled configurations will be discussed. This is followed by an analysis of the use of these materials to enhance the photocatalytic activity. Special attention is given here to how plasmonic hybrids are exploited to rigorously study the plasmonic photocatalytic operation mechanism. Finally, various recent innovative structures are compared towards H_2 production and H_2O_2 generation. Other important applications such as CO_2 conversion, pollutant degradation and disinfection have also been reviewed in our full article, but are omitted here for brevity, keeping the exclusive focus on hydrogen evolution [18].

1.2 Synthesis and structural properties of hybrid nanostructures

The above-mentioned main categories of plasmonic hybrid nanostructures will be treated in the following sections. Along with the synthetic techniques to obtain these different configurations, the distinct electronic and optical properties are discussed.

1.2.1 Alloyed nanostructures

When two or more metals are alloyed, the atoms are uniformly distributed in the crystal lattice. By alloying, new desired intrinsic optical properties or catalytic activity can be obtained, depending on the composition of the alloy. For instance, a second metal can be incorporated into a metal catalyst to control the surface composition, geometry of adsorption sites, selectivity, stability and electronic properties for catalysis, giving rise to a so-called ‘ensemble effect’ [19]. Additionally, the incorporation of a plasmonic metal yields a plasmonic effect, with the eye on improving photocatalytic reactions. Mixing of two or more plasmonic metals can be useful for tuning the plasmonic response itself, as well as improving the stability of the particles. Advanced synthesis techniques allow to synthesize not only mixed bimetallic and multi metallic alloy NPs, but also ordered alloys with different structuring of crystal facets [20–22].

Colloidal wet-chemical synthesis methods

As one of the best-known examples, the strongly plasmonic Ag is often alloyed with the more stable Au to prevent the oxidation of Ag [23, 24]. The simplest way to synthesize such alloy NPs is by colloidal wet chemical methods. This can be achieved by co-reduction of metal ions in solution, seed-mediated growth or galvanic replacement. Co-reduction relies on two metals having similar reduction potentials and/or similar physical characteristics, which is necessary to form a homogenous alloy. An example is the modified Turkevich method to synthesize bimetallic gold-silver alloy NPs [25]. There are several similarities between Au and Ag, *e.g*. a face-centered cubic crystal structure, similar lattice parameters (resp. 4.065 and 4.079 Å [26]) and surface energies [27]. Yet, the different reduction potentials still tend to lead to a 'core-shell type alloyed structure' with gold-rich cores and silver-rich shells, because the particle synthesis is initiated by the formation of gold seeds. This phenomenon was revealed in one of our previous studies, using energy dispersive x-ray spectroscopy (EDS) tomography at several stages throughout the synthesis procedure [25]. To obtain a more homogenous alloy, using appropriate molar ratios, reducing agents and ligands are important for the synchronized reduction of metal ions [28]. Note that there are also plasmonic NPs with an even higher tendency to be oxidized than Ag (*e.g.* Al, Mg and Cu). Their syntheses additionally require a more specialized oxygen- and water-free setup. The use of Schlenk lines and glove boxes is common for such syntheses [29, 30]. Utmost care should be taken in handling the Grignard compounds produced from such protocols. The use of oxygen-free setups deems the process challenging to bring to scale. In the presence of chemically inert Au, the synthesis of alloy NPs of AuCu by a simple co-reduction method already showed to yield stable alloy NPs compared to easily oxidizing Cu NPs [31]. Similarly, alloy NPs of different combinations, including Au, Pt, Pd, Rh, Ni *etc.*, have been synthesized by the co-reduction method [32–35]. Seed-mediated procedures can be used for the growth of different metal ions on separate crystal facets of the seed to have more control over the shape of the NPs [36], although it does not lead to homogeneous alloys and is more suitable for core-shell type structures [37, 38]. Thus, a subsequent thermal alloying step is important in seed-mediated processes for uniform distribution of the constituting elements. Furthermore, for galvanic replacement, one metal is oxidized, *i.e*. the sacrificial agent, by ions of another metal with a higher redox potential. Complex bi- and trimetallic alloyed structures can hence be formed [39–41]. However, this technique is more prevalent for the synthesis of core-shell NPs (see section 1.2.2) [42, 43].

In order to gain more control over the NP size distribution in colloidal syntheses, microreactor-based approaches are nowadays being studied [44, 45]. Here, reagents are introduced through microchannels at pre-decided flow conditions. Uniform mixing in the microliter regime results in the production of a highly monodisperse colloidal solution of NPs with an increased control over the size and shape [44]. By simply varying the flow conditions, different structures may be formed in a continuous flow. This offers an important time advantage over time-consuming trial-and-error syntheses using a batch setup. Nonetheless, understanding and controlling the flow and mixing conditions with high precision is challenging in a microreactor [45]. On the other hand, innovative colloidal synthesis techniques such as probe-based lithography also give a more controlled and varied geometry of NPs on a support material [46].

Physical synthesis methods

Although colloidal wet chemistry synthesis strategies have evolved significantly over recent years, they do not offer the highest degree of alloy structure control [25, 47]. For the formation of a more homogenous AuAg alloy, sophisticated physical methods such as laser ablation are preferred [47, 48]. As mentioned before, the wet chemical modified Turkevich method leads to the formation of 'core-shell type alloys' (Fig. 1.2a), while laser ablation generates a more homogenous alloy (Fig. 1.2b). The latter is partially attributed to having no deviations from Vegard's law which states that a linear relation exists at a constant temperature, between the crystal lattice constant of an alloy and the concentrations of the constituting elements. Compared to laser ablation, colloidal synthesis induces negative deviations to Vergard's law forming a non-homogenous alloy [47–51]. In laser ablation, the laser energy is absorbed by a macroscopic target material, generating a plasma. This plasma expands and condenses in the liquid environment, forming nano-size materials due to cavitation. Therefore, it can be considered as a combined top-down (target material) and bottom-up (NPs from generation of plasma) approach. Laser ablation is more ecofriendly as laser irradiation produces species with high energy states without producing byproducts and without the need for further high temperature treatment. Ligand-free alloys are often produced with no additional chemical agents, apart from the solvent [47]. Very recently, laser ablation has also been used to form alloys by co-reduction of Au and Ag ions [52]. The high initial cost of laser techniques is a drawback. Yet, considering operational costs at large scale, a study discussed laser ablation to be cost-effective in the long run. Currently used at an industrial scale, laser ablation can give output of NPs in the range of grams per hour, compared to milligrams per hour for wet chemical synthesis methods [53]. Magnetron sputtering can provide a homogeneous multi metal alloy, but is rather limited to be used as a film deposited on a substrate. Consequently, it is difficult to hybridize sputtered metal NPs with another metal, semiconductor, polymer *etc.* [54–56]. Similarly, other chemical and physical methods, such as chemical vapor deposition, lithographic patterning, thermal decomposition, plasma synthesis *etc.*, are either time-consuming, expensive or do not yield a good control over the structural properties for hybrid systems [57–60].

Optical and electronic properties

As mentioned above, the combination of metals as alloys allows the tuning of optical properties. For instance, alloying of Au and Ag leads to an optical response which is the intermediary of those of pure Au and Ag [61]. Classically, the optical constants for different alloy compositions can be conveniently modelled with the Lorentz-Drude oscillator framework. Here, the interband transitions introduced by Au are captured by a suitable number of Lorentzian oscillators [62]. By increasing the Au fraction, the LSPR of NPs can be redshifted with respect to pure Ag NPs, towards the LSPR of pure Au NPs, as observed from UV-VIS absorption spectra in Fig. 1.2c. This results in structures with a larger VIS light absorption component. However, the incorporation of Au also leads to interband transitions that suppress the overall plasmonic enhancement [63, 64]. The advantage of alloying over incorporation of Au as a shell, core or a Janus particle, is that the compositional homogeneity provides a proportionate displacement of the LSPR with changing composition [62]. In the case of core-shell structures, the hybridization of the individual plasmon modes of the core and shell leads to complex spectral features [65, 66]. The proportionate variation of the extinction spectra of AuAg alloy NPs against the very complex extinction spectra of Au@Ag

core-shell can be clearly observed from the examples in Fig. 1.2c and d. The optical features of core-shell NPs will be further discussed in section 1.2.2.

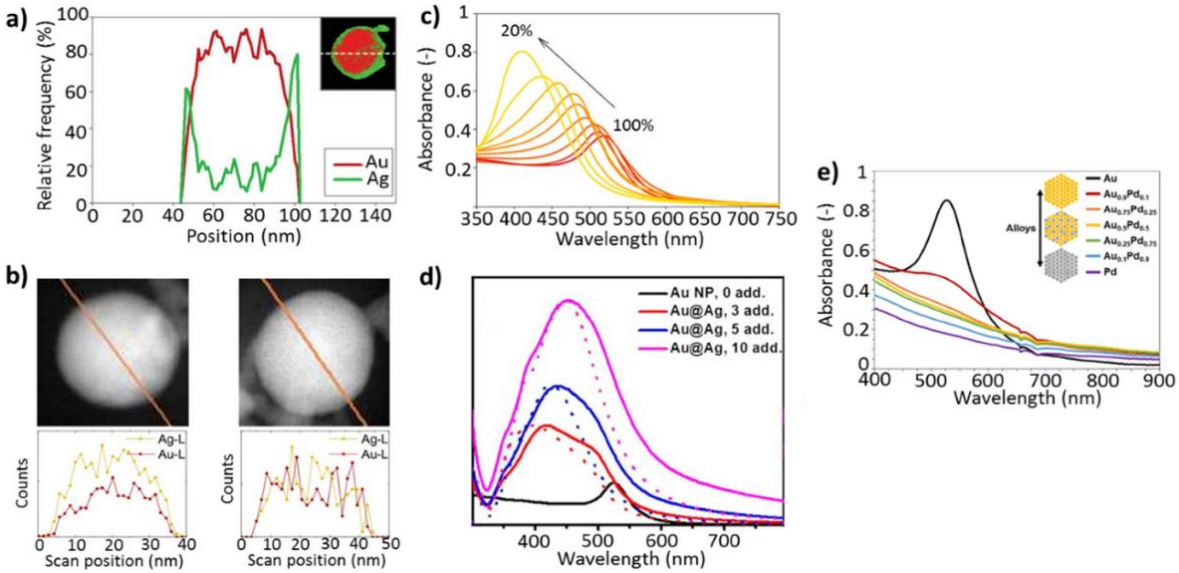

Figure 1.2: Schematic representations of an EDS line scan of AuAg alloy NPs synthesized by a) wet chemical co-reduction and b) laser ablation. c) Blueshift of the plasmon absorption band with decreasing Au percentage in AuAg alloy. d) Absorption spectra of Au@Ag core-shell NPs. e) Absorption spectra of a AuPd alloy with a sudden decrease of Au LSPR band with minor addition of Pd. Adapted with permission from a) [25]. Copyright (2019) John Wiley & Sons, b) [47] CC BY-NC 3.0, c) [61]. Copyright 2016 Elsevier , d)[66]. Copyright (2013), American Chemical Society and e) [67] CC BY 4.0

Also, other alloy combinations including catalytic elements such as Pd, Pt *etc.* and earth-abundant plasmonic metals such as Cu, Al, Mg *etc.*, gained considerable attention due to their promising application potential [32, 68, 69]. For instance, the incorporation of Cu in AuCu alloy NPs of different shapes such as nanospheres, nanorods, nanocubes, nanopentacles *etc*. further push the LSPR band towards the red end of the visible light spectrum as compared to pure Au [31, 70–72]. For AuPd alloy systems, Pd introduces some specific catalytic activity, although it also progressively suppresses the plasmonic excitation, even by an addition as small as 10% (Fig. 1.2e) [61]. This is due to the large absolute values of the real part and the relatively lower values of the imaginary part of the dielectric constants [73]. On the other hand, the sharp gradient of the imaginary dielectric constant enhances the refractive index sensitivity of the nanostructures [74]. For small NPs, < 10 nm, with weaker resonance (either due to size or quantum effects), the addition of a small fraction of a catalytic metal can quench the characteristic plasmonic response [75]. Due to a limited solid-phase solubility, the combination of Au and Pt limits the maximum size to 6 nm for full alloying. A strong SPR effect remains difficult for AuPt alloys with these very small sizes [75]. Similarly, such a limit in the solubility of Ag and Pt also leads to the tendency of forming core-shell structures [76]. Still, the addition of such catalytically active metals like Pd and Pt can certainly be beneficial. Several studies have already shown an enhancement in catalytic activity using alloy NPs due to a change in the electronic structure [61, 67, 70, 77, 78]. Alloying causes a shift in *d* band levels with respect to the Fermi energy levels and therefore affecting the overall reactivity. The dielectric constant of an alloy is not just a linear combination of that of the individual metals, partly due to changes in the *d* band structure. In AuPd alloys, Pd loses *s* and *p* band electrons to Au and gains *d* band electrons

from Au and *vice versa* [77]. Alloying also introduces different interband and intraband transition states compared to their single metallic counterparts [79]. For example, alloying of Ag with Au can lead to suppression of interband excitations and favor intraband excitations which eventually results in higher hot electron energies [78]. The hot electron energy transfer also depends on the work function and the Fermi energy levels and therefore can be different for various materials including different alloys. Typically, it is ideal for the work function to be closer to the Fermi energy levels. These higher hot electron energies are eventually useful for photocatalytic reactions and will be further discussed in section 1.3 [80]. It is important to note that to understand the properties of the wide spectrum of available materials, intensive computational studies are required. For example, Keast *et al.* (2014) studied the plasmonic response of alloying Au with various metal to show that only a set of combinations ($AuAl_2$, Au_3Cd, AuMg, AuCd and AuZn) would have a better plasmonic response [81]. Although most of the computational studies focus only on one aspect such as optical plasmonic response [65] or hot electron injection to band structure [82, 83], one alloy combination may behave differently for other catalytic reactions due to various other reasons, such as surface selectivity or surface energy. Therefore, rational design of materials is needed for each specific application (see section 1.3).

1.2.2 Core-shell

When the constituting materials (metal, semiconductors or polymers) are not homogeneously distributed throughout the nanostructure volume, the intrinsic functionalities of the components remain (largely) intact [84, 85]. It is important to note that the plasmonic component is influenced extrinsically by the presence of the other components, such as an extra shell. For instance, a major effect present in most plasmonic core-dielectric shell configurations is the redshift of the plasmon band as the refractive index of the dielectric environment, *i.e.* the shell, increases [23, 86–89]. In the following section, different core-shell configurations are discussed in sub-classes.

1.2.2.1 Metal@metal

Synthesis methods

Metal@metal core-shell NPs are more commonly synthesized using colloidal synthesis methods with satisfactory control over NP size, shape and morphology [97]. Co-reduction of metal precursors can yield core-shell structures when the difference between the reduction potentials of the constituting elements is sufficiently large [66]. In such systems, galvanic replacement can also lead to metal@metal core-shell structures with sub-nanometer shell thickness control [92]. During galvanic replacement, one element in a crystal lattice is replaced by another with higher reduction potential. Certain reagent mixtures, such as Ag NPs with Au3+ ions, always lead to spontaneous reactions. While the higher electronegativity of Au (1.9) than Ag (1.6) facilitates spontaneous formation of hollow Ag@Au core-shell systems by galvanic replacement, the formation of an Ag shell on Au NPs requires a reducing agent [98, 99].

With the recent advances, the synthesis procedures of core-shell NPs (just as for alloy NPs) have been developing in different directions such as microreactor-based synthesis, lithography and laser ablation [100–102]. Some techniques are also specifically convenient for the synthesis of bimetallic core-shell NPs. For instance, Forcherio et al. (2018) generated a core-shell morphology by exploiting the plasmonic excitation of the Au NP cores themselves. Sub 5 nm epitaxial growth of Pt ions could

be achieved at plasmonic hot spots. The photodeposition of Pt on Au nanorods was activated by the longitudinal surface plasmon excitation of the nanorods [103]. Thus, a thicker shell was formed at the Au nanorod tips, compared to the rest of the nanorod (the mean length extended by 4.7 nm, while the diameter only increased by 0.72 nm). This is due to the fact that the longitudinal plasmon mode is manifold stronger than the transverse mode perpendicular to the axis of the nanorod. Another unique method for obtaining core-shell structures is oxidative etching. Van der Hoeven et al. (2021) generated core-shell morphologies by the etching of Au@SiO_2 NPs using H_2O_2 followed by the addition of a shell metal (Ag, Pd or Pt) precursor. Thermal annealing resulted in better control over the shell morphology, while the shell thickness could be regulated from 3 nm to 10 nm via the metal overgrowth reaction time and precursor concentration [104]. The importance of the latter parameter cannot be underestimated. Huang et al. (2017) used transient absorption spectroscopy to show how the shell thickness affects the hot electron decay pathways in Au@Pd NRs. It was shown that, with the increase in shell thickness from only 0.4 to 2.8 nm, corresponding to 2 to 14 monolayers, Au's hot electrons interacted more with the Pd interface lattice. This led to increased heat generation with a decrease in their recombination rate. For a thicker shell of 5.4 nm or 27 monolayers, hot electrons were generated in the Pd shell itself, thereby having slower electron-phonon scattering relaxation of Au-generated hot electrons. Consequently, a lower ethylbenzene yield was recorded for the styrene hydrogenation reaction after 1h of 100 mW.cm-2 illumination (52% for 27 monolayers vs. 76% for 14 monolayers) [84]. In contrast, van der Hoeven et al. (2021) showed an optimal shell thickness of 6 atomic Pd monolayers around a gold NR core covered with mesoporous SiO_2 (Fig. 1.3c). They also showed that single-crystalline Au@Pd core-shell structures performed more than 30 times better than the alloyed equivalents, displaying TOFs of resp. 34.7 and 1.1 s-1 for the butadiene hydrogenation at 60°C (Fig. 1.3d) [85].

Optical and electronic properties

A metal@metal core-shell configuration can broadly be of two kinds. Firstly, both the core and the shell can be plasmonic metals. Secondly, a plasmonic core or shell can also be combined with a shell or core of catalytic metal(s). In the first system, including combinations of Au, Ag, Cu, Al *etc.*, the optical properties are considerably different from their alloy counterparts. In the case of AuAg alloys, the extinction spectra shift linearly from the blue to red spectral region with increasing Au fraction (Au%) (Fig. 1.2c). Whereas in Au@Ag core-shell systems, the hybridization of the individual plasmon modes of the core and the shell gives rise to band broadening and complicated trends of the LSPR absorption band vs. Au% (Fig. 1.2d) [66]. The theoretical framework of plasmonic hybridization given by Nordlander and co-workers (2003) is inspired by the molecular orbital hybridization theory and works well in explaining the optical response of core-shell NPs [90]. Kamimura *et al.* (2017) studied core-shell Au@Ag/$SrTiO_3$ vs. alloyed AuAg/$SrTiO_3$ for converting isopropanol to acetone and CO_2. It was shown that Ag in the AuAg alloy oxidizes, while being more stable by forming a shell in a core-shell structure. The authors explained the stability by stating that the chemical stability of the Ag shell can be enhanced by coupling to the Au core due to a charge transfer. This should increase electron density within the Ag shell, yielding a negative Ag oxidation state [91]. With the growing importance towards more abundant, but chemically unstable, plasmonic materials such as Cu, Al and Mg, incorporation of a thin shell of Au is seen as a viable stabilization strategy [92]. Use of Au as a shell is less detrimental to the plasmonic effect of the

nanostructures as shown for Cu@Au NPs, especially compared to the use of catalytic shells having a lower plasmonic response with plasmonic cores (*e.g.* Au@Pt) (Fig. 1.3a,b) [92, 93].

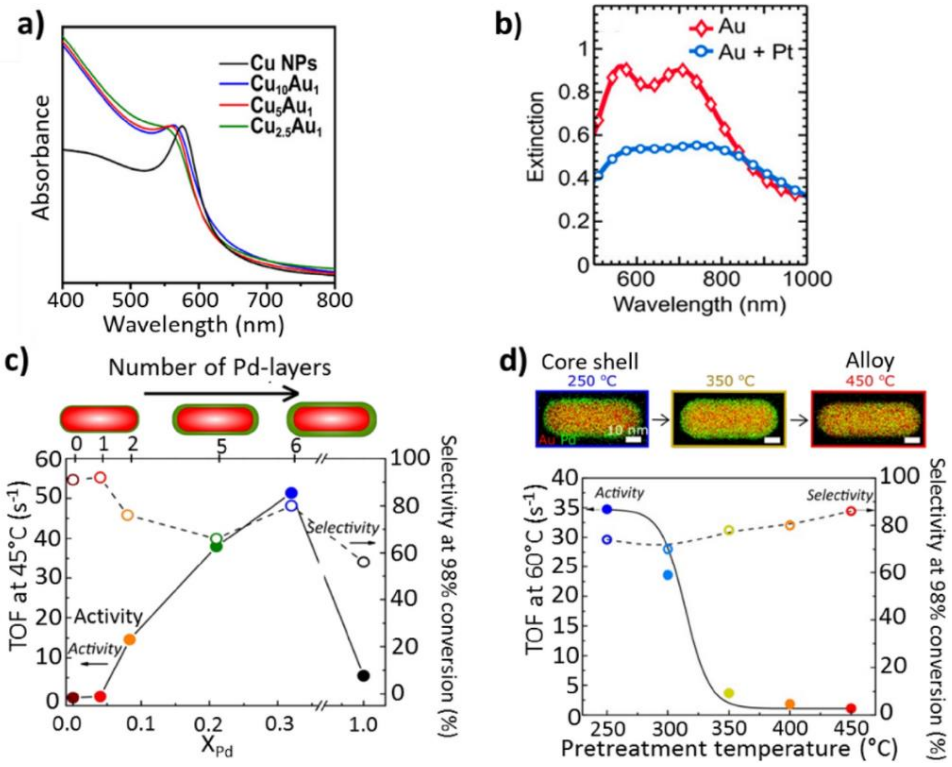

Figure 1.3: Schematic representation of a) the blueshift in UV-VIS absorption spectra of Cu@Au core-shell and b) a dampened UV-VIS response of Au@Pt core-shell NP. Change in activity (represented by the turnover frequency (TOF)) and selectivity in Au@Pd core-shell NPs with c) increasing Pd shell thickness and d) gradually changing from core-shell to alloy. Adapted with permission from a) [92]. Copyright (2021) American Chemical Society, b) [93]. Copyright (2017) American Chemical Society, c-d) [85]. Copyright (2021) Springer Nature

On the other hand, core-shell systems using a catalytic shell may still be preferred, depending on the application (*e.g.* Au@Pd systems for Heck coupling) [94]. In this second class, the plasmonic metal acts as an 'antenna' and the non-plasmonic material as the adsorbing and reactive surface [95]. The optical and electronic properties of the plasmonic materials are thus utilized to enhance the reactivity of the non-plasmonic material. Whereas in alloys, a complete new set of intrinsic properties is formed, in the case of core-shell NPs, the non-plasmonic shell has an extrinsic effect on the plasmonic core [4]. For instance, as mentioned above, a Pt shell around Au nanorods increasingly dampens the plasmonic absorption intensity of the nanorods with increasing shell thickness due to the non-plasmonic absorption of light by the Pt shell (Fig. 1.3b) [93]. Similar to Au@Pt, the extinction spectra of Ag@Pd core-shell NPs are different from the extinction spectra of either Au or Pd. The general trend is that the LSPR in extinction spectra loses intensity along with a blueshift or redshift of the resonance frequency, while the spectral shape is broadened due to the coupling of both materials. Besides the optical properties, bimetallic core-shells can have starkly different catalytic activities from their alloy counterparts. For example, several Au@Pd core-shell configurations, esp. with sharp branches, may have a slightly higher yield compared to AuPd alloys for both the Suzuki-Miyaura and Heck reactions (conversions of resp. ~80-90 vs. up to 99%) [94].

Core-shell systems can furthermore be more easily tuned towards an antenna-reactor system within their structure as compared to alloyed systems. An electronic and optical coupling with the plasmonic core hence enables enhanced activities [96].

1.2.2.2 Metal@semiconductor

Synthesis methods

Instead of simply depositing plasmonic NPs on top of SCs, both can also be combined as core-shell nanostructures. Mostly, SCs are introduced to plasmonic NPs for photocatalytic and stability purposes. In metal@SC systems, the metal and the SC crystals are connected by a Schottky junction that facilitates electron-hole separation at the semiconductor. In general, most of the works on metal@SC structures has been with TiO_2 as the shell covering a plasmonic core, resulting in structures like Au@TiO_2, Ag@TiO_2 and Cu@TiO_2 [87–89]. Photocatalytic semiconductors mostly include metal oxides and chalcogenides. The most convenient way to synthesize metal@SC core-shell nanostructures is by growing a shell of metal oxide precursor over plasmonic NPs. For the shell growth, metal oxide precursors are added to colloidal plasmonic NPs and the precursor molecules bind to the surface ligands on the particle surface [85]. Using the metal oxide precursor itself as the reducing and capping agent for the formation of plasmonic NPs, further simplifies the process [97]. Generally, titanium isopropoxide, titanium butoxide or titanium fluoride are used as Ti precursors, forming crystalline TiO_2 shells from 5 nm to more than 100 nm in thickness [87, 98] . In order to form uniform shells, controlled interaction of the precursor with the capping ligands and controlled hydrolysis and condensation of the precursors, are highly important. Anhydrous solvents or slow hydrolyzing precursors such as titanium(IV) (triethanoloaminato) isopropoxide tend to give a more uniform shells of thicknesses down to 2 nm (Fig. 1.4d) [99]. Since unstable metals like Ag, Cu and Al may oxidize during the subsequent annealing step required for crystallization of the oxide shell, hydrothermal crystallization procedures are often adopted. Alternatively, the photothermal effect of the plasmonic NPs itself can also be used for controlled TiO_2 shell formation by laser irradiation [100]. Different configurations such as Ag@TiO_2 NW arrays can also be formed using templated lithography [101]. The feasibility of core-shell structures by atomic layer deposition of ZnO on Ag NPs was demonstrated as well [102]. The effect of the metal oxide shell comes from the interband excitations as well as elastic scattering. For instance, a dielectric SiO_2 shell around plasmonic NPs contributes to the total scattering. This increasingly dampens the plasmon band with increasing shell thickness [103]. Importantly, it was also shown for Au@Cu_2O core-shell systems that the plasmonic response of the core depends on the crystal facets of the shell, which enable further optical tuning of these hybrid structures [104]. Note that sometimes M@SC core-shell materials form spontaneously. For instance, Al oxidizes very easily, generating a thin 2-3 nm self-limiting oxidized layer [105]. Better stabilization strategies are required for such chemically unstable metals in order to use them in realistic photocatalytic applications at industrial scale.

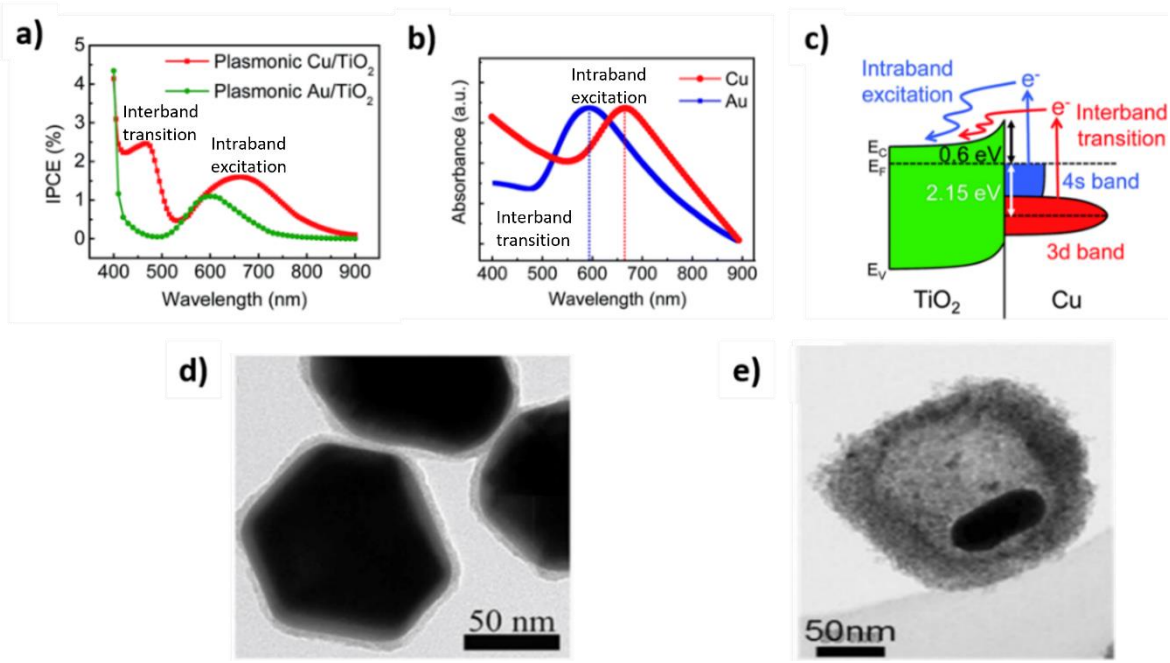

Figure 1.4: Schematic representation of the interband transition and intraband excitation in a) $Au@TiO_2$ vs. $Cu@TiO_2$ material system, showing the incident-photon-to-current efficiency (IPCE) as a function of the wavelength and b) single Cu and Au NPs. c) Contribution of both intraband excitation and interband transition in $Cu@TiO_2$ contact material system. TEM image of d) $Au@TiO_2$ core-shell NP and e) $Au@TiO_2$ nanorod yolk-shell structure. Adapted with permission from a-c) [80]. CC BY-NC 3.0, d) [99]. CC BY-NC-ND 4.0, e) [106]. Copyright (2015) John Wiley and Sons

In the past decades, also more VIS light active SCs such as Cu_2O, g-C_3N_4, CuS, CdS *etc.*, gained considerable attention for constructing plasmonic hybrids [107–110]. Lee *et al.* (2018) developed $Ag@Cu_2O$ NPs with varying shell thickness and observed a higher photocatalytic activity with increasing shell thickness. Photocatalytic degradation of methyl orange (MO) under VIS light with 11 nm Ag core@11 nm Cu_2O shell NPs was completed in 1h compared to only ~5% degradation by Cu_2O NPs. The higher activity was ascribed to the increase in surface area from 14 $m^2.g^{-1}$ to 25 $m^2.g^{-1}$ as well as the stabilization by the increasing shell thickness. Density functional theory (DFT) studies showed that as Cu_2O is in a metastable state, a thin shell of about 5 nm Cu_2O transforms into CuO and detaches from Ag. On the contrary, with thicker shells of about 15 nm, Cu_2O holds Ag and CuO together. This is explained by the large adhesion force between Cu_2O and CuO or Ag as compared to the adhesion forces between CuO and Ag. The long-term stability of Cu_2O is still an issue [109]. Interesting non-oxide semiconductors studies include the work of Ma *et al.* (2020). Four gap-(Au/AgAu)@CdS nanostructures were synthesized using several Ag and Au shell growth and galvanic replacement cycles. The nanoscale Kirkendall effect yielded nanogaps that resulted in efficient plasmonic coupling. Hence, broad absorption from UV to NIR was created, increasing the H_2 production activity under VIS light ($\lambda > 420$ nm) 47 times compared to Au@CdS without nanogaps (4.71 vs. 0.10 $mmol.g^{-1}.h^{-1}$) [108]. This configuration maintains its activity over 24h. Nonetheless, CdS is susceptible to photo corrosion. Thus, further modifications may be necessary for true long-term photostability [111].

Optical and electronic properties

When selecting a semiconductor shell, an important aspect is the band structure of the material. The characteristics of the metal@SC interface depend on the Fermi level of the metal and the relative position of the band edge potentials of the SC. The induced electronic states at the interface may play a role as well [112]. For a higher visible light activity, a small band gap (1.6 to 3 eV) is preferred. Yet, the CB level should be high enough and VB level should be low enough for the desired redox reactions to be enabled. *E.g.* for H_2 evolution, the former should be at least -0.413 V vs. NHE (normal hydrogen electrode). The plasmonic metal should also be carefully chosen, as selection of plasmonic cores with a strong plasmonic excitement does not necessarily guarantee effective energy transfer and thus activity enhancement of the semiconductor shell. Interband and intraband energy levels also play a very important role in energy transfer from metal to semiconductor. Studies have revealed Cu@TiO_2 lead to higher hot electron injection compared to Au@TiO_2. Cu@TiO_2 contributes to both interband and intraband energies with a lower Schottky barrier height, whereas Au@TiO_2 has a greater interband energy, but also a greater Schottky barrier height, leading to inefficient hot electron extraction (Fig. 1.4a-c) [80]. Hence, using an alloy NP with an appropriate energy band structure as a core would be promising [78]. More detailed mechanistic insights are provided in section 1.3.

Yolk-shell structures

Finally, yolk-shell structures can be considered as an extension of core-shell configurations. As seen in Fig. 1.4e, it consist of a plasmonic core material covered by a hollow shell of, for instance, a SC material. Such structures yield different optical properties as only a fraction of the plasmonic core material is in physical contact with the shell. The cavity volume leads to total internal reflections which enable the incoming light to be further used for photocatalytic reactions [113]. Au@TiO_2 yolk-shell structures were shown to have a reflectance of less than 15% compared to 63% for commercial P25 TiO_2. This is thus attributed to the internal reflections within the cavity of the yolk-shell structure [114]. For obtaining such structures, one can use a sacrificial material (*e.g.* organic compounds) to form a temporary shell. The latter will be removed after the real SC shell formation [115].

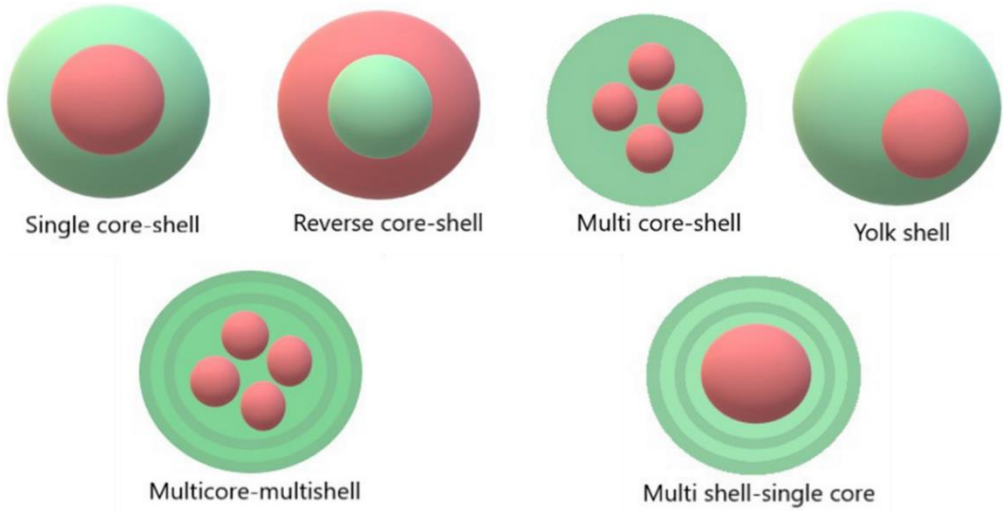

Figure 1.5: Schematic core-shell structure with different proposed configurations and related properties. Adapted with permission from [116].

Apart from sacrificial templating, other mechanisms such as Ostwald ripening and the Kirkendall effect may also lead to a yolk-shell structure [117, 118]. Along with a change in the optical properties, such structures make way for higher specific surface areas. Li *et al*. (2015) reported a surface area of 310 $m^2.g^{-1}$ for yolk-shell Au@TiO_2 NRs compared to 56.9 $m^2.g^{-1}$ for Au@TiO_2 core-shell NPs [106]. For more details, one can refer to the outstanding review of Li *et al*. (2019) on the complex formation mechanism of yolk-shell nanostructures along with the photocatalytic mechanisms involved [113]. Different forms of core-shell configurations have been proposed in Fig. 1.5 with yolk-shell being the most promising and easy to synthesize among other especially for plasmon enhanced photocatalysis[116].

1.2.2.3 Metal@polymer

Synthesis methods

Introducing an organic layer around metal NPs might be of interest for several reasons such as improving stability, ensuring compatibility with organic solvents, influencing the activity and improving the optical properties. Firstly, a distinction should be made between surface ligands and polymer shells. Surface ligands such as thiols, amines, oleate, xanthate *etc*., are often used for the colloidal stabilization of plasmonic NPs [119, 120]. In some instances, the same reagent can function as both reducing agent and the stabilizer. *E.g.,* citrate in the modified Turkevich method for the synthesis of Au_xAg_{1-x} NPs [25, 61, 121, 122]. The longer the alkyl chain, the easier the transfer to organic media, although nonpolar solvents may remain difficult for the suspension of plasmonic NPs [120, 123].

Polymer shells, can be created around the NPs by a separate polymerization step [123] or in a simultaneous process of NP and shell formation [124]. Other synthesis methods such as electrospinning provide geometric confinement from nanofibers and therefore bring control over the optical and electrical properties. Chen *et al.* (2014) prepared Ag@poly(vinyl pyrrolidone) (PVP) nanofibers by coaxial core-shell electrospinning with $Ag(NH_3)_2^+$ [125]. The PVP enabled appropriate viscoelastic properties for the nanofiber patterns and protection of Ag, which proved to be more effective than for smaller molecules like citrate [126]. However, the drawback with most organic linkers and single polymers is the lack of shell thickness control [23]. This is of paramount importance as the near-field enhancement (NFE) generated by the excited plasmonic NPs decreases with distance and the coupling of plasmons is strongly distance dependent as well [5]. Since the reaction rate of photocatalytic reactions is proportional to the square of the near-field, stronger electromagnetic fields are highly beneficial for photocatalytic reactions (*cfr*. section 1.3.1.1) [5]. In order to meet these requirements of accurate control over thin shell thicknesses, the LbL technique has been applied where alternatingly different polymer layers are deposited around a metal core. Schneider and Decher introduced the use of polyelectrolytes to 13.5 nm Au NPs, namely the positively charged poly(allylamine) hydrochloride (PAH) and negatively charged poly(sodium 4-styrenesulfonate) (PSS). Up to at least 20 layers could be applied based on electrostatic attraction, with minimal particle aggregation (> 95% NP recovery), yielding 7.5 nm shells [127]. To prepare eventual scale-up, they determined the range of practical concentrations to avoid bridging flocculation [128]. Asapu *et al.* (2017) further improved the LbL protocol by replacing PSS by the cheaper polyacrylic acid (PAA), also lowering the deposition time from 12 to 0.5h [23]. These LbL

stabilized Ag NPs were shown to be ultra stable in harsh reactive environments (hot air and NaCl solutions) [23]. The aforementioned polymers are yet all non-conductive which excludes the potential transfer of hot electrons (see also section 1.3.1.1). Therefore, the use of conductive polymers such as poly(3,4-ethylene dioxythiophene), poly(pyrole) and poly(aniline) (PANI) have also been studied [124, 129]. Xing *et al.* (2009) designed a kinetically controlled *in-situ* polymerization protocol for aniline with sodium dodecyl sulfate (SDS) on the Au surface. This one-step synthesis enables control over the shell thickness by adjusting the polymerization time. Shells on 22 nm Au nanospheres grew up to 14 nm after 4h (Fig. 1.6a). A further increase (14-92 nm) was achieved after multiple growth cycles by this 'mix-and-wait' technique (Fig. 1.6b-f) [124]. Asapu *et al.* (2019) compared varying thickness of PANI shells against polymer shells of PAH and PSS synthesized using LbL strategy. Conductivity of PANI shells was effectively proven using conductive tip atomic force microscopy [86].

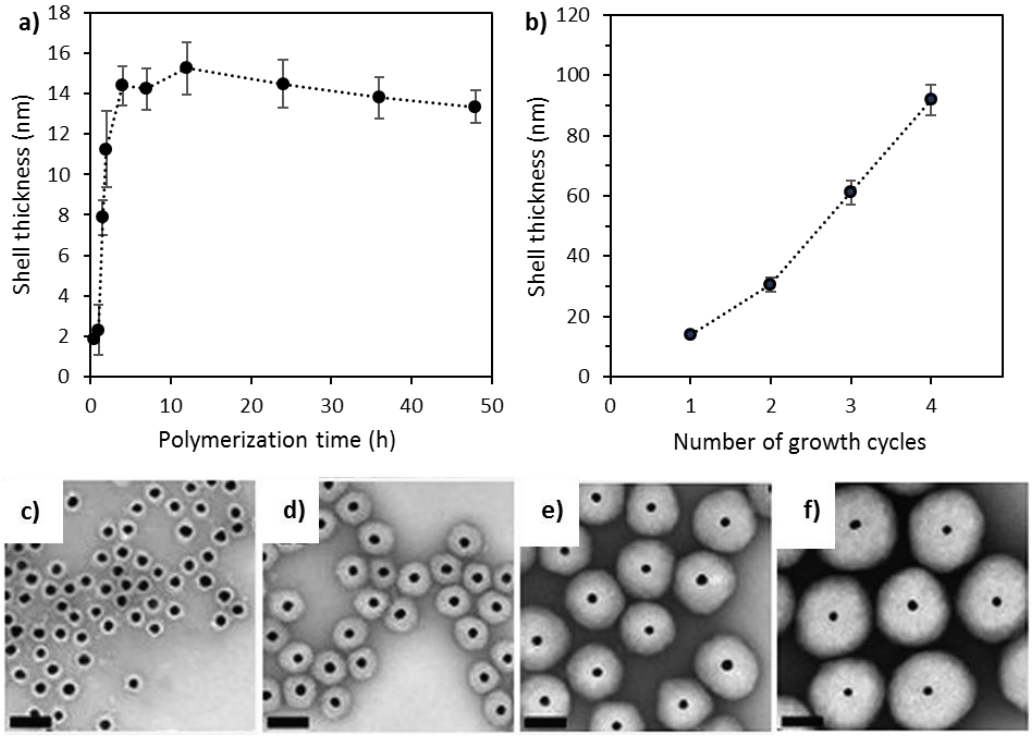

Figure 1.6: a) PANI shell thickness for 22 nm Au@PANI NPs in 1 'mix-and-wait-cycle' b) PANI shell thickness for multiple growth cycles with c-f) TEM images after resp. 1, 2, 3 and 4 growth cycles. Scale bars correspond to 100 nm. Adapted with permission from [124] . Copyright (2009) Royal Society of Chemistry.

Optical and electronic properties

The addition of a polymer shell also affects the optical properties due to the change in the dielectric environment [130]. As mentioned before, an increasing refractive index yields spectral redshifts, while the opposite leads to spectral blueshifts. Thus, small redshifts (1-3 nm) in the UV-VIS spectra can be observed with the formation of each PAH and PAA polymer layer over Ag, Au and AuAg alloy nanospheres in the LbL process [23, 86, 131]. On the other hand, Lisunova *et al.* (2012) demonstrated blueshifts after the addition of PVP or PMAA. When the fluorescent poly(*p*-phenylene ethynylene) was coated as final layer on this LbL assembly, the actual shell thickness did not seem to change the fluorescence peak positions [132]. Recently, more research has been done

on ‘plasmonic switching’ where shifts are quickly induced for metal@polymer NPs. Lu *et al.* (2016) showed that when applying small potentials (-0.1 - +0.5 V vs. $V_{AgCl|Ag}$), large plasmon shifts up to 150 nm can be attained for both colloidal Au nanospheres, NRs and nanobipyramids covered by PANI. The small potential changes enable swift switching in less than 10 ms between the half-oxidized and fully reduced states, without degradation of the PANI shell. This is 20,000 times faster than for proton doping and de-doping by adding acids or bases [130].

1.2.3 Self-assembly of plasmonic 3D suprastructures and 2D arrays

Other than the shape and the configurations discussed in the sections above, the organization of plasmonic NPs in small clusters or in lattices comprising thousands of NPs offers another degree of freedom in controlling and tuning their optical properties by coupling surface plasmons of adjacent NPs, thereby enhancing the electric field in interparticle gaps (in the so-called ‘‘hot spots’’) and hot electron generation/injection. Control over plasmonic properties of self-assembled nanostructures can be achieved by changing the number of NPs in the cluster, by varying the directionality of NP organization, and by finetuning interparticle distance, in addition to changing the composition, size and shape of individual NPs. While self-assembly is a very broad topic, in this section we will discuss only a few methods directed particularly towards the self-assembly of plasmonic NPs and their plasmonic properties. For a complete review of self-assembled nano-structures, the reader is directed towards other extensive articles on the topic[133].

A major part of early studies on the properties of plasmonic NP ensembles have been performed for clusters fabricated by electron beam lithography, however, this time and labor consuming process has a limited resolution of 2-5 nm and may lead to the formation of NPs with a rough surface and multiple crystalline domains[134, 135]. Colloidal self-assembly of plasmonic NPs offers the ability to reduce interparticle distance to 0.5-1 nm based on the technique and the type of ligands used in the process. Furthermore, colloidal self-assembly enables the fabrication of NP ensembles with a high complexity and can produce nanostructures with hierarchical architectures, which is challenging or not possible for conventional top-bottom technologies.

The organization of NPs in plasmonic nanostructures with well-defined geometries can be achieved in several ways, namely, by carefully tuning nanoscale forces acting between NPs is solution, by using various types of templates and by applying external fields, e.g., a shear field or electric field. It should be noted that that although a particular force may dominate the self-assembly process, in reality, the formation of a particular structure originates from the interplay of several forces. For example, for gold NPs functionalized with poly([2-(dimethylamino)ethyl] methacrylate) ligands, a decrease in pH was used to protonate the polymer and decrease the NP charge. Adjusting the pH of the system allowed for control of the aggregation number of the NP assemblies (Fig. 1.7a-b). The UV-Vis spectra in Fig. 1.7c, shows an additional plasmon band arising from interaction of the NP chains[136]. Going further, in emulsion directed self-assembly oil-in-water (or vice-versa) based emulsion can sustain micro-droplets trapping the colloidal NPs and form a 3D self-assembly with driving forces from the ligand type. Control in the size of assembly can be achieved by changing number of NPs, type of ligand, type of oil etc.[137]. A reverse emulsion based assembly was used to form black plasmonic Au colloidosomes (Fig. 1.7d). Compared to nano-chains, the UV-Vis absorbance spectra of colloidosomes is spread out across the complete visible region (Fig 1.7g)

making it advantageous for photothermal applications[138, 139]. Near-field coupling in assemblies of metal NP results in enhancement of electromagnetic field in the nanoscale gaps between NPs, which are referred to as 'hotspots''. This phenomenon can be observed in Fig. 1.7e-f, wherein the Au colloidosomes have an increased electromagnetic field compared to an array of Au NPs[140]. Such an enhancement in near-field is extremely useful for molecular and biological applications[141].

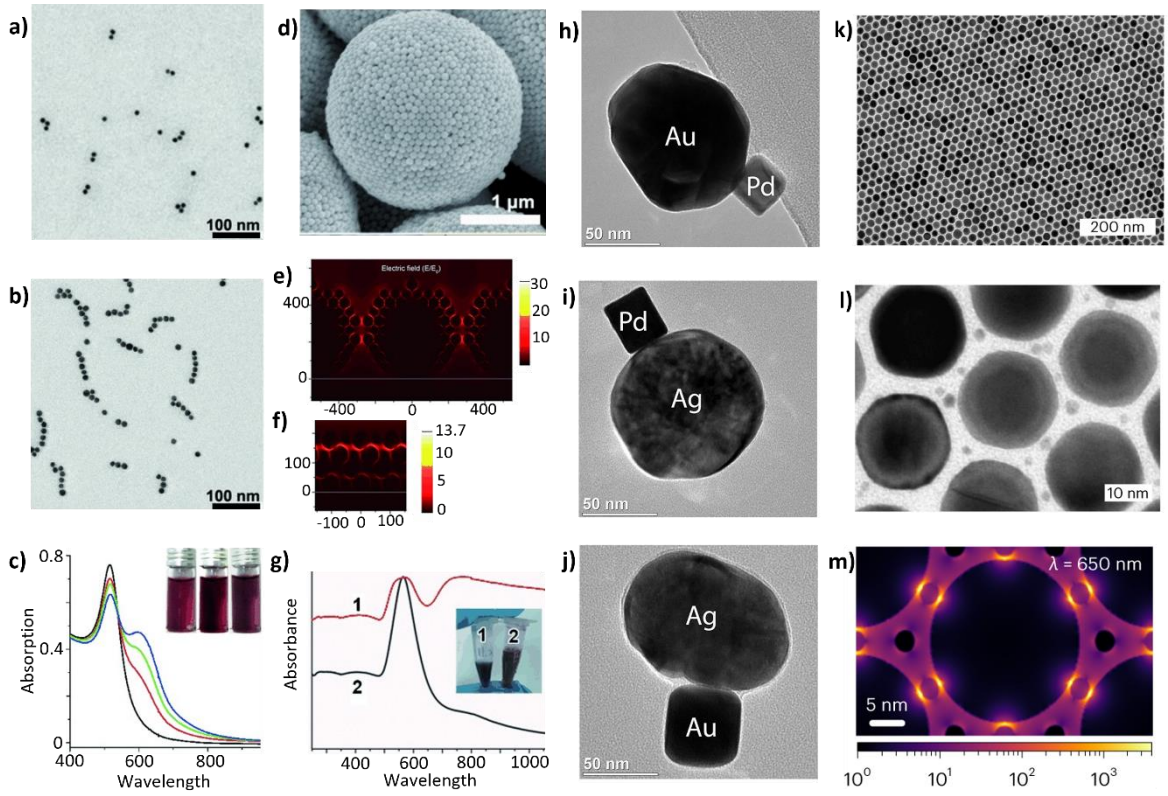

Figure 1.7: a-b) TEM image of isolated Au NPs and Au nanochains and c) its representative UV-Vis absorption spectra. d) self-assembled Au colloidosome with e) near-field enhancement in the colloidosome compared to that of f) an array of Au NPs. Scale bar represents the magnitude of enhancement in electromagnetic field surrounding the self-assembled colloidosome. g) UV-Vis spectra of isolated Au NPs and Au colloidosomes. h-j) electrostatic self-assembly of Au-Pd, Ag-Pd and Au-Au nanocrystals respectively. k) 2D self-assembled Au-Pt supercrystal with l) inset showing 20 nm Au NPs and 1-2 nm Pt NPs within the supercrystal and m) near-field enhancement in the gaps between Au NPs containing Pt NPs. Adapted with permission from [136, 140, 142, 143]

Combining a plasmonic NP with another material such as a metal, semiconductor or drug in a self-assembly can arise unique properties and usefulness for catalytic, photothermal and sensing applications[144–146]. A general self-assembly strategy to synthesize NP heterodimers of two different catalytic materials by electrostatic interactions was introduced by Moth-Poulsen et al. The method is based on the delicate balance between repulsive and attractive interactions responsible for colloidal stability, and allows the synthesis of tailored structures (heterodimers) with up to 42% of relative abundance among the population of single particles and aggregates. These heterodimers are obtained by combining spherical AuNPs and AgNPs with different kinds of PdNPs and AuNPs having distinctive crystallographic properties, shapes and sizes (Fig. 1.7h-j) [142]. Emulsion directed clustering of Au and CdSe NPs results in clusters with improved activity by plasmonic enhancement.

Shi et al. showed that such hybrid clusters yielded a 10 fold increase in the H_2 evolution reaction (73 $mmol.g^{-1}.h^{-1}$) over CdSe NPs[144]. It has been shown by Lee et al. that clustering induced the generation of strong electromagnetic hotspots that enhance the light-to-chemical energy conversion process. This is achieved by trimers of Au NPs coated with catalytic Pd and Pt shells, where the plasmonic Au cores are coupled electromagnetically [145]. The encapsulation of photosensitizer Ce6 in Au NP clusters enables three functionalities: strong fluorescence, photoacoustic signal, and photothermal effect, for imaging-guided synergistic photothermal/photodynamic therapy (PTT/PDT)[146]. Kim et al. showed that self-assembly is an effective strategy to obtain uniform photo-electro-catalytic interfaces from NPs. Their self-assembled films of Au-Cu alloy NPs also allowed unambiguous comparisons [70]. Herran *et al.* prepared a two-dimensional bimetallic catalyst by incorporating platinum NPs into a well-defined supercrystal array of gold NPs (Fig. 1.7k-l). The bimetallic supercrystal exhibited an H2 generation rate of 139 $mmolg^{-1h-1}$ via formic acid dehydrogenation under solar irradiance at room temperature. They observed a correlation between the intensity of the electric field in the hotspots and the boosted catalytic activity of platinum NPs(Fig 1.7m), while identifying a minor role of heat and gold-to-platinum charge transfer in the enhancement[143].

1.3 Hybrid plasmonic nanostructures in photocatalysis

Later in this chapter, the potential of the aforementioned classes of plasmonic hybrids will be discussed for H_2 evolution and H_2O_2 generation. But first, a closer look is briefly taken into the underlying mechanisms of hybrid plasmonic enhanced photocatalysis. Since this review aims at plasmonic hybrids and their role in photocatalysis, the interested reader is referred to the excellent review of Ma *et al.* (2016) for a more detailed discussion of the underlying plasmonic physics [147]. Here, also special attention is given to how these hybrids are helpful in the elucidation of the right mechanism.

1.3.1 Plasmon-enhanced photocatalytic mechanism

1.3.1.1 General aspects on photocatalysis and the role of plasmonics

Over the past four to five decades, a large variety of semiconductor photocatalysts have been studied that generate electron-hole pairs upon the absorption of light with an energy content large enough to overcome the SC band gap (Fig. 1.8a). These photogenerated charge carriers (*i.e.* holes in the valence band and electrons in the conduction band) migrate to the surface of the photocatalyst, where they initiate (a cascade of) redox reactions forming ROS. Among all SCs studied, TiO_2 has been investigated more extensively than any other material, due to its high chemical and thermal stability, appropriate conduction band and valence band positions, low cost and non-toxicity [148]. However, as mentioned before, the photoactivity of TiO_2 is hampered by a large band gap value (ca. 3.2 eV) which restricts its use to applications involving UV light only [147]. In that context, plasmonic nanostructures have emerged as a promising solution for a more optimal utilization of the solar spectrum due to the presence of the LSPR phenomenon. Unlike conventional light absorption processes by molecular sensitizers or interband excitation of metals, LSPR involves a *multi*-electron excitation that concentrates the absorbed light energy at the NP surface in the form of intense electric fields [149]. Thus, plasmonic nanostructures can work as nano antennas in light-driven processes to capture electromagnetic energy. Direct potential applications of this

phenomenon (other than photocatalysis), are several orders of magnitude enhancement of IR and Raman signals, enabling highly sensitive surface-enhanced infrared absorption [150] and SERS [151].

Once a plasmon is excited, it can decay in two competitive ways: through re-emission of photons or by non-radiative relaxation through electron-electron, electron-phonon, electron-surface or electron-adsorbate scattering [152–154]. The re-emission phenomenon is captured by the classical electromagnetic framework as the elastic scattering of an electromagnetic wave. Hot electrons that are not in thermodynamic equilibrium with the atoms in the material, are generated during the non-radiative relaxation process, primarily through electron-electron scattering [147]. The intense LSPR energy generated near the surface of the plasmonic NPs can then be transferred to a SC photocatalyst in contact with the plasmonic NPs. In this way, the photocatalytic activity of the SC is improved by the plasmonic NPs 'indirectly', as will be further discussed. On the other hand, the LSPR energy can also be transferred 'directly' to molecules adsorbed at the surface of the plasmonic NPs [155]. In that case, the plasmonic NPs thus simultaneously act as the light absorber and as the catalytic active site. An increased photoactivity, as well as selectivity, have been demonstrated for reactions based on this direct plasmonic reaction concept [156]. Three different main mechanisms have been proposed to explain this direct activation of adsorbed molecules by plasmonic excitation under visible light [18]:

(i) NP charging/discharging: Plasmonic NPs are charged by steady-state excitation in the presence of a hole scavenger and subsequently discharged by transferring photoexcited electrons to the lowest unoccupied molecular orbital (LUMO) of the metal (M)−reagent complex, thus forming radical reagent or a related species.

(ii) Chemical interface damping: A fraction of the hot electrons can coherently scatter into the unoccupied states of the adsorbed reagent molecule [157], leading to vibrational activation of the reagent for further reaction [158].

(iii) Direct photoexcitation of the M-reagent complex: Reagent molecules adsorbed onto a plasmonic metal surface are activated through direct excitation of the hybridized electronic states of the M−reagent complex [159].

As mentioned earlier and more importantly, the activity of a semiconductor photocatalyst can also be improved 'indirectly' by coupling it to a plasmonic NP. This is the most common and widely encountered type of plasmonic photocatalysis and has been demonstrated for various metal/SC composites such as metal/TiO_2, metal/ZnO, metal/Fe_2O_3, metal/CdS *etc.*, with photocatalytic applications in organic pollutant degradation, hydrogen production and CO_2 conversion, amongst others [160–163]. The main mechanisms that have been proposed to determine this plasmon-enhanced SC photocatalytic activity include:

(i) Promoting charge separation in the SC ((i) in Fig. 1.8b). When a junction between an n-type SC such as TiO_2 and a metal NP is formed, a Schottky barrier is created at the equilibrated interface, which limits the reverse metal to SC transfer [164]. This is also known as the electron sink effect. Although this is not a plasmonic effect as such, it may still contribute significantly to the overall efficiency enhancement.

(ii) Hot electron injection from plasmonic metal NPs to the SC conduction band ((ii) in Fig. 1.8b). LSPR-mediated hot electrons and holes produced and separated at the interface between the plasmonic metal NP and the SC, diffuse to the SC surface to participate in the further photocatalytic reaction. It is important to understand that this mechanism absolutely requires that the SC is in electrochemical contact with the plasmonic metal [165–167]. Note that several studies refer to this as the 'direct electron injection' (DEI) mechanism [5, 131].

(iii) NFE in the SC ((iii) in Fig. 1.8b). The strong plasmon-induced electric field near the plasmonic metal surface can significantly enhance the rate of photoexcitation in the nearby SC. It should be noted that the rate of charge carrier generation is proportional to the square of the electric field [5]. In this case it is crucial that the SC absorption spectrum and the LSPR spectrum overlap [168].

(iv) Increase of the optical path through resonant scattering ((iv) in Fig. 1.8b). Especially for large metal NPs (sizes comparable to the light wavelength [4]), the contribution of scattering to the total extinction becomes important. The more efficient scattering of incident light creates the effect of a mirror that prolongs the optical path length of incident photons throughout the SC. Hence, the probability of successful photo excitation increases [5]. Since in this work the NPs are all much smaller than 100 nm, this mechanism is less relevant.

(v) local heating ((v) in Fig. 1.8b). The non-radiative damping of the excited plasmons eventually leads to energy dissipation to the surrounding environment as heat. Depending upon the intensity of radiation and the thermal properties of the surrounding, this can result in temperature rise in the vicinity of the NPs. This effect is mainly important for ordered NP assemblies that can exhibit enhanced absorption by plasmonic coupling and high particle density per unit area with the additional condition that the incident irradiance is sufficiently strong. Thus, the heating effect is less dominant for single NPs and under ambient conditions [169].

In what follows the main focus will be laid on plasmon-enhanced SC photocatalysis as this also offers high impact real-life applications under ambient conditions. Indeed, while several excellent reports are available on direct plasmon-catalyzed reactions, these systems typically rely on more stringent reaction conditions, such as high irradiance levels (*e.g.* up to 20 sun equivalents or lasers), dedicated optical hardware (parabolic reflectors, lenses, *etc*.) or involve the interplay with heat [155]. Such conditions were not implemented in the experimental part of this PhD study.

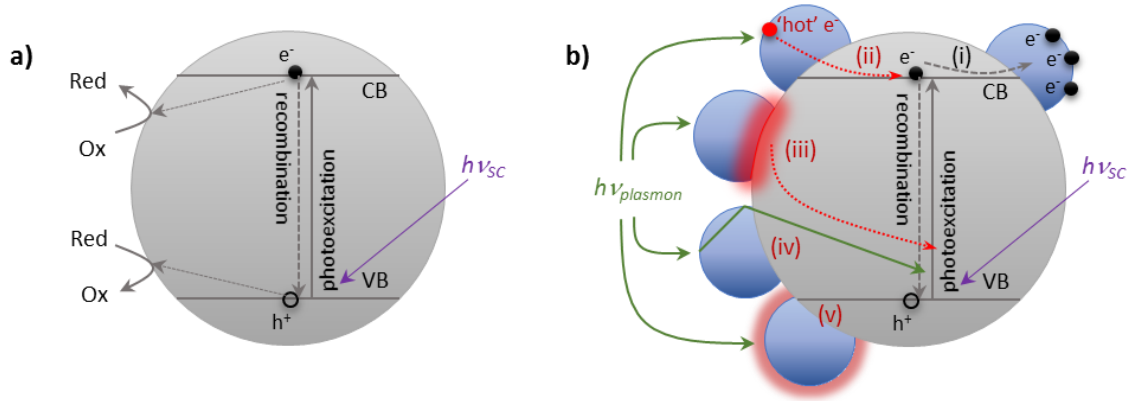

Figure 1.8: Schematic representations of a) the activation of a SC photocatalyst, b) the potential mechanisms driving plasmon-mediated SC photocatalysis: (i) the electron sink effect, (ii) hot electron transfer, (iii) near-field enhancement, (iv) resonant scattering, (v) local heating.

1.3.1.2 Mechanistic studies using hybrid plasmonic nanostructures

Unraveling the precise plasmonic metal-SC interaction mechanism driving the photocatalytic reactions is quite challenging. The relative importance of the various potential pathways (*cfr.* Fig. 1.8b) is still a matter of ongoing debate. The radiative damping of the plasmons results in scattering, *i.e.* energy loss to the surrounding, while non-radiative damping leads to generation of energetic hot electrons which can enhance photocatalytic reactions. The loss by scattering can however be safely neglected in most cases. The scattering component contributing to the total extinction of a plasmonic metal NP only becomes important for particle sizes well over 50 nm [170]. In the majority of studies, much smaller nanostructures are involved. In addition, for the local heating effect to occur effectively, high incident irradiance levels are required, as provided by lasers, powerful solar simulators or light concentrators [171, 172]. Using a standard solar simulator with a maximal output of 1-2 sun(s) or generic 300-500 W Xe sources with optical filters, the temperature rise around plasmonic NPs in aqueous or gaseous media is usually insignificant [173]. In the majority of cases,

this leaves either hot electron transfer, near-field enhancement or an interplay of both as most likely mechanisms.

The existence of the hot electron transfer mechanisms has been demonstrated by the Beller group [174], as well as our team [175], by means of electron paramagnetic resonance studies on traditional noble metal/TiO_2 composite materials. Excitation of the plasmonic composite by a visible light laser resulted in the detection of unpaired electrons associated with the TiO_2 phase, which was not the case when exciting the pristine SC alone. This evidences that the electrons originate from the plasmonic noble metal NP and are transferred to the TiO_2 conduction band.

The existence and influence of the NFE effect, on the other hand, has been convincingly demonstrated by the pioneering work of Awazu *et al.* (2008). They also introduced the term 'plasmonic photocatalysis' for the first time. Hybrid plasmonic composites were used in which Ag@SiO_2 core-shell NPs are deposited on a SiO_2 substrate and subsequently covered by a photocatalytic TiO_2 layer (Fig. 1.9a) [176]. In this structure, the SiO_2 shell acts as a spacer layer between the plasmonic metal and the SC, which was varied in thickness between 5 and 100 nm. While the insulating nature of the SiO_2 shell inhibits the transfer of (hot) electrons, it was shown that for thin shells a strong NFE was achieved, which resulted in the greatest enhancement of the photocatalytic activity. For SiO_2 shells as thick as 100 nm, the near-field was completely repressed and the resulting activity was similar as for the pristine TiO_2 photocatalyst. The presence of a thin shell may even intensify the near-field compared to bare plasmonic NPs, due to the polarizability of the shell electrons. This polarizability increases with the dielectric constant, favoring most shell materials over air or liquid environments for strong metal-dielectric coupling [177]. The ability of a nanoshell to gradually repress the near-field enhancement brought about by plasmonic NPs has also been demonstrated experimentally as well as theoretically for the case of Ag@polymer core-shell NPs of varying shell thickness [23, 178]. It is shown that for a polymer shell of 3 nm, the near-field enhancement protruding beyond the shell is well retained when compared to a bare Ag 18 nm nanosphere, while it is reduced already by 50% for a shell as thin as 5 nm (Fig. 1.9b).

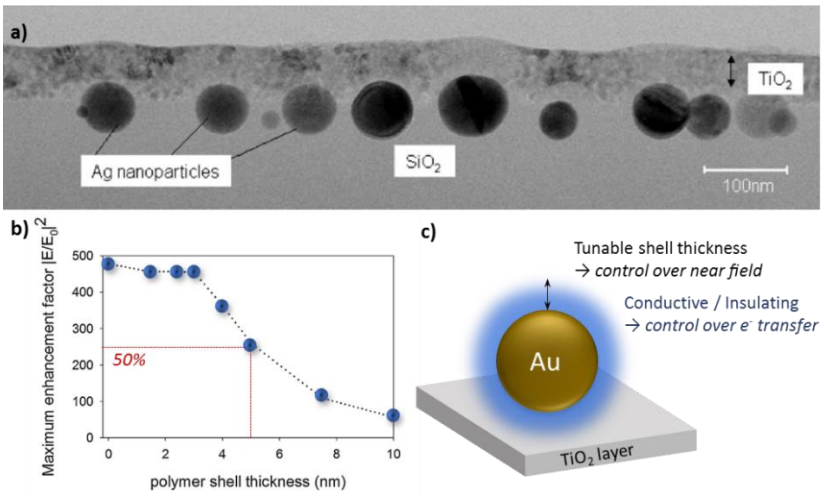

Figure 1.9: a) The plasmonic hybrid TiO_2/Ag@SiO_2/SiO_2 structure used by Awazu *et al.* (2008) b) Simulated near-field enhancement of Ag@polymer NPs as a function of shell thickness. c) Schematic representation of the experimental strategy used by Asapu *et al.* (2017) for disentangling hot electron transfer and near-field enhancement effects. Adapted with permission from a) [176]. Copyright 2008 American Chemical Society, b) [23]. Copyright 2017 Elsevier.

Inspired by the properties of the core-shell concept described above, Asapu *et al.* (2019) proposed a versatile experimental strategy to disentangle the relative contributions of hot electron transfer and near-field enhancement based on metal@polymer core-shell NPs of which the shell thickness as well as the shell's conductive nature can be tuned (Fig. 1.9c) [86]. Au@polymer NPs with electrically insulating shells of varying thicknesses were prepared using a controlled Layer-by-Layer approach, while Au@polymer NPs with electrically conductive shells of varying thickness were prepared using time-dependent *in-situ* polymerization of PANI. By altering the conductive nature of the shells, the existence of hot electron transfer could be regulated, while the tunability of the shell thickness enabled to control the extent of near-field enhancement. This way, both phenomena could be selectively repressed or evoked. By corroborating SERS measurements, theoretical field simulations and photocatalytic activity measurements, it was concluded that for the tested photocatalytic reaction (stearic acid degradation), the near-field enhancement mechanism clearly played a dominant role [86]. However, the strategy has not yet been applied to other photochemical reactions, which may yield a different outcome.

1.3.2 Hydrogen evolution reaction

An important photocatalytic application of plasmonic NPs is the evolution of green H_2 from water through the hydrogen evolution reaction (eq. 1.1,1.2) [179].

$$2H_2O + 4h^+_{VB} \rightarrow O_2 + 4H^+ \qquad (E = +0.82\ V_{NHE}) \qquad (1.1)$$

$$2H^+ + 2e^-_{CB} \rightarrow H_2 \qquad (E = -0.41\ V_{NHE}) \qquad (1.2)$$

With E^0 the standard redox potential. These are also plotted together with a selection of conventional photocatalysts in Fig. 1.10.

For this, core-shell structures containing SCs are the most studied class of hybrid plasmonic materials [180]. A comprehensive overview of selected pioneering and recent studies of hybrid HER photocatalysts is given in Table 1.1, reporting on the reaction conditions, activity and stability. Unfortunately, an accurate comparison among different studies is hampered, since the experimental conditions (*e.g.* the light intensity) are often not mentioned in sufficient detail, nor standardized.

Earlier, mostly Au@CdS chalcogenides were investigated due to the small band gap and favorable band edge positions of CdS (Fig. 1.10). The CB level allows H^+ reduction (-0.7 < -0.41 V_{NHE}). While the small band gap (2.4 eV) results in broad overlap with LSPR of Au, leading to efficient use of the NFE mechanism, next to hot electron transfer [181]. The H_2 production activity is often further boosted using co-catalysts (*e.g.* large Ag@SiO_2 antennas [182]) and morphological optimization (*e.g.* introduction of nanogaps in (AgAu/Ag)@CdS [108], see 1.2.2).

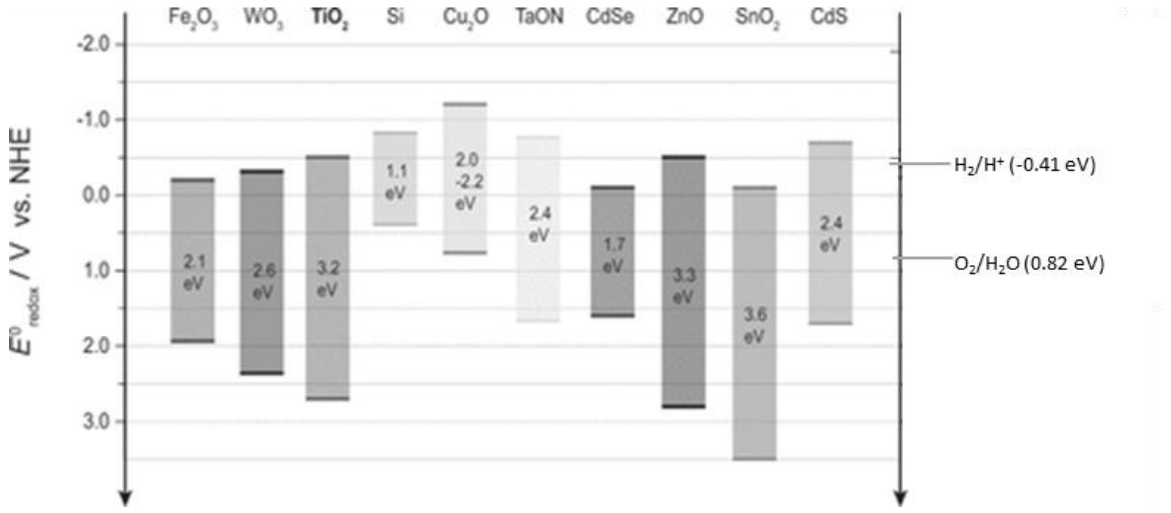

Figure 1.10: Band gaps and VB/CB energy levels of common photocatalysts, shown with the relevant redox potentials for water splitting. Adapted with permission from [181]. Copyright 2013 John Wiley and Sons

However, Cd species are notorious for being toxic and susceptible to photocorrosion [111]. Even though it is shown that the Au core may partially prevent the latter by hole scavenging [107], more sustainable alternatives are highly requested. Ha *et al.* (2015) introduced the less toxic Au@Cu_2FeSnS_4, even though these Cu_2FeSnS_4 species still remain relatively unknown [183]. On the contrary, a vast amount of literature exists on more sustainable, stable SCs such as g-C_3N_4 [110, 184] and especially TiO_2 [180, 185, 186]. These are often combined with plasmonic NPs to overcome their low light absorption capabilities due to relatively large band gaps (resp. 2.7 and 3.2 eV). Pioneers for the synthesis of metal@C_3N_4 were Zhu and co-workers [110]. Via their facile reflux treatment of C_3N_4 nanosheets, they produced 10 wt% Ag@C_3N_4 photocatalysts which yielded 30 times higher H_2 evolution rates (~25 $\mu mol.g^{-1}.h^{-1}$) than pure C_3N_4 under VIS light ($\lambda > 420$ nm). Metal@TiO_2 core-shell nanostructures for H_2 evolution from pure water are studied even more extensively. They also proved to be superior to catalysts consisting of metal particles simply deposited on the TiO_2 surface [187, 188]. Further morphological optimization within the core-shell structure may enhance the H_2 production rate even more. *E.g.*, Au@mesoporous TiO_2 hollow nanospheres core-shell (*i.e*. yolk-shell) structures outperformed Au deposited on TiO_2 spheres (69.77 vs. 37.80 $mmol.g^{-1}.h^{-1}$). The mesoporous hollow nanospheres facilitate internal multiple light scattering, greatly enhancing the light absorption by Au [188]. Nevertheless, none of these metal core@SC shell structures delivered yet a breakthrough in seawater splitting performance, which may point at insufficient capping of the metal.

Finally, as mentioned earlier, water splitting is also feasible with purely metallic photocatalysts. Often Pt is involved in these metal hybrids for its excellent electron sink and H_2 evolution capacities [189]. Pt benefits from its low Fermi level, large work function and special catalytic sites for H_2 formation. Compared with Pt, Au, Ag and Cu have much weaker metal-H-bonding capacity due to the rather high occupancy of anti-bonding *1s* hydrogen and *d* metal states [190]. On the other hand, Pt yields a weaker LSPR signal [191, 192]. Hence, it is regularly combined with plasmonic metals such as Au, both as alloys or as core-shell structures [193]. These metal hybrids are still often

combined with SCs to boost the H_2 generation. Hung *et al.* (2016) claimed the combination of SCs with core-shell Au@Pt to be superior to an alloy approach due to a better charge separation and migration. They contributed this to an extra electric field caused by the descending Fermi level in the well-defined Au@Pt nanostructure. This could facilitate the electron transport towards the reagent [189]. Bian *et al.* (2018) also noticed that their homogeneous AuPt alloys do not show a plasmon band in the VIS range [185].

Nowadays, there is also a push to substitute Pt for more abundant metals. Ding *et al*. (2017) proposed therefore the H_2 production potential of AuCu-$CaIn_2S$ [194]. Remarkably, they observed that the photocatalysts containing AuCu alloys outperformed the Au@Cu core-shell equivalents. They attributed the lower activity of the latter to more shielding of the Au and less efficient charge transport [194]. More recently, promising bimetallic CuCo photocatalysts were suggested by Zhang *et al*. (2019), since Co may simultaneously offer a modest H_2 storage property (0.42 wt%) [195]. It would also be interesting to exchange Pt for Ag. Next to its significantly lower cost, it also possesses a stronger optical response and good overlap with the absorption spectrum of TiO_2. Due to Ag's tendency to oxidize, protective measurements need to be taken, especially in harsher media such as waste water or seawater. In that context, Gao *et al.* (2016) stabilized Ag NPs by embedding them in a SiO_2 core (~200 nm) and applying afterwards a 10 nm TiO_2 shell [196]. Unfortunately, these structures hamper the DEI and NFE mechanism, rendering the photocatalyst less efficient. It would be interesting to protect plasmonic NPs with much thinner shells. Polymer approaches might offer the solution, leading to shells in the low nm range. In the following part of this work, TiO_2 will be modified with various bimetallic Au_xAg_{1-x} composites, wrapped in either insulating or conductive thin polymer shells.

Table 1.1: Recent H_2 evolution studies using plasmonic hybrid nanostructures, given with their reaction conditions, activity and reaction time of which at least 90% of its mentioned activity is retained ($t_{>90\%}$)

Photocatalyst	Light (intensity)[a]	Reaction medium (temperature, pressure)[a]	Activity [mmol.g^{-1}.h^{-1}]	$t_{>90\%}$ [h]	Ref.
Nanogap engineered (Au/AgAu)@CdS	VIS (> 420 nm, NA)[b]	0.25 M Na_2SO_3 and 0.35 M Na_2S in H_2O (RT)[b]	4.71	24	[108]
Au@CdS	VIS (> 420 nm, NA)	0.1 M Na_2SO_3 and 0.1 M Na_2S in H_2O	0.3836	16	[107]
Half-cut Au@CdS	Red light (640 nm, 3.4 mW.cm^{-2})	H_2O (25°C)	~0.08	>200	[197]
$Au_{0.4}Cu_{0.1}/CaIn_2S_4$	450-750 nm (NA)	0.25 M Na_2SO_3 and 0.25 M Na_2S in H_2O; N_2	45.28	8	[194]
$Cu_{0.1}@Au_{0.4}$ /$CaIn_2S_4$	450-750 nm (NA)	0.25 M Na_2SO_3 and 0.25 M Na_2S in H_2O; N_2	20.57	8	[194]
$Au@Cu_2FeSnS_4$	Solar (100 mW.cm^{-2})	0.25 M Na_2SO_3 and 0.35 M Na_2S in H_2O	0.090	19	[183]
Au@mesoporous TiO_2 hollow nanospheres	>420 nm (200 mW.cm^{-2})	0.1 M ascorbic acid in methanol:H_2O (1:1 v/v)); N_2	69.77	12	[188]
Au NRs @TiO_2 nanodumbbells	Solar (NA)	10 mM $NaHCO_3$ in methanol:H_2O (1:4 v/v); Ar (28-35°C)	0.0116	NA	[198]
SiO_2@1wt% Au@TiO_2	UV-VIS (NA)	Methanol:H_2O (1:3 v/v)	12	5	[187]

Janus Au-TiO_2	> 400 nm (NA)	Isopropanol:H_2O (1:2 v/v); Ar (1 atm)	56	3	[180]
10 wt% Ag@C_3N_4	> 420 nm (NA)	20 vol.% triethanolamine in H_2O; 2.7 kPa Ar (RT)	~0.025	10	[110]
SiO_2/Ag@TiO_2	Solar (100 $mW.cm^{-2}$)	20 vol.% glycerol in artificial seawater	0.857	2	[196]
Pt edged Au triangular nanoprisms	VIS-NIR (>420 nm, NA)	Methanol:H_2O (1:2 v/v); Ar	~1	NA	[193]
Pt tipped Au NRs	VIS-NIR (460-820 nm, NA)	Methanol:H_2O (1:4 v/v)	~1.96	6	[199]
TiO_2 NTs-Au@Pt	Solar (100 $mW.cm^{-2}$)	0.5 M $NaSO_4$ in methanol:H_2O (1:4 v/v); Ar	2.971	15	[189]
TiO_2 NTs-AuPt	Solar (100 $mW.cm^{-2}$)	0.5 M $NaSO_4$ in methanol:H_2O (1:4 v/v); Ar	2.18	15	[189]
Homogenously alloyed AuPt-TiO_2 NTs	Solar (100 $mW.cm^{-2}$)	Ethanol:H_2O (1:4 v/v); N_2	12.04 $\mu L.h^{-1}$[c]	5	[185]
PtAu/g-C_3N_4	UV-VIS (NA)	0.25 M $NaSO_3$ and 0.25 M Na_2S in H_2O; N_2 (43-45°C)	1.009	20	[184]
AuPt/Ti^{3+} inverse opal TiO_2	Solar (100 $mW.cm^{-2}$)	10% ethanol in H_2O (35°C)	181.77	6	[186]
0.5 wt% AuPd/g-C_3N_4	> 400 nm (35 $mW.cm^{-2}$)	10 vol.% triethanolamine in H_2O	0.326	6	[200]
Pt in Au supercrystal	Solar (110 $mW.cm^{-2}$)	Formic acid	139	NA	[143]

[a] if known

[b] NA and RT are resp. the abbreviations for not available and room temperature.

[c] No catalyst mass was mentioned.

1.3.3 Hydrogen peroxide generation

Next to photocatalytic H_2 evolution, hydrogen peroxide (H_2O_2) generation is regarded as a green and sustainable route towards production of hydrogen peroxide compared to the traditional 'anthraquinone process'[201]. H_2O_2 as a clean oxidant has been widely used in industry, such as organic synthesis[202], disinfection[203] and water treatment[204] etc. The primary pathways of photocatalytic H_2O_2 production include oxygen reduction (ORR) and water oxidation (WOR). The photoinduced WOR pathway for H_2O_2 generation is a two-hole pathway (eq 5). The light-driven two-hole WOR path involves a high oxidation potential, and the as formed H_2O_2 is easily decomposed [205]. Therefore, photocatalytic WOR reaction for H_2O_2 synthesis generally does not exist independently due to its inherent defects.

$$2H_2O + 4h^+ \rightarrow O_2 + 4H^+ \qquad E = +1.23\ V\ vs\ NHE \tag{1.3}$$
$$H_2O + h^+ \rightarrow OH\cdot + H^+ \qquad E = +2.73\ V\ vs\ NHE \tag{1.4}$$
$$OH\cdot + OH\cdot \rightarrow H_2O_2 \tag{1.5}$$
$$OH\cdot + H_2O_2 \rightarrow H_2O + HO_2\cdot \tag{1.6}$$
$$O_2 + e^- \rightarrow O_2^-\cdot \qquad E = -0.33\ V\ vs\ NHE \tag{1.7}$$
$$O_2 + H^+ + 2e^- \rightarrow HO_2\cdot \qquad E = +1.44\ V\ vs\ NHE \tag{1.8}$$
$$O_2 + 2H^+ + 2e^- \rightarrow H_2O_2 \qquad E = +0.69\ V\ vs\ NHE \tag{1.9}$$
$$O_2 + 4H^+ + 4e^- \rightarrow 2H_2O \qquad E = +1.23\ V\ vs\ NHE \tag{1.10}$$

The synthesis of H_2O_2 can be attributed to a two-step single-electron ORR route (eq. 1.7-1.10) or a one-step two-electron ORR route (eq. 1.8) through the proton coupled electron transfer process.

In addition, because the formation of $O_2^{-\circ}$ not only requires a more negative potential (−0.33 V) than the one-step two-electron route (0.68 V), but also involved multiple unpredictable reactions, so the low efficiency of equation 1.7 step also reduces the production of H_2O_2 yield and selectivity. Therefore, the one-step two-electron route is more advantageous in photoinduced H_2O_2 generation based on ORR reaction. Plasmonic NPs are a promising approach to promote one-step two-electron ORR route[206, 207].

Depositing Au NPs on semiconductors such as TiO_2[208], g-C_3N_4[209], $BiVO_4$[210], MoS_2[211] etc., is the most common way to utilize plasmonic NPs for hydrogen peroxide generation. The difference in band positions between materials can make one material intrinsically more active for H_2O_2 generation. For example, g-C_3N_4 has a more negative conduction band making it more ideal for ORR based reactions. The reason for the enhanced activity in Au NPs loaded semiconductors is attributed to enhanced charge separation due to the noble metal effect and plasmonic enhancement without clearly stating the plasmonic enhancement method. Interestingly, the studies also indicate 2-electron ORR as the mechanism for increase in H_2O_2 generation rate which is promising as per equation 1.9. In a study by Chang *et al.*, a carbon-layer-stabilized method was adopted to load Au NPs onto the g-C_3N_4 matrix[212]. The yield of H_2O_2 with the fabricated Au/g-C_3N_4 photocatalyst reached 66 $\mu mol.L^{-1}.g^{-1}$ after irradiation with light for 240 min; this yield is 2.3-times higher than that of the pristine g-C_3N_4. In the other study, Zuo et al. compared the effect of different co-catalysts (Au, Ag, Pd, and Pt) on g-C_3N_4 for the production of H_2O_2[209]. The results showed that g-C_3N_4 loaded with Au NPs exhibited the best performance for the generation of H_2O_2 owing to its better plasmonic response under solar irradiance.

Subsequently, to further increase the photocatalytic synthesis of H_2O_2, some hybrid plasmonic photocatalysts were also reported, such as Au-Ag/TiO_2[213] and Si/TiO_2/Au[214]. For example, Tsukamoto et al. reported the synthesis of a TiO_2 photocatalyst loaded with bimetallic Au-Ag alloy particles for the efficient production of H_2O_2 (7200 $\mu mol.L^{-1}.g^{-1}$ in 24h) from an O_2-saturated ethanol/water mixture. Under irradiation with UV light, it was found that the as-prepared Au-Ag/TiO_2 samples exhibited the highest rate of formation (kf) as well as the lowest rate of decomposition (kd) of H_2O_2, compared to TiO_2 and Au/TiO_2. The authors proposed that the alloy/TiO_2 junction could create an appropriate Schottky barrier larger than that of Ag/TiO_2 but smaller than that of Au/TiO_2 because the work function of the alloy lies between those of monometallic Au and Ag. This may allow efficient e−/h+ separation while promoting smooth e− transfer from TiO_2 to the alloy. In addition, the electron density of the Au atoms increased because Au is more electronegative than Ag, which promoted the efficient two-electron reduction of $O_2$for the production of H_2O_2[213]. Yamashita et al. synthesized Pd NPs supported on reduced graphene oxide (rGO) layer-coated Au nanorod (NR) nanocomposite catalysts as seen in Fig. 1.11a-c. The H_2O_2 decomposition test and the H_2-D_2 exchange reaction reveal that the SPR of Au NRs facilitates H_2 activation on the Pd NP surface, leading to efficient H_2O_2 production of 3600 $\mu mol.L^{-1}.g^{-1}$ in just 30 minutes[215]. Liu *et al.* prepared Ag-graphene-Cu nano-sandwich as shown in Fig. 1.11 d-g, utilizing solar energy without an external bias. The authors claim that the nano-sandwich can transfer hot-holes from Ag to Cu by a built-in field so that the hot-electrons on Ag NPs are directly utilized to initiate the H_2O_2 generation. Additionally, SPR can enhance the photon absorption and plasmonic near-field distribution around Ag NPs in visible wavelength [207].

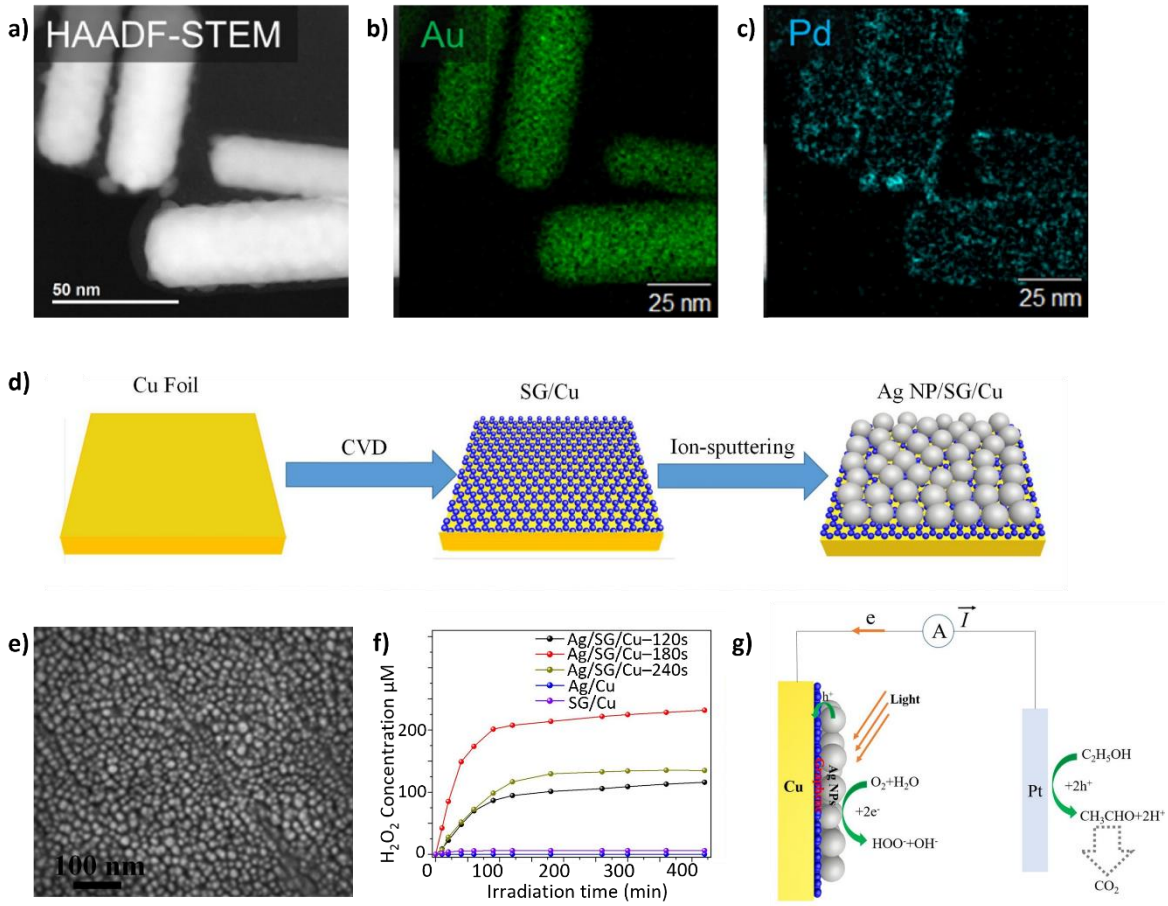

Figure 1.11: a) HAADF-STEM image of Pd deposited on Au nanorods, b-c) EDX maps of Au and Pd respectively. d) schematic representing synthesis of Ag-graphene-Cu nanosandwich. e) SEM image of Ag NP sputtered on Cu and graphene base, f) hydrogen peroxide evolution of the synthesized nanosandwich and g) reaction mechanism responsible for hydrogen peroxide evolution. Adapted with permission from [207, 215].

In Table 2, the disclosed reaction conditions (reagents, intensities, *etc.*) are summarized, together with the achieved activity, selectivity and stability for several recent H_2O_2 generation studies. An accurate mutual comparison remains difficult here as well for the same reason as for hydrogen evolution.

Table 2.2: Several recent H_2O_2 generation studies using plasmonic hybrid nanostructures, given with their reaction conditions, activity, selectivity and reaction time

Photocatalyst	**Light (intensity)[a]**	**Reaction medium**	**Activity [µmol.L^{-1}.g^{-1}]**	**Ref.**
Au - TiO_2	UV (3 mWcm^{-2})	H_2O, O_2 and NaF	1.2 (10 h)	[208]
Au atomic clusters – gC_3N_4	Vis light > 420 nm (N.A.)	H_2O, O_2 and C_2H_5OH	7273 (30h)	[209]
Au - $BiVO_4$	Vis light > 420 nm (N.A.)	H_2O, O_2	67 (10h)	[210]
Atomically dispersed Au - MoS_2	Simulated sunlight (N.A.)	H_2O, O_2, C_2H_5OH	800 (12 h)	[211]
Au - gC3N$_4$	Xe lamp (100 mW cm^{-2})	H_2O, O_2, C_3H_7OH	66 (4 h)	[212]

AuAg - TiO_2	280 – 400 nm (13.8 $mWcm^{-2}$)	H_2O, O_2, CH_3CHO	7200 (24h)	[213]
Au - TiO_2 - Si Nano wire	Simulated sunlight (100mW/cm^{-2})	H_2O, O_2, $Sc(NO_3)_3$	1600 (75 h)	[214]
Pd - Au nanorod on graphene	Vis light >420 nm (120$mWcm^{-2}$)	H_2O, O_2 and H_2	3600 (0.5 h)	[215]
Au – graphene - Cu nano-sandwich	Simulated sunlight (N.A.)	H_2O, O_2 and C_2H_5OH	187 (2h)	[207]
Cu-Au coreshell – $BiVO_4$	420 nm (12.5 $mWcm^{-2}$)	H_2O and O_2	69.2 (3 h)	[216]
CuPd - $BiVO_4$	420 nm (12.5 $mWcm^{-2}$)	H_2O and O_2	109 (2h)	[217]
AuPd - $BiVO_4$	420 nm (20 $mWcm^{-2}$)	H_2O and O_2	183 (2h)	[218]
Au - WO_3	Vis light >420 nm (4 $mWcm^{-2}$)	H_2O, O_2, CH_3OH	550 (5h)	[219]
Au - gC_3N_4-(110)$BiVO_4$	420 nm (50 $mWcm^{-2}$)	H_2O and O_2	108 (2h)	[220]
Au - Ultrathin gC_3N_4	Xe lamp (100 $mWcm^{-2}$)	H_2O and O_2	75 (1h)	[221]

1.4 Conclusion

Despite significant photocatalytic activity enhancements that have been obtained by a myriad of well-considered hybrid material combinations, the achieved efficiencies still leave ample room for improvement. Additional optimization may be achieved by further rational design of such plasmonic hybrid NPs. For instance, Halas's group is investigating core-shell [222] or single-atom alloy [223] plasmonic antenna-reactor systems, in efforts to optimize the activity, selectivity and stability. Self-assembled hierarchical structures and self-assembled array of NPs display even further promise to navigate even more sophisticated structures [143, 144]. Conversely, less complex rational design may also yield significant improvements. For example, based on a thorough understanding of the dominant underlying plasmon-mediated mechanism(s), better matching of the structure to the mechanism could boost the overall performance.

While the fabrication of hybrid plasmonic nanomaterials enables many opportunities, the progressive degree of hybrid complexity may not hamper the eventual scale-up of the catalyst synthesis. Research towards simplifying protocols is still very advantageous for the scientific community. One example is the improvement shown by Asapu *et al.* (2017) for the LbL stabilization strategy, leading to faster and cheaper synthesis of metal@polymer NPs [23, 86]. Generally, to further improve synthesis methods, there is still underexplored potential in using microreactor-based techniques.

During synthesis and catalysis, the NPs are subjected to elevated temperatures and harsh reaction environment from gas and salts involved in the reaction. Special care should then be taken with respect to long-term stability. More stable nanostructures would not only allow long term activity but also allow their introduction into more harsher reaction environments making the complete reaction system more robust. Nonetheless, Core-shell configurations with protective shells might provide a solution to that end. Hot spot engineering by adjusting the spacing layers in core-shell configurations seems promising, especially since sub-nanometer control of both insulating as well as conductive polymer shell layers has been proven to be practically feasibly using facile and versatile techniques [23, 86]. Although, the same control has been difficult to observe in

semiconductor shells. This core-shell aspect will be later studied in chapter 4. It should be noted furthermore that a fundamental, theoretical understanding of these processes remains crucial. Utilizing theoretical tools such as DFT and finite-difference time-domain (FDTD) simulations is key to identifying the loopholes and obtaining the most efficient structure and materials.

Given that sunlight is free, the incorporation of more solar active metals with an activity ranging from UV up until NIR light, is a key research line. Rational design of plasmonic hybrids enables the undisputed advantage of tuning and broadening the absorption towards the solar spectrum, improving the photocatalytic activity. An interesting example provided in that sense was the four times nano gapped gold-silver core with a CdS shell, yielding such a broad absorption band [108]. compared to isolated NPs exhibiting a strong plasmonic absorption from a particular limited band of wavelength, self-assembled structures can enable broadening the plasmonic absorption across the entire solar spectrum. The advent of self-assembly does not only increase the absorption across solar spectrum, but advances in the study can enable tuning of distance between plasmonic NPs and lead to better near-field enhancement and possibly photothermal response. Therefore, advancing from core-shell structures, self-assembled structures can allow hotspot engineering as well as broad absorption across the solar spectrum. By modifying the benchmark photocatalyst TiO_2 with these hybrids, the photocatalytic efficiencies can be significantly enhanced. This will be explored in the chapter 6.

Note that by improving the stabilization approaches and forming more complex structures, future research using more abundant, less stable metals such as Al, Mg and Cu could benefit greatly from the findings in this thesis. It is more promising to use materials relatively cheaper and more abundant than Au such as Al, Mg, Cu and Ag whose LSPR can be tuned in the range of solar spectrum [23, 105]. Self-assemblies of such cheaper and abundant materials is promising in terms of stability and efficiency. To elucidate the most promising materials, the use of more standardized photocatalytic activity measurements is recommended. In order to compare among different studies, as a minimum, the spectral output of the light source and especially the absolute irradiance incident on the sample, should be documented in each report. Following the proposed research opportunities, significant progress still lies ahead.

1.5 Motivation and summary

Taking inspiration from the above discussed chapter, the main goal of the current dissertation is to optimize the interaction between plasmonic nanoparticles by creating hybrid nanostructures with dielectric semiconductors serving as the photocatalytic medium to boost overall photocatalytic efficiency. Most of the previous studies based on plasmonic photocatalysis, either deposit plasmonic nanoparticles onto a semiconductor substrate or embed them within the semiconductor matrix. However, these methods do not fully exploit the near-field enhancement capabilities of plasmonic nanoparticles. Moving beyond such basic deposition strategies, research by Asapu et al. employed Ag@polymer and Au@polymer core-shell nanoparticles on TiO_2 for enhanced plasmonic photocatalysis. The non-conductive and conductive polymer layers act as spacer layers, facilitating only near-field enhancement or both near-field enhancement and electron injection as mechanisms for plasmonic enhancement. Even so, the group of plasmonic nanoparticles remain isolated from

each other, and the polymer layers may introduce resistance to charge transfer from the plasmonic nanoparticles to the semiconductor.

My objective therefore is to form hybrid nanostructures that can optimize the near-field enhancement mechanism and simultaneously have a direct contact of plasmonic nanoparticle with the semiconductor to avoid any resistance to charge transfer from the plasmonic nanoparticle to the semiconductor. Understanding the structure-property relationship is crucial, necessitating the visualization and characterization of the coated materials and their interfaces at the nanoscale. Thus, electron microscopy characterization of the prepared hybrid nanostructures is essential for the studies in this dissertation. To achieve the stated goals, Au@TiO_2 core-shell nanoparticles and Au-TiO_2 self-assembled supraparticles have been synthesized, studied using advanced electron microscopy and spectroscopy techniques, and tested for photocatalytic hydrogen evolution and hydrogen peroxide generation. This exploration has led to the proposal of novel structures and methodologies, advancing the technology toward practical application.

This **first** chapter highlights the limitations of traditional semiconductors in photocatalysis and emphasizes the use of plasmonic nanostructures to harness a larger portion of the solar radiation spectrum. It introduces the concept of hybrid plasmonic nanostructures, discussing their unique optical and catalytic properties in detail. Furthermore, the synthesis and structural properties of various hybrid nanostructures, such as alloyed structures, different forms of core-shell nanoparticles, and self-assembled nanostructures, are explored. The mechanisms related to plasmonic enhancement in photocatalysis are explained with examples of hybrid structures used in hydrogen evolution and hydrogen peroxide generation. **Chapter 2** will continue with an introduction to electron microscopy, including a brief historical overview, descriptions of components, and various imaging and spectroscopic techniques. This chapter also delves into electron tomography, discussing the theory and presenting the technique in practice.

In **chapter 3**, hard-soft core-shell nanoparticles are characterized using advanced electron microscopy techniques. Visualizing structures with significant differences in atomic number Z presents complexities. To address this, the use of graphene-supported grids has been employed. Au@TiO_2 core-shell nanoparticles are studied using multimode tomography to simultaneously visualize both the core and the shell, minimizing the electron dose impact on the samples. Additionally, Au@SiO_2 core-shell samples, which feature larger cores and thinner shells than their Au@TiO_2 counterparts, pose challenges in visualization due to thickness contrast issues. Thus, exit wave reconstruction is utilized to image the core and shell in 2D, and a novel reconstruction procedure has been developed for 3D visualization.

Chapter 4 explores the application of Au@TiO_2 core-shell nanoparticles in hydrogen evolution reaction. These nanoparticles are synthesized through the slow hydrolysis of titanium triethanolaminato isopropoxide, which allows for the formation of shells of varying thickness depending on the concentration of the titanium-based precursor. The optical properties are analyzed using UV-Vis and diffused reflectance spectroscopy, as well as electron energy loss spectroscopy, and are correlated with simulated spectra. Electromagnetic modeling conducted with COMSOL Multiphysics software elucidates the effects of near-field enhancement as the TiO_2 shell thickness around the Au nanoparticle changes. The modeling outcomes are validated through surface-enhanced Raman spectroscopy, demonstrating a 4 nm shell thickness as optimal for

enhancing hydrogen evolution reaction. Radical trapping experiments have shown that the reaction rate enhancement is electron-mediated, driven by electron injection from plasmonic interactions.

In **chapter 5**, further enhancement of the interaction between plasmonic nanoparticles is achieved by synthesizing self-assembled Au-TiO_2 supraparticles. These supraparticles are formed through electrostatic interactions between polymer-coated Au nanoparticles and titanium bis(ammonium lactato) dihydroxide. Their optical properties are assessed using UV-Vis and diffused reflectance spectroscopy, electron energy loss spectroscopy, and near-field enhancement is evaluated via surface-enhanced Raman spectroscopy. The largest Au-TiO_2 supraparticles demonstrate the highest efficacy for hydrogen peroxide generation. Radical trapping studies indicate the necessity of both UV (385 nm) and green light (525 nm) to facilitate electron-mediated reactions and achieve significant hydrogen peroxide production.

Finally, chapter 6 discusses conclusions from the significant findings of the experimental chapters. It proposes novel nanostructures, such as hollow nanostructures, to further enhance plasmonic interactions. The chapter introduces the concept of photothermal catalysis using concentrated light for Ag@Ni core-shell and core-satellite nanostructures as a viable approach toward practical applications of plasmon-enhanced photocatalysis. Additionally, it explores the potential of in-situ electron microscopy with integrated light within the microscope, from a fundamental perspective.

Chapter 2: Introduction to electron microscopy and electron tomography

2.1 Introduction to transmission electron microscopy – history and evolution

In order to understand the structure property relationship of hybrid plasmonic nanostructures, a detailed visualization and characterization is required. However, nanomaterials are not visible to the naked eye or conventional optical microscopes, because of a lack of spatial resolution. The resolution of an optical instrument is determined as the ability to distinguish separate points of an object that are located at a small angular distance. The resolution of an optical microscope is limited by the wavelength of its radiation source. Indeed, the resolution of a light microscopes is approximately 0.22 µm for the best available objective lenses [224]. Ernst Ruska stated in 1930 that a transmission electron microscope (TEM) can be built using the same principle as for an optical microscope by only replacing the glass lenses by electromagnetic lenses [225, 226]. Ernst Ruska received the Noble Prize in Physics in 1986 for his contribution to electron optics. The use of TEM enables us to acquire images with a spatial resolution which cannot be obtained using an optical microscope. The wavelength of accelerated electrons in a TEM depends on their energy E. When neglecting relativistic effects, de Broglie's equation is given by:

$$\lambda = \frac{1.22}{E^{\frac{1}{2}}} \tag{2.1}$$

with E in electron volts and λ, the wavelength, in nm. Typically, electrons in a TEM are accelerated by high acceleration voltages of 100 - 300 kV and result in electron wavelengths of approximately 2 - 4 pm [227], which is several magnitude orders smaller in comparison to an optical microscope. However, the resolution of a TEM is not only limited by the wavelength of the electrons, but also by the aberrations of the electromagnetic lenses in the microscope, which restricts the practical resolution to approximately 1 - 2 Å [227]. As shown in Fig. 2.1, spherical aberration induces a blurring of the image in the focal plane, because light rays through the center of the lens and through the edge of the lens deviate when intersecting with the optical axis. Chromatic aberration on the other hand, induces blurring of the image because light rays of different wavelengths (due to the energy spread) fail to intersect with each other on the optical axis. The idea of a TEM by Ruska was commercialized by Siemens and Halske in 1939 [228]. Commercial instruments could approach 0.5 nm resolution around the turn of the century and that seemed to be the limit due to aberrations, mainly spherical and chromatic aberrations of the electromagnetic lenses [229]. However, the introduction of spherical-aberration-corrected lenses in 1998 was a breakthrough [230]. The use of multipole lenses made further improvement in terms of resolution possible [231]. The obtainable spatial resolution limit nowadays lies at around 50 pm which opens new avenues in the characterization of materials[232].

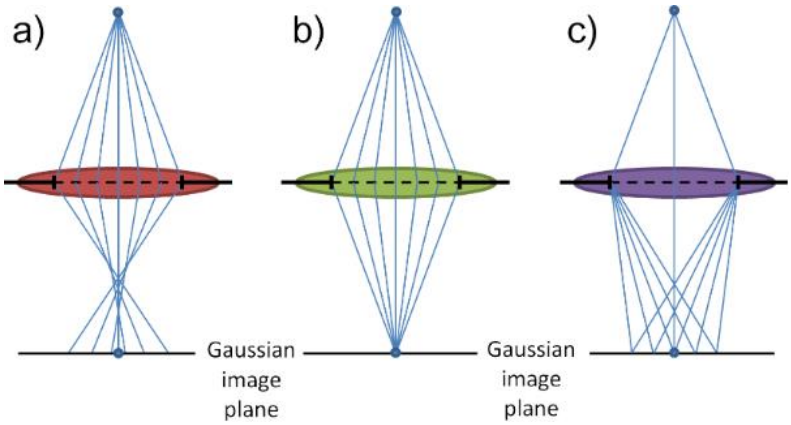

Figure 2.1: Illustration of (a) spherical aberration (b) ideal lens and (c) chromatic aberration. Adapted from [233]

2.2 Components of a basic TEM

As seen in Fig. 2.2, from top to bottom a TEM consists of an illumination system, a condenser lens system, the stage where the specimen is located, the objective lens system and the imaging lens system. The electrons are generated by an electron source which is either a thermionic gun or a field emission gun, which is currently more often used. The required size, intensity and convergence angle of the electron beam are formed by the condenser system. By using a set of electromagnetic lenses, the electron beam is directed to investigate the sample. A condenser aperture can be inserted to select the electrons that follow a path close to the optical axis, which will reduce the effect of the aberrations caused by the lenses in the condenser system. After passing the condenser system, the electrons interact with the specimen which is inserted with the use of a dedicated TEM holder. The objective lens, located close to the specimen, disperses the electrons and yields a diffraction pattern in the back focal plane of the objective lens. The diffracted beams recombine and form an enlarged image in the image plane of the objective lens. The use of an objective aperture in the back focal plane of the objective lens can reduce the effect of lens aberrations of the objective lens and/or select specific spots in the diffraction pattern. A selected area diffraction (SAD) aperture can be inserted in the image plane of the objective lens, which selects a specific region of the specimen from which information will be extracted. The projector lens system will form the final magnified projection image, which either uses the back focal plane or the image plane

of the objective lens as its object plane. A fluorescent viewing screen or a charged coupled device (CCD) is located at the bottom of the TEM and is used to visualize the image.

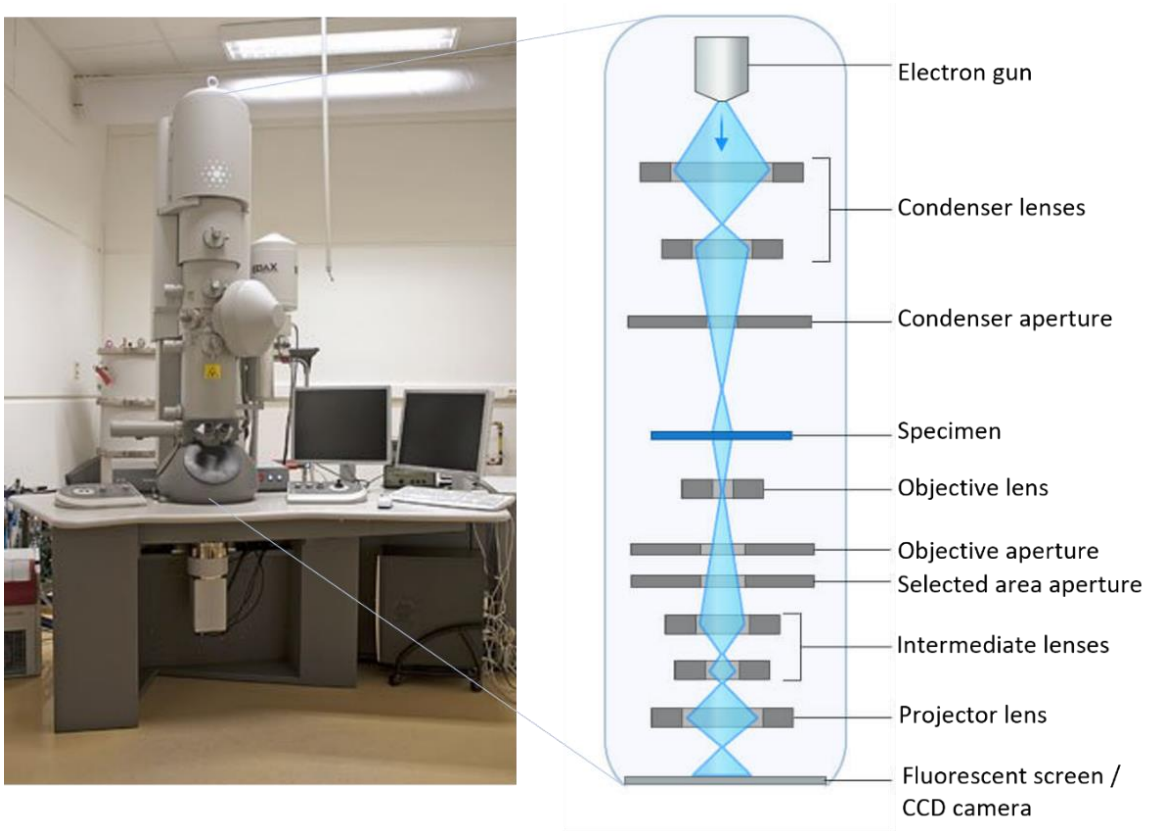

Figure 2.2: Image of Tecnai Osiris TEM at EMAT (left) and schematic representation of its components and ray diagram for BF TEM (right).

2.3 Electron beam and specimen interaction

When the electron beam interacts with the sample, a wide variety of signals can be formed. Since electrons correspond to low-mass, negatively charged particles, they can be deflected by passing close to other electrons or the positive nucleus of an atom. Transmitted electrons can be either elastically or inelastically scattered. When an electron passes through the electron cloud of an atom, it will be attracted by the positive potential of the nucleus (Coulomb interaction). Consequently its path is deflected towards the core. This is called elastic scattering. The closer the electrons come towards the core, the stronger the scattering and the larger the scattering angle. Dependent on the size of the scattering angle and the shape of the probe different imaging modes techniques can be applied. Electrons scattered to low angles (< 10 mrad) are used for bright field (BF-TEM) and electron diffraction, whereas electrons scattered at higher angles (> 100 mrad) are used in so-called high angle annular dark field scanning transmission electron microscopy (HAADF-STEM)[227]. In some cases, even complete backscattering can occur (backscattered electrons). Besides elastic scattering, also inelastic scatting occurs. Here energy is transferred from the electron beam to the atoms of the sample by producing secondary electrons, phonons, cathode-luminescence or ionization of atoms. This results in different types of signals such as X-rays, Auger

and secondary electrons, plasmons, phonons and cathode-luminescence. These signals can be investigated using specific detectors in the electron microscope.

2.4 Different TEM imaging and spectroscopy techniques

2.4.1 Bright field transmission electron microscopy

When applying BF-TEM, the specimen is illuminated by a parallel beam of electrons. Fig. 2.2 represents a schematic overview of the electron ray diagram for BF-TEM imaging. In this imaging mode, elastically scattered electrons contribute to the image formation and two main mechanisms occur: mass-thickness and diffraction contrast. When amorphous or non-crystalline specimens are imaged, thicker regions of the specimen will appear darker in the image (mass-thickness mechanism)[234]. For crystalline specimens, the incident parallel electron beam is diffracted by the crystal lattice of the specimen and the formed contrast is referred to as diffraction contrast[235]. By using an objective aperture, either the direct beam or a diffracted beam is selected. The selection of the direct, undiffracted beam results bright field image.

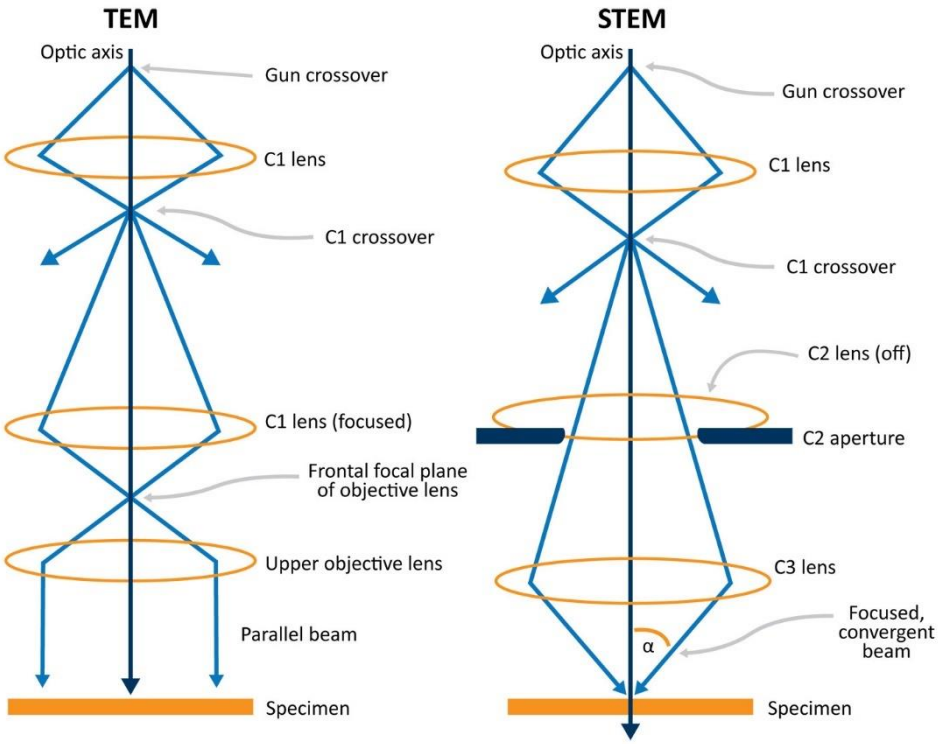

Figure 2.3: Ray diagram representing parallel beam operation in TEM and convergent beam operation in STEM. Reprinted with permission from [227].

2.4.2 Scanning transmission electron microscopy

In STEM, the electron beam is focused into a fine probe (probe sizes of << 1 nm) by the lenses of the illumination system, as visualized in Fig. 2.3. The region of interest is scanned line by line by the use of deflection coils. At each position, a signal is generated and for each pixel, the number of electrons scattered to an annular detector is detected. The quality of the image is only affected by the aberrations of the electron probe and possible scan noise during the acquisition [227]. In STEM mode,

the selection of the electrons for imaging is based on their scattering angle. The electrons scattered to a specific angular range are detected using an annular detector. The inner and outer angles can be adjusted by adapting the physical camera length at which the annular detector is positioned with respect to the specimen [227]. In the modern TEM's there is also the option to select multiple detectors with a different angular range. Medium angle annular dark field STEM (MAADF-STEM) collects the electrons scattered to an angle between 40 and 100 mrad. When a small camera length is used, electrons scattered to high angles (> 80 mrad) are collected and the technique is referred to as HAADF-STEM. An example of a HAADF-STEM image is shown in Fig. 2.5. In this case, scattering is associated with the interaction close to the nucleus of the atoms of the investigated specimen and the collected electrons can be considered as Rutherford scattered particles. The intensity of the formed images is proportional to Z^n (atomic number) with ($1.6<n<2$) of the elements under investigation and of the projected thickness of the specimen [236]. The presence of diffraction contrast is minimized since most of the diffracted electrons have a scattering angle less than inner collection angle of the annular detector.

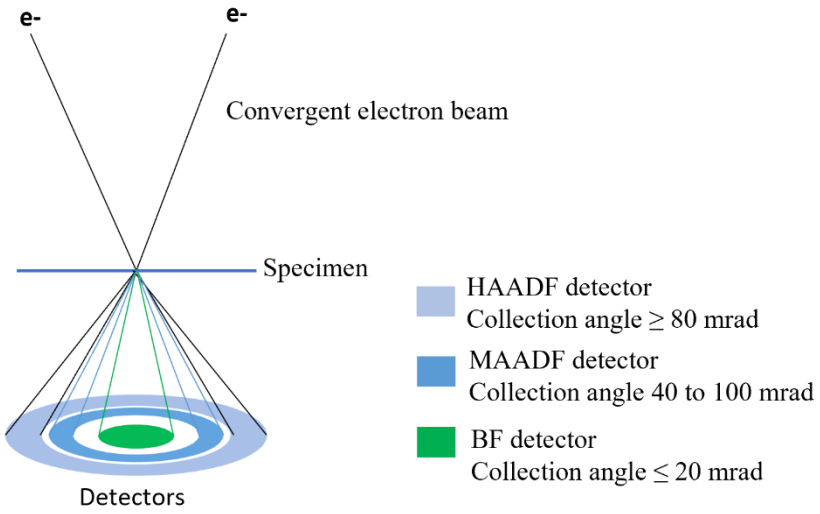

Figure 2.4: Schematic representation of various STEM detectors and their collection angle.

For MAADF-STEM, the dependency on Z decreases to less than Z^2 compared to HAADF-STEM. The resulting image is due to both coherently and incoherently scattered electrons leading to visualization of elements with lower atomic number [237]. Although one must be careful with diffraction contrast possibly present in MAADF-STEM images. In Fig. 2.5, a BF-TEM, HAADF-STEM and MAADF-STEM image is shown. The visualization of 2-3 nm SiO_2 shell with Au core is possible using MAADF and not HAADF detector in STEM.

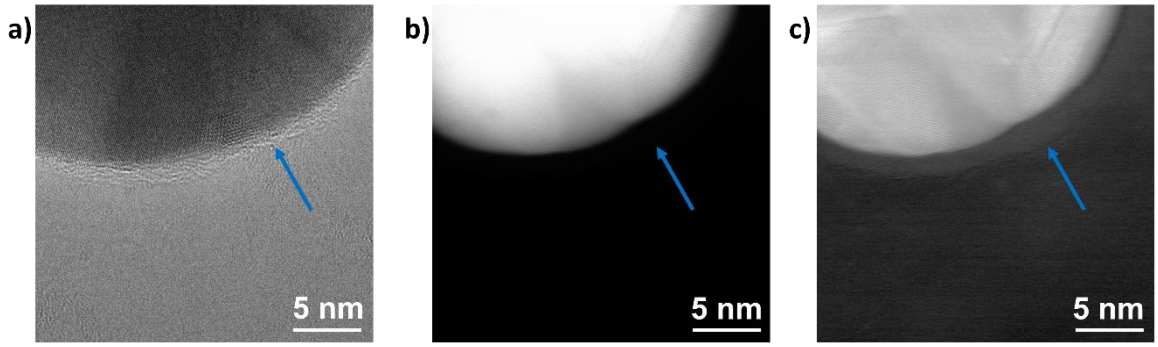

Figure 2.5: (a) BF-TEM, (b) HAADF-STEM and (c) MAADF-STEM image of Au@SiO_2 core-shell NPs.

2.4.3 Advanced imaging techniques

The development of new types of electron detectors can be used to retrieve more information about the studied materials. Exit wave reconstruction (EWR) is a technique previously used for high resolution imaging, is now also used for imaging of light elements. After interaction with the sample, the electron wave at the exit plane of the specimen (exit-wave) contains all the structural information (specimen thickness and atomic positions) about the specimen. The electron microscope transfers this exit-wave via the lenses towards the CCD camera leaving the exit-wave unchanged. However, the electromagnetic lenses are imperfect and the exit wave is distorted by the lens aberrations of the image forming lenses. A through focus series can be acquired, which allows the reconstruction of the electron exit wave function: amplitude and phase [238]. This technique will be discussed in more detail in chapter 3.

Using four-dimensional (4D) STEM, 2D diffraction pattern can be captured at each pixel position on a STEM map, producing maps of local crystal orientation, structural distortions, or crystallinity [239, 240]. The speed and sensitivity of 4D data combined with direct electron detectors enables the control over the incident electron dose and, therefore, the investigation of beam sensitive materials[240–242]. Although the method is data intensive. Another recent development, integrated differential phase contrast (iDPC-STEM) technique is capable of imaging light and heavy elements simultaneously even at low electron doses [243, 244]. In contrast to typical annular detectors used in STEM (Figure 2.2a) which display the integrated intensities of these electrons at each scan position of the incident probe, in iDPC-STEM a segmented detector, e.g., composed of four segments, is used[244, 245]. In this manner, by measuring the angle and the direction of the beam deflection the mapping of electrostatic potential fields of the specimen can be performed, thus, resulting in a direct phase imaging [246], beneficial for the visualization of heavy and light elements even in beam-sensitive materials [247].

2.4.4 Energy dispersive X-ray imaging

Energy dispersive X-ray (EDX) spectroscopy is used in a TEM to map the chemical elements present in a specimen. Incoming electrons of the beam can excite inner shell electrons of an atom in the specimen, which will generate X-rays and create an electron hole. A higher energy electron from an outer shell will then fill this vacancy and an X-ray will be emitted with the difference energy. The specific energies of these X-rays are characteristic for the chemical elements that are present in the specimen. Thereby, the obtained characteristic X-ray spectrum can be used for a chemical

characterization [227]. Such a spectrum consists of a superposition of a background signal caused by Bremsstrahlung and the characteristic X-ray peaks. As the background signal is rather constant throughout the energy window, it is straightforward to extract a spectrum only consisting of the characteristic peaks. When EDX is combined with STEM imaging, a complete 2D elemental map can be obtained since each pixel in the 2D image contains a measured spectrum [248]. In Fig. 2.6 a schematic overview of the position of the EDX and ADF detector are shown. The spectrum in each pixel can be evaluated and the characteristic X-ray peaks can be selected by an energy window around the characteristic energy to obtain 2D elemental maps.

2.4.5 Electron energy loss spectroscopy

Electron Energy Loss Spectroscopy (EELS) in the transmission electron microscope is an extremely powerful characterization tool, offering information about elemental composition, chemical bonds, optical properties and vibrational modes. Incoming electrons in a TEM can lose part of their energy due to interaction with the specimen. After interaction, the electrons are deflected by a magnetic prism (Fig. 2.6). This prism bends the inelastically scattered electrons and disperses them according to their different kinetic energies. However, most electrons will not suffer from any inelastic scattering. The greatest contribution to the spectrum is due to the elastically scattered electrons, giving rise to the so-called zero-loss peak (ZLP). The full width half maximum of the ZLP can be used to determine the energy resolution during the experiment. The energy distribution of all scattered electrons leads to a spectrum which can be recorded using a CCD camera. This energy distribution provides information about the local environment of the electrons which in turn relates to the physical and chemical properties of the specimen[249]. Typically, three different regions on the recorded spectrum can be distinguished: the zero-loss, low-loss (2-50 eV) and core-loss region (>50 eV). The low-loss region yields information on the plasmon oscillation of the valence electrons in the sample while the core-loss region of the spectrum contains information on the electron-electron interaction from the inner shells. To obtain information in the low-loss region, close to the ZLP, a good energy resolution (~0.1 eV) is necessary. The energy resolution can be improved by the use of a monochromator.

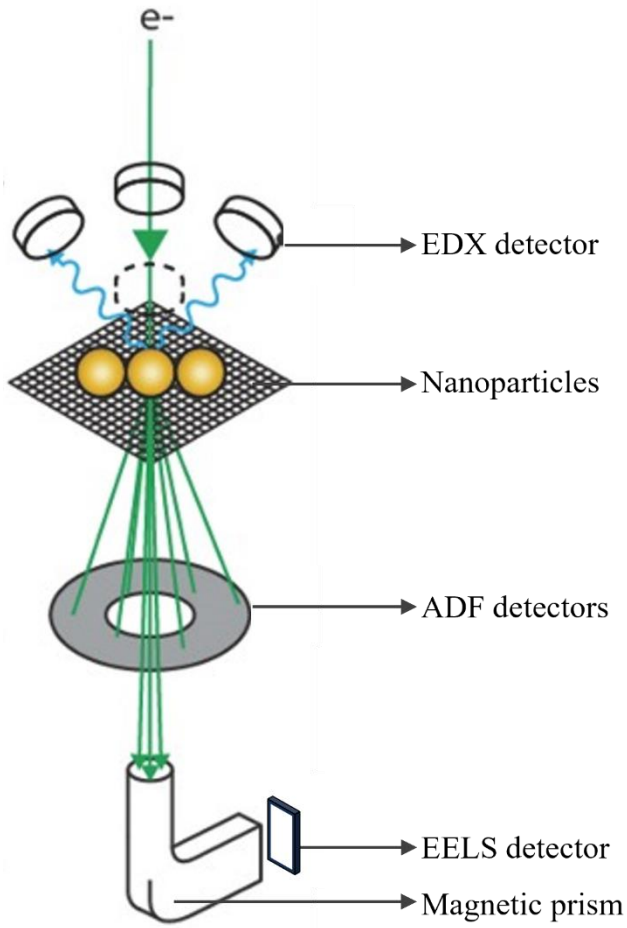

Figure 2.6: A schematic overview of setup of the EDX detector and EELS detector. Adapted with permission from[250]

2.5 Introduction and history of electron tomography – electron microscopy in three dimensions

The structural, chemical and electronic information of a nanoscale object can be retrieved using different TEM techniques mentioned above. However, the majority of these techniques provides only 2D information on the investigated 3D object. 2D imaging may be sufficient when investigating isotropic or periodic nanostructures, but may lead to an incomplete and unreliable characterization for highly asymmetric nanostructures. A 3D investigation of such materials is crucial to understand the relationship between the physical properties and the structure of these nanomaterials. To perform such studies, "electron tomography" (ET) is required, a technique from which a 3D reconstruction can be formed from a series of 2D projection images.

The mathematical basis of tomography was outlined by the mathematician Johann Radon who explained the principles behind the technique in his paper published in 1917 [251]. Half a century later, the first practical tomography scanner was realized. The device used X-rays for image formation and was called a computed axial tomography (CAT) scanner. For his accomplishment, Hounsfield

received a shared Nobel Prize in medicine in 1979 [252] together with Cormack, who developed the mathematical foundation[253]. Around the same time as the invention of the CAT scan, the first combination of tomography with electron microscopy was established. In 1968 three research groups published the theoretical principles of ET [254–256]. Still, it took more than a decade before ET was used for the first time in biological science. The reason for this is related to beam damage, the absence of dedicated tomography holders and the lack of computational power. It took another 30 years before tomography was widely used in materials sciences as well. This is mainly due to the violation of the projection requirement, stating that the intensity of the acquired images should be a monotonic function of a certain property of the sample under investigation [257]. In materials science, specimens are often crystalline and diffraction contrast becomes dominant in BF-TEM. A solution is the combination of ET by using annular detectors in STEM mode [257]. Nowadays ET has been applied to many different materials classes in combination with different techniques such as EDX, EELS and holography [258–260]. Different imaging modes and their applicability to ET will be further discussed in section 2.6.1.1.

2.6 How to perform tomography?

To broadly classify, there are four main steps involved in an ET experiment. The first step is the acquisition of a tilt series of projection images of the investigated object over an angular range as large as possible, with tilt increments of typically 1° or 2°. After the acquisition, the tilt series of projection images is aligned with respect to a common tilt axis to eliminate relative shifts and rotations between the successive images. In the next step, a mathematical reconstruction algorithm is used to compute the 3D reconstruction. During a last step, the outcome of the ET experiment is visualized / analyzed.

2.6.1 Acquisition of the tilt series

The acquisition of a tilt series from an object of interest is the first step in any tomography experiment. The imaging mode used for tomography should meet the so-called projection requirement, which states that the intensity in the projected images should be a monotonic function of a certain property of the sample under investigation [257]. Depending on the type of materials and the information which one wants to obtain, different imaging modes are better suited.

2.6.1.1 Imaging modes in electron tomography

For biological materials and non-crystalline inorganic systems, the use of BF-TEM is appropriate because mass-thickness contrast is dominant and satisfies the projection requirement. Unlike biological materials, samples in physical science are often crystalline and produce consequently diffraction contrast. Therefore, there is no longer a monotonic relation between the intensity in the projected images and the thickness of the sample, which implicates that the projection requirement is no longer fulfilled when using BF-TEM [261, 262]. Therefore, 3D studies of crystalline samples are often performed using HAADF-STEM images to overcome this problem. In HAADF-STEM, the projection requirement is satisfied for thin samples as the intensity scales with the thickness of the specimen. Due to the relation between the intensity and the average integrated atomic number of the elements in the specimen, relative chemical information can also be obtained. HAADF-STEM tomography was first introduced in materials science in 2003, which was used to study metal NPs

in a mesoporous silica support matrix [257]. Since then, a broad variety of specimens has been investigated successfully with HAADF-STEM tomography [232, 263–267].
In EDX-imaging, the intensity of a characteristic X-ray peak of an element present in the specimen in an EDX spectrum scales with the weight fraction, the fluorescence yield and the ionization cross-section of the element. Therefore, a 2D EDX map can in principle be used as a projection image for tomography [268, 269]. The SuperX EDX system uses four detectors symmetrically placed around the sample [270], to avoid signal blocking during tomography and makes EDX tomography feasible [271–274]. Typically, EDX maps are only acquired for a few projections, due to the long exposure time needed for an acquisition of a spectral map and, in this manner, prevent structural modifications from radiation damage. Generally, a tomographic series based on the HAADF-STEM mode is acquired over the full tilt range and combined with the spectroscopic data during the tomographic reconstruction [274, 275].

2.6.1.2 Tilt schemes

Prior to the acquisition of the tilt series, the height of the specimen is adjusted to the eucentric position. This is the center of the objective lens. TEMs use this reference position for magnification, camera length and correct focus. Moreover, when the sample height is set at the eucentric position, the specimen can be tilted around its axis while the movement of the specimen across the projection screen is reduced during tilting. As schematically depicted in Fig. 2.6, by tilting a dedicated tomography holder with respect to the electron beam, different projection images of a sample are obtained at different tilt angles.

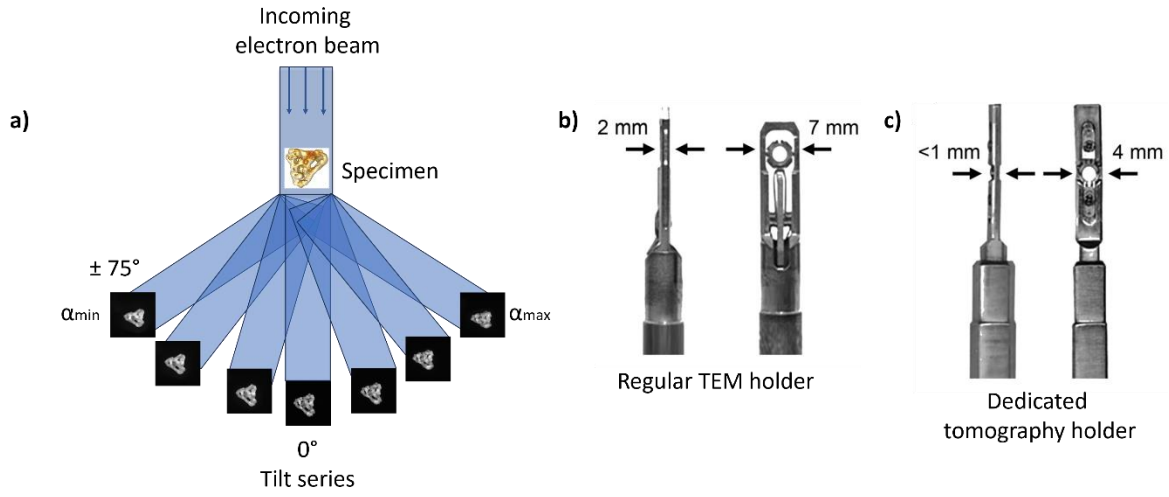

Figure 2.7 a) Illustration of the acquisition of a tilt series in an ET experiment, (b) regular double tilt holder which can be tilted to approximately ± 40° between the polepieces of the electron microscope, (c) Dedicated tomography holder which can be tilted to ±70°-80° due to the narrow tip of the holder.

Single tilt axis acquisition

The most commonly used acquisition technique in ET is based on the single-axis tilt scheme. Conventionally, the quality of a tomographic reconstruction is strongly related to the number and the angular range of the obtained projections. Ideally, the specimen is tilted over ± 90°, but since the specimen holder is placed between the limited space of the upper and lower pole pieces of the objective lens, this is impossible using a conventional holder. The tilt range is restricted to mostly ±40° for a regular specimen holder and ±80° for a dedicated tomography holder (Fig. 2.7). Still, the gap of missing information in the angular range will lead to a so-called "missing wedge" of information in the projection data. As a result, artefacts will occur in the final reconstruction such as fanning artefacts and an elongation in the direction of the optical axis [257]. Fig. 2.8 shows the effect of the missing wedge on the Shepp Logan phantom, from which it is clear that a larger missing wedge causes missing details and more elongation in the vertical direction. Besides the tilt range, the tilt step between every projection is another key parameter of the resolution of the reconstructed object. Larger tilt steps result in a larger blurring of the reconstructed object in real space, hampering the visualization and quantification of small features in the reconstructed object [257]. Conventionally, ET series are acquired with a tilt step of 1-2°, as most of the information can still be recovered.

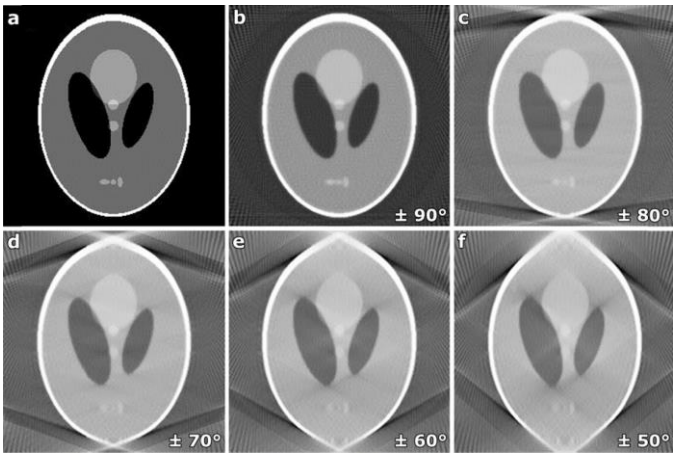

Figure 2.8 Visualization of the effect of the missing wedge on the Shepp Logan phantom image (a). A tilt series is simulated for the phantom image and a reconstruction is calculated using different missing wedges (b-f). An increasing elongation in the vertical direction with decreasing angular range of the tilt series can clearly be detected in the images.

Dual tilt axis acquisition

Multiple tilt series of the same object can be used to reduce missing wedge artefacts in the final reconstruction [276, 277]. When a dual tilt axis geometry is used, two tilt series of the same object are acquired. The tilt axis of the second tilt series is perpendicular to the tilt axis of the first tilt series. The missing wedge of information in Fourier space is reduced to a missing pyramid. However, the need for a longer total exposure time and the time-consuming alignment and reconstruction of such acquisition schemes make these schemes less favorable. In addition, the sensitivity of the specimen to the electron beam limits the applicability of the dual tilt axis acquisition as degradation of the specimen can occur. Therefore, only single tilt axis acquisition schemes are used in this thesis.

On axis tilt acquisition

A dedicated on-axis tomography holder has been developed to enable tilting of needle-shaped samples over a full tilt range of ± 180°. The possibility of acquiring a full range tilt series completely eliminates the missing wedge artefacts [278, 279]. Such needle-shaped samples are prepared by focused ion beam (FIB) milling and afterwards the sample is mounted on the dedicated rod-shaped on-axis tomography holder. The quality of the 3D reconstruction will improve due to the elimination of any missing wedge artefacts. However, the technique remains less popular as the sample preparation is challenging, especially to prepare needle-shaped samples for NPs [280].

Continuous fast acquisition

A different approach for the acquisition of a tomographic series consists in the image recording of the object under investigation while the holder is continuously rotated [281], where hundreds of frames are acquired during the process (Fig. 2.9). The rotation speed of the goniometer is chosen to ensure a good ratio between speed and image quality [281]. The total acquisition time for a tomographic series can be reduced from typically 1 hour to 5 minutes, when comparing conventional to fast acquisition schemes [281, 282]. Typically, the acquisition time required for each frame in the tomographic series is relatively low (1s per frame). As a consequence of the reduced acquisition time, more tomographic series can be recorded in the period of 1 hour when using the fast acquisition scheme. Therefore, the fast approach enables the acquisition of tomographic series of nanomaterials with higher throughput than conventional acquisition techniques.

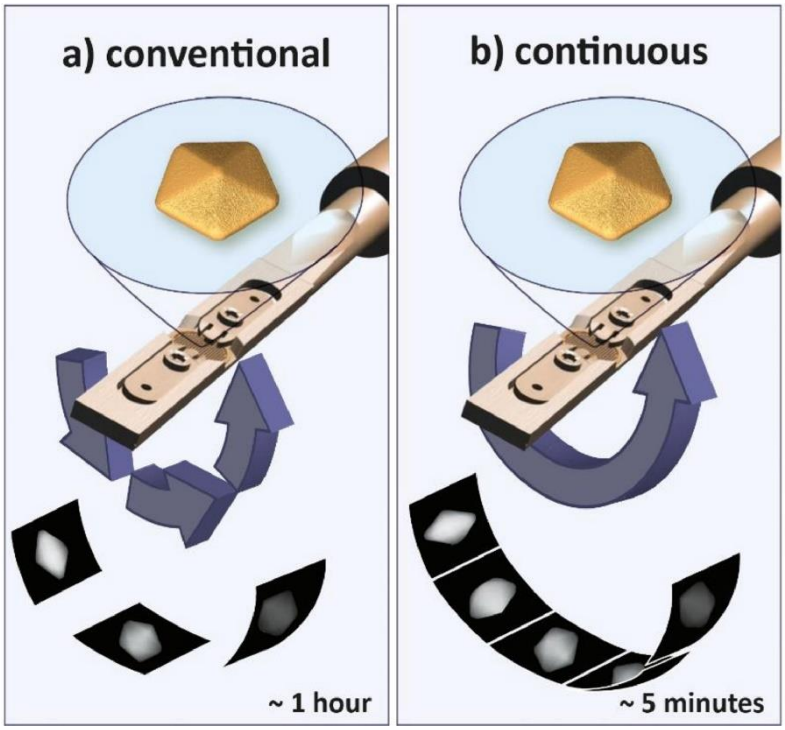

Figure 2.9 Graphic illustration of conventional, continuous and incremental tilting, during a tilt series acquisition. Adapted with permission from [282].

One of the challenges of the acquisition of fast tomographic series consists in the tracking (x- and y-direction of the stage) and re-focusing (z-direction of the stage) of the NP during the acquisition, since a displacement of the particle always take place in the x-, y- and z-direction of the stage after tilting the goniometer. Performing such an automated acquisition requires a careful choice of different parameters such as acquisition time for the different steps (tracking, focus, and final acquisition), focus interval and step size, image filters, maximum tilt angle and other parameters that are used during the acquisition process. These parameters should be optimized for each individual experiment as the automated acquisition needs to be finalized before beam damage occurs. Different types of automated acquisition software have been developed over the last years [283–285].

2.6.2 Alignment of the tilt series

During the acquisition of the tilt series, the dedicated tomography holder needs to make a mechanical rotation. With this rotation of the holder, a shift in the field of view will occur. The specimen is tracked back into the field of view at each tilt angle, which will induce local shifts between successive images. These relative shifts are measured and corrected for in the whole tilt series during the alignment. In practice, the shifts are measured by calculating the normalized cross correlation image between two succeeding projection images. Such a cross correlation image is formed by calculating the inverse Fourier transform of the product of the Fourier transform of the first projection image and the complex conjugate of the Fourier transform of the second projection image. The position of the maximum intensity in this cross correlation image presents the relative shift between the two original projection images.

Once the images are aligned, it is necessary to adjust the tilt axis before proceeding with tomographic reconstruction. This adjustment is essential because the projection geometry employed by reconstruction algorithms demands that the rotation axis be precisely vertical and intersect the center of each projection (as indicated by the red line in Fig. 2.10a). However, the actual rotation axis of the acquired tilt series often deviates from this required position. This deviation is typically caused by the experimental setup parameters, such as the scanning directions in STEM. Thus, the goal is to determine the optimal tilt axis for the tomography series, which minimizes artifacts in the reconstructed slices. This can be achieved by reconstructing three slices along the object at the top and bottom (blue and green lines in Fig. 2.10a) and examining the presence of “arc” artifacts (highlighted by dashed lines in Fig. 2.10). To minimize the arc artifacts, the position and inclination of the tilt axis can be manually adjusted during the data processing step. When the tilt axis is properly aligned, more accurate tomographic reconstructions are obtained (Fig. 2.10b), showing no indication of strong arc artifacts. If there is a rotation of the tilt axis, only slices above and below the central slice will show arc artifacts, pointing in opposite directions (Fig. 2.10c, dashed lines). If there is a misalignment in the position of the tilt axis, an arc artifact will be observed in all slices, pointing in the same direction (Fig. 2.10d, dashed lines). As can be seen, an incorrect estimation of the tilt axis results in a loss of information in the final reconstruction. After the rotation axis is aligned, the series of aligned images can be used as input for the tomographic reconstruction process.

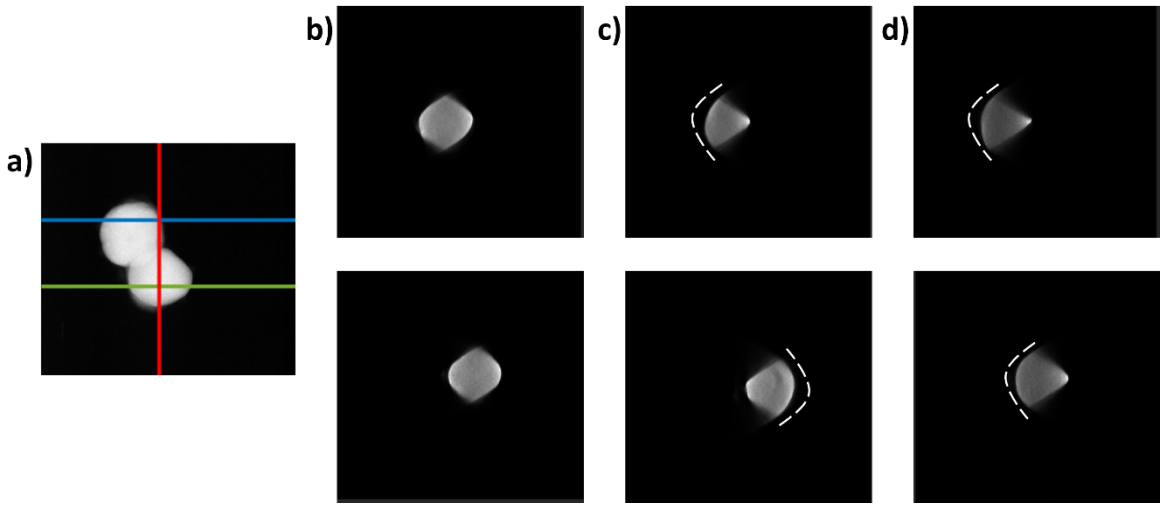

Figure 2.10 Alignment of the tit axis of a tomograph. (a) 0° projection of the studied Au@TiO_2 core-shell NP. The red line represents the position of the tilt axis, whereas the blue and green lines depict the positions of top and bottom slices through the 3D reconstructions corresponding to the top and bottom images in (b,c,d). In (b), the presence of arc artifacts is minimized due to the correct alignment of the tilt axis. In (c), an incorrect rotation of the tilt axis leads to the formation of arc artifacts, pointing to the opposite directions. In (d), a shift of the tilt axis results in the creation of arc artifacts, pointing to the same direction. White dashed lines correspond to arc artifacts.

2.6.3 Reconstruction of a tomographic tilt series

2.6.3.1 Theory of tomography

The Radon transform

The mathematical principles of ET are explained by considering a 2D object and its 1D projections. The extension to a 3D object is straightforward since a 3D object can be regarded as a set of independent 2D slices.

The Radon transform, which was introduced by Johan Radon in 1917, forms the basis of the mathematical principles for most tomographic techniques [251, 286, 287]. This transform describes the projection of an object f(x, y), which is equivalent to a line integral through f by a Radon transform R, as:

$$Rf = F(t,\theta) = \int_L f\,(x,y)ds \qquad (2.2)$$

where the function f is integrated along L with respect to line length. The (t, ϑ) coordinates of the Radon transform of function f(x, y) represent the projection angle (ϑ) and the distance of the projection line from the origin (t) as shown in Fig. 2.11.

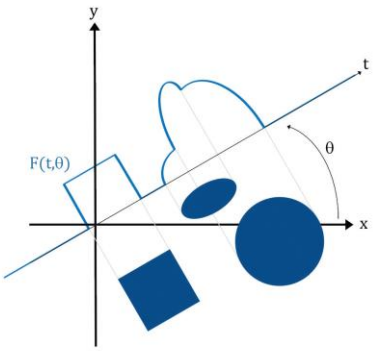

Figure 2.11 Schematic illustration of Radon transform. The object and its projection F(t, ϑ) is given for a certain projection angle ϑ.

The Radon transform converts a point into a sine curve. For this reason the Radon space image is called a 'sinogram' (Fig. 2.12). Fig. 2.14 shows examples of a sphere and a Shepp-Logan phantom (Fig. 2.12) and its Radon transform. By taking the inverse Radon transform of the projections, the reconstruction of the object f(x, y) can be retrieved. The Radon transform calculations intrinsically require a continuous function, and therefore, radial interpolation is required to fill the gaps in the Fourier space. Thus, the quality of the reconstruction is significantly affected by the type of implemented interpolation, where the smearing, data loss and creation of a non-unique solution from unique input data can be observed [288].

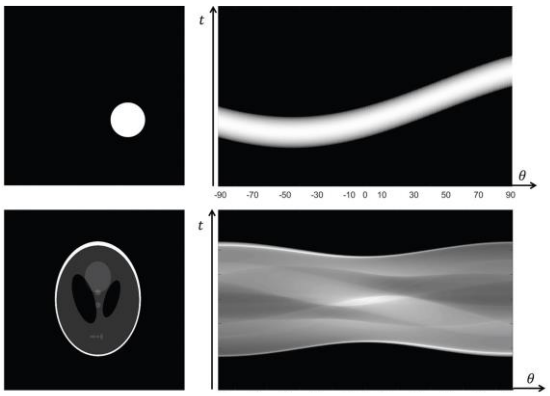

Figure 2.12 Top: Image of a sphere and its Radon transform. Bottom: Image the Shepp-Logan phantom and its Radon transform.

Fourier slice theorem

The Fourier slice theorem describes the relationship between the projections in real space and Fourier space. It states that the 1D Fourier transform of a projection of a 2D object is equal to a line through the 2D Fourier transform of that object. The line crosses the origin of the Fourier space and its direction is perpendicular to the projection direction. The Fourier slice theorem is illustrated in Fig. 2.13.

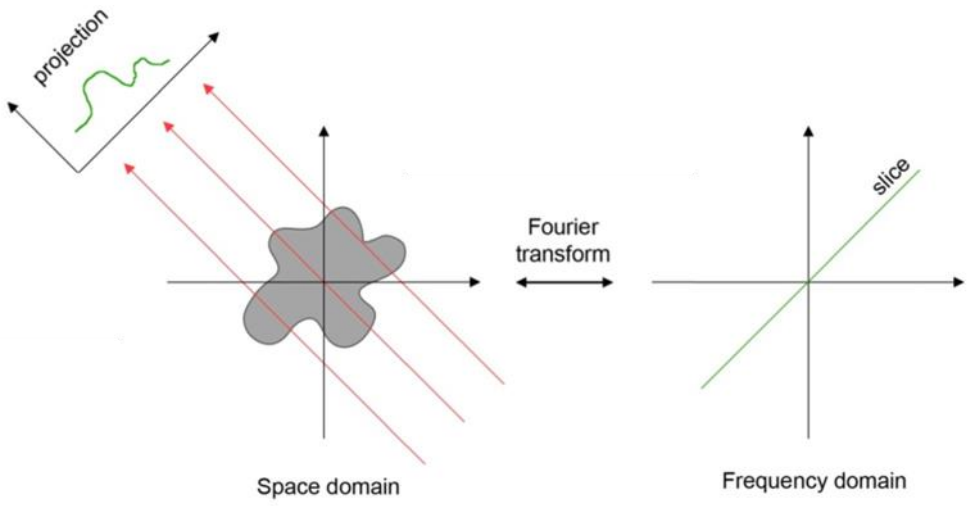

Figure 2.13: Illustration of the Fourier slice theorem which states that a projection at a certain angle at the space domain corresponds to a central section through the Fourier transform of that object.

The proof of the Fourier slice theorem is straightforward when a 2D object f(x, y) and its projection along the y direction are considered. The derivation however can be extended to higher dimensions as well. The projection through the 2D object can be described as:

$$p(x) = \int_{-\infty}^{+\infty} f(x,y)dy \tag{2.3}$$

The Fourier transform of the object f(x, y) is defined as:

$$F(u,v) = \int_{-\infty}^{+\infty} \int_{-\infty}^{+\infty} f(x,y)e^{-2\pi i(xu+yv)}dxdy \tag{2.4}$$

Choosing the slice perpendicular to the projection direction (v = 0) through this Fourier transform is then given by:

$$F(u,0) = \int_{-\infty}^{+\infty}[\int_{-\infty}^{+\infty} f(x,y)dy]e^{-2\pi i(xu)}dx \tag{2.5}$$

$$= \int_{-\infty}^{+\infty} p(x)e^{-2\pi i(xu)}dx \tag{2.6}$$

which equals the Fourier transform of the measured projection *p(x)*. When the proof needs to be generalized for an arbitrary direction, a rotation of axes needs to be included. By summing all the lines through the Fourier space of the object and calculating its inverse Fourier transform, a reconstruction can be obtained. However, it is not possible to sample over the full Fourier space because only a finite number of projections can be obtained in practice. As the projections are acquired at discrete angles, there are regular gaps in the Fourier space, which will hamper a perfect reconstruction of the investigated object. Additionally, this approach will lead to blurry reconstructions due to low frequency oversampling in Fourier space, which is illustrated in Fig. 2.14. It must be noted that here an interpolation in Fourier space is required due to its radial symmetry to reconstruct the object. The interpolation becomes problematic when only a limited number of projections is used, which is the main reason that this approach becomes less popular in practical tomography applications.

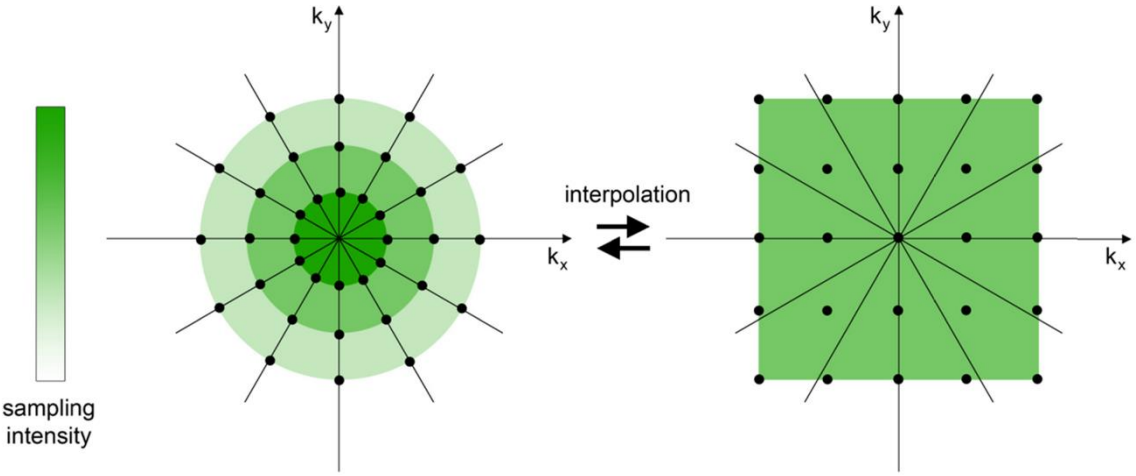

Figure 2.14: Due to the radial acquisition geometry, low frequencies will be oversampled in the Fourier space of the object in comparison to higher frequency values, which can be visualized by the closely packed black dots of the dark green circle close to the centre of the Fourier domain. To convert this radial lattice to a Cartesian grid an interpolation is required before the inverse Fourier transform can be calculated.Adapted from [289]

2.6.3.2 Reconstruction techniques

Following the discussion of the Fourier slice theorem, it is possible to execute tomographic reconstruction in real space. One frequently employed technique is weighted back-projection (WBP), which operates on the same principles as the Fourier slice theorem but is conducted in real space. In cases where a substantial number of projection angles is unavailable, WBP results in reconstructions of poor quality due to inadequate sampling [290]. To address this limitation, iterative methods are employed. A commonly used technique is the simultaneous iterative reconstruction technique (SIRT). SIRT involves refining the reconstruction at each iteration by solving the minimization problem:

$$\hat{x} = argminx\|Ax - b\|_2^2 \qquad (2.7)$$

where $\hat{x}$ is the vector that represents the reconstructed object, A denotes the projector operator, and b symbolizes the vector that represents the projection images. The initial iteration is obtained by applying the back projection method. Subsequently, images based on the first reconstructed volume are generated at the same projection angles and compared with the input images for reconstruction. The relative error, or residual, between the input and the generated projection image is computed simultaneously for each tilt angle and used to generate a new reconstructed volume [291]. This iterative process continues until convergence is achieved in minimizing the residual, as depicted in Fig. 2.15. For a typical SNR in HAADF-STEM tilt series of metallic NPs (SNR ≈ 8), it was reported that this method will converge after approximately 20 to 30 iterations [292]. Another reconstruction approach known as the Expectation-Maximization (EM) algorithm is employed for maximum likelihood estimation, particularly advantageous in scenarios involving missing variables, which can arise due to factors like the missing wedge in tilt series collection[293]. The EM algorithm operates by initially estimating the values of these missing variables and subsequently optimizing the reconstructed object. This two-step process of expectation (E) and maximization (M) is repeated iteratively until convergence is achieved. It is important to note that the SIRT algorithm can also be demonstrated to converge towards a maximum likelihood solution, but it is only suitable for situations where the noise in the input data is Gaussian distributed [291]. An advantage of EM is the adaptability to handle input data characterized by a Poisson distribution, experimentally arising from discrete number of events at each measured point – such as the number of scattered electrons in HAADF STEM, that makes EM algorithm a very popular practical method for obtaining ET reconstructions.

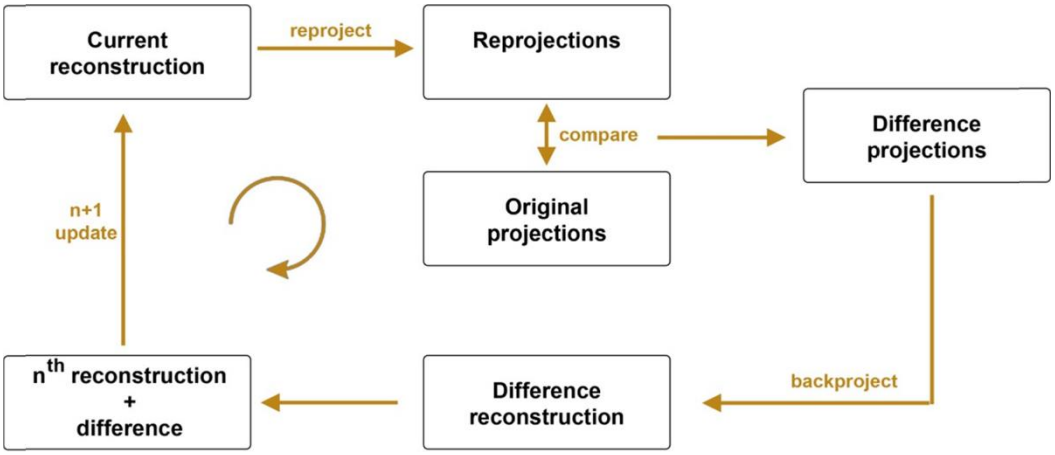

Figure 2.15 Schematic overview showing the principle of SIRT with n iterations.

Recently, significant advancements have been made in the development of more advanced algorithms that leverage prior knowledge in tomographic reconstructions. Two notable examples are the Discrete Algebraic Reconstruction Technique (DART) [294] and Total Variation Minimization (TVM) [295] algorithms. The DART algorithm operates under the assumption that only a limited number of materials exist, represented by a discrete set of grey values, within the reconstruction. During the iterative process, the DART algorithm performs segmentation of the reconstruction, enabling a direct quantifiable reconstruction (Figure 2.16). On the other hand, the TVM reconstruction algorithm is based on the principles of compressed sensing. In this method the prior

knowledge that the boundary of the specimen is sparse is used. By incorporating such prior knowledge, these advanced algorithms contribute to the improvement of tomographic reconstruction, but they are highly computationally demanding and require careful choice of reconstruction parameters, e.g. threshold intensity values for DART reconstruction.

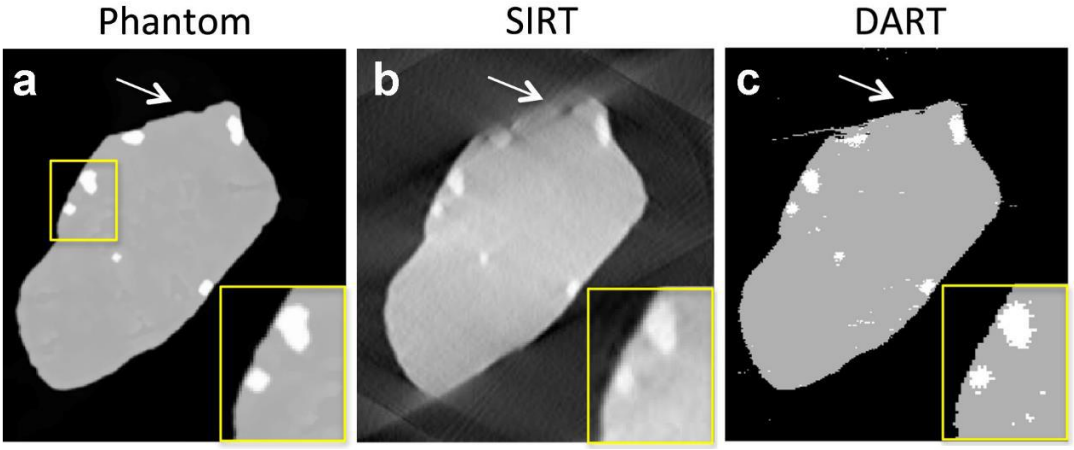

Figure 2.16 Numerical tomography simulations of (a) a phantom object and its reconstructions performed for a ±60° tilt range with 2° increments obtained using (b) WBP, (c) SIRT and (d) DART[296]. Adapted with permission from Elsevier (Copyright © 2017 Elsevier B.V.)

2.6.3.3 Visualization and Segmentation of a tomographic reconstruction

Three primary techniques are employed for visualization: orthoslices, isosurfaces, and volume rendering using voxels (voltex rendering). Orthoslices are essentially cross-sectional slices obtained from the reconstruction, enabling examination of the internal structure of the NP along various directions. These orthoslices are considered the most objective visualization method since they do not require a (manual) threshold. In addition, slices through the reconstruction can be used to analyze the inner structure of studied objects, e.g., holes in Ag-Au NPs (Fig. 2.17a). Apart from orthoslices aligned with the original x, y, and z directions of the 3D reconstruction, oblique slices, taken along arbitrary orientations, can also be employed to offer greater flexibility in visualizing specific features of interest.

In contrast, both isosurfaces and voltex rendering (Fig. 2.17b,c) involve selecting a threshold prior to their calculation. Only intensities surpassing the threshold are taken into consideration. For isosurfaces, voxels with identical intensities are connected to form a connected surface, effectively reducing the 3D volume to a 2D surface. This reduction significantly benefits calculation time. Conversely, voltex rendering projects the entire 3D volume onto the computer screen, allowing the manipulation of intensity, color, and transparency of the 3D reconstruction to emphasize specific details. These techniques allow for actions such as rotating the NP to various viewing angles, providing the means to analyze surface features effectively.

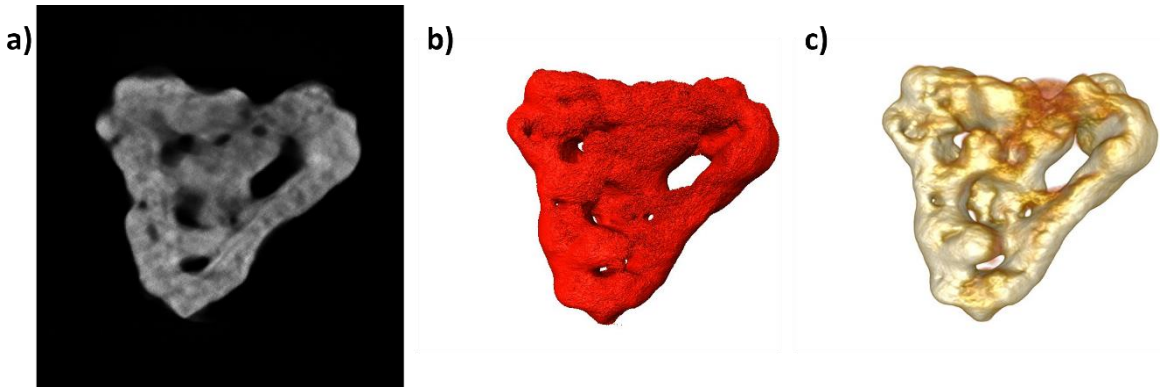

Figure 2.17 Example of 3D reconstruction representations of hollow Ag-Au NP: (a) central slice through the reconstruction, (b) isosurface and (c) voltex rendering.

To identify the location and distribution of different elements in a 3D reconstruction, segmentation of the voxels needs to be done. During this segmentation, voxels with a certain intensity value are assigned to a specific class. It should be performed in a careful manner as an incorrect segmentation can lead to incorrect conclusions on the 3D character of the specimen under investigation. If we are, for example, investigating a core/shell nanostructure, we would like to separate the core from the shell, which can be done with such a segmentation. The core voxels can be assigned to a first class and the shell voxels to another class. All the voxels in one class obtain the same value and a color can be addressed to this class (Fig. 2.18). A segmentation of different components in a material can be of great use when we want to investigate the volume of the different components. An automatic segmentation based on thresholding at different grey levels yields reliable quantitative results in case of a full tilt series of projection images [264]. Artefacts caused by the missing wedge of information will influence the quality of the reconstruction and complicate a straightforward automatic segmentation. Therefore, a careful manual segmentation needs to be performed. However, such a manual segmentation is highly subjective and time-consuming. For quantification purposes, more sophisticated dedicated methods such as spherical hough transform need to be applied [297].

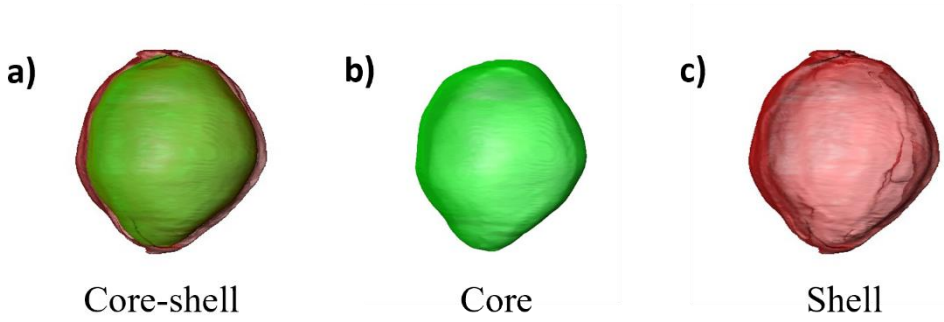

Figure 2.18 a) Segmentation of Au@TiO_2 core-shell NP, b-c) voxels representing the core and shell respectively.

Chapter 3: Advanced 2D and 3D electron microscopy for hybrid core-shell nanoparticles

Based on:

Joris Koek, Thomas Hartman, Peter de Peinder, Rajesh Ninakanti, Sara Bals, Freddy Rabouw, Bert M. Weckhuysen. Signal Origin in Shell-Isolated Nanoparticle-Enhanced Raman Spectroscopy. (Article under preparation)

Author contribution:

Synthesis and Raman spectroscopy was performed at Utrecht University

TEM characterization was carried out at the research group for electron microscopy for materials science (EMAT) at the University of Antwerp. I was responsible for all TEM acquisition, ET reconstructions and analysis

3.1 Introduction

Hybrid nanostructures are nanomaterials that consist of multiple elements, forming complex configurations in the geometry and/or at the atomic level. Referring back to chapter 1, it is well understood that determining the physical structure of a nanoparticle (NP) is crucial in the field of plasmonics for several reasons. The physical structure of a nanoparticle is a key factor that determines its plasmonic properties and thereby influences its functionality in various applications. We briefly summarize the dependance of plasmonic properties on its physical structure; the plasmonic properties directly or indirectly dependent on the size, shape, and material composition of a NP are its optical properties from localized surface plasmon resonance and electromagnetic field enhancement useful in catalysis and sensing applications [65, 298, 299]. The surface structure can help in determining stability to aggregation, absorption of molecules and interaction with biological systems which is vital for biosensing and drug delivery applications [300, 301]. In systems where multiple nanoparticles are used, their physical arrangement can lead to collective behaviors and coupling effects, influencing the overall plasmonic response [299]. Finally, understanding the physical structure allows control in the synthesis parameters to obtain new hybrid nanostructures [302].

As explained in chapter 2, TEM is an ideal technique to accurately determine the size and structure of such a hybrid plasmonic nanostructure. Every material will behave differently under the influence of the electron beam and exhibits its own challenges related to the imaging conditions. Core-shell structures form one such class of hybrid nanostructure. In this thesis, we examine Au@polymer and Au@TiO_2 core-shell structures by advanced electron microscopy techniques and we further exploit these structures in Chapters 4 and 5 for their application in photocatalysis. For core-shell nanoparticles resistant to beam damage, HAADF-STEM is ideal due to its enhanced contrast sensitivity based on atomic number (Z) [303]. In HAADF-STEM, pixel intensity is directly proportional to specimen thickness and the square of Z, providing better visualization of the core-shell structure. Core-shell nanoparticles with components such as polymers, that are easily damaged by the electron beam, are typically investigated by BF-TEM [304]. Recent approaches in TEM mitigate beam damage through the use of low electron doses[305, 306].

Additional challenges arise when core-shell nanoparticles exhibit significant differences in atomic number Z between the core and shell. In our study of Au@TiO_2 core-shell nanoparticles, the Au core is 65 nm thick with a Z of 79, whereas the TiO_2 shell is 2 to 4 nm thick with Z values of 22 and 8 for Ti and O, respectively. This large difference (in thickness) and Z leads to image contrast using HAADF-STEM, making the simultaneous visualization of core and shell far from straightforward. To overcome this limitation, the camera length of the HAADF detector can be increased, or a MAADF/ADF detector can be employed, as explored in previous studies [307]. These detectors collect signals from both incoherent and coherent inelastically scattered electrons, enhancing the visualization of lighter elements.

Electron microscopy images are inherently 2D projections of 3D objects. Comprehensive 3D characterization of core-shell nanoparticles using electron tomography is essential to accurately determine the plasmonic inter particle distances, shell uniformity, and coverage, which are critical parameters to be correlated with the nanoparticle's optical, chemical, and physical properties. Ideally, HAADF-STEM data is used as input for electron tomography, because these images fulfil the

projection requirement for tomograpgy stating that the pixel intensity scales monotonically with specimen thickness [257]. As already explained, for core-shell nanoparticles with significant thickness and Z differences, ADF-STEM is necessary to capture information from thinner and lighter elements. However, ADF-STEM introduces diffraction contrast in crystalline specimens, deviating from the projection requirement for electron tomography [237].

Previously, Sentosun *et al.* developed an advanced electron tomography approach to investigate Au@SiO_2 core-shell nanoparticles, combining HAADF-STEM and ADF-STEM data and using an inpainting technique to minimize diffraction contrast contributions [308]. In their study, the SiO_2 shell thickness was approximately 50 nm. In contrast, the core-shell nanoparticles in our study have shell thicknesses starting from 2 nm. The inpainting method, which relies on grey values from the edges of the shell, introduces background noise due to shell non-uniformity, making it unsuitable for our core-shell specimens.

In this chapter, we introduce a modified method for electron tomography study of core-shell nanoparticles with large differences in thickness and Z. We focus on the electron microscopy characterization of Au@polymer, Au@TiO_2, and Au@SiO_2 core-shell nanoparticles and detail the modified method for their 3D characterization, addressing the limitations of existing techniques and providing more accurate insights into these complex nanostructures.

3.2 Au@polymer core-shell nanoparticles

Covering plasmonic nanoparticles with a polymer shell has shown promise in several applications including sensing, photocatalysis, biomedical, meta surfaces and opto-electronic devices [298, 309–312]. In the current thesis, Au@polymer (Poly-allyl amine hydrochloride(PAH)) core-shell nanoparticles have been used in Chapter 5 for further exploitation in self-assembly into Au-TiO_2 supraparticles. Au nanoparticles are synthesized with citrate molecule as stabilizing ligands and coated with a polymer layer of poly allyl amine hydrochloride [298]. Visualizing the Au core and the polymer shell simultaneously presents challenges due to the minimal contrast between both compounds and the polymer's sensitivity to TEM analysis. As illustrated in Fig. 3.2a, an Au nanoparticle covered by a polymer layer on a commercially available carbon-coated Cu TEM grid is depicted. In this visualization, only the Au particle's contrast is noticeable and the polymer shell is hardly visible. In the past, visualization of polymer shells on core-shell nanoparticles made of inorganic materials was achieved by staining with ruthenium tetroxide [313]. However, these chemical treatments may alter the polymer's structure, affecting the accuracy of measuring the shell's thickness. Cryo-TEM has also been recognized as an effective method for observing nanoparticles within polymeric shells [314]. Yet, cryo-TEM often produces images with a low signal-to-noise ratio, making it difficult to quantitatively assess thin polymeric structures, such as those found in the Au@PAH core-shell NPs discussed in this study.

3.2.1 Study of supports for simultaneous visualization of Au core and polymer shell

Conventional carbon supported TEM grids do not yield enough contrast from Au@PAH core-shell NPs to visualize the polymer shell clearly (Fig. 3.2a). To improve the contrast between the Au nanoparticles, polymer shell and their support, we used carbon support grids consisting of a thin carbon layer (~3 nm) on top of a holey carbon TEM grid and carbon support grids consisting of single atomic layer graphene on top of a holey carbon TEM grid. The graphene based TEM grids are

prepared at EMAT laboratory using a novel process for which a patent has been granted. A conventional TEM grid consists of two layers: the supporting copper grid and a holey carbon film deposited on the grid. When the solution is drop casted on the grid, particles will deposit to the holey carbon film (Fig. 3.1a). Hereby, the particles observed in TEM images have the holey carbon film as support. On the other hand, the TEM grid coated by the ultrathin carbon layer has three different layers: the supporting copper grid, the holey carbon film and the ultrathin carbon film deposited on the grid. In the same way, the TEM grid coated with single layer graphene has three different layers: the supporting copper grid, the holey carbon film and the graphene film (Fig. 3.1b). After drop casting the solution, particles can have either only the graphene layer or only the thin carbon layer or the combination of the graphene/thin carbon layer and the holey carbon film as support.

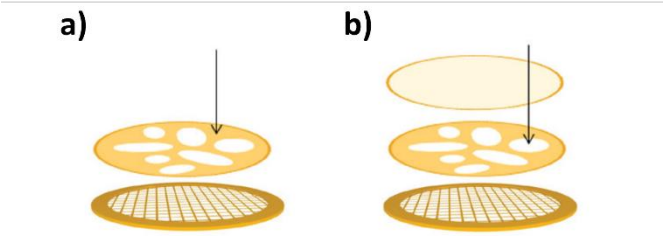

Figure 3.1: Schematic of a) holey carbon supported on TEM grid and b) ultrathin carbon or graphene supported on holey carbon TEM grid in a).

With the holey carbon TEM grid, the PAH shell surround Au nanoparticle is barely visible (Fig. 3.2a). By incorporating an ultrathin film carbon, the PAH shell can be more clearly demarcated (Fig. 3.2b). When the particle was positioned with only the graphene layer as support, we were able to observe the PAH shell very clearly in the BF-TEM images as there is less contribution from background (Fig. 3.2c). In this manner, the PAH shell could be visualized and its shell thickness could be accurately evaluated. The observations above indicate the importance of the supporting grid for TEM investigation. In general, the type of support is not questioned. Often, the scattering of electrons after interaction with nanoparticles is much stronger in comparison to scattering originating from the supporting grid, which result in direct observation of the nanoparticles after drop casting [315, 316]. In this study, the presence of the lower atomic number polymer material challenged the direct observation of the core-shell nanoparticles. Only by optimizing the support, we were able to visualize the core-shell nanoparticles. The synthesis and application of such Au@PAH core-shell nanoparticles is discussed in more detail in chapter 5. A more detailed electron tomography study of such Metal@polymer nanoparticles is done in a previous work by Claes *et.al.* [304]

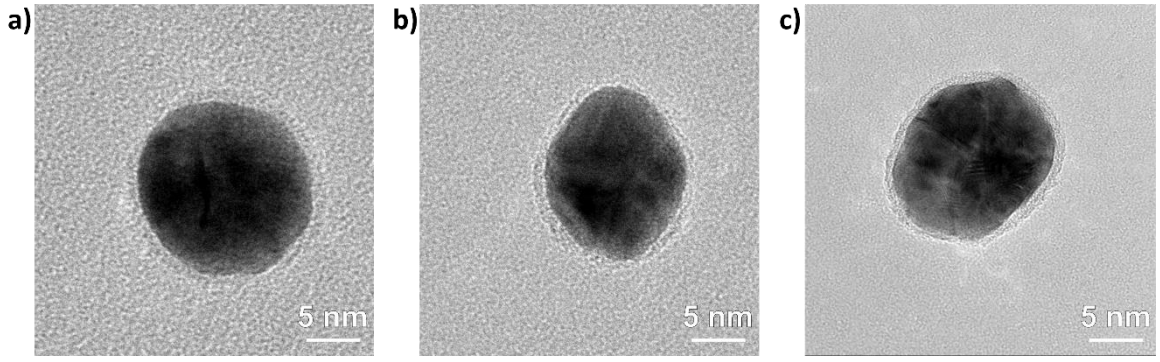

Figure 3.2: Au@PAH core-shell NPs with a) conventional carbon supported Cu grid, b) ultrathin carbon coated Cu grid and c) graphene coated Mo grid.

3.3 Au@TiO_2 core-shell nanoparticles

3.3.1 Introduction

The use of plasmonic Au nanoparticles to boost the activity of TiO_2 based photocatalysts by exploiting their plasmonic effect, is a widely applied strategy to improve solar light driven photocatalytic applications [4, 317]. However, Au nanoparticles sinter together when treated at high temperatures (>350 °C)[318], which is often required to calcine TiO_2 into the photocatalytic active anatase or rutile phase leading to reduction of the plasmonic enhancement effects. These limitations are overcome by stabilizing the plasmonic Au nanoparticles through the formation of a TiO_2 shell, that also directly acts as the semiconducting photocatalyst. Furthermore, the TiO_2 shell thickness is important to ensure that the near-field enhancement effect is strong enough on the surface of the TiO_2 and hot electron injection processes taking place at a short enough distance from the outer surface, where the photocatalytic processes are happening[298]. In this thesis, I have synthesized and studied the photocatalytic application of Au@TiO_2 core shell nanoparticles in Chapter 4 and in the current section we will discuss the electron microscopy and electron tomography techniques required for the same.

For Au@TiO_2 core-shell nanoparticles, three main questions will be attempted to be answered. 1) How thick is the TiO_2 shell? 2) Does the TiO_2 shell completely and uniformly cover the Au core? and 3) Does the Au core sinter upon calcination at 450 °C.

Simultaneous visualization of the Au core and the TiO_2 shell is far from straightforward due to the lack of contrast when being investigated by HAADF-STEM. Fig. 3.3a shows HAADF-STEM image of Au@TiO_2 core shell nanoparticle on a graphene TEM grid. Clearly, the TiO_2 shell is not visible in this case. This is primarily due to the difference in atomic number (Z) of Au (79) and Ti (21) as the image intensity in HAADF-STEM is proportional approximately to Z^2 and the thickness[236, 319]. Along with the difference in the atomic number, in the case of Au@TiO_2 core-shell nanoparticles the expected thickness of Au is 65 nm which is much higher than the expected 2-10 nm TiO_2 shell. Therefore the difference in image signal intensity between the Au core and TiO_2 shell is very high making it difficult to view the low intensity pixels of shell against the higher intensity pixels of gold.

3.3.2 Multimode tomography

Electron tomography studies are mostly based on HAADF-STEM imaging, since the image intensity in this technique scales with the thickness of the sample and the atomic number Z of the elements

under investigation [257]. As can be seen in Fig. 2.4 of chapter 2, for MAADF-STEM, the collection angle of the detector is adjusted in such a manner that both coherent and incoherent scattered electrons are collected, yielding information about both higher and lower atomic number elements [227]. A clear understanding can be obtained by referring to the schematic diagram of the HAADF-STEM and MAADF-STEM detector set-up in Fig. 2.4 in chapter 2. In Fig. 3.3, representative images of Au-TiO_2 core-shell nanoparticles, imaged by HAADF-STEM and MAADF-STEM are presented. Hereby, semi-collection angles of >80 mrad and 40 - 100 mrad are used, respectively. Clearly, the MAADF-STEM image in Fig. 3.3b yields better contrast to visualize the TiO_2 shell compared to the HAADF-STEM image.

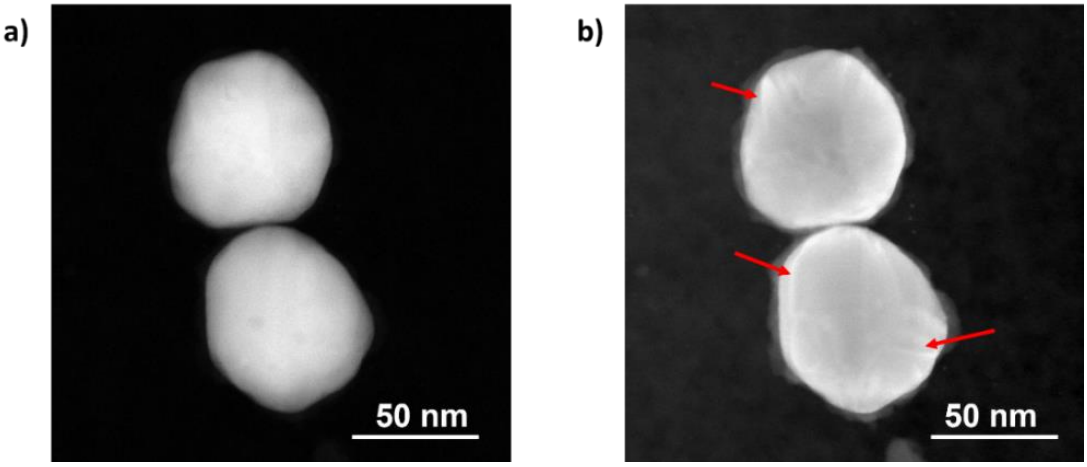

Figure 3.3: a) HAADF-STEM and b) MAADF-STEM image of Au@TiO_2 core-shell nanoparticles

Au in its bulk form starts melting at more than 1000 °C. Although, at the nanoscale Au nanoparticles can melt and sinter together when placed in close proximity at as low as 140 °C [320]. On the other hand TiO_2 nanoparticles are estimated to melt at more than 2000 °C [321]. Therefore, the TiO_2 shell can protect Au nanoparticles from sintering. From Fig. 3.4 the TiO_2 shell thickness is observed to be increasing starting from 2 ± 0.5 nm, 4 ± 0.7 nm, 8 ± 1.1 nm and up to 12 ± 1.5 nm with increasing TiO_2 precursor in its synthesis. The shell thickness was calculated using measurements from more than 100 nanoparticles. Single to five nanoparticle assemblies were observed on the TEM grid, but more than 80% of the specimen contained dimer core-shell assembly among more than 500 nanoparticles that have been studied. It can be seen in Fig. 3.4a-b that Au nanoparticles with 2 nm TiO_2 shell sinter and Au nanoparticle with 4 nm TiO_2 shell thickness do not sinter when subjected to elevated temperature of 450 °C. The reason for Au nanoparticles with 2nm shell to sinter could be due to presence of pinholes in the TiO_2 shell. The pinholes can be represented as space between two TiO_2 nanoparticles in the shell. With a 4 nm shell, the TiO_2 nanoparticles in the shell can be densely packed preventing the Au nanoparticles from sintering.

For such dimer core-shell structure for e.g. in Fig. 3.4a, it is difficult to understand whether the NPs have sintered due to heat treatment or they are just overlapping each other. Therefore, a 3D characterization using electron tomography of such a structure needs to be performed. For tomography of such NPs using MAADF-STEM, the main limitation is that the projection requirement for tomography needs to be fulfilled, which is not the case if diffraction contrast is present (as can be seen with the red arrows in Fig. 3.3) [257]. MAADF-STEM technique is advantageous to observe

the lighter elements with lower atomic number, but since less incoherently scattered electrons are also collected, the projection requirement is also violated [237]. It is therefore clear that when selecting an optimal value for the collection angle, one will always have to compromise between optimal contrast to visualize lower atomic number and fulfilment of the projection requirement. Therefore, we propose to exploit the flexibility of modern TEM instruments, in which more than one ADF detector is available. Through the simultaneous use of multiple ADF detectors, a reliable 3D reconstruction of both the core and shell of the nanoparticles and can be achieved. Since the requirement of multiple separate tomography series is replaced by acquiring a single tomography series with data from multiple detectors, the tomography series is acquired in an electron dose efficient manner and minimal impact on structure of the nanoparticles [237].

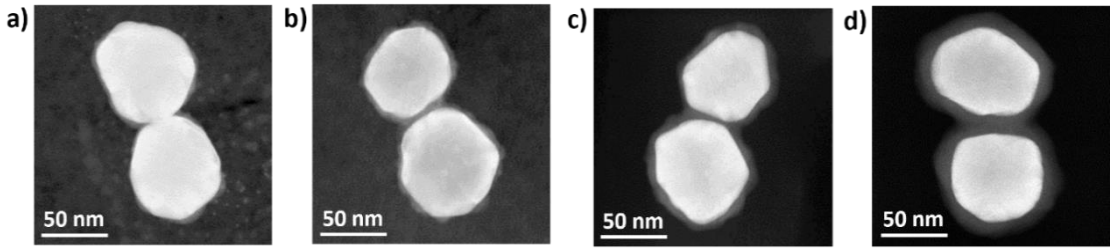

Figure 3.4: Au@TiO2 core shell nanoparticles with a core of 65 nm and a shell thickness of a) 2±0.5 nm, b) 4±1 nm, c) 8±1 nm, d) 12±1.5 nm.

Therefore, tomography series are acquired using both HAADF and MAADF detectors, over a tilt range from -70° to +72° with a tilt increment of 2° (Fig. 2.7a). Since the acquisition of tomographic series occurs simultaneously with multiple detectors we refer to it as multimode tomography. During the acquisition, the image intensities are all scaled between 10,000 and 50,000 counts per pixel [322]. In Fig. 3.3 b) limited diffraction contrast can be observed in the MAADF-STEM reconstruction as pointed by the green arrows. However, the diffraction contrast present in the MAADF- STEM signal violates the projection requirement for tomography and artefacts are expected in the reconstruction [257]. To overcome this problem, we propose to combine HAADF-STEM and MAADF-STEM reconstructions. Firstly, HAADF-STEM reconstruction is performed to obtain information about the Au nanoparticle in core. Then MAADF-STEM reconstruction is performed and the TiO_2 shell is segmented. Finally both the reconstructions are overlapped obtaining information about the core and the shell, and avoiding artifacts from diffraction contrast. In this manner, information on the shape of the NPs can be obtained, together with a clear visualization of the TiO_2 shell. To combine the MAADF-STEM and HAADF-STEM reconstructions in a straightforward manner, both tilt series are simultaneously acquired using two annular detectors with collection angles ranging from 40 to 100 mrad for MAADF-STEM and from >80 mrad for HAADF-STEM. These settings are used for all multimode tomography reconstructions. Because the acquisition is performed simultaneously, the alignment parameters for both series are identical. Next, 3D reconstructions are calculated by the expectation maximization algorithm [292]. To obtain a better visualization of the TiO_2 shell from the MAADF-STEM reconstruction, a manual segmentation is performed. This approach is necessary because reconstruction methods which includes a segmentation, such as DART and SSR, are unsuitable for the structure under study. In DART, grey values from the interior and exterior edges of the specimen are used as prior knowledge for reconstruction [323]. However, the thin TiO_2 shell makes accurately considering edge grey

values challenging. Additionally, other unsupervised image segmentation method like Watershed transform provided inaccurate segmentation as it could not identify the pixels belonging to the shell and background. Fig. 3.5 shows a 3D visualization of the HAADF-STEM reconstruction of the Au nanoparticle (Fig. 3.5 a)), as well as MAADF-STEM reconstruction of the TiO_2 shell (Fig. 3.5 b)). By superimposing both reconstructions (Fig. 3.5 c), we are able to determine the size of Au nanoparticle, thickness of the TiO_2 shell, volume of Au and TiO_2 and sintering of Au NP simultaneously without any artefacts from diffraction contrast. The processing of tomography data reveals that the volumes of the Au core and TiO_2 shell are 2.98 x 10^5 nm^3 and 2.01 x 10^4 nm^3, respectively, for an Au nanoparticle with a 2 nm TiO_2 shell, and 2.94 x 10^5 nm^3 and 5.42 x 10^4 nm^3, respectively, for an Au nanoparticle with a 4 nm TiO_2 shell. From the reconstruction, it could be seen that the TiO_2 shell is quite uniform with some indentations. Therefore, in conclusion, using multimode tomography we are able to investigate core shell nanoparticles with high and low atomic number and the Au@TiO_2 core-shell nanoparticles with 2 nm shell thickness sinters together (Fig. 3.5c) and one with 4 nm shell thickness do not sinter (Fig. 3.5d). This sintering of plasmonic nanoparticles has an effect on its optical and catalytic properties which will be studied further in chapter 4.

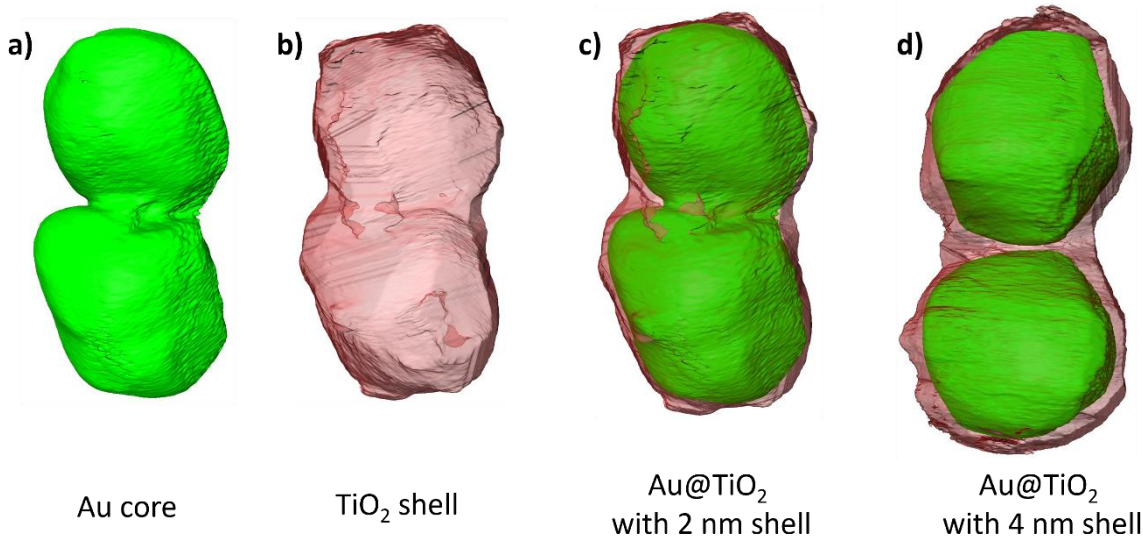

Figure 3.5: Segmentation of 3D reconstruction of a) Au core by HAADF-STEM, b) TiO_2 shell by MAADF-STEM. Superimposition of segmentation of Au and TiO_2 with c) 2nm shell and d) 4 nm shell thickness.

3.4 Au@SiO_2 core-shell nanoparticles

3.4.1 Introduction

Surface-enhanced Raman spectroscopy (SERS), an important technique for chemical and biological analysis, has been actively employed in many investigations due to its extremely high surface detection sensitivity coming mainly due to electromagnetic enhancement from LSPR properties of plasmonic nanoparticles and chemical enhancement due to binding of molecule to the nanoparticle surface [324]. Shell isolated nanoparticle enhanced Raman spectroscopy (SHINERS) improves SERS by using a thin dielectric layer to protect the plasmonic gold/silver cores from the surrounding atmosphere and the analyte [325–327]. Therefore, in the current SHINERS configuration, Au

nanoparticles (NPs) with a 1.5-2.5 nm silica layer are used to enhance the Raman signal. The Au@SiO_2 core-shell nanoparticles used in the current study are synthesized and studied in the research group of Prof. Bert Weckhuysen (Utrecht University, Netherlands) and characterized in collaboration with EMAT. The silica shell on Au nanoparticles is formed by functionalizing the Au nanoparticle with amine groups and further an inorganic precursor sodium silicate is added to interact with amine groups to form an ultrathin 2-4 nm SiO_2 shell. In SHINERS the signal contribution from electromagnetic enhancement and chemical enhancement is highly debated and therefore it is important to investigate whether 1.5-2.5 nm silica layer completely covers the Au nanoparticle and whether the SiO_2 shell is uniform [327]. In the current section we will therefore try to answer the question whether the Au@SiO_2 nanoparticles have a complete and uniform SiO_2 shell.
Stemming from Au@TiO2, Au@SiO2 offers a similar challenge of high pixel intensity of Au and lower pixel intensity of SiO_2 shell for TEM characterization. However, the difference in intensity is even more amplified due to larger size of Au nanoparticles (80-100 nm) and a lower Z of Si (14) compared to Ti (21).

3.4.2 Contrast optimization

Fig. 3.7 shows a MAADF STEM image of an Au@SiO_2 core-shell nanoparticle. Even after using a graphene TEM grid and MAADF-STEM, it is difficult to visualize and identify the SiO_2 shell from the background. Therefore, for better visualization of the uniformity of the silica shell we conducted exit wave reconstruction from high-resolution TEM images. We know from section 3.3, it is difficult to visualize the light elements of SiO_2 in a thin 2nm shell in contrast to a heavier element Au with a thickness of 80nm. Exit wave reconstruction (EWR) is a potential technique to overcome this problem and visualize light and heavy elements simultaneously[328].
Exit wave reconstruction is based on the acquisition of a focal series and consists of an experimental step followed by a computational one. In the experimental part, a series of images is acquired such that each image in the series has a different value of the objective lens defocus, as illustrated in Fig. 3.6. In the computational part, the acquired series is processed and the exit wave function, which has amplitude and phase, is reconstructed. By inverting the image formation process and hereby eliminating the lens aberrations, such as spherical aberration, all information can in principle be recovered up to the microscope's information limit [232, 238, 329–331]. Eventually residual aberrations, such as astigmatism and coma, can be compensated by applying appropriate phase shifts [332].
In order to visualize the surface ligands, the experimental conditions for the exit wave reconstruction should be thoughtfully chosen. As described above, a series of images is acquired such that each image in the series has a different defocus value. The question here is which defocus values should be present in the focal series. The midpoint of the focal series should be the optimal defocus. For a C*s* aberration corrected microscope, this optimal defocus lies close to zero defocus. In practice, this means that the focal series is acquired symmetrically around the zero defocus in an aberration corrected microscope. Focal series are often recorded with an equidistant focal spacing. The optimal defocus value δ can be calculated from the information limit of the microscope (highest transferred spatial frequency):

$$g_{max} \approx \sqrt{\lambda\delta} \leftrightarrow \delta \leq \frac{1}{\lambda g_{max}^2} \quad (1)$$

For a microscope operated at 300 kV with g_{max} equal to 1/80 pm, the optimal defocus is ≤ 3.2 nm. When the microscope is operated at 80 kV with g_{max} equal to 1/140 pm, the optimal defocus is ≤ 4.7 nm. On the other end, our main focus is on visualization of shell. Therefore, for the experiments performed in this section a focus step of 0.5 nm was used.

The range of defocus values L, of the series influences the lowest reconstructible spatial frequency g_{min}

$$g_{min} \approx \frac{1}{2}\sqrt{\frac{1}{\lambda L}} \quad (2)$$

$$L = (N-1)\delta \quad (3)$$

with N the number of images in the focal series. The increase of the number of images results in a decrease of the lowest reconstructible frequency. For a microscope operated at 300 kV ($\lambda\lambda$ = 1.97 pm), with a focal step of δ = 0.5 nm and g_{min} equal to 2.5 nm^{-1}, the number of images in the series should be N = 30. The range of defocus values L is approximately 15 nm, which means that the series will be acquired between +7.5 nm and -7.5 nm so that the zero defocus is in the middle. EWR was performed using a negative spherical aberration (Cs = -4.35 µm).

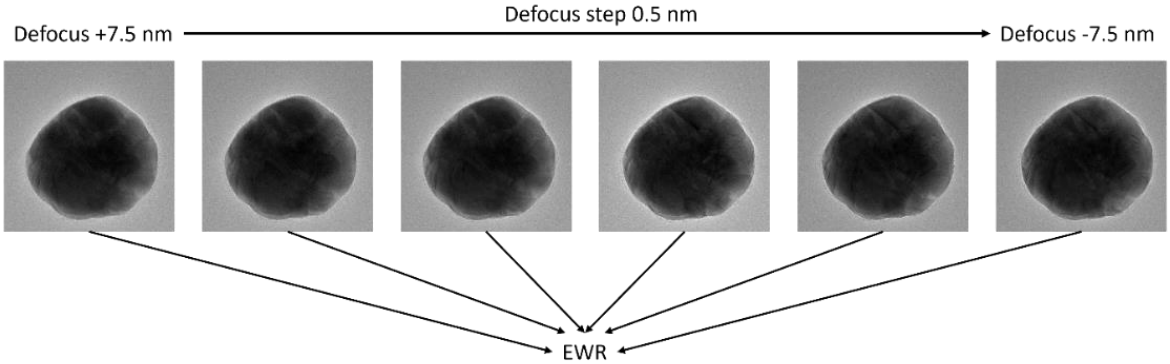

Figure: 3.6: A series of images is acquired such that each image in the series has a different value of the objective lens defocus. This focal series is used as input in the computational part.

On the computation side as per literature, X-Wave software in MacTempas [333] with the Gerchberg-Saxton algorithm [334] has the advantage that the defocus step can be variable and there is no restriction in the parameters (e.g. number of images and reconstruction area) and reconstructed area, in comparison to the other available software such as TrueImage [335] (based on a method of maximum likelihood [336]) and Digital Micrograph (Iterative Wave Function Reconstruction technique [337] and the Focal and Tilt Series Reconstruction[338]). In the first step of this algorithm, an initial guess for the wave function is obtained by the multiplication of the amplitude of the experimental images and a random phase. Next, the Fourier Transform of this initial wave function is calculated. The phases resulting from this Fourier transformation are combined with the FFT of the experimental data, resulting in a new estimate of the function at the reciprocal plane. Then, the inverse FFT is calculated and a new phase is computed [334, 339]. The calculated and experimental images are compared and the error is minimized by the repetition of the experiment.

Fig. 3.6 represents the phase image which is sensitive to light atoms such as Si and O. EWR consistently revealed the core-shell structure in all nanoparticles, although variations in the degree of uniformity in the silica shell were observed within individual nanoparticles. Fig. 3.6a-b provides

an overview of the phase image with non-uniform and uniform SiO_2 shell, respectively. Au is marked in red and SiO_2 shell is marked in blue to guide the reader's visualization. The phase image and its inset in Fig. 3.7c-d, clearly depicts the Au core with a non-uniform shell.

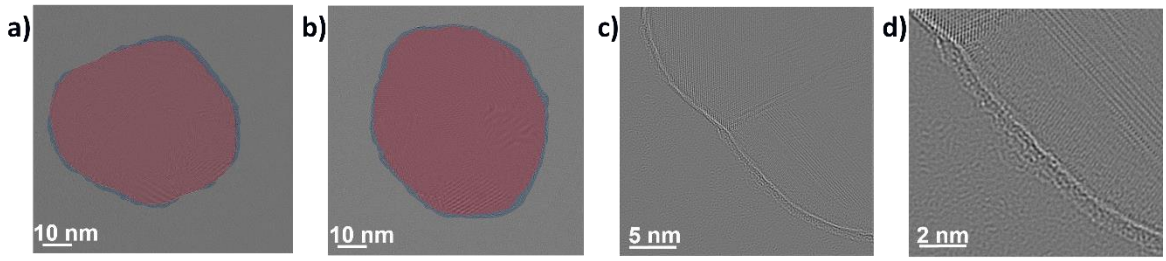

Figure 3.7: Overview of phase image from exit wave reconstruction of a Au(red)@SiO_2(blue) NP with a) non-uniform shell and b) uniform shell. c) Phase image from exit wave reconstruction of a Au@SiO_2 NP and d) inset of phase image(c)).

Electron tomography with a modified reconstruction process

The phase image from EWR is just a 2D projection of a 3D nanoparticle and electron tomography is necessary to study the uniformity of shell in 3D. EWR cannot be used for electron tomography as the pixel intensity does not scale with the thickness of nanoparticle under consideration, and therefore, we used scanning transmission electron microscopy (STEM). However, due to its dependence on Z contrast, similar to Au@TiO_2 nanoparticles in section 3.3, high angle annular dark field STEM (HAADF-STEM) is not appropriate and medium angle annular dark field STEM (MAADF-STEM) was used. Cupping artifact is also a problem when dealing with especially large Au nanoparticles, where a thickness dependent, non-linear damping of the image intensities occurs. Due to this artifact, the intensity in the interior of the reconstruction of a homogeneous particle is underestimated. The cupping artifact can impede interpretation when the reconstructed intensities are needed to discriminate between different elements in neighboring regions [340]. As observed in Fig. 3.8, from the MAADF-STEM image it is difficult to visualize and identify the SiO_2 shell from the background. While performing multimodal tomography and its reconstruction, it was difficult to differentiate the SiO_2 shell from the background and the cupping artifact due to large 80 nm Au nanoparticle in the core made it more difficult to visualize the SiO_2 shell. In MAADF-STEM, both coherent and incoherent scattered electrons can be collected, and this may not fulfil the projection requirement [237, 257] Taking this into consideration, only data from MAADF-STEM images was used for 3D reconstruction and as the projection requirement may not be fulfilled, an advanced 3D reconstruction was carried out. The scheme of reconstruction procedure is presented in Fig. 3.8. The image gamma was corrected by an automated procedure by maximizing the contrast difference between the background and SiO_2 shell in the intensity histogram [341]. A median filter was applied to remove specular noise from the background and shell [342]. The modified image was segmented to create a mask of the SiO_2 shell and Au core without the background. SiO_2 mask was used to obtain data from Au. The determined Au mask is used isolate and infill the SiO_2 shell. Reconstructions from Au nanoparticle, infilled SiO_2 shell and the original image were iterated until the best fit convolution is found. Reconstructions were performed with SIRT (Simultaneous Iterative Reconstruction Technique).

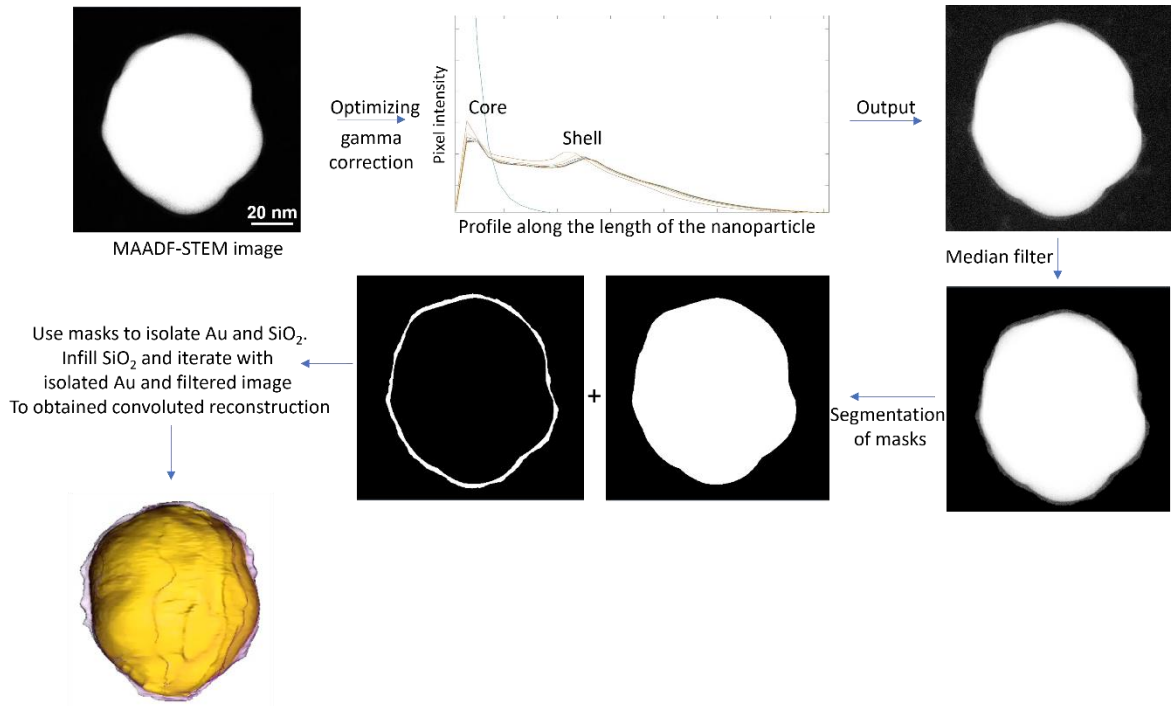

Figure 3.8: Schematic representation of the modified reconstruction procedure. The image gamma is corrected by maximizing the contrast difference between the background and SiO_2 shell followed by a median filter is to remove specular noise. A mask of the SiO_2 shell and Au core is created from the filtered image. SiO_2 mask is used to obtain data from Au. Au mask is used to isolate SiO_2 and further infill the SiO_2 shell. Au nanoparticle, infilled SiO_2 shell and the original image are iterated until the best fit convergent reconstruction is found using SIRT.

The result of this procedure is presented in Fig. 3.9, showing a 3D representation of the non-uniform silica shell around the Au nanoparticle. Nanoparticles with a more uniform silica shell, were also found to be present. Using electron tomography, it can be stated that different Au@SiO_2 nanoparticles possess a mix of either uniform or non-uniform silica shell. These high-resolution images and electron tomography collectively reveal the inhomogeneous nature of the silica layer. Therefore, in conclusion EWR allowed us to visualize SiO_2 shell in Au@SiO_2 core-shell NPs in a better way, and modifying the reconstruction steps allows for its 3D tomography reconstruction.

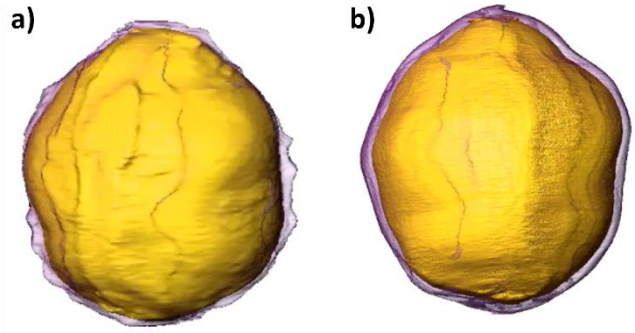

Figure 3.9: Visualization of reconstruction of Au@SiO2 core-shell NPs with a) non-uniform shell and b) uniform shell.

3.5 Conclusion and outlook

In this chapter, we have evaluated possible routes to visualize core-shell nanoparticles in two dimensions as well as in three dimensions leading to a better understanding on characterization of core-shell nanoparticles. The superiority of graphene TEM grids to visualize soft polymer materials

and simultaneous visualization of high contrast materials with low and high atomic number has been demonstrated. We have evaluated the potential of combined HAADF-STEM and MAADF-STEM tomography to simultaneously visualize Au core and TiO_2 shell. Tilt series have been acquired in a dose-efficient manner by simultaneously collecting images using two different annular detectors. Post-segmentation combining the reconstructions from both detectors provides a clear view of the Au@TiO_2 core-shell structure. Even though multimode tomography showed promising results for hard soft core-shell nanoparticles, due to the noisy background, a new image processing technique and further reconstruction was applied to perform tomography with Au@SiO_2 core-shell nanoparticles. For Au@SiO_2 core-shell nanoparticles, EWR was applied to visualize the lighter elements of SiO_2 against a heavier element Au. New electron microscopy techniques such as iDPC and 4D STEM provide opportunities to visualize lighter elements in a more dose efficient way and can be used as alternative strategies that can serve as better alternative to EWR. The methodologies discussed in this chapter are helpful and generally applicable to study hybrid core-shell nanoparticles, especially with a significant difference in their atomic number. The 3D characterization techniques applied in this study have yielded important information on the structure of core-shell nanoparticles, useful in photocatalytic applications as discussed in further chapters.

Chapter 4: $Au@TiO_2$ core-shell nanoparticles for plasmon enhanced photocatalysis

Based on:

Rajeshreddy Ninakanti, Rituraj Borah, Timothy Craig, Radu-George Ciocarlan, Pegie Cool, Sara Bals, and Sammy W. Verbruggen. Effect of varying shell thickness and sintering in $Au@TiO_2$ core-shell nanoparticles on plasmon enhanced photocatalysis

(Article under preparation)

Author contribution:

N.R. conceived the idea, synthesized and performed all the electron microscopy characterization

B.R. performed all the electromagnetic modelling

C.T. helped perform the post-processing of tomography reconstruction.

C.RG. performed Raman spectroscopy

C.P., B.S., V.W.S supervised the work

4.1 Introduction

TiO_2 is still the most widely used photocatalyst given its thermal and chemical stability and low cost, despite its wide bandgap (3.2 eV) that restricts the photoactivity to the ultraviolet region of the solar spectrum [343, 344].We know from chapter 1, to improve the photocatalytic efficiency of TiO_2, plasmonic metal nanoparticles are used to extend the limited UV light photocatalytic activity of TiO_2 to visible and NIR light. Exploiting their localized surface plasmon resonance (LSPR) properties, has been shown to be a promising strategy to enhance various photocatalytic reactions such as CO_2 reduction, water splitting, air purification, self-cleaning activity, *etc.* [18, 61, 317, 345, 346]. Multiple opto-physicochemical processes can lay at the basis of this plasmonic enhancement, for which the interested reader is referred to specialized literature [347]. When considering non-thermal pathways, as those occurring under ambient irradiation conditions, roughly speaking two different phenomena can be discerned. Firstly, the injection of hot electrons generated on plasmonic nanoparticles into the semiconductor conduction band can enhance the excitonic activity. Secondly, the extreme light concentration in the vicinity of the plasmonic nanoparticles, better known as the near-field enhancement, acts as an antenna that captures and concentrates electromagnetic energy [348–350].

A plasmonic photocatalyst can be further improved by rational design of the composing nanostructures and their interfaces. The most common method to prepare a metal-TiO_2 composite material is by simply depositing plasmonic nanoparticles on semiconductor surface, for instance through wet impregnation [351–353]. Such a configuration, however, strongly limits the contact region between the plasmonic nanoparticle and the TiO_2 surface. Since the plasmonic enhancement is highly polarization dependent, the nanoscale configuration of TiO_2 and metal nanoparticle composite systems is crucial for achieving high photocatalytic activity. This nanoscale control over such structures and interfaces is intrinsically difficult, especially by wet-chemical synthesis procedures. For example, any synthesis procedure involving high temperature calcination (>350 °C), as would be required for crystallization of TiO_2, would also lead to oxidation or sintering of plasmonic metal nanoparticles in the composite material, hence compromising their plasmonic properties [354–356]. It is a true challenge to obtain TiO_2 and plasmonic metal composite nanostructures with high controllability so that the optical enhancement brought about by the plasmonic nanoparticles can be efficiently exploited.

As a solution to both main issues listed above: (i) a low contact interface between plasmonic metal and TiO_2 surface, and (ii) poor stability of plasmonic metals in composite structures that need to undergo heat treatment, we propose the use of plasmonic metal@semiconductor core-shell nanoparticles as a basic building block in this work. Metal@semiconductor core-shell nanoparticles provide an interesting configuration that inherently favors efficient plasmonic enhancement, *i.e.* the plasmonic core enhances the photocatalytic processes happening at the surface of the shell, and provides an all-round 360° contact interface [87, 357–359]. Furthermore, sintering can be inhibited by the presence of this protective shell around the plasmonic core. For enhanced photocatalytic activity and stability in core-shell nanostructures, both the size of the plasmonic core and the thickness of the shell are vital parameters. The size of the core determines the extent of plasmonic enhancement due the strong size/shape dependence of the LSPR effect. The shell thickness on the other hand is important to ensure that the near-field enhancement effect is still

strong at the surface of the TiO_2 shell, as it is known to decay exponentially with distance from the metal surface[23]. Also, hot electron injection processes should be enabled at a short enough distance from the outer surface, where the photocatalytic reactions occur. Near-field enhancement is higher at the surface of the nanoparticles and reduces by orders of magnitude as one moves a few nanometers away from the surface. Most studies involving metal@TiO_2 core-shell nanostructures report shell thicknesses exceeding 5 nm, this significantly undermines the potential for near-field enhancement [87, 357–359].

In the present chapter, we have synthesized Au@TiO_2 core-shell nanoparticles, with slow hydrolysis of the titanium triethanolaminato isopropoxide (TTEAIP) precursor allowing to accurately control the shell thickness at the nanometer scale with shell thickness ranging from 2 nm to 12 nm. As already studied in chapter 3, electron microscopy and electron tomography was very important in understanding the structure with respect to thickness of TiO_2 shell and sintering of Au nanoparticles with vary shell thickness. Photocatalytic hydrogen evolution and stearic acid degradation tests have been performed to find an optimal shell thickness to maximize near field enhancement and avoid sintering. The results have been further substantiated with classical electromagnetic computations, surface enhanced Raman spectroscopy (SERS), and quantification of reactive radicals using terephthalic acid (TA) and 2,3-bis-(2-methoxy-4-nitro-5-sulphenyl)-(2H)-tetrazolium-5-carboxanilide (XTT) as probe molecules. Based on these experiments, we revealed that controlling the TiO_2 shell thickness and sintering of Au for an optimal near-field enhancement can help achieve better photocatalytic activity.

4.2 Results and discussion

4.2.1 Synthesis and structural characterization

The synthesis of Au@TiO_2 core-shell nanoparticles builds on the procedure described by Hartman *et al*. [99]. Firstly, Au nanoparticles are synthesized using a seed mediated synthesis in the presence of citrate. Next, titanium tri-ethanol aminato iso-propoxide (TTEAIP) is added to the suspension of Au nanoparticles to allow interaction of TTEAIP with the citrate capping ligands around Au. It is critical to disperse Au nanoparticles in isopropanol and not water to avoid immediate hydrolysis of TTEAIP. Slow hydrolysis of TTEAIP in isopropanol by increasing the pH is proven to be the key to accurately control the thickness of TiO_2 shell. By increasing the concentration of TTEAIP, the TiO_2 shell thickness around the Au cores can quite easily be increased. The samples are here on referred to as Au2, Au4, Au8 and Au12 with the number representing TiO_2 shell thickness in nanometers.

As shown in Fig. 4.1a-d, the high angle annular dark field scanning transmission electron microscopy (HAADF STEM) images confirm that increasing the concentration of TTEAIP in the mixture, effectively results in Au@TiO_2 core-shell nanoparticles with increasing TiO_2 shell thickness, reaching values of 2, 5, 8, and 12 nm. Two nanoparticle assemblies have been used for study as they dominate over one, two, three, four and five nanoparticle assemblies in the sample. It can be observed in Fig. 4.1e-h that adjacent Au nanoparticles with 2 nm shell undergo sintering during calcination, whereas Au nanoparticle with 5 nm and higher remain well separated. The sintering of nanoparticles at high temperatures is a spontaneous process towards a more energetically favorable state with lower specific surface area [360]. In Au2, sintering is possibly facilitated by the

presence of micropores and pinholes in the TiO_2 shell. In Au5, Au8 and Au12, the thinker shell acts as a physical barrier that prevents the Au cores from touching each other.

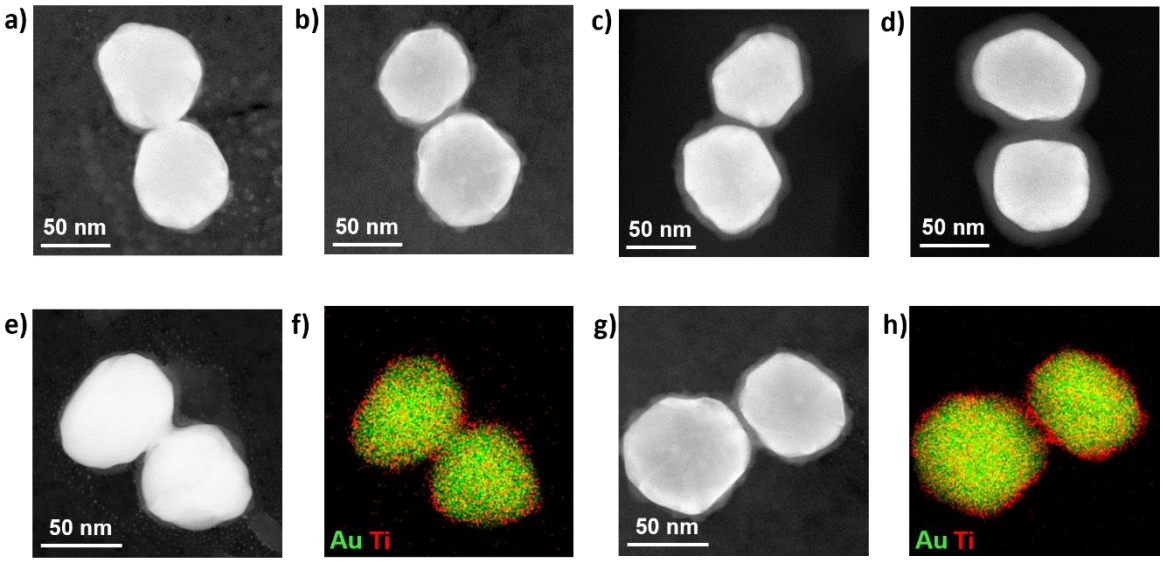

Figure 4.1: Au@TiO_2 core-shell nanoparticles with a core of 65 nm and a shell thickness of a) 2±0.5 nm, b) 4±0.7 nm, c) 8±1.1 nm, d) 12±1.5 nm. HAADF-STEM image and representative EDX map of e-f) Au2 and g-h) Au4.

2D electron microscopy images of such core-shell nanoparticles are usually inadequate to analyze the structure-property relation of nanomaterials because they only provide a projected image of a 3D structure. Since a 2D projection can be misinterpreted, electron tomography was performed to confirm the sintering in Au2 and Au5. Tomography visualization in Fig. 4.2a-b represent electron tomography reconstructions of Au2 and Au5, respectively, confirming the sintering of Au cores in Au2 while they remain fully separated in Au5. Nanoparticle sintering in Au2 and no sintering in Au5, Au8 and Au12 is also evident from larger area scans taken by scanning electron microscopy (SEM) in Fig. 4.2c-f. High resolution HAADF-STEM image in Fig. 4.2g identifies Au (111) and TiO_2 (101) crystal planes and X-ray diffraction data in Fig. 4.2h identifies other major Au and TiO_2 crystal planes along with that of the supporting silicon wafer.

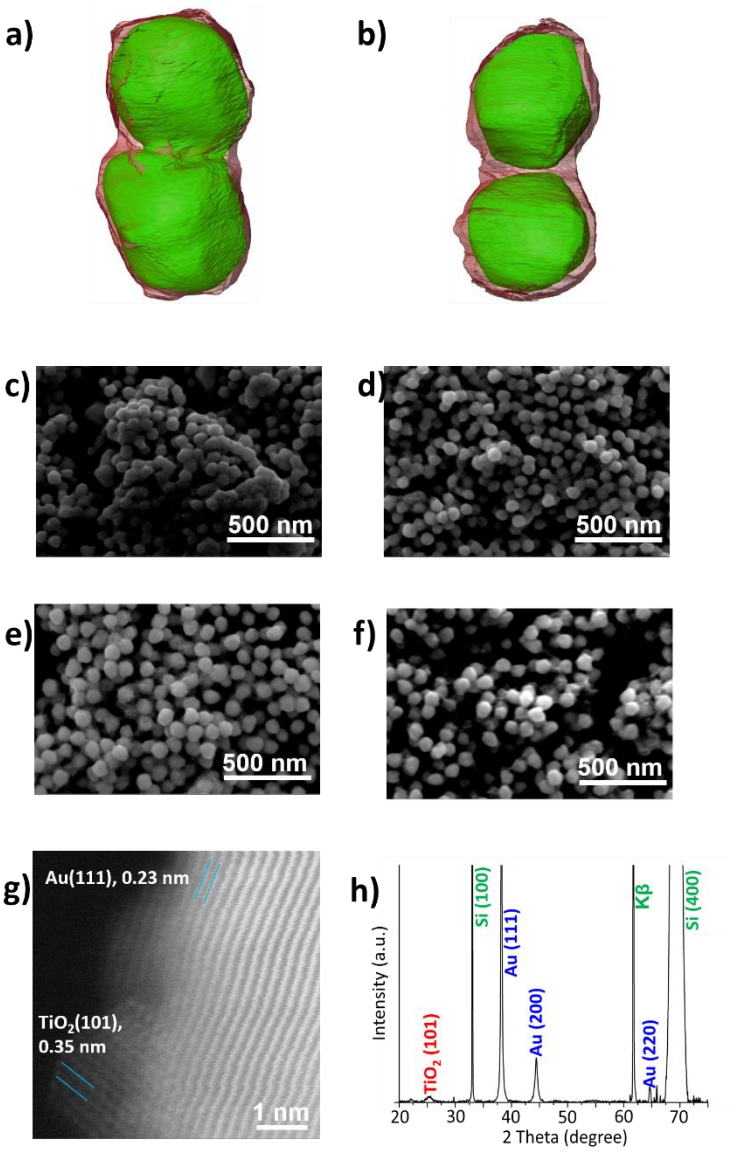

Figure 4.2: Visualization of electron tomography reconstruction of a) Au2 and b) Au4. SEM image of c) Au2, d) Au4, e) Au8 and f) Au12. g) High-resolution HAADF-STEM image of Au2 and h) XRD pattern of Au2 representing the crystal planes of Au and TiO_2.

4.2.2 Optical characterization and Near field enhancement in core shell structures

When light interacts with plasmonic nanoparticles, the collective oscillation of conduction electrons creates a localized surface plasmon resonance effect, leading to generation of an enhanced local electromagnetic near-field [86]. Besides the size, shape and type of metal, which are all constant in this work, the intensity of this near-field and its spatial variation are also dictated by the dielectric properties of the shell (*i.e*. TiO_2), the surrounding medium and the distance between adjacent nanoparticles [86, 178]. The role of near-field enhancement in surface enhanced processes such as scattering, fluorescence, photocatalytic reactions, *etc*., driven by plasmonic-dielectric hybrid nanoparticles can be studied by electromagnetic models, and validated experimentally using electron energy loss spectroscopy (EELS). As EELS is performed using an electron microscope in high

vacuum conditions, a complementary experimental validation can be done using Surface enhanced Raman spectroscopy under atmospheric conditions.

4.2.2.1 Optical characterization

Fig. 4.3a-b represents the UV-Vis spectra of core-shell nanoparticles suspended in isopropanol. With the increase in shell thickness, a red shift in the plasmon resonance band can be observed (550 nm for Au, to 575 nm for Au12) due to the higher refractive index of TiO_2 compared to that of Au [358]. When compared to the UV DRS spectra with air as the medium in Fig. 4.3c, three main changes occur. Firstly, the plasmon resonance band shifts to 530 nm, secondly, the red shift in plasmon resonance band with varying shell thickness is less prominent, and thirdly, a shoulder appears around 650 nm. The first two changes are observed mainly due to the change in refractive index of the medium from isopropanol (n-1.37-1.39) to air (n – 1.003). The appearance of a shoulder around 650 nm in Fig. 4.3c is attributed due to the longitudinal excitation of nanoparticles in a two or more nanoparticle assembly. Indeed, when simulating the extinction spectra of two adjacent nanoparticles with varying shell thickness (based on the experimentally determined configurations in Fig. 4.1) using COMSOL Multiphysics, the longitudinal excitation mode actually dominates over the transverse excitation mode going in accord with previous studies of Au nanorods [361]. This is not reflected in the experimental spectra of particle suspensions in Fig. 3c, as the latter arise from the collective plasmonic excitation of one, two, three or more nanoparticle assemblies (mainly two nanoparticle assembly) in random orientations, whereas the simulated spectra consist of only a two nanoparticle assembly in one defined orientation (Fig. 4.4). The simulated spectra can be considered more valid when compared to the experimental EELS spectra (Fig. 4.3e) of a single two nanoparticle assembly without the influence of other nanoparticles. In both simulated spectra and EELS spectra, the distance between two plasmon bands changes due to the change in aspect ratio brought about by the increasing TiO_2 shell thickness. On a single two nanoparticle assembly scale, the EELS spectra match well with the energy frequency predicted in the simulated spectra.

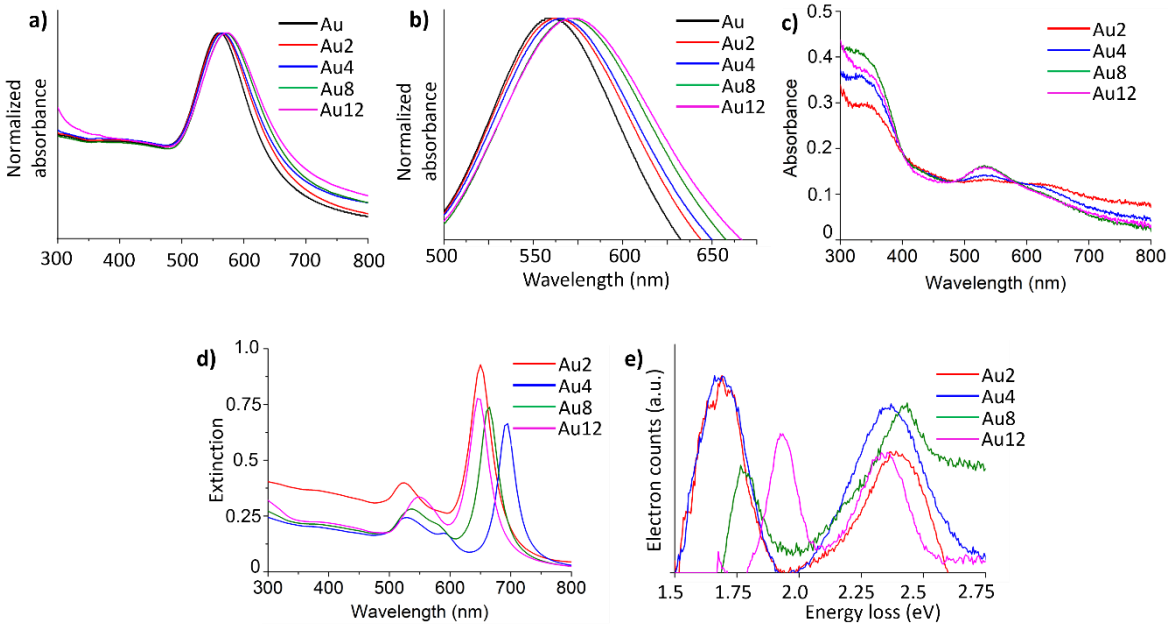

Figure 4.3: Au@TiO_2 core shell nanoparticles a) UV Vis spectra, b) zoomed in view representing a red shift in plasmon band, c) UV DRS, d) Simulated extinction spectra, e) EELS spectra

4.2.2.2 FEM electromagnetic simulations

Electromagnetic field simulations were performed using COMSOL Multiphysics to quantify the near-field enhancement brought about by sintered and un-sintered Au@TiO_2 core-shell nanoparticles with varying shell thickness. The Au nanoparticle size (65 nm) and TiO_2 shell size are again retrieved from HAADF-STEM images (Fig. 4.1). Fig. 4.3 represents the near field enhancement maps. As observed in Fig. 4.4a, the enhancement in near-field for sintered Au2 is restricted to the sintered edge between two nanoparticles, whereas in Au4 to Au12 (Fig. 4.4b-c) the near-field is strong in the spacer region between the two nanoparticles, with the dipole extending towards the two outer edges of the nanoparticles. For the sintered Au2 architecture, the enhanced field is not only restricted to the sintered edges, its intensity is also poor compared to Au4, for which it reaches its maximum value. As the TiO_2 shell thickness increases, the gap between nanoparticles also increases and therefore the near-field enhancement intensity of Au12 decreases to only *ca*. 30% that of Au4.

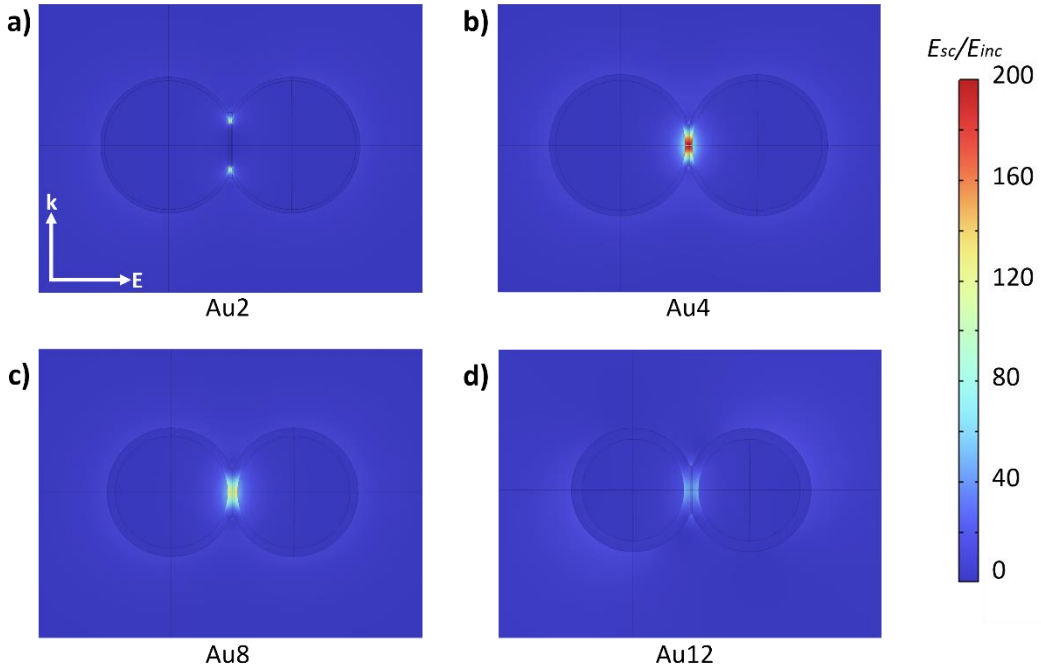

Figure 4.4: Near field enhancement maps of a. Au2, b. Au5, c. Au8 and d. Au12 at the wavelength of LSPR.

4.2.2.3 Surface enhanced Raman spectroscopy (SERS)

The dependence of plasmonic near-field enhancement on the TiO_2 shell thickness around Au cores is experimentally substantiated by means of surface enhanced Raman spectroscopy (SERS) using a probe of Rhodamine 6G molecules on drop casted films of Au@TiO_2 core-shell nanoparticles. Equal amounts of R6G has been deposited on equal weights of nanoparticle films. Given the size of the Au nanoparticles compared to the very thin TiO_2 shell, the number of nanoparticles within the film should not differ by a large margin. It can be observed from Fig. 4.5 that the order in SERS enhancement is as follows: Au4 > Au2 > Au8 = Au12. However, it should be noted that SERS intensity of Au2 from different locations on the film has a varying SERS enhancement. The trend in near-field decay derived from electromagnetic simulations due to sintering and increasing shell thickness, corroborates well with the experimental trend in SERS enhancement.

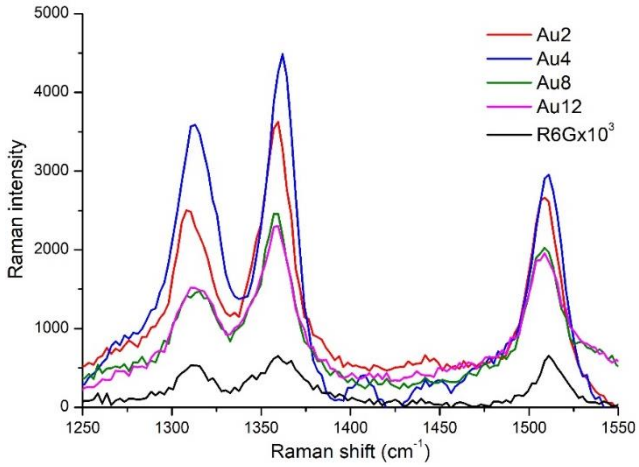

Figure 4.5: Surface enhanced Raman spectra of Au@TiO_2 core shell nanoparticles with varying shell thickness using R6G as the probe molecule.

4.2.3 Photocatalytic activity

For photocatalytic hydrogen evolution reaction (HER) and stearic acid (SA) degradation tests, thin films were first prepared by drop casting core-shell nanoparticles on infrared transparent low p-doped Si wafers. When irradiating the samples with UV light, pristine TiO_2 has the best hydrogen evolution performance compared to all the other composites. The hydrogen evolution performance gradually increases going from Au2 to Au12, because of the increasing amount of TiO_2 in the shell. Using simulated solar light, however, the photocatalytic HER performance was most pronounced for Au4, reaching 1.54 $mmol.m^{-2}.h^{-1}$, which is 50% more than for Au2 (1.01 $mmol.m^{-2}.h^{-1}$), and twice the evolution rate of Au8 (0.83 $mmol.m^{-2}.h^{-1}$) and Au12 (0.79 $mmol.m^{-2}.h^{-1}$). Most importantly, compared to pristine TiO_2 the Au4 sample under solar light showed a promising fourfold increase in HER. A similar trend of photocatalytic activity with Au4 having the best performance using simulated solar light is also observed for SA degradation under simulated solar light illumination. Bare Au nanoparticles have very low photocatalytic activity under both solar and UV light as they are unable to transfer charge carriers on their surface due to their short lifetime[347]. It is expected that a thin shell of TiO_2 around Au should yield high photocatalytic activity due to two reasons. Firstly, the near-field enhancement generated by the Au core still protrudes beyond the thin TiO_2 shell as observed in Fig. 4.4, quite effectively reaching the outer shell surface where the photocatalytic reactions occur. Thus, an overall doubling in the activity of Au2 over pristine TiO_2 is apparent (Fig. 4.6). Interestingly, for Au4 nanoparticles with a thicker shell, an even higher activity is observed. This can be explained by partial sintering of Au cores in Au2 nanoparticle samples during calcination. The sintering leads to loss of plasmonic enhancement of the Au cores as shown in electromagnetic simulations (Fig. 4.4) and SERS (Fig 4.5). In contrast, in Au4 nanoparticles the Au cores remain well separated, with a well-defined nanometer sized particle gap in-between adjacent cores. This enables plasmonic coupling between neighboring particles, also known as hot-spot formation, resulting in extraordinary near-field enhancement in the inter particle gap (Fig. 4.4). It is to be noted that, for near-field mediated processes, there exists an optimum thickness of the dielectric shell in such plasmonic core-dielectric shell nanoparticles, where a strong near-field enhancement results from metal-dielectric coupling[65, 298]. Beyond a shell thickness of 4 nm, with further increase in shell thickness for Au8 and Au12, the photocatalytic activity decreased by a factor of two.

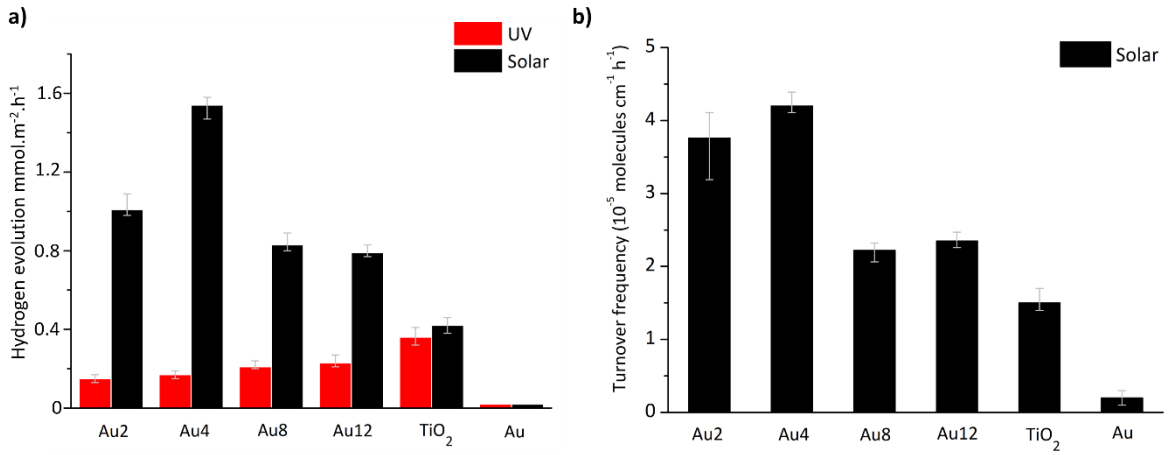

Figure 4.6: a) Hydrogen evolution of Au@TiO_2 core shell nanoparticles with varying shell thickness under the effect of UV and simulated solar light. b) Stearic acid degradation reaction of Au@TiO_2 core shell nanoparticles with varying shell thickness.

4.2.4 Mechanism

It is a well-known fact that photocatalytic reactions in atmospheric air mainly occur through hydroxyl and superoxide radicals generated by oxidizing water and reducing oxygen using photogenerated holes and electrons [343]. In the present study, XTT was used as probe molecule to be selectively reduced by superoxide radicals, reacting to formazan, and thus enables to measure the electron mediated reaction pathway as shown in [362]. Also, terephthalic acid was used as a probe to measure hydroxyl radical formation quantifying a mix of electrons as well as hole mediated reaction pathway as shown in [363]. As observed in Fig 6a, all plasmonic samples are more efficient in converting XTT to formazan, indicating they are more performant in activating oxygen using photogenerated electrons compared to pristine TiO_2. In contrast, from the terephthalic acid conversion experiments, pristine TiO_2 is more capable of generating holes compared to plasmonic samples.

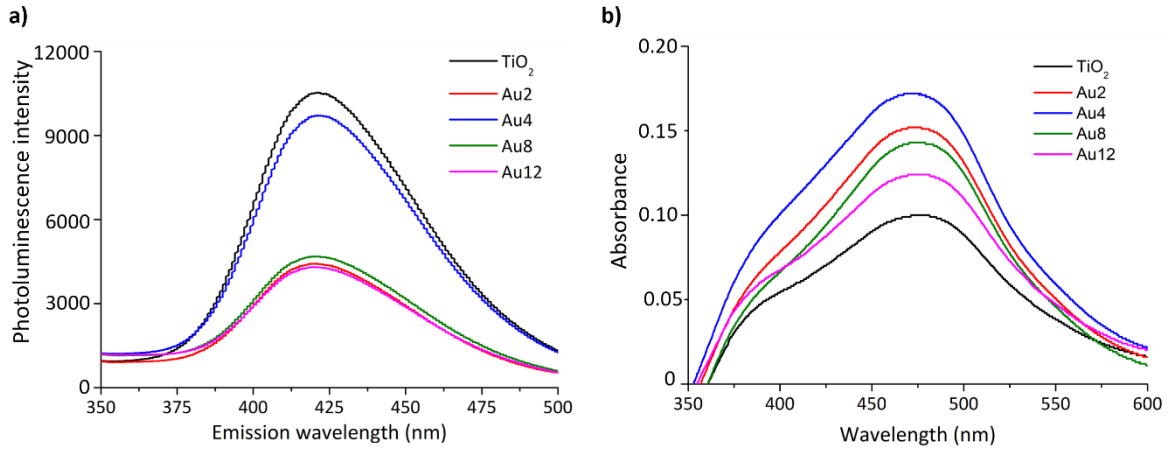

Figure 4.7: a) UV-vis spectra indicating concentration of superoxide radicals using XTT as probe molecule. b) PL spectra indicating concentration of hydroxyl radicals using Terephthalic acid as probe molecule. The radical trapping experiments were performed using simulated sunlight AM 1.5G with an irradiance of 100 $mW.cm^{-2}$.

By combining the activity data, characterization, simulations and probe experiments, it is clear that Au4 optimally benefits from surface plasmon resonance effects under solar light. Based on the data available and the using previous literature, the following three hypothesis can be described. 1) The photocatalytic activity of all the samples, and especially Au4, correlates well with the simulated near field enhancement maps and experimental surface enhanced Raman spectra. This points at an important contribution of plasmonic near field enhancement to the overall photocatalytic activity. As the absorption edge of TiO_2 and plasmon band of Au do not match, it is counter intuitive to think that near-field enhancement is the reason for enhanced electron generation. Still, theoretical studies strongly suggest that an increase in near-field enhancement is correlated to an increase in efficiency of hot electron generation. This effect is due to surface scattering decay, a quantum mechanism where collective plasmon excitations turn into hot electrons due to scattering at the surfaces [364–367]. Au4 has the highest field enhancement compared to other composite samples in the current study and could therefore promote hot electron generation, and consequent electron injection from Au into TiO_2. The combined beneficial effect of enhanced near field and greater availability of hot electrons at the surface, strongly declines with increasing shell thickness. Not only does the near field become weaker, as shown in the numerical field simulations and SERS experiments, the thicker shell also promotes charge recombination, leaving less photogenerated carriers available at the surface for reaction, as clear from the probe assays [359]. Secondly, the thin shell TiO_2 shell is quite likely to contain defects. The disordered TiO_2 can induce a change the valence band/conduction band edge leading to absorption of visible light [368], which can further use near-field enhancement for enhanced plasmonic photocatalytic activity. Thirdly, the 2 nm to 4 nm TiO_2 belonging to the shell are more influenced by quantum effects and do not behave the same as the larger 8 nm or 12 nm TiO_2. Studies have shown better charge transfer efficiency from Au to TiO_2 quantum dots compared larger TiO_2 nanoparticles. This makes thinner shells within the regime of quantum effects can be more efficient for charge transfer and utilization. Either one or an inter-relation of the above three hypothesis is a possible mechanism for enhancement in photocatalytic activity. Overall, the XTT probe assay directs us towards a greater availability of photogenerated electrons for oxygen activation at the nanoparticle surface. While the discussion above motivates why thin shells are preferred, our experiments also clearly show there is a bottom limit. In Au2, the shell was found to be too thin to guarantee the structural stability of the core-shell hybrids, and sintering of the plasmonic metal cores could not be avoided, leading to loss of plasmonic properties.

4.3 Conclusion

The study demonstrated a controlled and slow hydrolysis of titanium precursor leading to formation of TiO_2 shell of tunable shell thickness around Au nanoparticle. Due to the high temperatures used to calcine TiO_2 to its required anatase crystal structure, sintering of Au nanoparticles was observed for a TiO_2 shell thickness of 2 nm. For a shell thickness greater than 5 nm, sintering was not observed due to the higher spacing between Au nanoparticles. It is shown using a combination of photocatalytic activity tests, theoretical simulations, SERS experiments and quantification of reactive radicals, that in sintered and unsintered structures the near-field enhancement has a significant effect in plasmonic photocatalytic studies. The nanogap between plasmonic nanoparticles which serves as a hot spot for near-field enhancement in an unsintered Au

nanoparticle with 4 nm TiO_2 shell is lost in a sintered nanoparticle with 2 nm TiO_2 shell thereby decreasing its photocatalytic activity. However, as the TiO_2 shell thickness further increases, the near-field enhancement decreases. Therefore, the most optimized plasmonic core shell structure would be to have the thinnest possible TiO_2 shell without sintering the Au nanoparticle. The insights from the current chapter will aid in identifying the optimal shell thickness and interparticle distance to obtain more efficient near-field enhancement in stable core-shell nanoparticles for various plasmon based applications.

4.4 Experimental section

4.4.1 Synthesis

Chemicals

The following chemicals were purchased and used as received: trisodium citrate dihydrate (Chem-lab); chloroauric acid (Sigma-Aldrich, >99.9%); titanium (IV) (triethanolaminato) isopropoxide (TTEAIP, Sigma-Aldrich, 80 wt% in 2-propanol), hydroxylamine hydrochloride (Sigma-Aldrich, >98%), ammonia solution (Fischer, 25%), 2-propanol (Chem-lab, >99.8%), chloroform, stearic acid (Sigma-Aldrich, 95%).

Au nanoparticle synthesis

The synthesis of gold nanoparticles (~65 nm) is a process based on the protocol in [325]. The stepwise procedure can be mentioned as: (1) the first step is the synthesis of gold seeds based on the addition of a 0.25 mM $HAuCl_4.3H_2O$ solution in a round bottom flask in a total volume of 30 mL. The solution was rapidly brought to boil in a heating mantle under vigorous stirring. Once the solution started boiling, 0.9 mL of a 1 wt% sodium citrate was added as the reducing agent. After 10 minutes, the solution turned ruby and was quickly cooled down to room temperature to stop the reaction; (2) the second step is the growth of the particles. This is done by adding 1 mL of the freshly prepared seeds to 100mL of water and 2 mL of a 1 wt% solution of sodium citrate. The nanoparticles are grown by dropwise adding 2.4 mL of a 10mM hydroxylamine hydrochloride solution and 1.7mL of a 25 mM $HAuCl_4.3H_2O$ solution at room temperature over a time period of 30 min. Afterwards, the solution was left stirring for 10 minutes.

Au@TiO_2 core-shell nanoparticle synthesis

Encapsulation of Au nanoparticles with TiO_2 was performed with slight modifications based on procedure described in [99]. 10 mL of the as synthesized gold nanoparticles were centrifuged and concentrated in 200 µL water and 3.8 mL 2-propanol. Vigorous stirring ensures good mixing of organic and aqueous phase. After 10 min, an appropriate amount (50 - 400 µL for 2 – 12 nm TiO_2 shell) of 10 mM TTEAIP was added dropwise (10 µL drops). After one hour, 50 µL of ammonia was added to start the hydrolysis, after which the solution was left stirring overnight. Afterwards, the nanoparticles were first diluted with water and then centrifuged and washed. Au@TiO_2 thin films were prepared by drop casting the as-prepared core shell photocatalyst suspension in isopropanol on a precleaned silicon wafer (1.5 cm × 3 cm) and further calcined at 450 °C for 30 minutes. This led to a photocatalyst loading of 50 µg cm^{-2}. Photometric measurements were performed to determine the gold mass concentration per unit volume in the colloids by appropriate dilution to detection limits using the Spectroquant® gold test kit.

4.4.2 Photocatalytic hydrogen evolution reaction and stearic acid degradation

Photocatalytic HER experiments were performed in a batch reactor (Fig. A4.1). The thin film was placed in a Teflon liner filled with 40 mL of a water:methanol (v/v 9:1) mixture. Prior to the actual measurement, the head space of the reactor is purged by N2 overnight to remove traces of oxygen. The temperature was controlled by a cooling mantle and verified by a sensor. The slurry was irradiated through a circular quartz window (5 cm diameter). Simulated sunlight with AM1.5G filter was used (SciSun-300, Sciencetech). The intensity amounted to 100 mW.cm-2 (i.e. 1 sun) at the bottom of the reactor. For the UV light measurements, a Philips fluorescence S 25 W UV-A lamp was placed on top of the reactor surface, reaching an incident intensity of 2.35 mW cm-2. Incident light intensity was measured by a calibrated spectroradiometer (Avantes Avaspec-3648-USB2). 2 mL gas samples are harvested from the head space by inserting a syringe with 12 cm needle in the tilted inlet. Consequently, these are analysed by a gas chromatograph (Compact4 GC, Interscience) with pulsed discharge detector (PDD) with detection limit of ~1 ppm. Sample intervals were adjusted according to the activity of the photocatalyst.

The general protocol for the stearic acid (SA) degradation experiment is described in our previous works [317] and is based on the early work of [369]. In brief, 100 µL of a 0.25 wt % SA (Sigma–Aldrich, ≥99.5%) in chloroform solution were spin coated on the thin films. A Laurell Technology Corporation spin coater was used for this at a speed of 1000 rpm during 1 min. Finally, the samples were dried for 20 min at 105 °C after which they were allowed to acclimatize at room temperature in the dark. The SA was degraded by the photocatalysts under 100 mW·cm−2 simulated solar light. The degradation itself was monitored by Fourier transform infrared (FTIR) spectroscopy using a NicoletTM 380 (Thermo Fisher Scientific) with ZnSe windows at a resolution of 1 cm−1. The samples were positioned at a vertical angle of 9° in order to minimize internal reflections. The SA concentration was determined by integration over the wavelength range 2800–3000 cm^{-1}, corresponding to a symmetric vs(CH_2) in-plane C-H stretch at 2853 cm^{-1}, an asymmetric vas(CH_2) in-plane C-H stretch at 2923 cm^{-1} and the asymmetric vas(CH_3) in-plane C-H stretch at 2958 cm^{-1} [29,30]. One unit of integrated absorbance corresponded here to 1.39 × 1016 SA molecules/cm^2, as determined by a calibration curve from earlier work (R2 = 0.99) [17]. Both the northern and southern parts of the wafer were tested. The measurements were stopped if an integrated absorbance of ~0.3, corresponding to 4.1015 SA molecules/cm^{-2}, was attained. The photocatalytic degradation of large organic molecules by TiO_2 generally follows a zero order kinetics for a flat nonporous films and does not depend on the initial SA concentration[317]. As a reference, hydrogen evolution reaction and stearic acid degradation on blank Si wafer was performed to omit effects of direct photolysis and heat from light irradiation.

4.4.3 Characterization

Electron microscopy and electron tomography

Nanoparticle solution (3 µL) was drop-cast on a Mo grid with a single layer graphene and left to dry in ambient air. High-angle annular dark field scanning transmission electron microscopy (HAADF-STEM) and energy dispersive X-ray spectroscopy (EDS) was performed using a Thermo Fischer Tecnai Osiris microscope operated at 200kV. HR HAADF-STEM images were acquired using an

aberration corrected Titan microscope (Thermo Fischer Scientific) operated at 300 kV using a medium angle annular dark field (MAADF) / DF4 detector under a collection angle of 80-120 mrad. For electron tomography, the tomography tilt series was acquired using a Fischione 2020 tomography holder over ± 72° with an increment of 3°. The tilt-series images were aligned using intensity cross correlation [370]. The image gamma was corrected manually by maximizing the contrast difference between the background and SiO_2 shell in the intensity histogram[341]. A median filter was applied to remove specular noise from the background and shell[342]. The modified image was segmented to create a mask of the SiO_2 shell and Au core. The TiO_2 and Au were segmented from the original images using the determined masks. Reconstructions were performed with 25 iterations of SIRT (Simultaneous Iterative Reconstruction Tomography) using the MATLAB 2020 implementation of ASTRA toolbox 1.9.0 [371]. Visualization of the 3D reconstructions was performed using Amira 5.4.0 software.

Electron energy loss spectroscopy

EELS measurements were carried out using an aberration corrected ThermoFischer Scientific – Titan Cubed electron microscope, operating at 300 kV, equipped with an energy monochromator excited to a value of 0.7. The energy resolution provided by the electron monochromator, as measured from the full-width half maximum of acquired zero-loss peaks, was 100 meV. The dispersion of the spectrometer was set to 0.002 $eV.ch^{-1}$ to visualize the plasmon edges. To analyze the EELS data sets, EELS Model software was used [372].

UV-Vis absorption and UV- Vis DRS

A UV–vis absorption spectrum and UV-Vis diffused reflectance spectrum was recorded from 300 nm to 800 nm with a resolution of 0.2 nm using Shimadzu UV–vis 2501 PC double beam spectrophotometer. UV–vis absorption spectrum was recorded using liquid sample holder and UV-Vis DRS was recorded by pressing the powdered sample on Barium Sulfate background.

Surface enhanced Raman spectroscopy

Rhodamine 6G (Sigma Aldrich, Fluorescence bioreagent) dye was used as the Raman probe molecule for SERS measurements and all the measurements were done using the same sample and substrate as used for hydrogen evolution reaction and stearic acid degradation tests after clearing off all the organic matter. These substrates were prepared for SERS measurements by drop casting a mixture of known concentration of R6G, 10^{-4}M (20 µL) on the Au@TiO_2 core shell thin films. Reference neat R6G Raman substrate is prepared by drop casting 50 µL of 1M pure R6G dye solution. All the samples were allowed to dry in a desiccator for one full day before measurement. The Raman spectra were recorded on a Horiba XploRA Plus Raman spectrometer equipped with a diode-pumped solid-state laser of 785 nm and a power of 25 mW. The samples were measured with an acquisition time of 10 s, 10 accumulations and in a spectral range of 100 – 2000 cm^{-1}. Raman spectra were recorded multiple times at different locations for each sample. Fluorescence was observed using 532 nm laser and therefore a laser of 785 nm wavelength was used.

Terephthalic acid and XTT radical trapping experiments

All the measurements were done using the same sample and substrate as used for hydrogen evolution reaction and stearic acid degradation tests. For hydroxyl radical trapping experiments, the thin film was inserted in 20 mL of TA (0.5 mM) and NaOH (2 mM) and illuminated with simulated solar light (100 $mW.cm^{-2}$). The fluorescent emission intensity of 2-hydroxyterephthalic acid was

detected with λmax at 425 nm under the excitation at 315 nm using a Shimadzu RF-6000 spectrofluorometer, equipped with a Xe lamp. For both excitation and emission, the slit width was set to 2 nm. Fur superoxide radical trapping experiments, the thin film was inserted in 10 mL of XTT sodium salt solution (0.1 mM) in DMSO in a glass vessel and illuminated with simulated solar light (100 mW.cm^{-2}). The resulting supernatant was analyzed using UV-VIS for the formation of XTT formazan with λmax at 475 nm.

Electromagnetic Modeling

From an electromagnetic point of view, the light-matter interaction is described as the variation of the electric field and the magnetic field of light in space and time as a result of varying material dielectric properties. Mathematically this is described by the Maxwell's equations as follows:

$$\nabla \cdot D(t) = \rho_e(t) \quad (4.1)$$

$$\nabla \cdot B(t) = 0 \quad (4.2)$$

$$\nabla \cdot Esc(t) = -\frac{\partial B(t)}{\partial t} \quad (4.3)$$

$$\nabla \cdot H(t) = -\frac{\partial D(t)}{\partial t} + J(t) \quad (4.4)$$

In equations (4.1) to (4.4), Esc and H are the scattered electric field intensity and magnetic field intensity vectors. D and B are the electric displacement vectors and magnetic induction vectors, respectively. J is the current density. While E and H are the fundamental fields, the fields D and B account for the polarization and magnetization effects of the materials. Thus, the material dielectric properties relate E to D and B to H as:

$$D(t) = \varepsilon_e(t) * Esc(t) \quad (4.5)$$

$$B(t) = \mu_e(t) * H(t) \quad (4.6)$$

The equation(s) (4.5) and (4.6) are known as the constitutive relations where $\varepsilon_e(t)$ and $\mu_e(t)$ are the permittivity and permeability of the medium, respectively. Also, * denotes a convolution in equation(s) (4.5) and (4.6). These time-domain forms of the Maxwell's equations give the transient response of light's electromagnetic wave. However, the central problem in this dissertation mainly concerns the spectral response of nanomaterials in terms of the rate of energy flow and dissipation. Thus, it is convenient to rather solve the equations in the frequency domain to analyze the electromagnetic response at desired frequencies (or wavelengths). This requires the frequency domain form of the Maxwell's equations, which can be obtained by Fourier transformation of equations (4.1 to 4.6), yielding equations (4.7 to 4.12):

$$\nabla \cdot D = \rho_e \quad (4.7)$$

$$\nabla \cdot B = 0 \quad (4.8)$$

$$\nabla \cdot Esc = -j\omega B \quad (4.9)$$

$$\nabla \cdot H = j\omega D + J \quad (4.10)$$

$$D = \varepsilon_e \omega Esc \quad (4.11)$$

$$B = \mu_e \omega H \quad (4.12)$$

The frequency domain form from equation (4.7) to equation (4.12) now facilitates direct solution of an electromagnetic problem for any frequency. The free charge density, ρ_e is zero in the cases considered here as there is no charge accumulation. The convolutions in equation(s) (4.5) and (4.6) now become multiplications and the complex frequency dependent dispersion relations of materials can be used. In equation (4.10), the current density J can be expressed in terms of the

electric field as $J = \sigma Esc$. Thus, equations (4.9) to (4.12) can be combined to derive the wave equation that is solved numerically in the computational investigations in this dissertation:

$$\nabla \times (\mu_r^{-1} \nabla \times Esc) - {k_0}^2 \left(\varepsilon_r' - j\frac{\sigma_e}{\omega \varepsilon_0}\right) Esc = 0 \quad (4.13)$$

Where, μ_r, ε_0 and σ_e denote material properties namely relative permeability, permittivity of free space and electrical conductivity respectively, and k_0 denotes the wavenumber. The relative permeability in this case is assumed to 1 as the present work does not concern with magnetic response. Now, ε_r' is the real part of the complex relative permittivity (or dielectric constant) and importantly, σ_e is directly connected to the imaginary part of the dielectric constant as $\sigma_e = \varepsilon'' r\omega$, where $\varepsilon'' r$ is the imaginary part of the dielectric constant. Thus, the problem at hand can be completely specified with only the complex dielectric constants as the input material optical properties and then, σ_e is redundant in equation (4.13). Also, the optical properties of different materials in literature are reported in the form of both dielectric constants and refractive index. The conversion from one to the other is simple by well-known mathematical relations. The numerical framework COMSOL Multiphysics (wave optics module) used in this dissertation converts the wave equation along with the imposed boundary conditions into a set of algebraic equations by FEM (finite element method) discretization that forms a sparse matrix for numerical solution. This formulation is implemented according to the computational domain and the boundary conditions defining the plasmonic nanostructures and the surrounding dielectric environment. Spherical computational domains (radius: 800 nm) surrounded by a perfectly matched layer (thickness: 200 nm) that completely absorbed any radiation. Thus, the total field *E* was the superposition of the scattered and incident electric fields, E_{sc} and E_0, respectively with air as the surrounding medium. The perfectly matched layer was discretized by prismatic elements of five layers, while the rest of the computational domain with the nanoparticles was discretized by tetrahedral elements. To represent the gold nanoparticle, a 3D sphere of 65 nm in diameter was built and a shell was added around the gold core with varying thickness to represent the TiO_2 shell. The dielectric constants of Au and TiO_2 in this work are taken from [373] and [374] respectively. The surrounding medium properties were assumed that for air. The computational domains were discretized by tetrahedral elements with refinement in the narrow and corner regions near intersection of cores or shells. A maximum element size of 1 nm and a minimum element size of 0.1 nm was used in the narrow and corner regions. A grid independence study was carried out by varying the number of grid elements and comparing local electric field to ensure that the mesh elements are small enough for numerical accuracy. Air is taken as the surrounding medium and for the scattered field solution, an incident field was excited in the direction perpendicular to the dimer nanoparticles.

After the solution, the magnetic field can be directly obtained from the electric field by the relationship:

$$H = \frac{1}{Z} k \times Esc = \sqrt{\frac{\varepsilon}{\mu}} k \times Esc \quad (4.14)$$

or,

$$H = \frac{1}{Z_0} \sqrt{\frac{\varepsilon}{\mu}} k \times Esc \quad (4.15)$$

Where, Z is the complex impedance of the medium/material. In equation (4.14), ε and μ are the permittivity of the medium. For the consistency with equation (4.15), the impedance is expressed in terms of relative permittivity ε_r, relative permeability μ_r and free space impedance Z_0. From the numerical solution of the electric field and magnetic field, the optical intensities are obtained by mathematical post-processing. The energy absorbed per unit time, W_{abs}, by the nanoparticles can be calculated by both the following equations:

$$W_{abs} = \frac{1}{2}\iiint_V R_e[(\sigma Esc + j\omega D).Esc^* + j\omega B.H^*]dV \quad (4.16)$$

$$W_{abs} = \frac{1}{2}\oiint_S R_e[Esc \times H^*].ndS \quad (4.17)$$

The superscript * and D stand for complex conjugate and displacement currents respectively. The volume integration and the surface integration in the above equations are applied over the volume and outer surface of the nanoparticle respectively [375].

Chapter 5: Self-assembled plasmonic Au-TiO_2 supraparticles for enhanced photocatalytic hydrogen peroxide generation

Based on:

Rajeshreddy Ninakanti, Andrea Guidetti, Radu-George Ciocaralan, Kimberly Elbrink, Rituraj Borah, Filip Kiekens, Pegie Cool, Sabine van Doorslaer, Sara Bals, Sammy W. Verbruggen. Self-assembled plasmonic Au-TiO_2 supraparticles for enhanced photocatalytic hydrogen peroxide generation

(Article under preparation)

Author contribution:

N.R. conceived the idea, synthesized and performed all the electron microscopy characterization

G.A. performed electron paramagnetic resonance spectroscopy

C.RG. performed Raman spectroscopy

E.K. performed zeta potential measurements

B.R. performed all the electromagnetic modelling

K.F., C.P., D.S., B.S., V.W.S supervised the work

5.1 Introduction

Hydrogen peroxide (H_2O_2) as a clean oxidant has been widely used in industry, such as organic synthesis [202], disinfection [203], water treatment [204], etc. Photocatalysis is a green way for hydrogen peroxide production compared to the industrially applied anthraquinone process[201], since the latter involves energy intensive process and needs large amounts of organic solvents making it an environmental pollution problem. The primary pathways of photocatalytic H_2O_2 production include the oxygen reduction reaction (ORR) and the water oxidation reaction (WOR). The photoinduced WOR pathway for H_2O_2 generation is a two-hole pathway (eq. 5.2). At the same time, competitive reactions of single-hole and four-hole WOR occur that yield hydroxy radicals ($OH^{\cdot}$) (eq. 5.1) and O_2 (eq. 5.3), respectively [376, 377]. Although the hole induced $OH^{\cdot}$ can pair together to form H_2O_2 (eq. 5.4), the high concentration of $OH^{\cdot}$ is a prerequisite, which limits the yield of H_2O_2 [377]. Moreover, the light-driven two-hole WOR path involves a high oxidation potential, and the as-formed H_2O_2 is easily decomposed (eq. 5.5) [205]. Therefore, photocatalytic WOR for H_2O_2 synthesis is generally not the preferred route due to these inherent difficulties. The energy potential (E) required to carry out the WOR is expressed with respect to normal hydrogen electrode (NHE) at pH 7.

$$H_2O + h^+ \rightarrow OH^{\cdot} + H^+ \qquad E = +2.73\ V \qquad (5.1)$$

$$2H_2O + 2h^+ \rightarrow H_2O_2 + 2H^+ \qquad E = +1.78\ V \qquad (5.2)$$

$$2H_2O + 4h^+ \rightarrow O_2 + 4H^+ \qquad E = +1.23\ V \qquad (5.3)$$

$$OH^{\cdot} + OH^{\cdot} \rightarrow H_2O_2 \qquad (5.4)$$

$$H_2O_2 + h^+ \rightarrow O_2^{-\cdot} + H^+ \qquad E = +1.00\ V \qquad (5.5)$$

Redox reactions relating to the photocatalytic production of H_2O_2 from ORR are summarized below (eq. 6-10) with the energy potentials (E) expressed with respect to the normal hydrogen electrode (NHE) at pH 7.

$$O_2 + e^- \rightarrow O_2^{-\cdot} \qquad E = -0.33\ V \qquad (5.6)$$

$$O_2^{-\cdot} + 2H^+ + e^- \rightarrow H_2O_2 \qquad E = +1.44\ V \qquad (5.7)$$

$$O_2 + 2H^+ + 2e^- \rightarrow H_2O_2 \qquad E = +0.69\ V \qquad (5.8)$$

$$O_2 + 2H^+ + 4e^- \rightarrow 2H_2O \qquad E = +1.23\ V \qquad (5.9)$$

$$H_2O_2 + e^- \rightarrow OH^{\cdot} + OH^- \qquad E = +0.87\ V \qquad (5.10)$$

The synthesis of H_2O_2 can be attributed to a two-step single-electron ORR route (eq. 5.6-7) or a one-step two-electron ORR route (eq. 5.8) through the proton coupled electron transfer process, in which the protons are predominantly originated from H_2O or organic electron donors. Due to the presence of four-electron ORR competition reaction (eq. 5.9) the selectivity of H_2O_2 formation employing oxygen is diminished. In addition, because the formation of $O_2^{-\circ}$ not only requires a more negative potential (−0.33 V) than the one-step two-electron route (0.68 V), but also involved multiple unpredictable reactions, so the low efficiency of equation 5.7 step also reduces the production of H_2O_2 yield and selectivity. Therefore, the one-step two-electron route is more advantageous in photoinduced H_2O_2 generation based on ORR reaction. The decomposition of H_2O_2 in equation 5.10 cannot be negated entirely, but the one-step two-electron ORR is thermodynamically more favorable. Thus, the key challenge to photocatalytic H_2O_2 synthesis is the development of a catalyst that has both high activity and selectivity for two-electron ORR. Adding

plasmonic Au nanoparticles to TiO_2 has previously been studied and shows an increase in H_2O_2 generation rate owing to 2-electron ORR which is promising as per equation 7[378], and can be further enhanced using hybrid structures.

Plasmon-enhanced photocatalysis represents a promising avenue due to its potential to harness solar energy more efficiently [18, 347, 379, 380]. This technology typically involves the use of plasmonic nanoparticles such as gold (Au) and silver (Ag), coupled with semiconductor materials such as TiO_2 to enhance light absorption and catalytic efficiency[18]. When coupled with plasmonic nanoparticles, TiO_2 can benefit from enhanced light absorption and improved charge carrier generation, separation and utilization, leading to increased photocatalytic efficiency. The localized surface plasmon resonance (LSPR) of these metal nanoparticles results in enhanced electromagnetic fields that can be harnessed to drive photocatalytic reactions[18, 65, 379]. However, despite the progress, the efficiency of plasmon-enhanced photocatalysis is often limited by the extent of interaction between the plasmonic nanoparticles and the semiconductor. Most systems rely on the LSPR of isolated metal nanoparticles, which constrains the photoconversion efficiency due to limited energy transfer. The synthesis of composite materials that combine plasmonic nanoparticles with semiconductors offers a pathway to overcome these limitations [18, 133, 379, 381]. For instance, our group has recently shown the advantage of fully embedding randomly organized Au NPs in a TiO_2 thin film to increase the area of interaction between the plasmonic particles and the semiconductor [317]. Organizing Au nanoparticles into self-assembled, closely arranged structures could be promising to further enhance the photocatalytic activity through plasmonic coupling of closely separated particles in the assembly, a concept that is already commonly exploited in photothermal and sensing applications [65]. The challenge thus lies in creating a composite structure where the plasmonic nanoparticles are in close proximity to each other as well as to the semiconductor to enhance the energy transfer efficiency.

Recent advances in nanotechnology and colloidal synthesis procedures have enabled the synthesis of such closely packed nanostructures, including nano-chains [382], self-assembled films where nanoparticles are assembled equidistantly into layers [143], and self-assembled supraparticles where nanoparticles form a single three dimensional entity unlike layered films [144]. These structures can potentially provide a more effective platform for plasmon-plasmon and plasmon-semiconductor interactions compared to traditional composites with isolated nanoparticles [18, 379]. For example, Shi *et al.* prepared self-assembled Au-CdSe nanocrystal clusters with a 10 fold enhancement in photocatalytic H_2 evolution [144]. Electrostatic self-assembly provides a straightforward and effective method for creating self-assembled structures. The mechanism of electrostatic self-assembly is based on the attractive forces between oppositely charged particles or molecules. Research has demonstrated the versatility and effectiveness of electrostatic self-assembly in a broad range of applications, including photocatalysis [383, 384]. In the current chapter, electrostatic self-assembly maintains the stability, with TiO_2 on surface having the photocatalytic active sites without the influence of ligands, in contrast to surfactant-based self-assembly approaches where ligand coverage may hamper the availability of active site and decrease the photocatalytic activity [384].

In the current chapter, we advance from the core-shell nanoparticles studied in chapter 4 to report on the synthesis of Au-TiO_2 supraparticles (SPs) as a novel approach to enhance plasmon-enhanced

photocatalytic hydrogen peroxide generation. The unique aspect of these SPs is their ability to facilitate collective plasmonic excitation, a phenomenon where the plasmonic response of the entire particle assembly is greater than the sum of its individual components [385, 386]. This collective behavior is expected to enhance the plasmonic effects on the semiconductor, leading to more efficient energy transfer and improved photocatalytic performance. The synthesis of these SPs involves a controlled electrostatic interaction between poly(allylamine hydrochloride)-coated Au nanoparticles and titanium bis(ammonium lactato) dihydroxide (TALH). This process not only allows for the formation of the SPs but also offers a tunable approach to manipulate their size, which is crucial for optimizing their photocatalytic activity. Surface Enhanced Raman Spectroscopy (SERS) and radical trapping experiments give an understanding that the enhancement can primarily be attributed to a combination of near-field enhancement and hot electron injection from the Au nanoparticles to TiO_2, facilitating the electron mediated photocatalytic ORR of O_2 to H_2O_2. The results from this chapter not only demonstrate the potential of Au-TiO_2 SPs in plasmon-enhanced photocatalysis but also provide valuable insights into the design of more efficient photocatalytic materials.

5.2 Results and discussion

5.2.1 Synthesis

Au nanoparticles of 15 nm in size were synthesized using a modified Turkevich method [298]. The nanoparticles are stabilized by citrate molecules and therefore have a negative zeta potential as mentioned in Fig. 5.1. Next, a thin layer of PAH (1.5±0.3 nm) is coated on the Au nanoparticle. Since PAH is a cationic polyelectrolyte, consequently, the zeta potential of the colloidal solution containing Au@PAH core-shell nanoparticles changes from negative to positive. Subsequently, TALH of varying concentration was added to the prepared Au@PAH solution. TALH has a negative zeta potential arising from the lactate and hydroxyl groups. By increasing the amount of TALH injected into the Au@PAH colloid, this results in structures of a) closely arranged small SPs (Au@CloseSmall), b) closely arranged large SPs (Au@CloseLarge), and c) distantly arranged small SPs (Au@DistantSmall) of Au@PAH@TALH. For full clarity, the notation ‘small/large’ is with respect to the overall supraparticle size, and not the size of the constituting Au nanoparticles, which is fixed at 15 nm. TALH in itself is not photocatalytically active and is therefore subjected to a calcination step at 450 °C for 30 mins to convert it into a photocatalytically active crystalline TiO_2 phase in the SPs.

As schematically represented in Fig 5.1, as the volume of TALH increases, the zeta potential of the solution changes from positive to approximately zero and eventually to negative. When the zeta potential is positive/negative, the net positive/negative charge results in electrostatic repulsion. It is clear that as the zeta potential changes from positive to zero, the SP size increases and reaches a maximum close to zero. With further decrease of the zeta potential to negative values, the supraparticle size again decreases. As surface charge decreases, the repulsion is also decreased and the net charge results in attractive forces between the negatively charged Au@polymer nanoparticle and positively charged TALH. Therefore, the nanoparticles interact with TALH and start forming SPs. As the zeta potential is close to zero, we observe strong clustering of nanoparticles as

the repulsive forces decrease and attracting forces increase leading to the formation of large supraparticles.

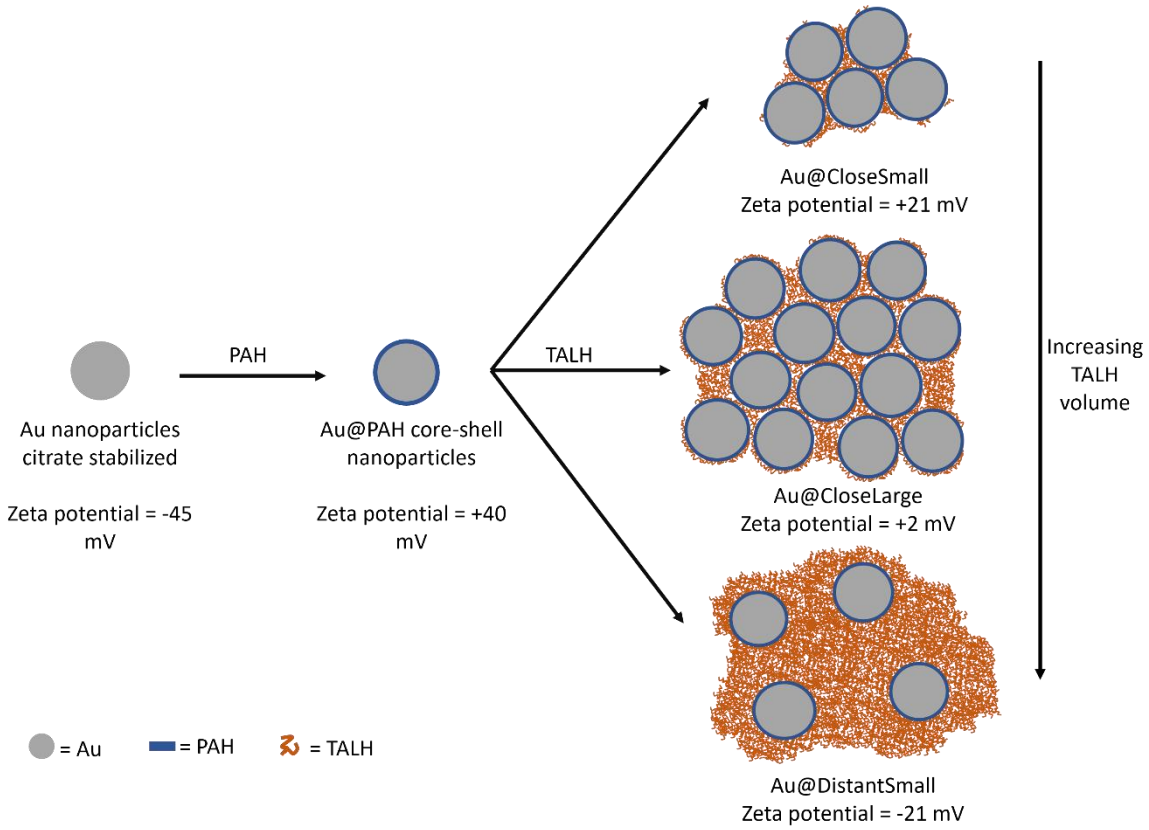

Figure 5.1: Schematic representation of synthesis of Au-TiO_2 supraparticles with varying size as Au@CloseSmall, Au@CloseLarge and Au@DistantSmall

5.2.2 Structural characterization

The structure of SPs was studied using bright field transmission electron microscopy (BFTEM), high angle annular dark field scanning transmission electron microscopy (HAADF-STEM) and scanning electron microscopy (SEM). As seen in Fig. 5.2a-b), the Au nanoparticles have an average size of 15 nm with a 1±0.3 nm shell of PAH. After mixing the Au@PAH core-shell nanoparticles with TALH, the Au@CloseSmall SPs are formed due to net attracting charges with formation of SPs ranging from 100 nm to 500 nm. As the amount of TALH is increased, Au@CloseLarge SPs are formed. As seen in Fig 5.2e, the Au@CloseLarge SPs can attain dimensions of over a micrometer and do not fit the full field of view of the HAADF-STEM image. For knowing the size of such SPs, scanning electron microscopy (SEM) was employed. The SEM image in Fig. 5.2 f-g, reveals Au@CloseLarge SPs of 2 µm to 4 µm in size. Upon adding even higher amount of TALH, the SP size again decreases to between 100 nm to 500 nm, but the Au nanoparticles within the SP are arranged more distantly compared to the closely arranged structure of Au@CloseSmall and Au@CloseLarge SPs with the space between the Au nanoparticles filled with a network of TiO_2. It can be observed that for all the SPs the size and shape of SPs is non-uniform. This is mainly as kinetics of electrostatic interactions are in general difficult to control. Some studies have attempted to control the kinetics by varying pH

and using different solvents, but in that case controlling the directionality to form a structured crystal is not viable [387].

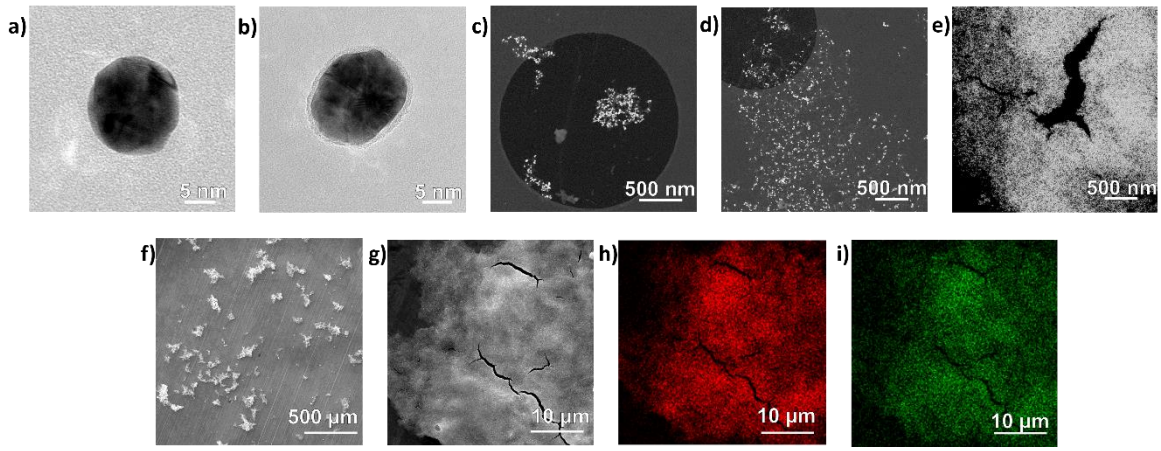

Figure 5.2: TEM image of a) 15 nm Au nanoparticle and b) Au nanoparticle with PAH shell of 1.5 nm. HAADF-STEM image of c) Au@CloseSmall, d) Au@CloseLarge and , e) Au@DistantSmall. f-g) SEM image of Au@CloseLarge with varying magnification. EDS map of Au@CloseLarge SPs with map of h) Au and i) Ti.

5.2.3 Optical characterization

5.2.3.1 UV-Vis and diffused reflectance spectra (DRS)

The UV-Vis and DRS of all the synthesized materials before and after calcination are represented in Fig. 5.3a-b. Fig. 5.3a represents the UV-Vis spectra of Au-TiO_2 SP before calcination. It can be observed that the clear plasmon band between 500–550 nm becomes less pronounced and the absorptance is extended across the entire visible range when moving from Au@CloseSmall to Au@CloseLarge. The extended absorption cross-section of larger Au@CloseLarge SPs is in accordance with previous studies [388]. For the Au@DistantSmall SPs, the plasmon band reemerges. After calcination at 450 °C, the DRS spectra are quite similar to those before calcination with minor differences as observed in Fig. 5.3b. One of the main differences is a more clear and pronounced absorption onset from 380 nm and below, which can be attributed to the bandgap of TiO_2. An extended broadening is observed around 450 nm which can be attributed to the supporting silicon wafer. In these experimental far-field spectra, the Au nanoparticles can be considered to be a continuous and infinite thin film. The 15 nm Au nanoparticles considered in the current study have low scattering intensity, making the far field coupling very low or negligible.

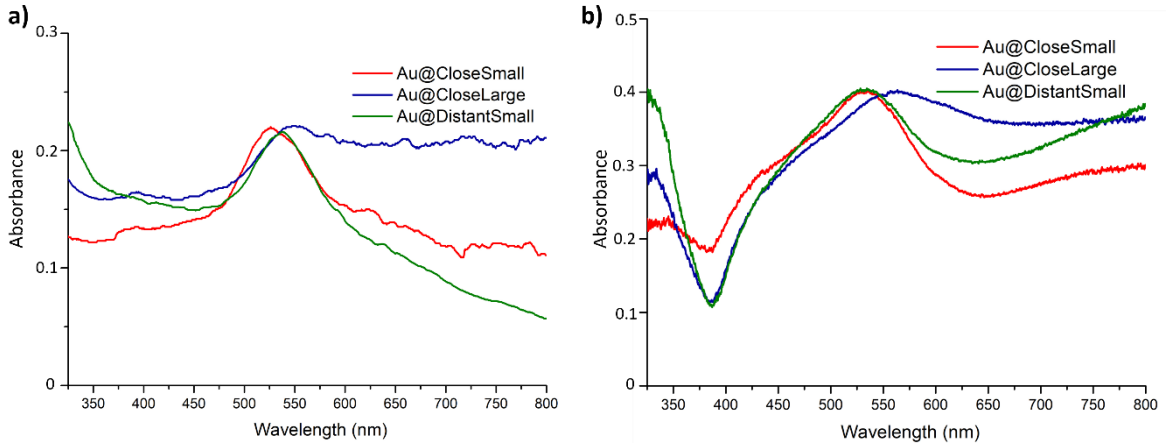

Figure 5.3: a) UV-Vis spectra of Au-TiO_2 composites in solution before calcination, b) UV-DRS of Au-TiO_2 composites on a silicon wafer after calcination

5.2.3.2 Electron energy loss spectroscopy (EELS)

The UV-Vis and DRS spectra demonstrate the far-field effects but do not provide much information about the near-field interactions. Using EELS, more insight are gained into the near-field interactions of Au nanoparticles surrounded by dielectric TiO_2. The EELS spectra obtained adjacent to the surface of Au@CloseLarge display very pronounced coupling of plasmon bands from closely separated Au nanoparticles as shown in Fig. 5.4. In contrast, the spectra obtained from the core region of the same SP present a single plasmon band, corresponding to that of an isolated Au nanoparticle. This indicates that the plasmon resonance from an array of multilayer Au nanoparticles significantly enhances near-field coupling compared to that from two adjacent Au nanoparticles. The extended absorption observed in the UV-Vis spectra in Fig. 5.3a may arise from the coupling of multiple plasmon modes from the SP surface.

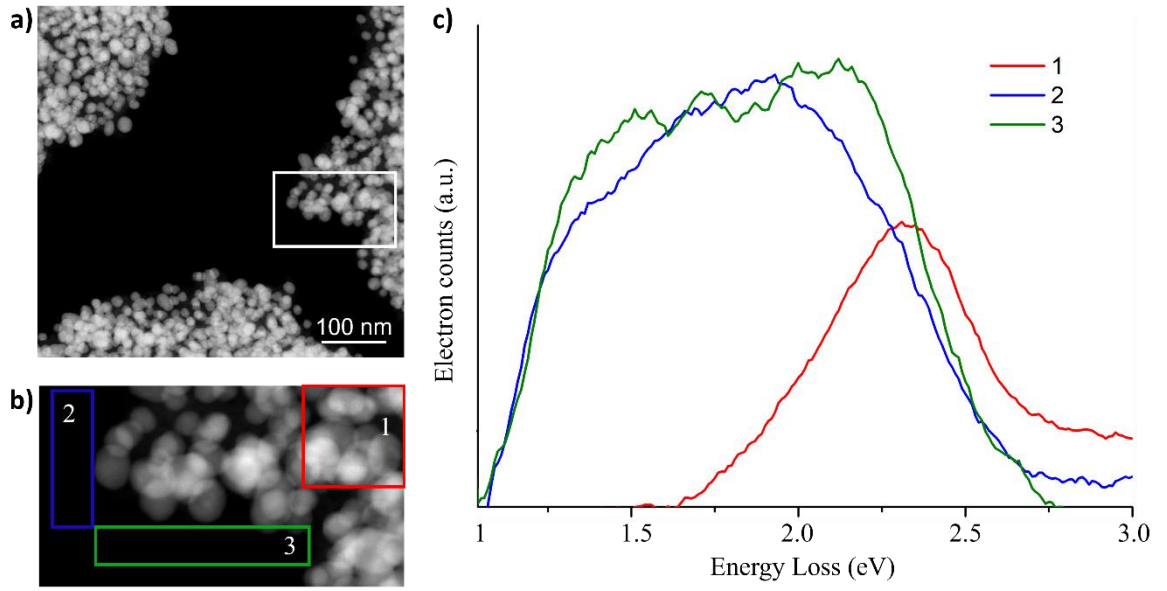

Figure 5.4: a) HAADF-STEM image of Au@CloseLarge, b) inset of HAADF-STEM image in a) used for EELS and, c) EELS spectrum of 3 different selected regions.

5.2.3.3 Surface enhanced Raman spectroscopy (SERS)

The effect of near-field enhancement with varying sizes of SPs is experimentally substantiated by means of SERS using Rhodamine 6G as probe molecule on thin films of Au-TiO_2 SPs (Fig. 5.5). Equal amounts of R6G have been deposited on equal weights of nanoparticle films. Notably, Au@CloseLarge has a higher enhancement in SERS signal compared to the other supraparticles, which is in line of the expectations based on the EELS data. On the other hand, the weight-basis deposition may have an influence on the number of nanoparticles available for Au@DistantSmall. However, despite being closely spaced, Au@CloseSmall shows a lower SERS enhancement compared to Au@CloseLarge, indicating the coupling of plasmon response in larger supraparticles with closely spaced plasmonic nanoparticles leads to greater near-field enhancement.

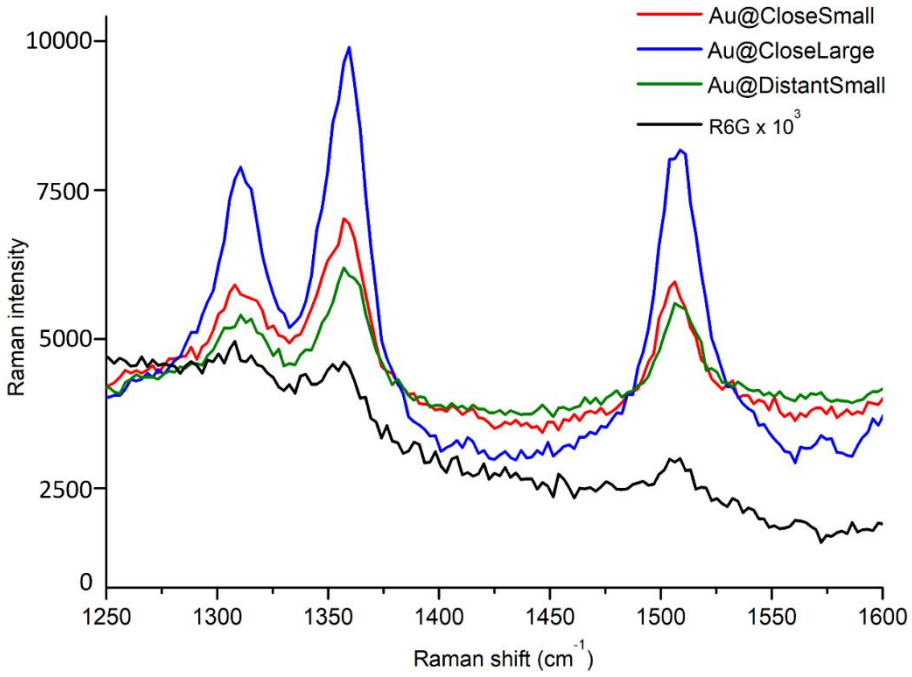

Figure 5.5: SERS spectra of Au-TiO_2 supraparticle composites.

5.2.4 Photocatalytic hydrogen peroxide generation

The photocatalytic hydrogen peroxide production of the as-prepared photocatalysts was studied in water and 10% methanol at atmospheric pressure and an excess of oxygen. The reaction conditions were optimized with the temperature controlled at 5 – 8 °C using ice and a pH of 4, as also observed in previous works [205]. Fig. 5.6 clearly shows the effect of the larger SPs on the photocatalytic performance of the composite catalyst, indicating that using Au@CloseLarge enhances the catalytic activity by more than 300% compared to pristine TiO_2, and it is twice that of the smaller Au-TiO_2 SPs. The pure TiO_2 generates H_2O_2 at a rate of 771 µmol.h^{-1}.m^{-2}. Au@CloseLarge show the best activity of 2100 µmol.h^{-1}.m^{-2} using simulated solar light (100 mW.cm^{-2}) among the catalysts studied in this work. To further understand the photocatalytic mechanism of the catalysts, the difference in hydrogen peroxide production rate between varying wavelengths was studied. The intensity of UV light (385 nm) was kept at 5 mW.cm^{-2}, and the intensity of green light (515 nm) at 25 mW.cm^{-2}. Surprisingly, the Au-TiO_2 SPs demonstrate lower H_2O_2 generation rates using individual wavelengths of 385 nm and 515 nm compared to using both the wavelengths simultaneously or using simulated

solar light. Moreover, the H_2O_2 generation simultaneously using 385 nm and 515 nm wavelength is equivalent to the H_2O_2 generation using simulated solar light indicating that the photocatalytic activity arises from simultaneous illumination of 385 nm and 515 nm is necessary to excite the plasmonic Au and create electron-hole pair separation in TiO_2. In summary, the larger SPs have enhanced photocatalytic hydrogen peroxide generation, which is proposed to be guided by plasmonic enhancement.

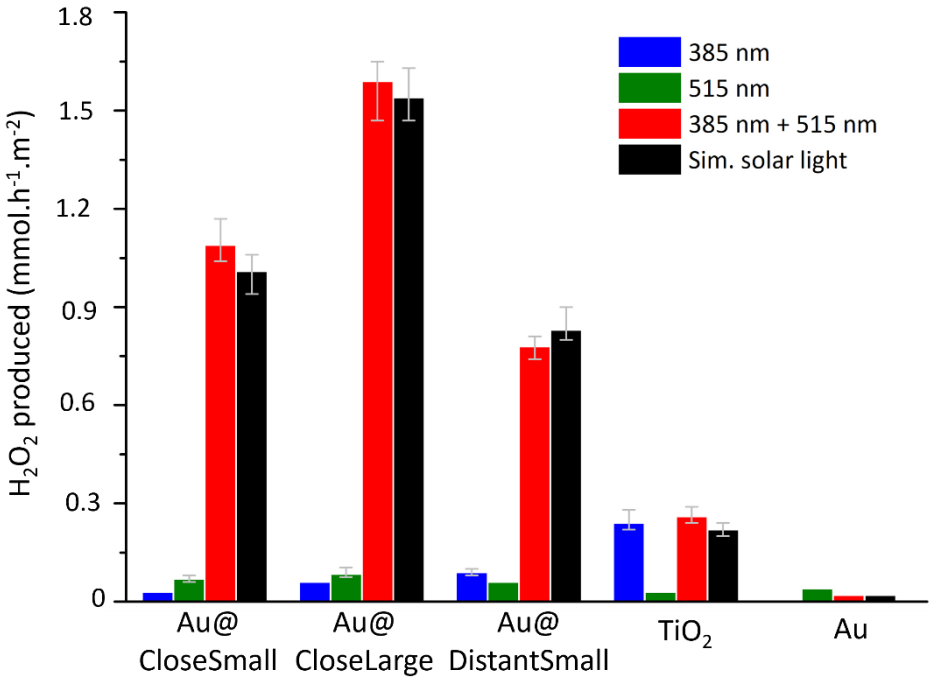

Figure 5.6: Photocatalytic hydrogen peroxide production of Au, TiO_2 and its composites under light illumination of 532 nm, 385 nm and simulated solar light.

5.2.5 Mechanism

To elucidate the mechanism of hydrogen peroxide generation by these SPs, electron paramagnetic resonance (EPR) spectroscopy, alongside other radical trapping experiments, was conducted. EPR, employing a DMPO trap under conditions akin to those of photocatalytic H_2O_2 generation, captured the generated radicals. Fig. 5.7a shows that UV irradiation on TiO_2 and Au@CloseSmall generates the $CH_2OH^{\cdot}$ radical, while no signal was detected for Au@CloseLarge. With green light alone, no signal was observed for any catalyst, indicating negligible radical generation. When both UV and visible light were used simultaneously, the EPR spectra for Au@CloseSmall SPs remained unchanged, whereas an additional $OH^{\cdot}$ radical signal was observed for Au@CloseLarge SPs. Since these experiments were conducted *ex situ* and subsequently analyzed by EPR, the time lag was sufficient for the $CH_2OH^{\cdot}$ radicals to form from the interaction of holes, $OH^{\cdot}$ radicals, and $O_2^{\cdot-}$ radicals with methanol. While EPR may not provide a fully detailed picture of the ongoing processes, the fact that $OH^{\cdot}$ radicals are only observed upon simultaneous excitation of UV and visible light, indicates that a synergistic effect occurs under those conditions. One of the obvious reason to observe the signal from $OH^{\cdot}$ radicals on simultaneous wavelength illumination can be the that the

excess $OH^{\cdot}$ radicals that did not react with the medium. Another more probable reason can be excessive electrons back reacting with H_2O_2 to produce H_2O and $OH^{\cdot}$ [389].

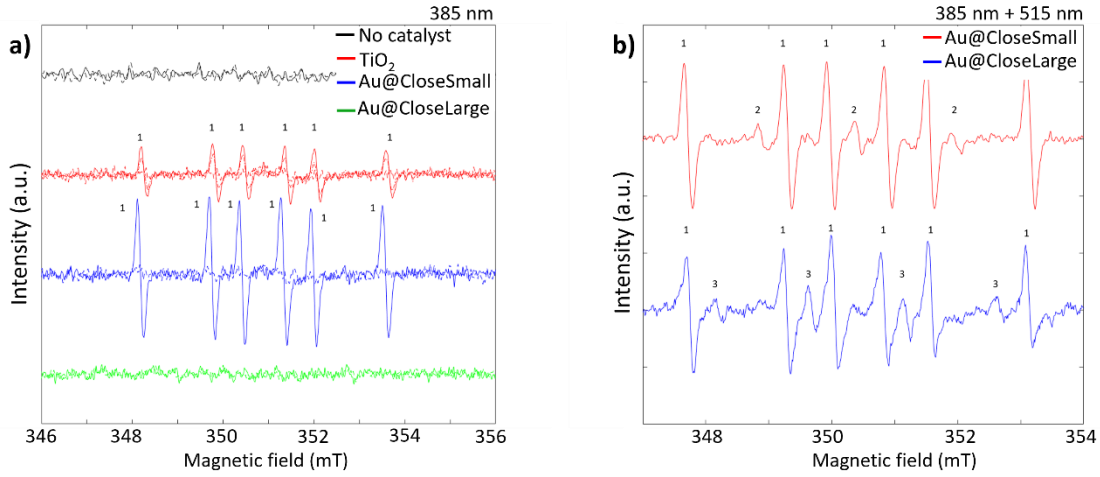

Figure 5.7: EPR spectra of Au-TiO_2 composites under UV light (385 nm) and UV & Green light (385 nm & 532 nm). 1 represents $CH_2OH^{\cdot}$, 2 represents DMPO degradation product and, 3 represents hydroxyl radical.

To further understand the different effects at play, additional radical trapping experiments were performed. Probe molecules of 2,3-bis-(2-methoxy-4-nitro-5-sulphenyl)-(2H)-tetrazolium-5-carboxanilide (XTT) and terephthalic acid (TA) were used as electron scavenger and hydroxyl radical scavenger, respectively, and without the interference from methanol. Hydroxyl radicals react with terephthalic acid to produce 2-hydroxyterphthalic acid quantifying the hole mediated reaction pathway as demonstrated in [363]. On the other hand, XTT is reduced by superoxide radicals and an electron to formazan, and is used to measure the electron mediated reaction pathway as demonstrated in [362]. As observed in Fig. 5.8a, the terephthalic acid probe experiments indicate that the photocatalytic activity of pristine TiO_2 relies more strongly on hole-mediated pathways compared to all of the Au-TiO_2 SP composites under both solar light and UV light. Under Visible light with 515 nm there was negligible signal for conversion of terephthalic acid, indicating the plasmon response for hole mediated reactions is not more significant compared to just using TiO_2 under UV light (Fig. A5.2 a-b). In contrast, as observed in Fig. 5.8d, electron-mediated pathways under solar light irradiation are much more pronounced for Au@CloseLarge compared to TiO_2, Au@CloseSmall and Au@DistantSmall, as concluded from the XTT assay. When the light source is changed to UV light, pristine TiO_2 again dominates the XTT conversion, while using visible light of 532 nm, there is negligible conversion of XTT (Fig. A5.2 c-d).

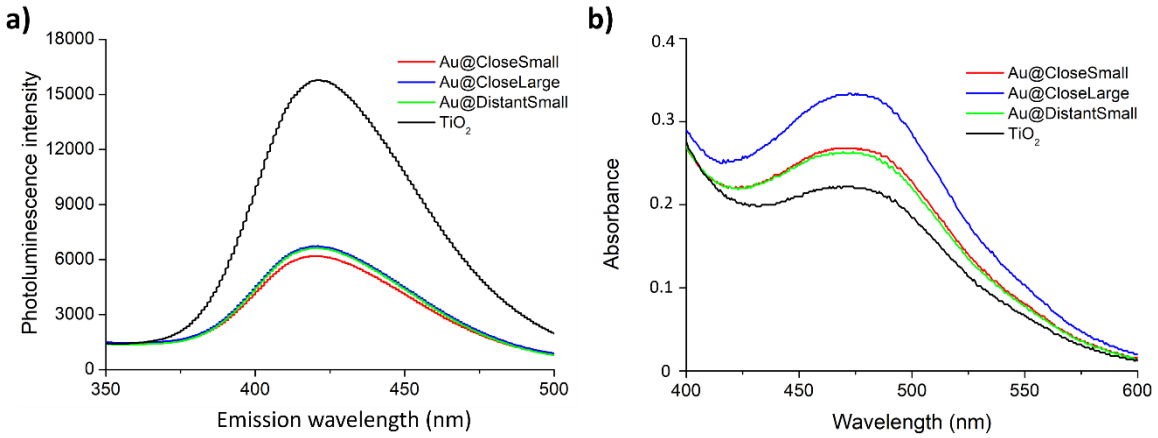

Figure 5.8: a) Photoluminescence spectra of conversion of terephthalic acid to 2-hydroxyterephthalic acid under simulated solar light illumination on all the Au-TiO_2 composites. b) UV-Vis absorption spectra of conversion of XTT to formazan under simulated solar light illumination on all the Au-TiO_2 composites.

The higher electron and superoxide generation for Au@CloseLarge under solar light corresponds well with the photocatalytic hydrogen peroxide generation. This leads us to an understanding that the H_2O_2 generation on such SPs is occurring mainly through either 2 electron or 4 electron O_2 reduction pathways. This confirms former studies that have indicated H_2O_2 generation using Au-TiO_2 composites occurs mainly through 2 electron reduction of O_2 [209, 378, 390].

Using all information from catalytic and spectroscopic we hypothesize that the generation of hot electrons upon plasmonic excitation of the SP is a crucial factor for explaining the superior performance of these materials. Hot electrons are generated at the Au metal sites and subsequently transferred to the TiO_2 conduction band, leading to an increase in the hydrogen peroxide generation rate through electron-mediated ORR. For Au@CloseLarge SPs, the photocatalytic hydrogen peroxide from electron based reactions could be enhanced because, 1) the close packing of Au nanoparticles can lead to collective lattice resonances which increases the near-electric field through plasmonic coupling, correlating it to a more efficient hot electron generation [364, 365], 2) the packing of Au nanoparticles into a single assembly, has shown to promote plasmon enhanced resonant energy transfer (PIRET) albeit in Au-CdSe self-assembly of 100 nm in size and micrometer sized Au-CuS nanochains which promoting charge separation and charge transfer into the TiO_2 conduction band [144, 391], and 3) the packing of Au nanoparticles into a single assembly of TiO_2 in multiple layers can promote the dark plasmon modes and therefore hot electron injection through landau damping [392]. The TiO_2 band edge with possible charge transfer mechanism can be seen in Fig 5.9.

We further argue that the generation of hot electrons is the pivotal plasmonic mechanism for the present system, as other plasmonic effects are less likely to occur under the present set of experimental conditions. Indeed, the size of Au nanoparticles used in this work (15 nm) implies that scattering of light is not a significant factor, as it only becomes important for nanoparticles exceeding 50 nm. Additionally, plasmonic local thermal heating within the Au composites is expected to be minimal, given the light intensity used is only 100 mW cm^{-2}, while it has been shown

that for photothermal effects to occur, much higher irradiance levels are required[65]. Furthermore, the optical absorption band of TiO_2 and the LSPR band of Au do not align, hence the direct effect of increased charge carrier generation at the semiconductor boosted by the enhanced near-field is hampered. It should be noted that these hypotheses remain theoretical and could be the subject of follow-up experimental studies using time-resolved transient absorption spectroscopy to understand electron transfer dynamics[393], as well as theoretical investigations using density functional theory (DFT) to validate the electron transfer dynamics and detect the source of enhanced electron generation[394]. Time-resolved transient absorption spectroscopy can reveal electron relaxation dynamics in plasmonic nanoparticles and semiconductors, shedding light on the origins of charge carrier excitation. Atwater *et al.* demonstrated that *ab initio* calculations based on density functional theory (DFT) can predict charge transfer dynamics between plasmonic nanoparticles and TiO_2 within a supraparticle assembly [395]. A significant area of interest is understanding the differences in these dynamics at the surface versus the interior of the supraparticles.

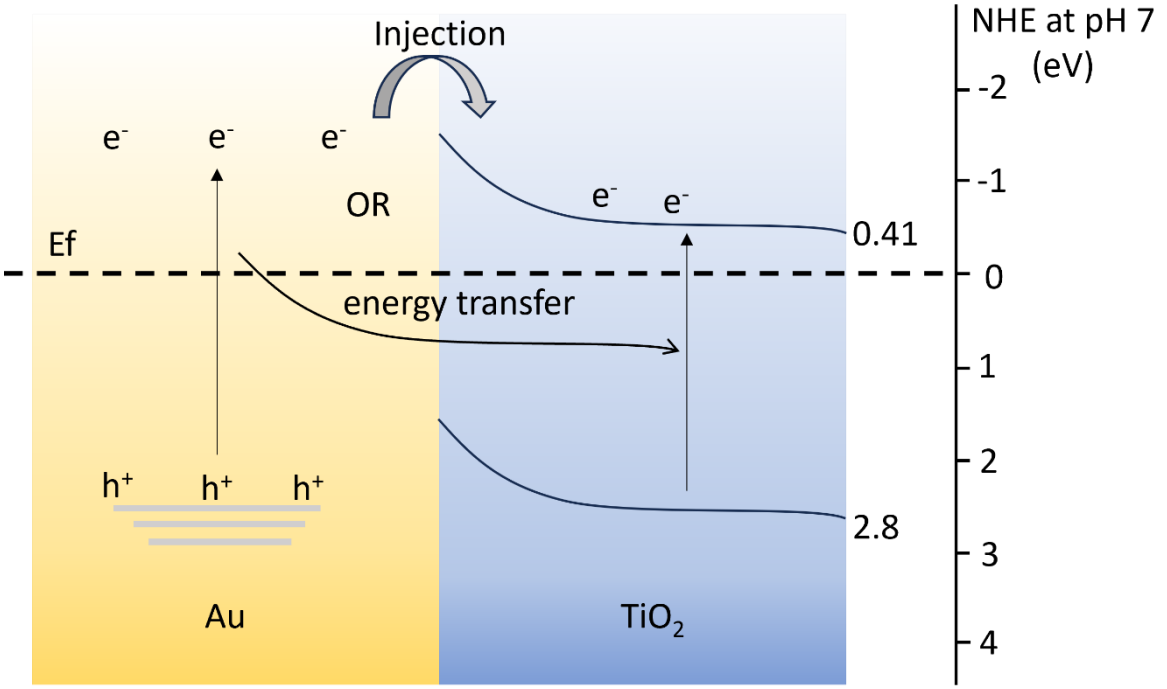

Figure 5.9: Schematic representing possible charge carrier transfer mechanism

5.3 Conclusion

Our findings indicate a significant enhancement in the photocatalytic production of hydrogen peroxide when using Au-TiO_2 SPs, and the enhancement increases with increase in SP size. This enhancement is primarily attributed to two factors: the near-field enhancement resulting from the collective plasmonic excitation and the efficient hot electron injection from the Au nanoparticles to the TiO_2. Using SERS it can be understood that the near-field enhancement increases the local electromagnetic field between Au nanoparticles and around the TiO_2, thus drastically improving light absorption. Meanwhile, the hot electron injection pathway facilitates a more efficient transfer of energetic electrons from the Au nanoparticles to the TiO_2, enhancing the photocatalytic reaction

through electron-mediated pathways. To further understand the underlying mechanisms, radical quenching experiments were conducted, indicating that the enhanced photocatalytic activity is in fact dominated by electron-mediated reactions, confirming the role of 2 electron or 4 electron oxygen reduction pathways as major routes towards photocatalytic hydrogen peroxide production using the present system. The results from this chapter not only demonstrate the potential of Au-TiO_2 SPs in plasmon-enhanced photocatalysis, but also provide valuable insights into the design of more efficient photocatalytic materials.

5.4 Experimental section

5.4.1 Synthesis

Au@PAH core-shell nanoparticle synthesis

Au nanoparticles were synthesized using a modified Turkevich procedure as described in earlier work of our research group [61]. Briefly, adequate amounts of HAuCl4 was dissolved in a round bottom flask in a total volume of 100 mL and brought to boil. Once the solution started to boil, 1 mL of a 1 wt% solution of sodium citrate was added and the solution was left boiling for 30 min under vigorous stirring. After 30 min, the solution is rapidly cooled to room temperature using an ice bath to quench the reaction. The nanoparticles were centrifuged (12000 rpm) and redispersed in water.

Stock solutions of polyelectrolytes polyallylamine hydrochloride (PAH, MW 17.5 KDa, Sigma-Aldrich) were prepared in ultrapure water by sonication for 30 min and used as required. 12 mL of the as-prepared colloidal solution was centrifuged at 4700 g for 40 min and redispersed in water. This was done to remove most of the excess citrate in the colloidal silver solution, in order to reduce the interference of charge on the citrate molecule and to have optimal deposition of the first polycation layer (PAH). 12 mL of this centrifuged silver colloidal solution was added dropwise to 6 mL of 5g/L PAH solution under vigorous stirring in a glass vial. The stirring was continued at room temperature for 20 min in dark. The resulting colloidal solution was centrifuged in 1.5 mL Eppendorf tubes to remove the excess polyelectrolyte. Around 1460–1480 mL of supernatant was discarded and the remaining dark-brownish gel-like pellet was redispersed in ultrapure water. The centrifuge process was repeated one more time as a washing step and the final redispersion in water was adapted to obtain 12 mL of colloid.

Au-TiO_2 supraparticle synthesis

The synthesized Au@PAH core-shell nanoparticle colloid is further diluted to 15 mL and 1mL of 10 mM titanium bis(ammonium lactato) dihydroxide (TALH) was added in 100 µL steps. After each 100 L step a zeta potential measurement is taken. Depending on the size of supraparticle to be achieved, the reaction can be stopped when zeta potential reaches +20, around 0 or -20 to obtain Au@CloseSmall, Au@CloseLarge or Au@DistantSmall supraparticles. The supraparticles are drop casted on a precleaned silicon wafer (3 cm × 6 cm) and further calcined at 450 °C for 30 minutes. This led to an approximate photocatalyst loading of 75 µg.cm^{-2}. Photometric measurements were performed to determine the gold mass concentration per unit volume in the colloids by appropriate dilution to detection limits using the Spectroquant® gold test kit.

5.4.2 Photocatalytic Hydrogen Peroxide generation

Schematic representation of the experimental setup is as shown in Fig A5.1. The coated silicon wafer was kept in a petri dish surrounded by ice and 27 mL milli-Q water with 3 mL methanol (10%) was added to it. The pH of the reaction solution was adjusted using 10mM nitric acid. Suitable light was illuminated onto the sample to produce H_2O_2. For simulated sunlight AM1.5G filter was used (SciSun-300, Sciencetech) and the intensity amounted to 100 $mW.cm^{-2}$ (i.e. 1 sun) at the top surface of the silicon wafer. LED light sources were used to illuminate using UV (385 nm) and green light (515 nm). The intensity of UV and green light was kept at 5 $mW.cm^{-2}$ and 25 $mW.cm^{-2}$ respectively. As a reference, hydrogen peroxide generation reaction on blank silicon wafer was performed to omit effects of direct photolysis and heat from light irradiation. Incident light intensity was measured by a calibrated spectroradiometer (Avantes Avaspec-3648-USB2). Hydrogen peroxide measurement was carried out using KMnO4 titration method [396].

5.4.3 Characterization

Electron microscopy

Nanoparticle solution (3 µL) was drop-cast on a Mo grid with a single layer graphene and left to dry in ambient air. High-angle annular dark field scanning transmission electron microscopy (HAADF-STEM) and energy dispersive X-ray spectroscopy (EDS) was performed using a Thermo Fischer Tecnai Osiris microscope operated at 200kV.

Scanning electron microscopy (SEM) images of the films were acquired using an FEG-ESEM-EDX, Thermo Fisher Scientific Quanta 250 at an accelerating voltage of 20 kV.

Electron energy loss spectroscopy

EELS measurements were carried out using an aberration corrected ThermoFischer Scientific – Titan Cubed electron microscope, operating at 300 kV, equipped with an energy monochromator excited to a value of 0.7. The energy resolution provided by the electron monochromator, as measured from the full-width half maximum of acquired zero-loss peaks, was 100 meV. The dispersion of the spectrometer was set to 0.002 $eV.ch^{-1}$ to visualize the plasmon edges. To analyze the EELS data sets, EELSModel software was used[372].

Zeta potential

Zeta potential measurements were carried out on a Zetasizer Nano ZS (Malvern, United Kingdom). The samples were diluted with ultrapure water and measured in triplicate at a temperature of 25 °C. 100 µL of solution was inserted using a syringe into a capillary cuvette with positive and negative potential at each end to measure the zeta potential.

UV-Vis absorption and UV- Vis DRS

A UV–vis absorption spectrum and UV-Vis diffused reflectance spectrum was recorded from 300 nm to 800 nm with a resolution of 0.2 nm using Shimadzu UV–vis 2501 PC double beam spectrophotometer. UV–vis absorption spectrum was recorded using liquid sample holder and UV-Vis DRS was recorded by pressing the powdered sample on Barium Sulfate background.

Surface enhanced Raman spectroscopy

Rhodamine 6G (Sigma Aldrich, Fluorescence bioreagent) dye was used as the Raman probe molecule for SERS measurements and all the measurements were done using the same sample and substrate as used for hydrogen evolution reaction and stearic acid degradation tests after

clearing off all the organic matter. These substrates were prepared for SERS measurements by drop casting a mixture of known concentration of R6G, 10^{-4} M (20 µL) on the Au@TiO_2 core shell thin films. Reference neat R6G Raman substrate is prepared by drop casting 50 µL of 1 M pure R6G dye solution. All the samples were allowed to dry in a desiccator for one full day before measurement. The Raman spectra were recorded on a Horiba XploRA Plus Raman spectrometer equipped with a diode-pumped solid-state laser of 785 nm and a power of 25 mW. The samples were measured with an acquisition time of 10 s, 10 accumulations and in a spectral range of 100 – 2000 cm^{-1}. Raman spectra were recorded multiple times at different locations for each sample. Fluorescence was observed using 532 nm laser and therefore a laser of 785 nm wavelength was used.

Terephthalic acid and XTT radical trapping experiments

All the measurements were done using the same sample and substrate as used for hydrogen evolution reaction and stearic acid degradation tests. For hydroxyl radical trapping experiments, the thin film was inserted in 20 mL of TA (0.5 mM) and NaOH (2 mM) and illuminated with simulated solar light (100 $mW.cm^{-2}$). The fluorescent emission intensity of 2-hydroxyterephthalic acid was detected with λmax at 425 nm under the excitation at 315 nm using a Shimadzu RF-6000 spectrofluorometer, equipped with a Xe lamp. For both excitation and emission, the slit width was set to 2 nm. Fur superoxide radical trapping experiments, the thin film was inserted in 10 mL of XTT sodium salt solution (0.1 mM) in DMSO in a glass vessel and illuminated with simulated solar light (100 $mW.cm^{-2}$). The resulting supernatant was analyzed using UV-VIS for the formation of XTT formazan with λmax at 475 nm.

Electron paramagnetic resonance spectroscopy

Room-temperature continuous-wave (cw) X-band EPR measurements were carried out on a Bruker Elexsys E680 spectrometer mounted with an optically accessible ER4104OR resonator working at ~ 9.44 GHz. The spectra were collected at 5 mW microwave power, 0.05 mT modulation amplitude, and 100 kHz modulation frequency. DMPO (5,5-dimethyl-1-pyrroline N-oxide) was used to trap any short-lived radicals generated during a photoreaction. The resulting DMPO adduct generally have longer lifetimes allowing for detection by EPR spectroscopy. Here, DMPO was added to water with 10% methanol mixture and EPR spectra were recorded before and after illumination with UV and green light under air atmosphere.

Chapter 6: General conclusions and outlook – A pathway into advancing hybrid plasmonic structures for photocatalysis and photothermal catalysis using advanced electron microscopy techniques

In this chapter, general conclusions are drawn regarding the methodologies and insights presented in this thesis. It also entails a discussion of future perspectives for the research presented in this thesis, along with the demonstration of promising results that will motivate further exploration.

6.1 General conclusions

In order to sustainably meet the world's energy needs, emerging technologies such as electrolysis and photocatalysis are needed to be applied at a larger scale. Photocatalysis, being fully solar-driven, has potential to be more eco-friendly and renewable but lacks the efficiencies needed for large scale application. A composite of plasmonic nanoparticles with semiconductors has shown great promise in absorbing a larger portion of the solar spectrum and enhancing photocatalytic efficiencies[4]. To address this issue, plasmonic hybrids were suggested. They are known for the unique optical feature of SPR, allowing absorption at well-determined wavelengths and across the solar spectrum. These can be tuned by varying the metal type, size, shape or dielectric environment of a plasmonic NP[18]. In chapter 1, such plasmonic hybrid nanostructures were discussed in detail, along with their effects on optical properties and the photocatalytic mechanism. Finally, interesting literature examples for H_2 evolution and hydrogen peroxide generation came up for discussion showcasing the importance of hybrid plasmonic nanostructures.

To understand the structure-activity relation of these photocatalysts, firstly, it is very important to know the structure at nanoscale. Therefore, in chapter 2, general and advanced electron microscopy techniques have been discussed. Furthermore, it is followed up by a detailed description of electron tomography for 3D characterization of nanomaterials. The latter part focuses on High-Angle Annular Dark Field Scanning Transmission Electron Microscopy (HAADF-STEM) as the basis for electron tomography and provides an in-depth explanation of the technique and its further processing.

During my PhD journey, I have been able to develop and gain novel insights into hybrid plasmonic structures for enhanced photocatalysis by applying and developing advanced electron microscopy techniques as conveyed in the current thesis. I started with synthesizing and studying the structure of core-shell nanoparticles, namely Au@polymer, Au@TiO_2 and Au@SiO_2 core-shell nanoparticles. In chapter 3, the focus was on performing in-depth analysis of the characterization techniques used for the visualization of hybrid core-shell nanoparticles through advanced 2D and 3D electron microscopy techniques. The first challenge I addressed was simultaneous visualization of Au and thin polymer shells by using graphene TEM grids. This allowed me to accurately measure the polymer shell thickness. Further, to simultaneously visualize materials with significant differences in atomic numbers such as Au and TiO_2 in 3D, multimode tomography was performed. In multimode tomography, a combination of two modes of electron microscopy HAADF-STEM and MAADF-STEM was performed offering understanding into the uniformity of TiO_2 shell thickness and sintering of Au nanoparticles for a shell thickness of 2 nm which is not observed for higher shell thickness. In the case of Au@SiO_2 core-shell nanoparticles developed at Utrecht University, exit wave reconstruction was used to visualize the SiO_2 shell in high-resolution and gain an understanding that the SiO_2 shell is not always uniform. The uniformity was studied using electron tomography where a new technique was developed for 3D reconstruction. The tomography study confirmed that uniformity of SiO_2 shell can vary from batch to batch.

Chapter 4 presented a comprehensive study on the synthesis, characterization, and photocatalytic applications of Au@TiO_2 core-shell nanoparticles, emphasizing the optimization of shell thickness for enhanced photocatalytic activity using simulated solar light. By controlling the hydrolysis of the titanium precursor, I could successfully achieve TiO_2 shells of varying thicknesses from 2 nm to 12 nm around Au nanoparticles. The electron tomography techniques discussed in chapter 3, were vital to demonstrate that a shell thickness of approximately 4 nm offers the optimum balance between preventing sintering of the Au core and maximizing photocatalytic activity. Through a combination of experimental and theoretical approaches, including photocatalytic activity tests, electromagnetic simulations, and surface-enhanced Raman spectroscopy, the chapter explains the critical role of near-field enhancement and hot electron injection in the photocatalytic efficiency of these core-shell nanostructures. This outcome substantiates the crucial influence of TiO_2 shell thickness on the photocatalytic performance, providing valuable insights for the rational design of hybrid plasmonic photocatalysts.

Chapter 5 went a step further in enhancing the near-field and hot electron injection from plasmonic nanoparticles by self-assembling Au nanoparticles in a large close packed structure along with TiO_2. Electrostatic interactions between a polymer PAH and a titania precursor TALH allowed assembly of Au-TiO_2 with different sizes ranging from 200 nm to 5 µm and with varying distance between Au nanoparticles within the assembly. Such assemblies into larger particles were termed Au-TiO_2 supraparticles. The supraparticles enhanced plasmon-plasmon and plasmon-semiconductor interactions, leading to a marked increase in H_2O_2 production rates compared to traditional TiO_2 photocatalysts under simulated solar light. The enhanced photocatalytic activity is attributed to improved light absorption, near-field enhancement due to collective plasmonic excitation and efficient hot electron injection from Au nanoparticles into the TiO_2 matrix. Furthermore, the investigation into the photocatalytic mechanisms was supported by electron paramagnetic resonance (EPR) spectroscopy and radical trapping experiments, providing more insights into the hydroxyl radical (hole mediated) and superoxide radical (electron mediated) generation processes underpinning H_2O_2 production. This approach confirms the critical role of electron-mediated reactions and the role of oxygen reduction reaction pathways in photocatalytic H_2O_2 generation in this system. The findings emphasize the potential of Au-TiO_2 SPs offering a sustainable alternative to conventional H_2O_2 production methods. The chapter also advanced the general understanding of plasmon-enhanced photocatalysis, demonstrating that the physical arrangement and size of SPs are crucial for maximizing photocatalytic efficiency.

In summary, the advanced electron microscopy studies in this thesis shed light on the critical roles of nanoparticle size, shell thickness, and overall nanostructure morphology in governing the photocatalytic activity. By highlighting the synergy between plasmonic excitation and semiconductor photocatalysis, this thesis paves the way for the development of more efficient and effective plasmon-assisted photocatalytic materials. As the demand for sustainable and green technologies continues to grow, the insights gained from this study are expected to contribute to the development of novel materials capable of harnessing solar energy more effectively, marking a significant step forward in the utilization of hybrid plasmonic nanostructures for energy applications.

6.2 Outlook

There are several directions for further development of methods, materials and material configurations explored in the current thesis. The promising topics that hold great potential to be studied further in terms of plasmonic photocatalysis and electron microscopy are:

1. Alternative materials to Au with different structural configurations
2. Photothermal catalysis
3. *In situ* electron microscopy (with light)

6.2.1 Alternative materials to Au with different structural configurations

In the current thesis, I focused on tuning the interplay of plasmonic Au nanoparticles with TiO_2 by creating various composite structures, leading to enhancement in photocatalysis and Au is the most extensively studied plasmonic material because of its chemical stability[397]. Although, it should be noted that Au is expensive and an alternate plasmonic material would be desirable for a more widescale application in photocatalysis. Compared to Au, other materials with a good plasmonic response such as Ag, Cu, Ni, Al and Mg etc. are prone to oxidation, leading to a substantial decrease in their plasmonic response[23, 30, 105, 398, 399].

Ag, due to its dielectric properties, has an intrinsically better plasmonic response compared to Au and the plasmon response can be tuned to extend across the visible region of the solar spectrum by changing the shape, size and configuration (such as core-shell, alloy, yolk-shell and self-assemblies)[65]. As mentioned above, Ag nanoparticles are prone to oxidation and solutions are needed to stabilize them. There are two viable solutions by either covering the nanoparticle with a protective shell, or by forming an alloy which is not (or less) prone to oxidation. Here, the idea is not just to protect the Ag NPs from losing its plasmonic properties but also to modify the structure to further enhance its plasmonic properties.

As a first lead into this strategy, Ag nanotriangle platelets were synthesized which we know from our previous research that they have enhanced plasmonic hotspots at its edges and corners[65]. The Ag nanotriangles were further modified to form Ag@Au core-shell nanotriangles or Ag-Au hollow nanotriangles by pH controlled galvanic replacement (Fig. 6.1). At a lower pH due to high mobility of positively charged Au^+ ions, the kinetics of galvanic replacement tend to be higher leading to a hollow structure. Whereas at a higher pH of 11, the mobility of H^+ ions is low leading to galvanic replacement only from the surface of the nanotriangle and forming a core-shell structure. We can observe from Fig 6.1e that the Ag nanotriangles have an absorption band around 550 nm. For the Ag@Au core-shell structures, the plasmon band is broadened and red shifted to around 750 nm. For Ag-Au hollow structures, the center of the plasmon band is maintained around 550 nm and the absorption is extended across the entire spectrum. EELS maps in Fig. 6.1g-h convey that for an energy between 2.1 – 2.3 eV, the electron energy loss corresponds to the plasmonic excitement from the hollow cavities, whereas the energy loss between 1.6 - 1.8 eV corresponds to the plasmonic excitement at the edges and corners of the nanotriangle. Correlating the EELS maps with UV-Vis spectra, we understand that a major part of the light absorption from Ag-Au hollow structures comes from hollow cavities, which may hold great promise for application in catalysis.

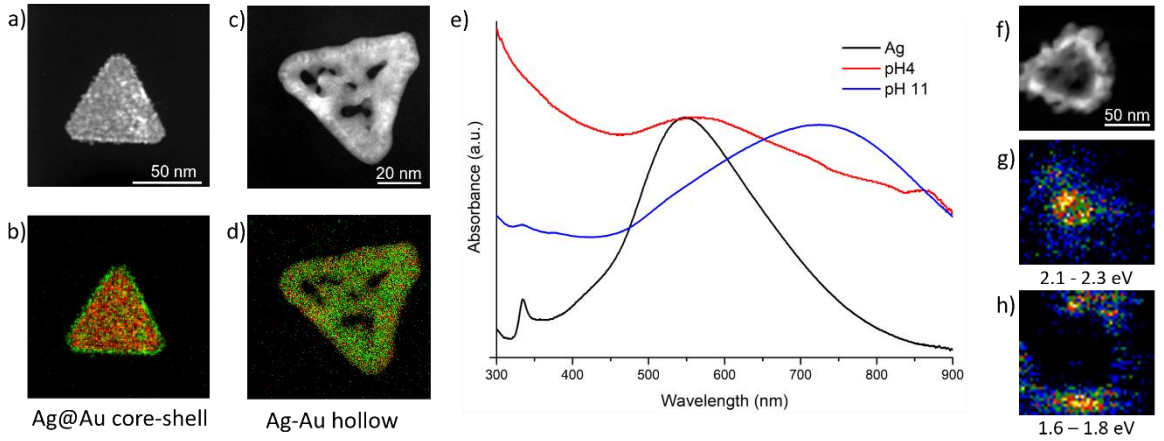

Figure 6.1: HAADF-STEM image and EDX map of Au-Ag nanotriangles with a-b) core-shell and c-d) hollow structure. e) UV-Vis spectra of Ag, Ag@Au core-shell and Ag-Au hollow nanotriangles. f) HAADF-STEM image of Ag-Au hollow nanotriangle and representative g-h) EELS plasmon map for the energy range 2.1 – 2.3 eV and 1.6 – 1.8 eV respectively.

As a proof of principle, these structures were employed in photocatalytic H_2 evolution experiments. To this end, 2wt% of Ag and Ag-Au composites were photo-deposited on TiO_2 and $ZnIn_2S_4$. For simplicity, the sample names are shortened as Ti for TiO_2, ZIS for $ZnIn_2S_4$, 'CS' for 'core-shell' and 'hol' for 'hollow'. The H_2 evolution for all the samples in this preliminary experiment, is performed only under simulated solar light. H_2 evolution activity for ZIS is twice that of TiO_2 when using solar light. This could be due to its absorbance in the visible region of the electromagnetic spectrum. Furthermore, clearly there is an increase in H_2 evolution for Ag and Ag-Au composites compared to pristine TiO_2 and $ZnIn_2S_4$. For TiO_2 based composites, the photocatalytic H_2 evolution increases by a factor of 2.5 for Ag-Ti but for Ag@Au CS Ti and Ag-Au hol Ti, the H_2 evolution increases approximately by a factor of 8 and 10 times that of TiO_2, respectively. For ZIS based composites, the increase in H_2 evolution compared to ZIS is 1.6 times for Ag-ZIS, 4.5 times for Ag@Au CS ZIS and 6.5 times for Ag-Au hol ZIS having the best overall H_2 evolution reaction rate of (338.78 $\mu mol.g^{-1}.h^{-1}$). The increased H_2 evolution can be attributed to several factors: higher absorption across the solar spectrum, near-field enhancement from the hollow cavities, and increased surface area due to these cavities within the nanoparticles. The near-field enhancement within the cavities is influenced by their size. For larger cavities (> 5 nm), the field enhancement and plasmonic response within the cavity are dampened; however, enhancement can still occur at both the inner and outer edges of the hollow nanoparticle. Conversely, for smaller cavities (1 nm - 5 nm), the field enhancement within the cavity is either enhanced or remains intact, depending on the specific size of the cavity [400]. For a complete understanding of the mechanistic insights, electromagnetic modelling studies, photocatalytic action spectrum and radical trapping experiments still need to be performed. Still, the bright prospect of a higher hydrogen evolution rate from the core-shell and hollow nanoparticles show the promise of such structural modifications by incorporating Ag based nanostructures or partially replacing Au with Ag.

In the hindsight of H_2 evolution in the current thesis, instead of using methanol as a sacrificial agent, overall water splitting without any use of methanol or performing other organic reaction to obtain a suitable fuel is a more practical and sustainable approach. By using methanol, the cost of methanol makes it extremely difficult to bring down the cost of renewable hydrogen to less than 1

USD. Furthermore, once the methanol is oxidized, it leaves a trail of CO2 or carbon based product making the whole process not sustainable anymore.

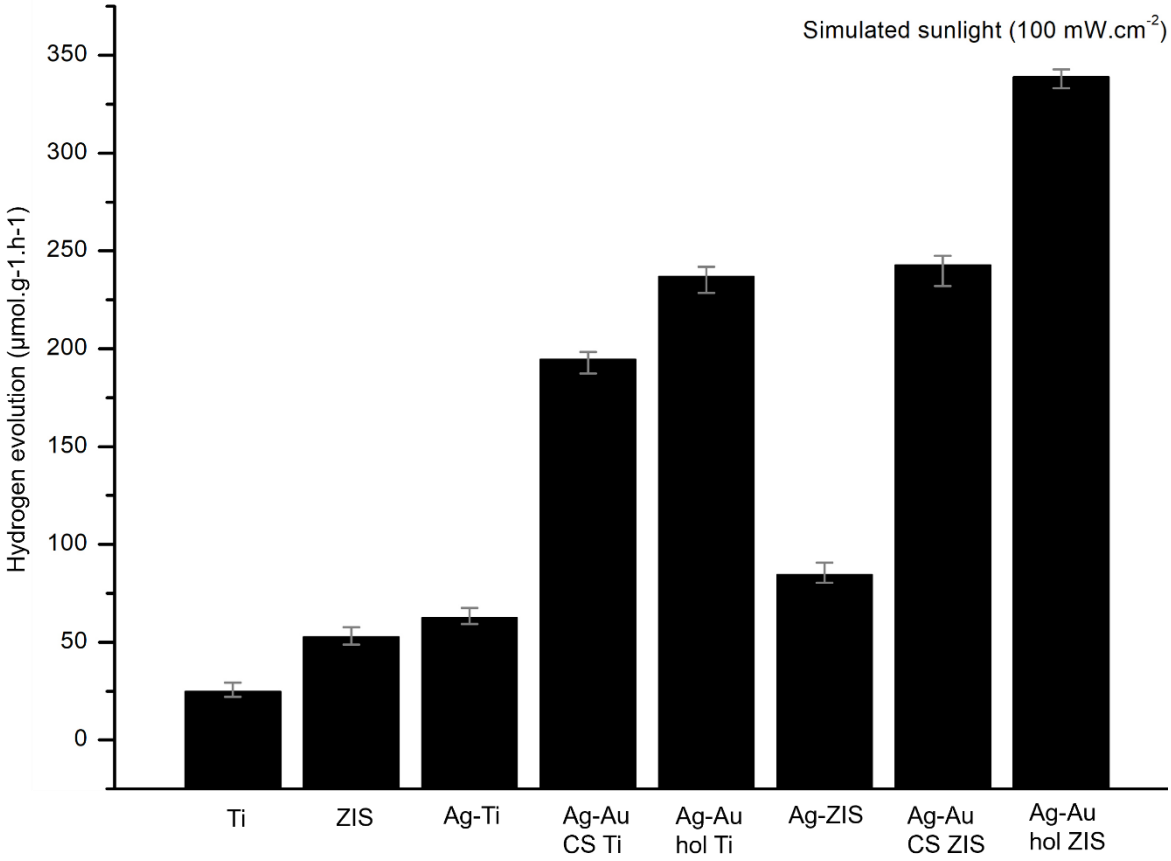

Figure 6.2: Hydrogen evolution rates for Ti, ZIS, Ag-Ti, Ag-Au CS Ti, Ag-Au hol Ti, Ag-ZIS, Ag-Au CS ZIS, Ag-Au hol ZIS.

Similar to chapter 5 of the thesis, it would also be interesting to arrange these hollow and core-shell structures as self-assembled suprastructures with better control over the size and shape of the supraparticle and also the distance between the nanoparticles within the supraparticle. To obtain such a control, as explained in chapter 1, the self-assembly strategy needs to switch from electrostatic self-assembly to other self-assembly techniques such as emulsion directed self-assembly. A control in distance between nanoparticles can be beneficial in observing differences in near-field enhancement and therefore the catalytic efficiencies.

Another approach to have a better effect of near-field enhancement on the photocatalytic activity is to use semiconductors with absorption edge overlapping with plasmon resonance band of the plasmonic nanoparticles. Although, to have an absorption edge in the visible region of electromagnetic spectrum, the semiconductors need a smaller band gap, increasing the charge carrier recombination. Therefore, it's a balancing act between having a higher effect of near-field enhancement and decreasing charge carrier recombination.

6.2.2 Photothermal catalysis

Photocatalysis has been studied extensively, but it is still quite far from commercial implementation. Photocatalysis is hindered by sluggish reaction kinetics and limited photonic

efficiency, making it unviable for commercial application in the short term. Nearing the end of my PhD marked the beginning of a newer concept of photothermal catalysis. As an attractive alternative to exclusively light-based catalysis, photothermal catalysis combines renewable solar energy and thermal energy into one effective, economical and eco-friendly solution. Photo-assisted thermal catalysis can promote reaction rates due to the increased local temperature, while thermal-assisted photocatalytic reactions lead to a reduction of the apparent activation energy. The synergy of these two systems has been shown to exceed the simple sum of photocatalytic and thermal catalytic reactions [401].

To enable such implementation, novel catalytic materials with enhanced photothermal properties need to be developed. Plasmonic NPs are more interesting for photothermal catalysis compared to dark materials such as carbon black because they can create high local temperatures compared to mild temperatures radiated by a black body due to absorption from incident photons. Bimetallic nanoparticles composed of a plasmonic material (Au or Ag) with a thermally catalytic material suitable for a particular reaction is a promising combination in the context of enhancing photothermal catalytic applications. In such plasmonic bimetallic systems, the plasmonic nanoparticle is acting as light-antenna and transfers the locally generated photothermal heat (resulting from its local surface plasmon resonance property) to the thermal catalyst, which acts as the reactive active site[402]. Such hybrid nanostructures can be configured in a core-satellite system (*i.e*. a larger plasmonic nanoparticle that is covered with several small thermocatalytic nanoparticles) or a core-shell system (plasmonic nanoparticle in the core, completely covered with a thermocatalytic shell). In that respect, I have already been successful in synthesizing Ag-Ni core-satellite (Fig. 6.3a) and Ag@Ni core-shell nanoparticles (Fig. 6.3b) in a preliminary experiment aimed towards reverse water gas shift reaction to produce CO from CO_2 and H_2. Ag can act as the antenna, absorbing the light to simultaneously excite electrons and convert it into heat, while Ni serves as a catalyst activating CO_2. The core-satellite system is beneficial to aid side reactions towards the required end product CO while core-shell structure can possibly protect the Ag NPs from oxidation and sintering. Still, precise control over the distribution of thermally catalytic satellites on the plasmonic core and achieving uniformity in the thermally catalytic shell coverage on the plasmonic core remains a challenge. Moving further, forming self-assembled suprastructures with these core-satellite and core-shell NPs can be even more promising especially for photothermal catalysis due to its collective interaction.

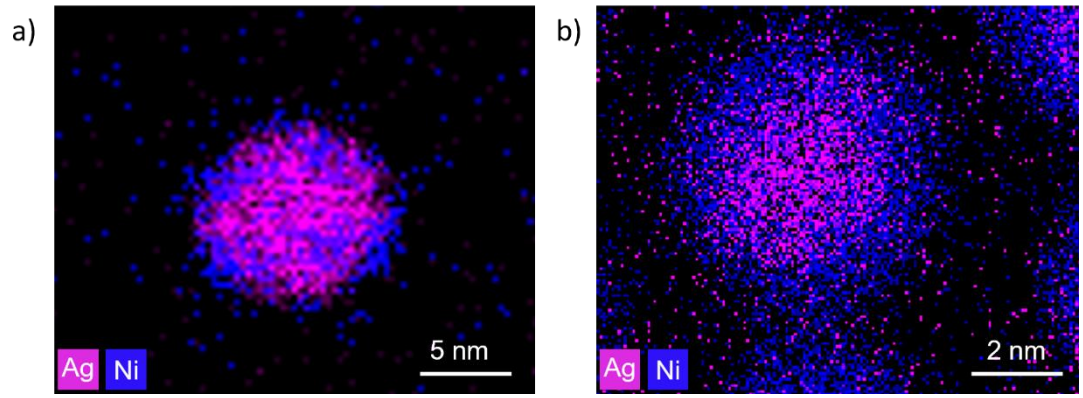

Figure 6.3: EDX map of a) Ag-Ni core-satellite and b) Ag@Ni core-shell nanoparticles.

6.2.3 Electron tomography and *In situ* electron microscopy

In the current thesis, I have used some advanced electron microscopy techniques to study the structure of catalytic materials. Typically, such techniques are used to image the structure before and/or after catalysis. Additionally, the imaging is done in high vacuum conditions. The missing information of structural changes occurring during dynamic real time processes is being filled up with the latest advent of *in situ* electron microscopy. The EMAT research group already possesses *in situ* heating, *in situ* liquid, *in situ* biasing and *in situ* gas holders to perform such experiments. In Chapter 4, where dimer particles were predominantly observed, one hypothesis is that nanoparticles form dimers upon drying on a TEM grid. This phenomenon can be studied using such an *in situ* liquid holder. In this setup, the colloidal solution is inserted into the liquid chip of the TEM holder, allowing observation of nanoparticles as the liquid evaporates and they dry on the chip. Similarly, the formation of supraparticles through electrostatic interactions, as discussed in Chapter 5, can also be examined using the *in situ* liquid holder.

Beyond the understanding and optimization of synthesis parameters, recent studies have shown that exposing nanoparticles to various gases and pressures can result in changes to their crystal facets and phase transitions [403, 404]. These changes can be investigated using *in situ* holders or environmental electron microscopes. Still, throughout the literature the information on structure dynamics during light illumination with gas or liquid is missing to a large extent and can also be considered non-existent in most of the cases. There are numerous research articles in photocatalysis indicating degradation of catalysts, but the mechanism of degradation and structural changes during and after photocatalysis is a blank book to filled with more understanding. Therefore, understanding real-time degradation of photocatalysts can feed researchers with more information on preparing a more stable catalysts. For instance, in Fig. 6.4a-b we observe for Ag@Ni core-shell nanoparticles, the Ni shell starts disintegrating and Ag nanoparticles start sintering upon exposure to CO_2 + H_2 and 700 $mW.cm^{-2}$ of simulated solar light.

Other than degradation of catalysts, the observation of reactive facets in faceted nanoparticles for example through visualization of H_2 evolution bubbles from a certain facet in water splitting catalysis, or change in active crystal facets during gas or liquid phase photocatalysis can lead us to prepare more efficient photocatalysts with exposed active crystal facets. Another helpful aspect of *in situ* electron microscopy in development of more active photocatalysts is to know what is the surface active site during photocatalysis. For example Lu *et al.* showed how the surface of TiO_2 converts into a disordered hydrogenated form during H_2 evolution using light illumination [405]. Furthermore, dynamic processes such as metal support interactions (MSI) and strong metal-support interactions (SMSI) are theoretically possible in photothermal catalysis due to very high local temperatures [406–409]. The possibility of visualizing and understanding such MSI and SMSI could be a breakthrough in solar assisted photothermal catalysis. Studying *in situ* the transformations in self-assembled structures during photothermal catalysis due to its complexity and ability to create intense electromagnetic fields and local increase in photothermal temperature will be complex, but will also reveal useful insights into structural properties by using EELS, including changes in structure. Even though there are numerous research opportunities to explore in light induced *in situ* electron microscopy, interpretation and differentiating the influence of the electron beam on the nanostructure compared to that of light is extremely crucial and complex. There exist low electron dose techniques such as 4D STEM, integrated differential phase contrast STEM (iDPC-

STEM) and real-time integration center of mass (riCOM) at the EMAT group equipped with ultrafast cameras to possibly circumvent this interpretation aspect. A combination of research with novel hybrid plasmonic structures in photothermal catalysis and its study using *in situ* electron microscopy would undoubtedly be a promising strategy to advance the field of plasmonic photocatalysis towards a myriad of applications.

As mentioned in Chapter 3, electron tomography of Au@TiO_2 core-shell nanostructure was visualized by manual segmentation of the voxels in the core and shell. Manual segmentation was applied since the reconstruction methods including segmentation such as DART are not suitable for the core-shell nanostructures studied in this thesis and other unsupervised image segmentation methods such as watershed transform gave inaccurate segmentation results. However, manual segmentation can still introduce user bias due to the subjective thresholding of voxels belonging to the core and shell. A lot of progress is being made in using newer segmentation methods based on deep learning and convolutional neural networks. Given sufficient training data, can perform automatic segmentation of challenging core-shell structures. These methods can provide more reliable data without user bias and do so more quickly than manual segmentation [410–412].

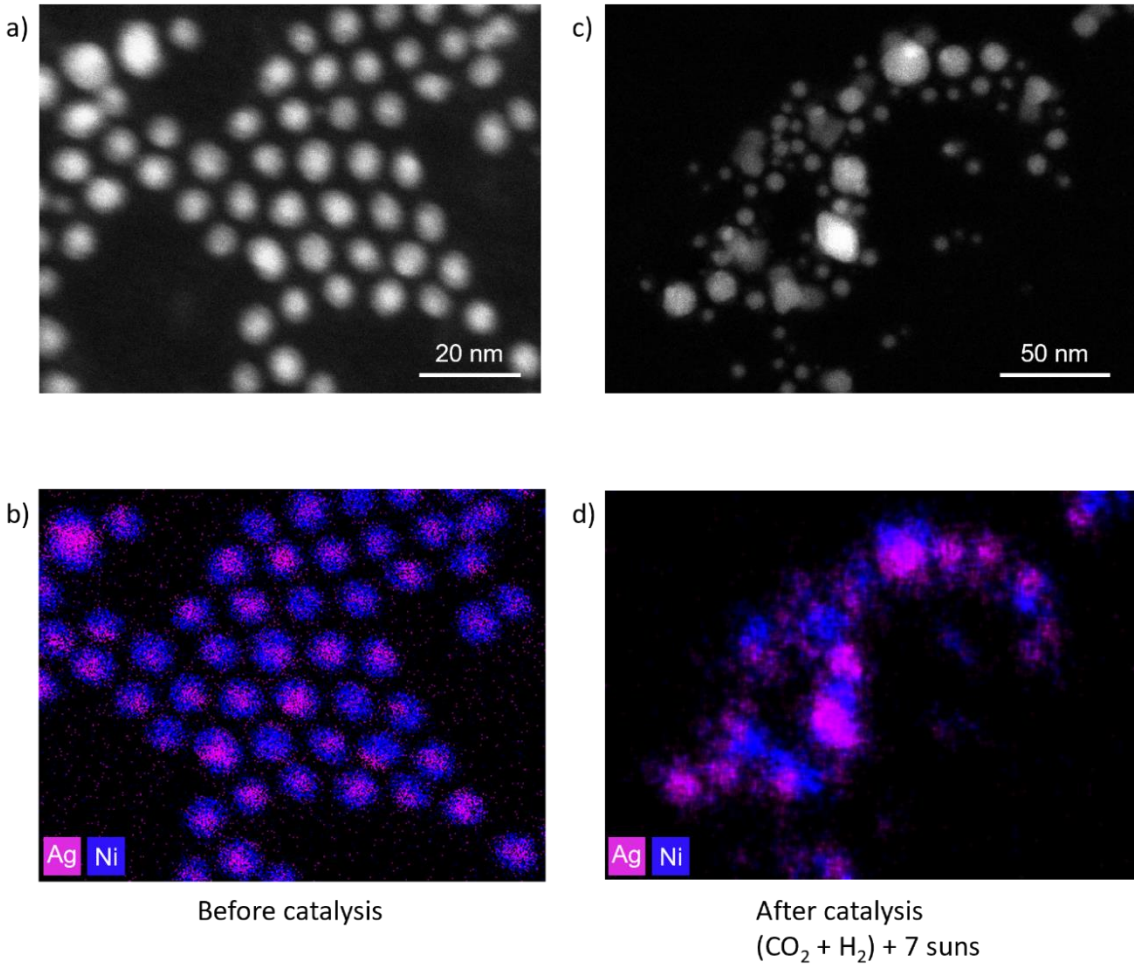

Figure 6.4: HAADF-STEM image and EDX map of Ag@Ni core-shell nanoparticles a-b) before catalysis and c-d) after catalysis.

Appendix

Chapter 4

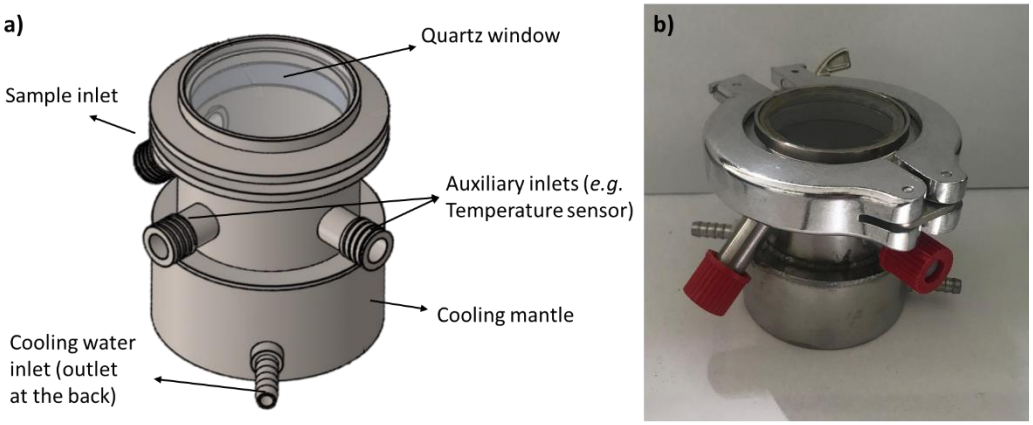

Figure A4.1: a) Schematic representation and b) image of custom-made batch reactor for photocatalytic hydrogen evolution reaction. Light illuminated from top.

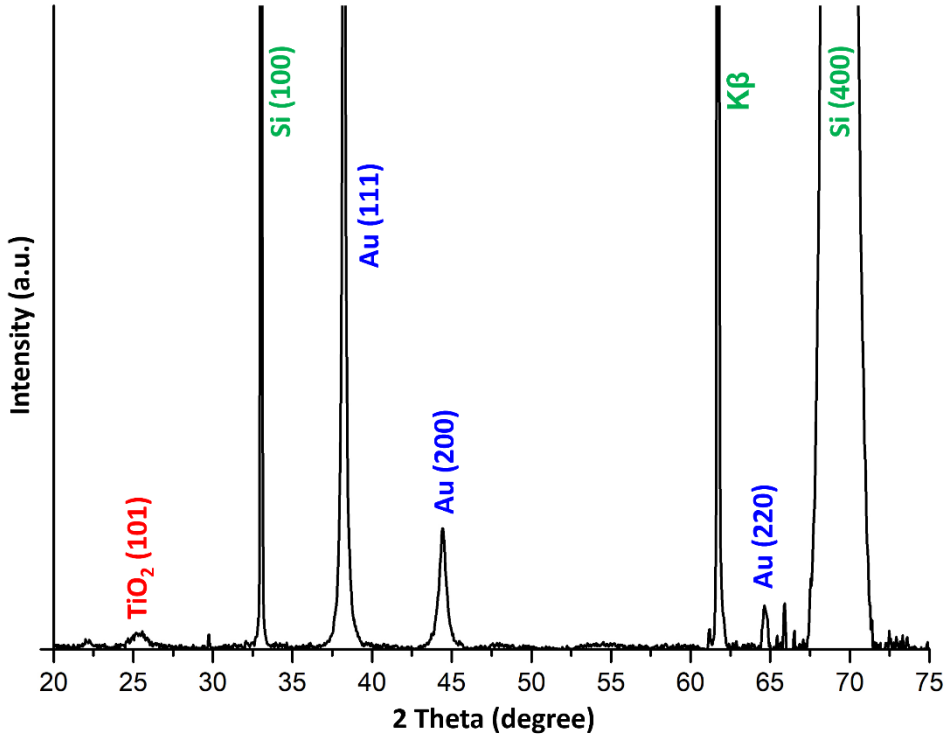

Figure A4.2: XRD pattern of Au4 showing reflections from Anatase phase of TiO_2, Au and the supporting Si wafer.

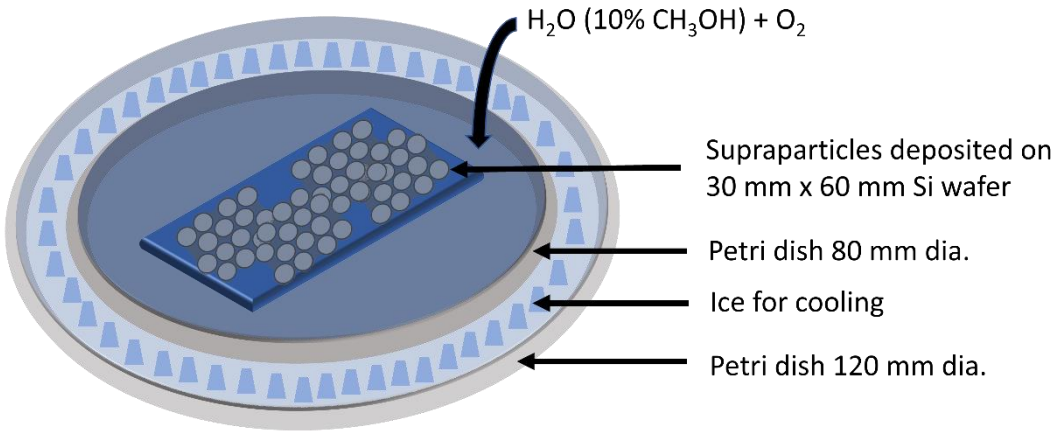

Figure A5.1: Schematic representation of setup for hydrogen peroxide generation. Light illuminated from top.

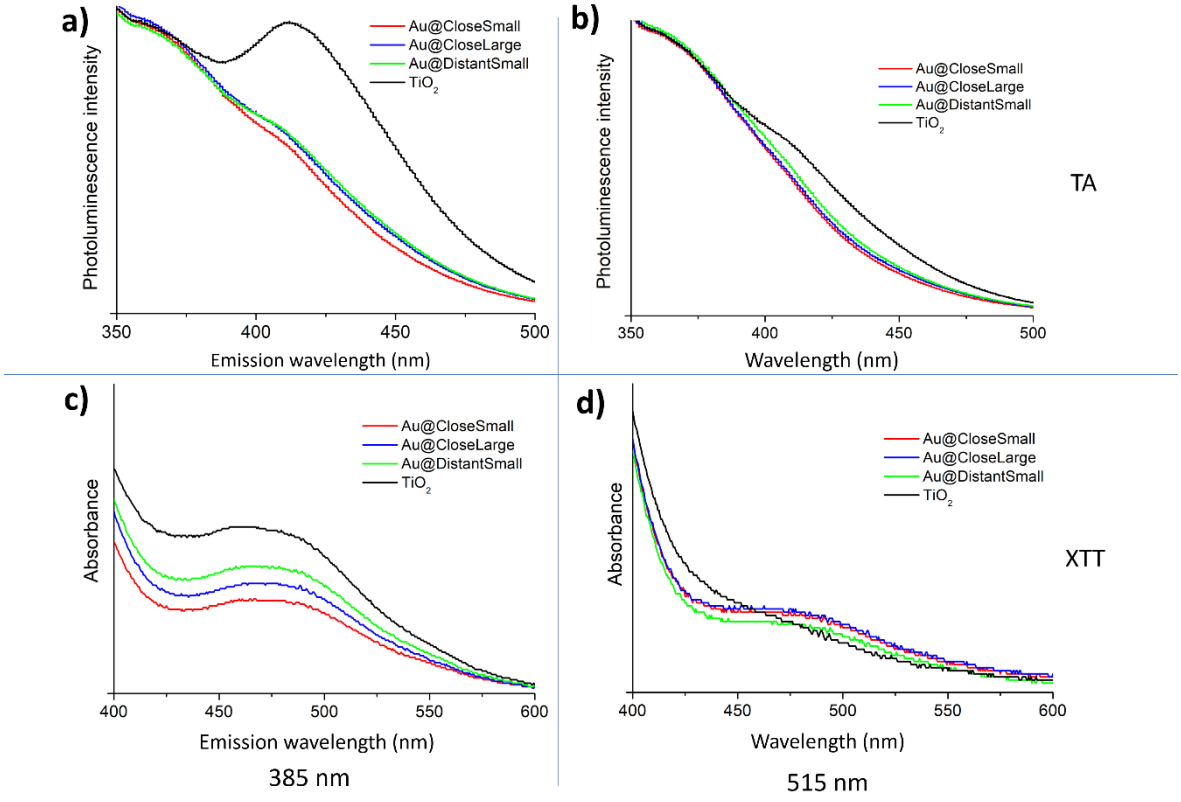

Figure A5.2: a-b) Photoluminescence spectra of conversion of terephthalic acid to 2-hydroxyterephthalic acid under UV (385 nm) and green (515 nm) light illumination on all the Au-TiO_2 composites. b) UV-Vis absorption spectra of conversion of XTT to formazan under UV (385 nm) and green (515 nm) light illumination on all the Au-TiO_2 composites.

Curriculum Vitae

Personal information

Name: Rajeshreddy Ninakanti
Address: Prins Boudewijnlaan 319, 16, Edegem 2650, Belgium
E-mail (private): rajesh.17891@gmail.com

Education

2020-2024 - PhD in Bioscience Engineering, University of Antwerp, Belgium
2017-2019 Master in Environmental Science and Engineering, IIT Dhanbad, India
2009-2013 Bachelor in Civil Engineering, Pune University, India

Publications during PhD

- Raes, A., **Ninakanti, R.**, Van den Bergh, L., Borah, R., Van Doorslaer, S., & Verbruggen, S. W. (2023). Black titania by sonochemistry: A critical evaluation of existing methods. Ultrasonics Sonochemistry, 100, 106601.
- Zhang, K., Wang, J., **Ninakanti, R**., & Verbruggen, S. W. (2023). Solvothermal synthesis of mesoporous TiO_2 with tunable surface area, crystal size and surface hydroxylation for efficient photocatalytic acetaldehyde degradation. Chemical Engineering Journal, 474, 145188.
- Raj, A. K., Minja, A. C., **Ninakanti, R.,** Van Hal, M., Dingenen, F., Borah, R., & Verbruggen, S. W. (2023). Impact of soot deposits on waste gas-to-electricity conversion in a TiO_2/WO_3 based photofuel cell. Chemical Engineering Journal, 470, 144390.
- Volders, J., Elen, K., Raes, A., **Ninakanti, R.,** Kelchtermans, A. S., Sastre, F., ... & Van Bael, M. K. (2022). Sunlight-powered reverse water gas shift reaction catalysed by plasmonic Au/TiO_2 nanocatalysts: Effects of Au particle size on the activity and selectivity. *Nanomaterials*, *12*(23), 4153.
- **Ninakanti, R.,** Dingenen, F., Borah, R., Peeters, H., & Verbruggen, S. W. (2022). Plasmonic hybrid nanostructures in photocatalysis: Structures, mechanisms, and applications. Topics in Current Chemistry, 380(5), 40.
- Dingenen, F., Borah, R., **Ninakanti, R.,** & Verbruggen, S. W. (2022). Probing oxygen activation on plasmonic photocatalysts. *Frontiers in Chemistry*, *10*, 988542.
- Borah, R., Smets, J., **Ninakanti, R.,** Tietze, M. L., Ameloot, R., Chigrin, D. N., ... & Verbruggen, S. W. (2022). Self-assembled ligand-capped plasmonic Au nanoparticle films in the Kretschmann configuration for sensing of volatile organic compounds. ACS Applied Nano Materials, 5(8), 11494-11505.
- Borah, R., **Ninakanti, R.,** Bals, S., & Verbruggen, S. W. (2022). Plasmon resonance of gold and silver nanoparticle arrays in the Kretschmann (attenuated total reflectance) vs. direct incidence configuration. Scientific Reports, 12(1), 15738.
- Yildiz, A., Chouki, T., Atli, A., Harb, M., Verbruggen, S. W., **Ninakanti, R.,** & Emin, S. (2021). Efficient iron phosphide catalyst as a counter electrode in dye-sensitized solar cells. ACS Applied Energy Materials, 4(10), 10618-10626.
- Borah, R., **Ninakanti, R.,** Nuyts, G., Peeters, H., Pedrazo-Tardajos, A., Nuti, S., ... & Verbruggen, S. W. (2021). Selectivity in the Ligand Functionalization of Photocatalytic

Metal Oxide Nanoparticles for Phase Transfer and Self-Assembly Applications. Chemistry–A European Journal, 27(35), 9011-9021.

Conferences attended

Oral presentations

- Plasmon-enhanced photocatalytic activity of Au@TiO_2 core-shell nanoparticles: effect of shell thickness, 8th International Conference on Semiconductor Photochemistry (SP8), September 2023, Strasbourg, France.
- Effect of tunable shell thickness on the plasmon-enhanced photocatalytic activity of Au@TiO_2 core-shell nanoparticles, 15th European Congress on Catalysis (EuropaCat) 2023, August 2023, Prague, Czech Republic.
- Plasmon-enhanced photocatalytic activity of Au@TiO_2 core-shell nanoparticles: effect of shell thickness, Netherlands Catalysis and Chemistry Conference (NCCC), March 2023, Noordwijkerhout, Netherlands.
- Nanoparticle clusters and core-shell nanoparticles for plasmon-enhanced self-cleaning surfaces, National Symposium for Applied Biological Sciences (NSABS), July 2022, Antwerp, Belgium

Poster presentations

- Effect of tunable shell thickness on the plasmon-enhanced photocatalytic activity of Au@TiO_2 core-shell nanoparticles, Netherlands Catalysis and Chemistry Conference (NCCC), May 2022, Noordwijkerhout, Netherlands.
- Plasmon-enhanced photocatalytic activity of Au@TiO_2 core-shell nanoparticles: effect of shell thickness, CRF-chemCYS 2022, October 2022, Blankenberge, Belgium.

Supervision of 2 Bachelor thesis, 2 intern students and 4 summer job students

Bibliography

1. Artioli G, Angelini I, Polla A (2008) Crystals and phase transitions in protohistoric glass materials. Phase Transitions 81:233–252. https://doi.org/10.1080/01411590701514409
2. Bobin O, Schvoerer M, Ney C, et al (2003) The role of copper and silver in the colouration of metallic luster decorations (Tunisia, 9th century; Mesopotamia, 10th century; Sicily, 16th century): A first approach. Color Res Appl 28:352–359. https://doi.org/https://doi.org/10.1002/col.10183
3. Freestone I, Meeks N, Sax M, Higgitt C (2007) The Lycurgus Cup — A Roman nanotechnology. Gold Bull 40:270–277. https://doi.org/10.1007/BF03215599
4. Verbruggen SW (2015) TiO_2 photocatalysis for the degradation of pollutants in gas phase: From morphological design to plasmonic enhancement. J Photochem Photobiol C Photochem Rev 24:64–82. https://doi.org/https://doi.org/10.1016/j.jphotochemrev.2015.07.001
5. Linic S, Christopher P, Ingram DB (2011) Plasmonic-metal nanostructures for efficient conversion of solar to chemical energy. Nat Mater 10:911–921
6. Atwater HA, Polman A (2010) Plasmonics for improved photovoltaic devices. Nat Mater 9:205
7. Anker JN, Hall WP, Lyandres O, et al (2009) Biosensing with plasmonic nanosensors. In: Nanoscience and Technology. Co-Published with Macmillan Publishers Ltd, UK, pp 308–319
8. Barbillon G (2020) Latest Novelties on Plasmonic and Non-Plasmonic Nanomaterials for SERS Sensing. Nanomater. 10
9. Wang D, Pillai SC, Ho S-H, et al (2018) Plasmonic-based nanomaterials for environmental remediation. Appl Catal B Environ 237:721–741. https://doi.org/https://doi.org/10.1016/j.apcatb.2018.05.094
10. Statista (2021) Annual global CO_2 emissions from 2000 to 2019
11. Fuel Cells and Hydrogen Joint Undertaking (FCH) (2019) Hydrogen Roadmap Europe - a Sustainable Pathway for the European Energy Transition
12. Sharma G, Kumar A, Sharma S, et al (2019) Novel development of nanoparticles to bimetallic nanoparticles and their composites: A review. J King Saud Univ - Sci 31:257–269. https://doi.org/https://doi.org/10.1016/j.jksus.2017.06.012
13. Major KJ, De C, Obare SO (2009) Recent Advances in the Synthesis of Plasmonic Bimetallic Nanoparticles. Plasmonics 4:61–78. https://doi.org/10.1007/s11468-008-9077-8
14. Kavitha R, Kumar SG (2020) Review on bimetallic-deposited TiO_2: preparation methods, charge carrier transfer pathways and photocatalytic applications. Chem Pap 74:717–756. https://doi.org/10.1007/s11696-019-00995-4
15. Sytwu K, Vadai M, Dionne JA (2019) Bimetallic nanostructures: combining plasmonic and catalytic metals for photocatalysis. Adv Phys X 4:1619480. https://doi.org/10.1080/23746149.2019.1619480

16. Srinoi P, Chen Y-T, Vittur V, et al (2018) Bimetallic Nanoparticles: Enhanced Magnetic and Optical Properties for Emerging Biological Applications. Appl. Sci. 8

17. Loos M (2015) Chapter 1 - Nanoscience and Nanotechnology. In: Loos MBT-CNRC (ed). William Andrew Publishing, Oxford, pp 1–36

18. Ninakanti R, Dingenen F, Borah R, et al (2022) Plasmonic Hybrid Nanostructures in Photocatalysis: Structures, Mechanisms, and Applications. Top Curr Chem 380:40. https://doi.org/10.1007/s41061-022-00390-w

19. Chen T, Rodionov VO (2016) Controllable Catalysis with Nanoparticles: Bimetallic Alloy Systems and Surface Adsorbates. ACS Catal 6:4025–4033. https://doi.org/10.1021/acscatal.6b00714

20. Ahn J, Kim J, Qin D (2020) Orthogonal deposition of Au on different facets of Ag cuboctahedra for the fabrication of nanoboxes with complementary surfaces. Nanoscale 12:372–379. https://doi.org/10.1039/C9NR08420G

21. Gloag L, Benedetti TM, Cheong S, et al (2018) Three-Dimensional Branched and Faceted Gold–Ruthenium Nanoparticles: Using Nanostructure to Improve Stability in Oxygen Evolution Electrocatalysis. Angew Chemie Int Ed 57:10241–10245. https://doi.org/https://doi.org/10.1002/anie.201806300

22. Zhang Q, Kusada K, Wu D, et al (2018) Selective control of fcc and hcp crystal structures in Au–Ru solid-solution alloy nanoparticles. Nat Commun 9:510. https://doi.org/10.1038/s41467-018-02933-6

23. Asapu R, Claes N, Bals S, et al (2017) Silver-polymer core-shell nanoparticles for ultrastable plasmon-enhanced photocatalysis. Appl Catal B Environ 200:31–38. https://doi.org/10.1016/j.apcatb.2016.06.062

24. Ni Y, Kan C, He L, et al (2019) Alloyed Au-Ag nanorods with desired plasmonic properties and stability in harsh environments. Photonics Res 7:558–565. https://doi.org/10.1364/PRJ.7.000558

25. Blommaerts N, Vanrompay H, Nuti S, et al (2019) Unravelling structural information of Turkevich synthesized plasmonic gold-silver bimetallic nanoparticles. Antwerp

26. Davey WP (1925) Precision Measurements of the Lattice Constants of Twelve Common Metals. Phys Rev 25:753–761. https://doi.org/10.1103/PhysRev.25.753

27. Combettes S, Lam J, Benzo P, et al (2020) How interface properties control the equilibrium shape of core–shell Fe–Au and Fe–Ag nanoparticles. Nanoscale 12:18079–18090. https://doi.org/10.1039/D0NR04425C

28. Lohse SE, Burrows ND, Scarabelli L, et al (2014) Anisotropic Noble Metal Nanocrystal Growth: The Role of Halides. Chem Mater 26:34–43. https://doi.org/10.1021/cm402384j

29. Jacobson CR, Solti D, Renard D, et al (2020) Shining Light on Aluminum Nanoparticle Synthesis. Acc Chem Res 53:2020–2030. https://doi.org/10.1021/acs.accounts.0c00419

30. Ringe E (2020) Shapes, Plasmonic Properties, and Reactivity of Magnesium Nanoparticles. J Phys Chem C 124:15665–15679. https://doi.org/10.1021/acs.jpcc.0c03871

31. Thota S, Wang Y, Zhao J (2018) Colloidal Au–Cu alloy nanoparticles: synthesis, optical properties and applications. Mater Chem Front 2:1074–1089.

https://doi.org/10.1039/C7QM00538E

32. Zhang J, Yu Y, Zhang B (2020) Synthesis and characterization of size controlled alloy nanoparticles. Phys Sci Rev 5:. https://doi.org/doi:10.1515/psr-2018-0046

33. Zhao H, Qi W, Zhou X, et al (2018) Composition-controlled synthesis of platinum and palladium nanoalloys as highly active electrocatalysts for methanol oxidation. Chinese J Catal 39:342–349. https://doi.org/https://doi.org/10.1016/S1872-2067(18)63020-7

34. Leteba GM, Lang CI (2013) Synthesis of Bimetallic Platinum Nanoparticles for Biosensors. Sensors 13

35. Gu J, Lan G, Jiang Y, et al (2015) Shaped Pt-Ni nanocrystals with an ultrathin Pt-enriched shell derived from one-pot hydrothermal synthesis as active electrocatalysts for oxygen reduction. Nano Res 8:1480–1496. https://doi.org/10.1007/s12274-014-0632-7

36. Xia Y, Gilroy KD, Peng H-C, Xia X (2017) Seed-Mediated Growth of Colloidal Metal Nanocrystals. Angew Chemie Int Ed 56:60–95. https://doi.org/https://doi.org/10.1002/anie.201604731

37. Emam HE (2019) Arabic Gum as Bio-Synthesizer for Ag–Au Bimetallic Nanocomposite Using Seed-Mediated Growth Technique and Its Biological Efficacy. J Polym Environ 27:210–223. https://doi.org/10.1007/s10924-018-1331-3

38. Dong P, Wu Y, Guo W, Di J (2013) Plasmonic Biosensor Based on Triangular Au/Ag and Au/Ag/Au Core/Shell Nanoprisms onto Indium Tin Oxide Glass. Plasmonics 8:1577–1583. https://doi.org/10.1007/s11468-013-9574-2

39. Sutter E, Zhang B, Sutter P (2020) DNA-Mediated Three-Dimensional Assembly of Hollow Au–Ag Alloy Nanocages as Plasmonic Crystals. ACS Appl Nano Mater 3:8068–8074. https://doi.org/10.1021/acsanm.0c01528

40. Yue X, Hou J, Zhao H, et al (2020) Au–Ag alloy nanoparticles with tunable cavity for plasmon-enhanced photocatalytic H2 evolution. J Energy Chem 49:1–7. https://doi.org/10.1016/j.jechem.2020.01.005

41. Sui N, Yue R, Wang Y, et al (2019) Boosting methanol oxidation reaction with Au@AgPt yolk-shell nanoparticles. J Alloys Compd 790:792–798. https://doi.org/https://doi.org/10.1016/j.jallcom.2019.03.196

42. Kamat GA, Yan C, Osowiecki WT, et al (2020) Self-Limiting Shell Formation in Cu@Ag Core–Shell Nanocrystals during Galvanic Replacement. J Phys Chem Lett 11:5318–5323. https://doi.org/10.1021/acs.jpclett.0c01551

43. Reboul J, Li ZY, Yuan J, et al (2021) Synthesis of small Ni-core–Au-shell catalytic nanoparticles on TiO2 by galvanic replacement reaction. Nanoscale Adv 3:823–835. https://doi.org/10.1039/D0NA00617C

44. Wang Z, Ai B, Wang Y, et al (2019) Hierarchical Control of Plasmonic Nanochemistry in Microreactor. ACS Appl Mater Interfaces 11:35429–35437. https://doi.org/10.1021/acsami.9b10917

45. Sebastian V, Smith CD, Jensen KF (2016) Shape-controlled continuous synthesis of metal nanostructures. Nanoscale 8:7534–7543. https://doi.org/10.1039/C5NR08531D

46. Chen P-C, Liu G, Zhou Y, et al (2015) Tip-Directed Synthesis of Multimetallic Nanoparticles.

J Am Chem Soc 137:9167–9173. https://doi.org/10.1021/jacs.5b05139

47. Neumeister A, Jakobi J, Rehbock C, et al (2014) Monophasic ligand-free alloy nanoparticle synthesis determinants during pulsed laser ablation of bulk alloy and consolidated microparticles in water. Phys Chem Chem Phys 16:23671–23678. https://doi.org/10.1039/C4CP03316G

48. Prymak O, Jakobi J, Rehbock C, et al (2018) Crystallographic characterization of laser-generated, polymer-stabilized 4 nm silver-gold alloyed nanoparticles. Mater Chem Phys 207:442–450. https://doi.org/https://doi.org/10.1016/j.matchemphys.2017.12.080

49. Vegard L (1921) Die Konstitution der Mischkristalle und die Raumfüllung der Atome. Zeitschrift für Phys 5:17–26. https://doi.org/10.1007/BF01349680

50. Petkov V, Shastri S, Shan S, et al (2013) Resolving Atomic Ordering Differences in Group 11 Nanosized Metals and Binary Alloy Catalysts by Resonant High-Energy X-ray Diffraction and Computer Simulations. J Phys Chem C 117:22131–22141. https://doi.org/10.1021/jp408017v

51. Bozzolo G, Garcés JE, Derry GN (2007) Atomistic modeling of segregation and bulk ordering in Ag–Au alloys. Surf Sci 601:2038–2046. https://doi.org/https://doi.org/10.1016/j.susc.2007.02.035

52. Nguyen CM, Frias Batista LM, John MG, et al (2021) Mechanism of Gold–Silver Alloy Nanoparticle Formation by Laser Coreduction of Gold and Silver Ions in Solution. J Phys Chem B 125:907–917. https://doi.org/10.1021/acs.jpcb.0c10096

53. Zhang D, Gökce B, Barcikowski S (2017) Laser Synthesis and Processing of Colloids: Fundamentals and Applications. Chem Rev 117:3990–4103. https://doi.org/10.1021/acs.chemrev.6b00468

54. Liao W, Lan S, Gao L, et al (2017) Nanocrystalline high-entropy alloy (CoCrFeNiAl0.3) thin-film coating by magnetron sputtering. Thin Solid Films 638:383–388. https://doi.org/https://doi.org/10.1016/j.tsf.2017.08.006

55. Li B, Huang L, Zhou M, et al (2014) Preparation and spectral analysis of gold nanoparticles using magnetron sputtering and thermal annealing. J Wuhan Univ Technol Sci Ed 29:651–655. https://doi.org/10.1007/s11595-014-0973-9

56. Atef N, Emara SS, Eissa DS, et al (2021) Well-dispersed Au nanoparticles prepared via magnetron sputtering on TiO_2 nanotubes with unprecedentedly high activity for water splitting. Electrochem Sci Adv 1:e2000004. https://doi.org/https://doi.org/10.1002/elsa.202000004

57. Sun L, Yuan G, Gao L, et al (2021) Chemical vapour deposition. Nat Rev Methods Prim 1:5. https://doi.org/10.1038/s43586-020-00005-y

58. HARVEY E, GHANTASALA M (2006) 12 - Nanofabrication. In: Hannink RHJ, Hill AJBT-NC of M (eds). Woodhead Publishing, pp 303–330

59. Bakrania SD, Rathore GK, Wooldridge MS (2009) An investigation of the thermal decomposition of gold acetate. J Therm Anal Calorim 95:117–122. https://doi.org/10.1007/s10973-008-9173-1

60. Hirayama Y, Takagi K (2019) Evaluation of compositional homogeneity of Fe-Co alloy nanoparticles prepared by thermal plasma synthesis. J Alloys Compd 792:594–598.

https://doi.org/https://doi.org/10.1016/j.jallcom.2019.04.083

61. Verbruggen SW, Keulemans M, Goris B, et al (2016) Plasmonic 'rainbow' photocatalyst with broadband solar light response for environmental applications. Appl Catal B Environ 188:147–153. https://doi.org/https://doi.org/10.1016/j.apcatb.2016.02.002

62. Etchegoin PG, Le Ru EC, Meyer M (2006) An analytic model for the optical properties of gold. J Chem Phys 125:164705. https://doi.org/10.1063/1.2360270

63. Balamurugan B, Maruyama T (2005) Evidence of an enhanced interband absorption in Au nanoparticles: Size-dependent electronic structure and optical properties. Appl Phys Lett 87:143105. https://doi.org/10.1063/1.2077834

64. Kolwas K, Derkachova A (2020) Impact of the Interband Transitions in Gold and Silver on the Dynamics of Propagating and Localized Surface Plasmons. Nanomater. 10

65. Borah R, Verbruggen SW (2020) Silver–Gold Bimetallic Alloy versus Core–Shell Nanoparticles: Implications for Plasmonic Enhancement and Photothermal Applications. J Phys Chem C 124:12081–12094. https://doi.org/10.1021/acs.jpcc.0c02630

66. Samal AK, Polavarapu L, Rodal-Cedeira S, et al (2013) Size Tunable Au@Ag Core–Shell Nanoparticles: Synthesis and Surface-Enhanced Raman Scattering Properties. Langmuir 29:15076–15082. https://doi.org/10.1021/la403707j

67. Boltersdorf J, Leff AC, Forcherio GT, Baker DR (2021) Plasmonic Au–Pd Bimetallic Nanocatalysts for Hot-Carrier-Enhanced Photocatalytic and Electrochemical Ethanol Oxidation. Cryst. 11

68. Ponzellini P, Giovannini G, Cattarin S, et al (2019) Metallic Nanoporous Aluminum–Magnesium Alloy for UV-Enhanced Spectroscopy. J Phys Chem C 123:20287–20296. https://doi.org/10.1021/acs.jpcc.9b04230

69. Pujari A, Thomas T (2021) Aluminium nanoparticles alloyed with other earth-abundant plasmonic metals for light trapping in thin-film a-Si solar cells. Sustain Mater Technol 28:e00250. https://doi.org/https://doi.org/10.1016/j.susmat.2021.e00250

70. Kim D, Resasco J, Yu Y, et al (2014) Synergistic geometric and electronic effects for electrochemical reduction of carbon dioxide using gold–copper bimetallic nanoparticles. Nat Commun 5:4948. https://doi.org/10.1038/ncomms5948

71. Liu Y, Walker ARH (2010) Monodisperse Gold–Copper Bimetallic Nanocubes: Facile One-Step Synthesis with Controllable Size and Composition. Angew Chemie Int Ed 49:6781–6785. https://doi.org/https://doi.org/10.1002/anie.201001931

72. Henkel A, Jakab A, Brunklaus G, Sönnichsen C (2009) Tuning Plasmonic Properties by Alloying Copper into Gold Nanorods. J Phys Chem C 113:2200–2204. https://doi.org/10.1021/jp810433e

73. De Marchi S, Núñez-Sánchez S, Bodelón G, et al (2020) Pd nanoparticles as a plasmonic material: synthesis, optical properties and applications. Nanoscale 12:23424–23443. https://doi.org/10.1039/D0NR06270G

74. Sugawa K, Tahara H, Yamashita A, et al (2015) Refractive Index Susceptibility of the Plasmonic Palladium Nanoparticle: Potential as the Third Plasmonic Sensing Material. ACS Nano 9:1895–1904. https://doi.org/10.1021/nn506800a

75. Cortie MB, McDonagh AM (2011) Synthesis and Optical Properties of Hybrid and Alloy Plasmonic Nanoparticles. Chem Rev 111:3713–3735. https://doi.org/10.1021/cr1002529

76. Peng Z, Yang H (2008) Ag–Pt alloy nanoparticles with the compositions in the miscibility gap. J Solid State Chem 181:1546–1551. https://doi.org/https://doi.org/10.1016/j.jssc.2008.03.013

77. Zhu X, Guo Q, Sun Y, et al (2019) Optimising surface d charge of AuPd nanoalloy catalysts for enhanced catalytic activity. Nat Commun 10:1428. https://doi.org/10.1038/s41467-019-09421-5

78. Valenti M, Venugopal A, Tordera D, et al (2017) Hot Carrier Generation and Extraction of Plasmonic Alloy Nanoparticles. ACS Photonics 4:1146–1152. https://doi.org/10.1021/acsphotonics.6b01048

79. Kadkhodazadeh S, Nugroho FAA, Langhammer C, et al (2019) Optical Property–Composition Correlation in Noble Metal Alloy Nanoparticles Studied with EELS. ACS Photonics 6:779–786. https://doi.org/10.1021/acsphotonics.8b01791

80. Lee C, Park Y, Park JY (2019) Hot electrons generated by intraband and interband transition detected using a plasmonic Cu/TiO_2 nanodiode. RSC Adv 9:18371–18376. https://doi.org/10.1039/C9RA02601K

81. Keast VJ, Barnett RL, Cortie MB (2014) First principles calculations of the optical and plasmonic response of Au alloys and intermetallic compounds. J Phys Condens Matter 26:305501. https://doi.org/10.1088/0953-8984/26/30/305501

82. Rossi TP, Erhart P, Kuisma M (2020) Hot-Carrier Generation in Plasmonic Nanoparticles: The Importance of Atomic Structure. ACS Nano 14:9963–9971. https://doi.org/10.1021/acsnano.0c03004

83. Ma J, Zhang X, Gao S (2021) Tunable electron and hole injection channels at plasmonic Al–TiO_2 interfaces. Nanoscale 13:14073–14080. https://doi.org/10.1039/D1NR03697A

84. Huang H, Zhang L, Lv Z, et al (2016) Unraveling Surface Plasmon Decay in Core–Shell Nanostructures toward Broadband Light-Driven Catalytic Organic Synthesis. J Am Chem Soc 138:6822–6828. https://doi.org/10.1021/jacs.6b02532

85. van der Hoeven JES, Jelic J, Olthof LA, et al (2021) Unlocking synergy in bimetallic catalysts by core–shell design. Nat Mater. https://doi.org/10.1038/s41563-021-00996-3

86. Asapu R, Claes N, Ciocarlan R-G, et al (2019) Electron Transfer and Near-Field Mechanisms in Plasmonic Gold-Nanoparticle-Modified TiO_2 Photocatalytic Systems. ACS Appl Nano Mater 2:4067–4074. https://doi.org/10.1021/acsanm.9b00485

87. Pougin A, Dodekatos G, Dilla M, et al (2018) Au@TiO_2 Core–Shell Composites for the Photocatalytic Reduction of CO_2. Chem – A Eur J 24:12416–12425. https://doi.org/https://doi.org/10.1002/chem.201801796

88. Hong D, Lyu L-M, Koga K, et al (2019) Plasmonic Ag@TiO_2 Core–Shell Nanoparticles for Enhanced CO2 Photoconversion to CH4. ACS Sustain Chem Eng 7:18955–18964. https://doi.org/10.1021/acssuschemeng.9b04345

89. Mondal I, Gonuguntla S, Pal U (2019) Photoinduced Fabrication of Cu/TiO_2 Core–Shell Heterostructures Derived from Cu-MOF for Solar Hydrogen Generation: The Size of the Cu Nanoparticle Matters. J Phys Chem C 123:26073–26081.

https://doi.org/10.1021/acs.jpcc.9b07171

90. Prodan E, Radloff C, Halas NJ, Nordlander P (2003) A Hybridization Model for the Plasmon Response of Complex Nanostructures. Science (80-) 302:419 LP – 422. https://doi.org/10.1126/science.1089171

91. Kamimura S, Yamashita S, Abe S, et al (2017) Effect of core@shell (Au@Ag) nanostructure on surface plasmon-induced photocatalytic activity under visible light irradiation. Appl Catal B Environ 211:11–17. https://doi.org/https://doi.org/10.1016/j.apcatb.2017.04.028

92. Wang Y, Zhang Q, Wang Y, et al (2021) Ultrastable Plasmonic Cu-Based Core–Shell Nanoparticles. Chem Mater 33:695–705. https://doi.org/10.1021/acs.chemmater.0c04059

93. Joplin A, Hosseini Jebeli SA, Sung E, et al (2017) Correlated Absorption and Scattering Spectroscopy of Individual Platinum-Decorated Gold Nanorods Reveals Strong Excitation Enhancement in the Nonplasmonic Metal. ACS Nano 11:12346–12357. https://doi.org/10.1021/acsnano.7b06239

94. Song HM, Moosa BA, Khashab NM (2012) Water-dispersable hybrid Au–Pd nanoparticles as catalysts in ethanol oxidation, aqueous phase Suzuki–Miyaura and Heck reactions. J Mater Chem 22:15953–15959. https://doi.org/10.1039/C2JM32702C

95. Wang F, Li C, Chen H, et al (2013) Plasmonic Harvesting of Light Energy for Suzuki Coupling Reactions Plasmonic Harvesting of Light Energy for Suzuki Coupling Re- actions. J Am Chem Soc 135:5588–5601. https://doi.org/10.1021/ja310501y

96. Lai H, Xiao W, Wang Y, et al (2021) Plasmon-induced carrier separation boosts high-selective photocatalytic CO_2 reduction on dagger-axe-like Cu@Co core–shell bimetal. Chem Eng J 417:129295. https://doi.org/https://doi.org/10.1016/j.cej.2021.129295

97. Spitaleri L, Nicotra G, Zimbone M, et al (2019) Fast and Efficient Sun Light Photocatalytic Activity of Au_ZnO Core–Shell Nanoparticles Prepared by a One-Pot Synthesis. ACS Omega 4:15061–15066. https://doi.org/10.1021/acsomega.9b01850

98. Huang J, He Y, Wang L, et al (2017) Bifunctional Au@TiO_2 core–shell nanoparticle films for clean water generation by photocatalysis and solar evaporation. Energy Convers Manag 132:452–459. https://doi.org/https://doi.org/10.1016/j.enconman.2016.11.053

99. Hartman T, Weckhuysen BM (2018) Thermally Stable TiO_2- and SiO_2-Shell-Isolated Au Nanoparticles for In Situ Plasmon-Enhanced Raman Spectroscopy of Hydrogenation Catalysts. Chem – A Eur J 24:3733–3741. https://doi.org/https://doi.org/10.1002/chem.201704370

100. Kamarudheen R, Kumari G, Baldi A (2020) Plasmon-driven synthesis of individual metal@semiconductor core@shell nanoparticles. Nat Commun 11:3957. https://doi.org/10.1038/s41467-020-17789-y

101. Eom H, Jung J-Y, Shin Y, et al (2014) Strong localized surface plasmon resonance effects of Ag/TiO2 core–shell nanowire arrays in UV and visible light for photocatalytic activity. Nanoscale 6:226–234. https://doi.org/10.1039/C3NR04388F

102. Seong S, Park I-S, Jung YC, et al (2019) Synthesis of Ag-ZnO core-shell nanoparticles with enhanced photocatalytic activity through atomic layer deposition. Mater Des 177:107831. https://doi.org/https://doi.org/10.1016/j.matdes.2019.107831

103. Liz-Marzán LM, Giersig M, Mulvaney P (1996) Synthesis of Nanosized Gold−Silica

Core−Shell Particles. Langmuir 12:4329–4335. https://doi.org/10.1021/la9601871

104. Huang MH, Rej S, Chiu C-Y (2015) Facet-Dependent Optical Properties Revealed through Investigation of Polyhedral Au–Cu_2O and Bimetallic Core–Shell Nanocrystals. Small 11:2716–2726. https://doi.org/https://doi.org/10.1002/smll.201403542

105. Knight MW, King NS, Liu L, et al (2014) Aluminum for Plasmonics. ACS Nano 8:834–840. https://doi.org/10.1021/nn405495q

106. Li A, Zhang P, Chang X, et al (2015) Gold Nanorod@TiO_2 Yolk-Shell Nanostructures for Visible-Light-Driven Photocatalytic Oxidation of Benzyl Alcohol. Small 11:1892–1899. https://doi.org/https://doi.org/10.1002/smll.201403058

107. Ma X, Zhao K, Tang H, et al (2014) New Insight into the Role of Gold Nanoparticles in Au@CdS Core–Shell Nanostructures for Hydrogen Evolution. Small 10:4664–4670. https://doi.org/https://doi.org/10.1002/smll.201401494

108. Ma L, Chen Y-L, Yang D-J, et al (2020) Multi-interfacial plasmon coupling in multigap (Au/AgAu)@CdS core–shell hybrids for efficient photocatalytic hydrogen generation. Nanoscale 12:4383–4392. https://doi.org/10.1039/C9NR09696E

109. Lee C, Shin K, Lee YJ, et al (2018) Effects of shell thickness on Ag-Cu_2O core-shell nanoparticles with bumpy structures for enhancing photocatalytic activity and stability. Catal Today 303:313–319. https://doi.org/https://doi.org/10.1016/j.cattod.2017.08.016

110. Bai X, Zong R, Li C, et al (2014) Enhancement of visible photocatalytic activity via Ag@C3N4 core–shell plasmonic composite. Appl Catal B Environ 147:82–91. https://doi.org/https://doi.org/10.1016/j.apcatb.2013.08.007

111. Ning X, Lu G (2020) Photocorrosion inhibition of CdS-based catalysts for photocatalytic overall water splitting. Nanoscale 12:1213–1223. https://doi.org/10.1039/C9NR09183A

112. Monga A, Bathla A, Pal B (2017) A Cu-Au bimetallic co-catalysis for the improved photocatalytic activity of TiO2 under visible light radiation. Sol Energy 155:1403–1410. https://doi.org/https://doi.org/10.1016/j.solener.2017.07.084

113. Li A, Zhu W, Li C, et al (2019) Rational design of yolk–shell nanostructures for photocatalysis. Chem Soc Rev 48:1874–1907. https://doi.org/10.1039/C8CS00711J

114. Sun H, He Q, Zeng S, et al (2017) Controllable growth of Au@TiO_2 yolk–shell nanoparticles and their geometry parameter effects on photocatalytic activity. New J Chem 41:7244–7252. https://doi.org/10.1039/C7NJ01491K

115. Wang Y, Yang C, Chen A, et al (2019) Influence of yolk-shell Au@TiO_2 structure induced photocatalytic activity towards gaseous pollutant degradation under visible light. Appl Catal B Environ 251:57–65. https://doi.org/https://doi.org/10.1016/j.apcatb.2019.03.056

116. Singh R, Bhateria R (2021) Core–shell nanostructures: a simplest two-component system with enhanced properties and multiple applications. Environ Geochem Health 43:2459–2482. https://doi.org/10.1007/s10653-020-00766-1

117. Yang H, Li M, Li S, et al (2020) A critical structured TiO_2 with enhanced photocatalytic activity during the formation of yolk-shell structured TiO_2. J Mater Sci Mater Electron 31:2–9. https://doi.org/10.1007/s10854-018-9986-z

118. Zhao B, Guo X, Zhao W, et al (2017) Facile synthesis of yolk–shell Ni@void@SnO_2(Ni_3Sn_2)

ternary composites via galvanic replacement/Kirkendall effect and their enhanced microwave absorption properties. Nano Res 10:331–343. https://doi.org/10.1007/s12274-016-1295-3

119. Wang W, Efrima S, Regev O (1998) Directing Oleate Stabilized Nanosized Silver Colloids into Organic Phases. Langmuir 14:602–610. https://doi.org/10.1021/la9710177

120. Tzhayik O, Sawant P, Efrima S, et al (2002) Xanthate Capping of Silver, Copper, and Gold Colloids. Langmuir 18:3364–3369. https://doi.org/10.1021/la015653n

121. Turkevich J, Stevenson PC, Hillier J (1951) a Study of the Nucleation and Growth Processes I N the Synthesis of. Discuss Faraday Soc 55:. https://doi.org/10.1039/DF9511100055

122. Verbruggen SW, Keulemans M, Filippousi M, et al (2014) Plasmonic gold–silver alloy on TiO_2 photocatalysts with tunable visible light activity. Appl Catal B Environ 156–157:116–121. https://doi.org/https://doi.org/10.1016/j.apcatb.2014.03.027

123. Cao M, Liu Q, Chen M, et al (2017) Dispersing hydrophilic nanoparticles in nonaqueous solvents with superior long-term stability. RSC Adv 7:25535–25541. https://doi.org/10.1039/C7RA03472E

124. Xing S, Tan LH, Yang M, et al (2009) Highly controlled core/shell structures: tunable conductive polymer shells on gold nanoparticles and nanochains. J Mater Chem 19:3286–3291. https://doi.org/10.1039/B900993K

125. Chen J-Y, Wu H-C, Chiu Y-C, Chen W-C (2014) Plasmon-Enhanced Polymer Photovoltaic Device Performance Using Different Patterned Ag/PVP Electrospun Nanofibers. Adv Energy Mater 4:1301665. https://doi.org/10.1002/aenm.201301665

126. Yu S, Wilson AJ, Heo J, Jain PK (2018) Plasmonic Control of Multi-Electron Transfer and C–C Coupling in Visible-Light-Driven CO_2 Reduction on Au Nanoparticles. Nano Lett 18:2189–2194. https://doi.org/10.1021/acs.nanolett.7b05410

127. Schneider G, Decher G (2004) From Functional Core/Shell Nanoparticles Prepared via Layer-by-Layer Deposition to Empty Nanospheres. Nano Lett 4:1833–1839. https://doi.org/10.1021/nl0490826

128. Schneider G, Decher G (2008) Functional Core/Shell Nanoparticles via Layer-by-Layer Assembly. Investigation of the Experimental Parameters for Controlling Particle Aggregation and for Enhancing Dispersion Stability. Langmuir 24:1778–1789. https://doi.org/10.1021/la7021837

129. Liang L, Lam SH, Ma L, et al (2020) (Gold nanorod core)/(poly(3,4-ethylene-dioxythiophene) shell) nanostructures and their monolayer arrays for plasmonic switching. Nanoscale 12:20684–20692. https://doi.org/10.1039/D0NR05502F

130. Jiang N, Zhuo X, Wang J (2018) Active Plasmonics: Principles, Structures, and Applications. Chem Rev 118:3054–3099. https://doi.org/10.1021/acs.chemrev.7b00252

131. Dingenen F, Blommaerts N, Van Hal M, et al (2021) Layer-by-Layer-Stabilized Plasmonic Gold-Silver Nanoparticles on TiO2: Towards Stable Solar Active Photocatalysts. Nanomater. 11

132. Lisunova M, Mahmoud M, Holland N, et al (2012) The unusual fluorescence intensity enhancement of poly(p-phenyleneethynylene) polymer separated from the silver nanocube surface by H-bonded LbL shells. J Mater Chem 22:16745–16753.

https://doi.org/10.1039/C2JM32450D

133. Borah R, AG KR, Minja AC, Verbruggen SW (2023) A Review on Self-Assembly of Colloidal Nanoparticles into Clusters, Patterns, and Films: Emerging Synthesis Techniques and Applications. Small Methods 7:2201536. https://doi.org/https://doi.org/10.1002/smtd.202201536

134. Manfrinato VR, Zhang L, Su D, et al (2013) Resolution Limits of Electron-Beam Lithography toward the Atomic Scale. Nano Lett 13:1555–1558. https://doi.org/10.1021/nl304715p

135. Hughes RA, Menumerov E, Neretina S (2017) When lithography meets self-assembly: a review of recent advances in the directed assembly of complex metal nanostructures on planar and textured surfaces. Nanotechnology 28:282002. https://doi.org/10.1088/1361-6528/aa77ce

136. Xia H, Su G, Wang D (2013) Size-Dependent Electrostatic Chain Growth of pH-Sensitive Hairy Nanoparticles. Angew Chemie Int Ed 52:3726–3730. https://doi.org/https://doi.org/10.1002/anie.201209304

137. Grzelczak M, Vermant J, Furst EM, Liz-Marzán LM (2010) Directed Self-Assembly of Nanoparticles. ACS Nano 4:3591–3605. https://doi.org/10.1021/nn100869j

138. Zhang Q, Yin X, Zhang C, et al (2022) Self-Assembled Supercrystals Enhance the Photothermal Conversion for Solar Evaporation and Water Purification. Small 18:2202867. https://doi.org/https://doi.org/10.1002/smll.202202867

139. Dey P, Tabish TA, Mosca S, et al (2020) Plasmonic Nanoassemblies: Tentacles Beat Satellites for Boosting Broadband NIR Plasmon Coupling Providing a Novel Candidate for SERS and Photothermal Therapy. Small 16:1906780. https://doi.org/https://doi.org/10.1002/smll.201906780

140. Liu D, Zhou F, Li C, et al (2015) Black Gold: Plasmonic Colloidosomes with Broadband Absorption Self-Assembled from Monodispersed Gold Nanospheres by Using a Reverse Emulsion System. Angew Chemie Int Ed 54:9596–9600. https://doi.org/https://doi.org/10.1002/anie.201503384

141. Zhang D, Tang L, Chen J, et al (2021) Controllable Self-Assembly of SERS Hotspots in Liquid Environment. Langmuir 37:939–948. https://doi.org/10.1021/acs.langmuir.0c03323

142. Gschneidtner TA, Fernandez YAD, Syrenova S, et al (2014) A Versatile Self-Assembly Strategy for the Synthesis of Shape-Selected Colloidal Noble Metal Nanoparticle Heterodimers. Langmuir 30:3041–3050. https://doi.org/10.1021/la5002754

143. Herran M, Juergensen S, Kessens M, et al (2023) Plasmonic bimetallic two-dimensional supercrystals for H_2 generation. Nat Catal 6:1205–1214. https://doi.org/10.1038/s41929-023-01053-9

144. Shi R, Cao Y, Bao Y, et al (2017) Self-Assembled Au/CdSe Nanocrystal Clusters for Plasmon-Mediated Photocatalytic Hydrogen Evolution. Adv Mater 29:1700803. https://doi.org/https://doi.org/10.1002/adma.201700803

145. Lee S, Hwang H, Lee W, et al (2020) Core–Shell Bimetallic Nanoparticle Trimers for Efficient Light-to-Chemical Energy Conversion. ACS Energy Lett 5:3881–3890. https://doi.org/10.1021/acsenergylett.0c02110

146. Huang P, Lin J, Wang S, et al (2013) Photosensitizer-conjugated silica-coated gold

nanoclusters for fluorescence imaging-guided photodynamic therapy. Biomaterials 34:4643–4654. https://doi.org/https://doi.org/10.1016/j.biomaterials.2013.02.063

147. Ma X-C, Dai Y, Yu L, Huang B-B (2016) Energy transfer in plasmonic photocatalytic composites. Light Sci Appl 5:e16017. https://doi.org/10.1038/lsa.2016.17

148. Linsebigler AL, Lu GQ, Yates JT (1995) Photocatalysis on Tio2 Surfaces - Principles, Mechanisms, and Selected Results. Chem Rev 95:735–758

149. Mubeen S, Lee J, Singh N, et al (2013) An autonomous photosynthetic device in which all charge carriers derive from surface plasmons. Nat Nanotechnol 8:247–51. https://doi.org/10.1038/nnano.2013.18

150. Brown L V., Zhao K, King N, et al (2013) Surface-Enhanced Infrared Absorption Using Individual Cross Antennas Tailored to Chemical Moieties. J Am Chem Soc 135:3688–3695. https://doi.org/10.1021/ja312694g

151. Chen X-J, Cabello G, Wu D-Y, Tian Z-Q (2014) Surface-enhanced Raman spectroscopy toward application in plasmonic photocatalysis on metal nanostructures. J Photochem Photobiol C Photochem Rev 21:54–80. https://doi.org/10.1016/j.jphotochemrev.2014.10.003

152. Burda C, Chen X, Narayanan R, El-Sayed MA (2005) Chemistry and Properties of Nanocrystals of Different Shapes. Chem Rev 105:1025–1102. https://doi.org/10.1021/cr030063a

153. Hodak JH, Martini I, Hartland G V. (1998) Spectroscopy and Dynamics of Nanometer-Sized Noble Metal Particles. J Phys Chem B 102:6958–6967. https://doi.org/10.1021/jp9809787

154. Lehmann J, Merschdorf M, Pfeiffer W, et al (2000) Surface Plasmon Dynamics in Silver Nanoparticles Studied by Femtosecond Time-Resolved Photoemission. Phys Rev Lett 85:2921–2924. https://doi.org/10.1103/PhysRevLett.85.2921

155. Kale MJ, Avanesian T, Christopher P (2014) Direct photocatalysis by plasmonic nanostructures. ACS Catal 4:116–128. https://doi.org/10.1021/cs400993w

156. Kim C, Suh BL, Yun H, et al (2017) Surface Plasmon Aided Ethanol Dehydrogenation Using Ag–Ni Binary Nanoparticles. ACS Catal 7:2294–2302. https://doi.org/10.1021/acscatal.7b00411

157. Petek H (2012) Photoexcitation of adsorbates on metal surfaces: One-step or three-step. J Chem Phys 137:091704. https://doi.org/10.1063/1.4746801

158. Mukherjee S, Libisch F, Large N, et al (2013) Hot Electrons Do the Impossible: Plasmon-Induced Dissociation of H_2 on Au. Nano Lett 13:240–247. https://doi.org/10.1021/nl303940z

159. Boerigter C, Campana R, Morabito M, Linic S (2016) Evidence and implications of direct charge excitation as the dominant mechanism in plasmon-mediated photocatalysis. Nat Commun 7:10545. https://doi.org/10.1038/ncomms10545

160. Zhao H, Zheng X, Feng X, Li Y (2018) CO_2 Reduction by Plasmonic Au Nanoparticle-Decorated TiO_2 Photocatalyst with an Ultrathin Al_2O_3 Interlayer. J Phys Chem C 122:18949–18956. https://doi.org/10.1021/acs.jpcc.8b04239

161. Silva CG, Juárez R, Marino T, et al (2011) Influence of excitation wavelength (UV or visible

light) on the photocatalytic activity of titania containing gold nanoparticles for the generation of hydrogen or oxygen from water. J Am Chem Soc 133:595–602. https://doi.org/10.1039/C0CP00917B.(17)

162. Torimoto T, Horibe H, Kameyama T, et al (2011) Plasmon-Enhanced Photocatalytic Activity of Cadmium Sulfide Nanoparticle Immobilized on Silica-Coated Gold Particles. J Phys Chem Lett 2:2057–2062. https://doi.org/10.1021/jz2009049

163. Tu W, Zhou Y, Li H, et al (2015) Au@TiO_2 yolk–shell hollow spheres for plasmon-induced photocatalytic reduction of CO_2 to solar fuel via a local electromagnetic field. Nanoscale 7:14232–14236. https://doi.org/10.1039/C5NR02943K

164. Hirakawa T, Kamat P V (2005) Charge separation and catalytic activity of Ag@TiO_2 core-shell composite clusters under UV-irradiation. J Am Chem Soc 127:3928–34. https://doi.org/10.1021/ja042925a

165. Clavero C (2014) Plasmon-induced hot-electron generation at nanoparticle/metal-oxide interfaces for photovoltaic and photocatalytic devices. Nat Photonics 8:95–103. https://doi.org/10.1038/nphoton.2013.238

166. Subramanian V, Wolf EE, Kamat P V (2004) Catalysis with TiO_2/gold nanocomposites. Effect of metal particle size on the Fermi level equilibration. J Am Chem Soc 126:4943–4950

167. Li J, Cushing SK, Meng F, et al (2015) Plasmon-induced resonance energy transfer for solar energy conversion. Nat Photonics 9:601–607. https://doi.org/10.1038/nphoton.2015.142

168. Ingram DB, Christopher P, Bauer JL, Linic S (2011) Predictive Model for the Design of Plasmonic Metal/Semiconductor Composite Photocatalysts. ACS Catal 1:1441–1447. https://doi.org/10.1021/cs200320h

169. Borah R, Verbruggen SW (2019) Coupled Plasmon Modes in 2D Gold Nanoparticle Clusters and Their Effect on Local Temperature Control. J Phys Chem C 123:. https://doi.org/10.1021/acs.jpcc.9b09048

170. Kreibig U, Vollmer M (1995) Optical Properties of Metal Clusters. Springer-Verlag Berlin Heidelberg

171. Baffou G, Berto P, Bermúdez Ureña E, et al (2013) Photoinduced Heating of Nanoparticle Arrays. ACS Nano 7:6478–6488. https://doi.org/10.1021/nn401924n

172. Baffou G, Quidant R, Girard C (2010) Thermoplasmonics modeling: A Green's function approach. Phys Rev B 82:165424. https://doi.org/10.1103/PhysRevB.82.165424

173. Ni G, Miljkovic N, Ghasemi H, et al (2015) Volumetric solar heating of nanofluids for direct vapor generation. Nano Energy 17:290–301. https://doi.org/https://doi.org/10.1016/j.nanoen.2015.08.021

174. Priebe JB, Karnahl M, Junge H, et al (2013) Water reduction with visible light: synergy between optical transitions and electron transfer in Au-TiO_2 catalysts visualized by in situ EPR spectroscopy. Angew Chem Int Ed Engl 52:11420–4. https://doi.org/10.1002/anie.201306504

175. Caretti I, Keulemans M, Verbruggen SW, et al (2015) Light-Induced Processes in Plasmonic Gold/TiO_2 Photocatalysts Studied by Electron Paramagnetic Resonance. Top Catal 58:776–782. https://doi.org/10.1007/s11244-015-0419-4

176. Awazu K, Fujimaki M, Rockstuhl C, et al (2008) A plasmonic photocatalyst consisting of sliver nanoparticles embedded in titanium dioxide. J Am Chem Soc 130:1676–1680

177. Sun S, Rasskazov IL, Carney PS, et al (2020) Critical Role of Shell in Enhanced Fluorescence of Metal–Dielectric Core–Shell Nanoparticles. J Phys Chem C 124:13365–13373. https://doi.org/10.1021/acs.jpcc.0c03415

178. Asapu R, Ciocarlan R-G, Claes N, et al (2017) Plasmonic Near-Field Localization of Silver Core–Shell Nanoparticle Assemblies via Wet Chemistry Nanogap Engineering. ACS Appl Mater Interfaces 9:41577–41585. https://doi.org/10.1021/acsami.7b13965

179. Dingenen F, Verbruggen SW (2021) Tapping hydrogen fuel from the ocean: A review on photocatalytic, photoelectrochemical and electrolytic splitting of seawater. Renew Sustain Energy Rev 142:110866. https://doi.org/https://doi.org/10.1016/j.rser.2021.110866

180. Seh ZW, Liu S, Low M, et al (2012) Janus Au-TiO_2 Photocatalysts with Strong Localization of Plasmonic Near-Fields for Efficient Visible-Light Hydrogen Generation. Adv Mater 24:2310–2314. https://doi.org/https://doi.org/10.1002/adma.201104241

181. Habisreutinger SN, Schmidt-Mende L, Stolarczyk JK (2013) Photocatalytic Reduction of CO_2 on TiO_2 and Other Semiconductors. Angew Chemie Int Ed 52:7372–7408. https://doi.org/https://doi.org/10.1002/anie.201207199

182. Yang J-L, He Y-L, Ren H, et al (2021) Boosting Photocatalytic Hydrogen Evolution Reaction Using Dual Plasmonic Antennas. ACS Catal 11:5047–5053. https://doi.org/10.1021/acscatal.1c00795

183. Ha E, Lee LYS, Man H-W, et al (2015) Morphology-Controlled Synthesis of Au/Cu_2FeSnS_4 Core–Shell Nanostructures for Plasmon-Enhanced Photocatalytic Hydrogen Generation. ACS Appl Mater Interfaces 7:9072–9077. https://doi.org/10.1021/acsami.5b00715

184. Bhunia K, Chandra M, Khilari S, Pradhan D (2019) Bimetallic PtAu Alloy Nanoparticles-Integrated g-C_3N_4 Hybrid as an Efficient Photocatalyst for Water-to-Hydrogen Conversion. ACS Appl Mater Interfaces 11:478–488. https://doi.org/10.1021/acsami.8b12183

185. Bian H, Nguyen NT, Yoo J, et al (2018) Forming a Highly Active, Homogeneously Alloyed AuPt Co-catalyst Decoration on TiO_2 Nanotubes Directly During Anodic Growth. ACS Appl Mater Interfaces 10:18220–18226. https://doi.org/10.1021/acsami.8b03713

186. Rahul TK, Mohan M, Sandhyarani N (2018) Enhanced Solar Hydrogen Evolution over In Situ Gold–Platinum Bimetallic Nanoparticle-Loaded Ti^{3+} Self-Doped Titania Photocatalysts. ACS Sustain Chem Eng 6:3049–3059. https://doi.org/10.1021/acssuschemeng.7b02898

187. Gesesse GD, Wang C, Chang BK, et al (2020) A soft-chemistry assisted strong metal–support interaction on a designed plasmonic core–shell photocatalyst for enhanced photocatalytic hydrogen production. Nanoscale 12:7011–7023. https://doi.org/10.1039/C9NR09891G

188. Ngaw CK, Xu Q, Tan TTY, et al (2014) A strategy for in-situ synthesis of well-defined core–shell Au@TiO_2 hollow spheres for enhanced photocatalytic hydrogen evolution. Chem Eng J 257:112–121. https://doi.org/https://doi.org/10.1016/j.cej.2014.07.059

189. Hung S-F, Yu Y-C, Suen N-T, et al (2016) The synergistic effect of a well-defined Au@Pt core–shell nanostructure toward photocatalytic hydrogen generation: interface engineering to improve the Schottky barrier and hydrogen-evolved kinetics. Chem

Commun 52:1567–1570. https://doi.org/10.1039/C5CC08547K

190. Nasrallah H, Douma F, Hamoud HI, El-Roz M (2021) Chapter 5 - Metal nanoparticles in photocatalysis: Advances and challenges. In: Nguyen V-H, Vo D-VN, Nanda SBT-NP (eds). Elsevier, pp 119–143

191. Pandit S, Kunwar S, Pandey P, Lee J (2019) Improved LSPR Properties of Ag–Pt and Pt Nanoparticles: A Systematic Study on Various Configurations and Compositions of NPs via the Solid-State Dewetting of Ag–Pt Bilayers. Met. 9

192. Sui M, Kunwar S, Pandey P, Lee J (2019) Strongly confined localized surface plasmon resonance (LSPR) bands of Pt, AgPt, AgAuPt nanoparticles. Sci Rep 9:16582. https://doi.org/10.1038/s41598-019-53292-1

193. Lou Z, Fujitsuka M, Majima T (2016) Pt–Au Triangular Nanoprisms with Strong Dipole Plasmon Resonance for Hydrogen Generation Studied by Single-Particle Spectroscopy. ACS Nano 10:6299–6305. https://doi.org/10.1021/acsnano.6b02494

194. Ding J, Li X, Chen L, et al (2018) Photocatalytic hydrogen production over plasmonic AuCu/$CaIn_2S_4$ composites with different AuCu atomic arrangements. Appl Catal B Environ 224:322–329. https://doi.org/https://doi.org/10.1016/j.apcatb.2017.10.045

195. Zhang P, Zeng G, Song T, et al (2019) Design of plasmonic CuCo bimetal as a nonsemiconductor photocatalyst for synchronized hydrogen evolution and storage. Appl Catal B Environ 242:389–396. https://doi.org/https://doi.org/10.1016/j.apcatb.2018.10.020

196. Gao M, Connor PKN, Ho GW (2016) Plasmonic photothermic directed broadband sunlight harnessing for seawater catalysis and desalination. Energy Environ Sci 9:3151–3160. https://doi.org/10.1039/C6EE00971A

197. Naya S, Kume T, Akashi R, et al (2018) Red-Light-Driven Water Splitting by Au(Core)–CdS(Shell) Half-Cut Nanoegg with Heteroepitaxial Junction. J Am Chem Soc 140:1251–1254. https://doi.org/10.1021/jacs.7b12972

198. Wu B, Liu D, Mubeen S, et al (2016) Anisotropic Growth of TiO_2 onto Gold Nanorods for Plasmon-Enhanced Hydrogen Production from Water Reduction. J Am Chem Soc 138:1114–1117. https://doi.org/10.1021/jacs.5b11341

199. Zheng Z, Tachikawa T, Majima T (2014) Single-Particle Study of Pt-Modified Au Nanorods for Plasmon-Enhanced Hydrogen Generation in Visible to Near-Infrared Region. J Am Chem Soc 136:6870–6873. https://doi.org/10.1021/ja502704n

200. Han C, Wu L, Ge L, et al (2015) AuPd bimetallic nanoparticles decorated graphitic carbon nitride for highly efficient reduction of water to H_2 under visible light irradiation. Carbon N Y 92:31–40. https://doi.org/https://doi.org/10.1016/j.carbon.2015.02.070

201. Campos-Martin JM, Blanco-Brieva G, Fierro JLG (2006) Hydrogen Peroxide Synthesis: An Outlook beyond the Anthraquinone Process. Angew Chemie Int Ed 45:6962–6984. https://doi.org/https://doi.org/10.1002/anie.200503779

202. Poursaitidis ET, Gkizis PL, Triandafillidi I, Kokotos CG (2024) Organocatalytic activation of hydrogen peroxide: towards green and sustainable oxidations. Chem Sci 15:1177–1203. https://doi.org/10.1039/D3SC05618J

203. McDonnell G (2014) The Use of Hydrogen Peroxide for Disinfection and Sterilization

Applications. In: Patai's Chemistry of Functional Groups. pp 1–34

204. Guan R, Yuan X, Wu Z, et al (2018) Principle and application of hydrogen peroxide based advanced oxidation processes in activated sludge treatment: A review. Chem Eng J 339:519–530. https://doi.org/https://doi.org/10.1016/j.cej.2018.01.153

205. Hou H, Zeng X, Zhang X (2020) Production of Hydrogen Peroxide by Photocatalytic Processes. Angew Chemie Int Ed 59:17356–17376. https://doi.org/https://doi.org/10.1002/anie.201911609

206. Adnan RH, Jalil AA (2023) Gold photocatalysis in sustainable hydrogen peroxide generation. Mater Today Chem 27:101322. https://doi.org/https://doi.org/10.1016/j.mtchem.2022.101322

207. Liu Y, Chen F, Wang Q, et al (2018) Direct unassisted hydrogen peroxide generation from oxygen and water on plasmonic Ag-graphene-Cu nanosandwitch. Appl Catal B Environ 224:940–950. https://doi.org/https://doi.org/10.1016/j.apcatb.2017.11.026

208. Teranishi M, Naya S, Tada H (2010) In Situ Liquid Phase Synthesis of Hydrogen Peroxide from Molecular Oxygen Using Gold Nanoparticle-Loaded Titanium(IV) Dioxide Photocatalyst. J Am Chem Soc 132:7850–7851. https://doi.org/10.1021/ja102651g

209. Zuo G, Liu S, Wang L, et al (2019) Finely dispersed Au nanoparticles on graphitic carbon nitride as highly active photocatalyst for hydrogen peroxide production. Catal Commun 123:69–72. https://doi.org/https://doi.org/10.1016/j.catcom.2019.02.011

210. Hirakawa H, Shiota S, Shiraishi Y, et al (2016) Au Nanoparticles Supported on $BiVO_4$: Effective Inorganic Photocatalysts for H_2O_2 Production from Water and O2 under Visible Light. ACS Catal 6:4976–4982. https://doi.org/10.1021/acscatal.6b01187

211. Song H, Wei L, Chen C, et al (2019) Photocatalytic production of H_2O_2 and its in situ utilization over atomic-scale Au modified MoS_2 nanosheets. J Catal 376:198–208. https://doi.org/https://doi.org/10.1016/j.jcat.2019.06.015

212. Chang X, Yang J, Han D, et al (2018) Enhancing Light-Driven Production of Hydrogen Peroxide by Anchoring Au onto C_3N_4 Catalysts. Catalysts 8

213. Tsukamoto D, Shiro A, Shiraishi Y, et al (2012) Photocatalytic H_2O_2 Production from Ethanol/O2 System Using TiO_2 Loaded with Au–Ag Bimetallic Alloy Nanoparticles. ACS Catal 2:599–603. https://doi.org/10.1021/cs2006873

214. Kaynan N, Berke BA, Hazut O, Yerushalmi R (2014) Sustainable photocatalytic production of hydrogen peroxide from water and molecular oxygen. J Mater Chem A 2:13822–13826. https://doi.org/10.1039/C4TA03004D

215. Yoshii T, Kuwahara Y, Mori K, Yamashita H (2021) Promotional effect of surface plasmon resonance on direct formation of hydrogen peroxide from H_2 and O_2 over Pd/Graphene-Au nanorod catalytic system. J Catal 394:259–265. https://doi.org/https://doi.org/10.1016/j.jcat.2020.05.028

216. Wang K, Wang M, Yu J, et al (2021) BiVO4 Microparticles Decorated with Cu@Au Core-Shell Nanostructures for Photocatalytic H2O2 Production. ACS Appl Nano Mater 4:13158–13166. https://doi.org/10.1021/acsanm.1c02688

217. Wang K, Li Y, Shi H, et al (2022) Optimizing Oxygen and Intermediate HOO* Adsorption of Cu–Pd Alloy Cocatalyst for Boosting Photocatalytic H2O2 Production of $BiVO_4$. Adv Sustain

Syst 6:2200144. https://doi.org/https://doi.org/10.1002/adsu.202200144

218. Shi H, Li Y, Wang K, et al (2022) Mass-transfer control for selective deposition of well-dispersed AuPd cocatalysts to boost photocatalytic H_2O_2 production of $BiVO_4$. Chem Eng J 443:136429. https://doi.org/https://doi.org/10.1016/j.cej.2022.136429

219. Wang Y, Wang Y, Zhao J, et al (2021) Efficient production of H_2O_2 on Au/WO_3 under visible light and the influencing factors. Appl Catal B Environ 284:119691. https://doi.org/https://doi.org/10.1016/j.apcatb.2020.119691

220. Shi H, Li Y, Wang X, et al (2021) Selective modification of ultra-thin g-C_3N_4 nanosheets on the (110) facet of Au/BiVO4 for boosting photocatalytic H2O2 production. Appl Catal B Environ 297:120414. https://doi.org/https://doi.org/10.1016/j.apcatb.2021.120414

221. Cai J, Huang J, Wang S, et al (2019) Crafting Mussel-Inspired Metal Nanoparticle-Decorated Ultrathin Graphitic Carbon Nitride for the Degradation of Chemical Pollutants and Production of Chemical Resources. Adv Mater 31:1806314. https://doi.org/https://doi.org/10.1002/adma.201806314

222. Robatjazi H, Zhao H, Swearer DF, et al (2017) Plasmon-induced selective carbon dioxide conversion on earth-abundant aluminum-cuprous oxide antenna-reactor nanoparticles. Nat Commun 8:27. https://doi.org/10.1038/s41467-017-00055-z

223. Zhou L, Martirez JMP, Finzel J, et al (2020) Light-driven methane dry reforming with single atomic site antenna-reactor plasmonic photocatalysts. Nat Energy 5:61–70. https://doi.org/10.1038/s41560-019-0517-9

224. Gustafsson MGL (2000) Surpassing the lateral resolution limit by a factor of two using structured illumination microscopy. J Microsc 198:82–87. https://doi.org/https://doi.org/10.1046/j.1365-2818.2000.00710.x

225. Ruska, E., & Knoll M (1931) Die magnetische Sammelspule für schnelle Elektronenstrahlen. The magnetic concentrating coil for fast electron beams.). Z techn Phys 12:389–400

226. Knoll M, Ruska E (1932) Das Elektronenmikroskop. Zeitschrift für Phys 78:318–339. https://doi.org/10.1007/BF01342199

227. Williams, D. B. and Carter CB (2009) The transmission electron microscope

228. Big EJ (1956) A Short History of the Electron Microscope. Bios 27:33–37

229. Javed Y, Ali K, Akhtar K, et al (2018) TEM for Atomic-Scale Study: Fundamental, Instrumentation, and Applications in Nanotechnology BT - Handbook of Materials Characterization. In: Sharma SK (ed). Springer International Publishing, Cham, pp 147–216

230. Haider M, Uhlemann S, Schwan E, et al (1998) Electron microscopy image enhanced. Nature 392:768–769. https://doi.org/10.1038/33823

231. Hetherington C (2004) Aberration correction for TEM. Mater Today 7:50–55. https://doi.org/https://doi.org/10.1016/S1369-7021(04)00571-1

232. G. Van Tendeloo DVD and SJP (2012) Handbook of Nanoscopy. Wiley-VCH

233. Ke X, Bittencourt C, Van Tendeloo G (2015) Possibilities and limitations of advanced transmission electron microscopy for carbon-based nanomaterials. Beilstein J Nanotechnol 6:1541–1557. https://doi.org/10.3762/bjnano.6.158

234. Fultz B, Howe J (2013) High-Resolution TEM Imaging BT - Transmission Electron Microscopy and Diffractometry of Materials. In: Fultz B, Howe J (eds). Springer Berlin Heidelberg, Berlin, Heidelberg, pp 521–586

235. Fultz B, Howe J (2013) Diffraction Contrast in TEM Images BT - Transmission Electron Microscopy and Diffractometry of Materials. In: Fultz B, Howe J (eds). Springer Berlin Heidelberg, Berlin, Heidelberg, pp 349–427

236. Pennycook SJ (1989) Z-contrast stem for materials science. Ultramicroscopy 30:58–69. https://doi.org/https://doi.org/10.1016/0304-3991(89)90173-3

237. Winckelmans N, Altantzis T, Grzelczak M, et al (2018) Multimode Electron Tomography as a Tool to Characterize the Internal Structure and Morphology of Gold Nanoparticles. J Phys Chem C 122:13522–13528. https://doi.org/10.1021/acs.jpcc.7b12379

238. Op de Beeck M, Van Dyck D (1996) Direct structure reconstruction in HRTEM. Ultramicroscopy 64:153–165. https://doi.org/https://doi.org/10.1016/0304-3991(96)00006-X

239. Ophus C (2019) Four-Dimensional Scanning Transmission Electron Microscopy (4D-STEM): From Scanning Nanodiffraction to Ptychography and Beyond. Microsc Microanal 25:563–582. https://doi.org/DOI: 10.1017/S1431927619000497

240. Bustillo KC, Zeltmann SE, Chen M, et al (2021) 4D-STEM of Beam-Sensitive Materials. Acc Chem Res 54:2543–2551. https://doi.org/10.1021/acs.accounts.1c00073

241. Li G, Zhang H, Han Y (2022) 4D-STEM Ptychography for Electron-Beam-Sensitive Materials. ACS Cent Sci 8:1579–1588. https://doi.org/10.1021/acscentsci.2c01137

242. Levin B.D.A.; Zhang, C.; Bammes, B.; Voyles, P. M.; Bilhorn RB (2020) 4D STEM with a direct electron detector

243. Lazić I, Bosch EGT (2017) Chapter Three - Analytical Review of Direct Stem Imaging Techniques for Thin Samples. In: Hawkes PWBT-A in I and EP (ed). Elsevier, pp 75–184

244. Li Z, Biskupek J, Kaiser U, Rose H (2022) Integrated Differential Phase Contrast (IDPC)-STEM Utilizing a Multi-Sector Detector for Imaging Thick Samples. Microsc Microanal 28:611–621. https://doi.org/10.1017/S1431927622000289

245. Yücelen E, Lazić I, Bosch EGT (2018) Phase contrast scanning transmission electron microscopy imaging of light and heavy atoms at the limit of contrast and resolution. Sci Rep 8:2676. https://doi.org/10.1038/s41598-018-20377-2

246. Lazić I, Bosch EGT, Lazar S (2016) Phase contrast STEM for thin samples: Integrated differential phase contrast. Ultramicroscopy 160:265–280. https://doi.org/https://doi.org/10.1016/j.ultramic.2015.10.011

247. Lazić I, Wirix M, Leidl ML, et al (2022) Single-particle cryo-EM structures from iDPC–STEM at near-atomic resolution. Nat Methods 19:1126–1136. https://doi.org/10.1038/s41592-022-01586-0

248. Allen LJ, D'Alfonso AJ, Freitag B, Klenov DO (2012) Chemical mapping at atomic resolution using energy-dispersive x-ray spectroscopy. MRS Bull 37:47–52. https://doi.org/DOI: 10.1557/mrs.2011.331

249. Hofer F, Schmidt FP, Grogger W, Kothleitner G (2016) Fundamentals of electron energy-

loss spectroscopy. IOP Conf Ser Mater Sci Eng 109:12007. https://doi.org/10.1088/1757-899X/109/1/012007

250. Rossouw D, Knappett BR, Wheatley AEH, Midgley PA (2016) A New Method for Determining the Composition of Core–Shell Nanoparticles via Dual-EDX+EELS Spectrum Imaging. Part Part Syst Charact 33:749–755. https://doi.org/https://doi.org/10.1002/ppsc.201600096

251. Radon J (1917) Uber die bestimmug von funktionen durch ihre integralwerte laengs geweisser mannigfaltigkeiten. Berichte Saechsishe Acad Wissenschaft Math Phys 69:262–277

252. Hounsfield GN (1980) Computed Medical Imaging. J Comput Assist Tomogr 4:

253. Cormack AM (1964) Representation of a Function by Its Line Integrals, with Some Radiological Applications. II. J Appl Phys 35:2908–2913. https://doi.org/10.1063/1.1713127

254. Hart RG (1968) Electron Microscopy of Unstained Biological Material: The Polytropic Montage. Science (80-) 159:1464–1467. https://doi.org/10.1126/science.159.3822.1464

255. Hoppe W, Langer R, Knesch G, Poppe C (1968) Protein-Kristallstrukturanalyse mit Elektronenstrahlen. Naturwissenschaften 55:333–336. https://doi.org/10.1007/BF00600449

256. DE ROSIER DJ, KLUG A (1968) Reconstruction of Three Dimensional Structures from Electron Micrographs. Nature 217:130–134. https://doi.org/10.1038/217130a0

257. Midgley PA, Weyland M (2003) 3D electron microscopy in the physical sciences: the development of Z-contrast and EFTEM tomography. Ultramicroscopy 96:413–431. https://doi.org/https://doi.org/10.1016/S0304-3991(03)00105-0

258. Altantzis T, Zanaga D, Bals S (2017) Advanced electron tomography of nanoparticle assemblies(a). Europhys Lett 119:38001. https://doi.org/10.1209/0295-5075/119/38001

259. Bladt E, van Dijk-Moes RJA, Peters J, et al (2016) Atomic Structure of Wurtzite CdSe (Core)/CdS (Giant Shell) Nanobullets Related to Epitaxy and Growth. J Am Chem Soc 138:14288–14293. https://doi.org/10.1021/jacs.6b06443

260. Serrano-Montes AB, Langer J, Henriksen-Lacey M, et al (2016) Gold Nanostar-Coated Polystyrene Beads as Multifunctional Nanoprobes for SERS Bioimaging. J Phys Chem C 120:20860–20868. https://doi.org/10.1021/acs.jpcc.6b02282

261. Burnett TL, Kelley R, Winiarski B, et al (2015) Large volume 3D characterization by plasma FIB DualBeam microscopy. Microsc Microanal 21:2003–2004. https://doi.org/10.1017/S143192761501079X

262. Friedrich H, McCartney MR, Buseck PR (2005) Comparison of intensity distributions in tomograms from BF TEM, ADF STEM, HAADF STEM, and calculated tilt series. Ultramicroscopy 106:18–27. https://doi.org/https://doi.org/10.1016/j.ultramic.2005.06.005

263. Kübel C, Voigt A, Schoenmakers R, et al (2005) Recent Advances in Electron Tomography: TEM and HAADF-STEM Tomography for Materials Science and Semiconductor Applications. Microsc Microanal 11:378–400. https://doi.org/10.1017/S1431927605050361

264. Biermans E, Molina L, Batenburg KJ, et al (2010) Measuring Porosity at the Nanoscale by Quantitative Electron Tomography. Nano Lett 10:5014–5019. https://doi.org/10.1021/nl103172r

265. Midgley PA, Dunin-Borkowski RE (2009) Electron tomography and holography in materials science. Nat Mater 8:271–280. https://doi.org/10.1038/nmat2406

266. Van Tendeloo G, Bals S, Van Aert S, et al (2012) Advanced Electron Microscopy for Advanced Materials. Adv Mater 24:5655–5675. https://doi.org/https://doi.org/10.1002/adma.201202107

267. Leary R, Saghi Z, Armbrüster M, et al (2012) Quantitative High-Angle Annular Dark-Field Scanning Transmission Electron Microscope (HAADF-STEM) Tomography and High-Resolution Electron Microscopy of Unsupported Intermetallic $GaPd_2$ Catalysts. J Phys Chem C 116:13343–13352. https://doi.org/10.1021/jp212456z

268. Möbus G, Doole RC, Inkson BJ (2003) Spectroscopic electron tomography. Ultramicroscopy 96:433–451. https://doi.org/https://doi.org/10.1016/S0304-3991(03)00106-2

269. Bals S, Goris B, Liz-Marzán LM, Van Tendeloo G (2014) Three-Dimensional Characterization of Noble-Metal Nanoparticles and their Assemblies by Electron Tomography. Angew Chemie Int Ed 53:10600–10610. https://doi.org/https://doi.org/10.1002/anie.201401059

270. Schlossmacher P, Klenov DO, Freitag B, von Harrach HS (2010) Enhanced Detection Sensitivity with a New Windowless XEDS System for AEM Based on Silicon Drift Detector Technology. Micros Today 18:14–20. https://doi.org/10.1017/S1551929510000404

271. Genc A, Kovarik L, Gu M, et al (2013) XEDS STEM tomography for 3D chemical characterization of nanoscale particles. Ultramicroscopy 131:24–32. https://doi.org/https://doi.org/10.1016/j.ultramic.2013.03.023

272. Lepinay K, Lorut F, Pantel R, Epicier T (2013) Chemical 3D tomography of 28nm high K metal gate transistor: STEM XEDS experimental method and results. Micron 47:43–49. https://doi.org/https://doi.org/10.1016/j.micron.2013.01.004

273. Goris B, Polavarapu L, Bals S, et al (2014) Monitoring Galvanic Replacement Through Three-Dimensional Morphological and Chemical Mapping. Nano Lett 14:3220–3226. https://doi.org/10.1021/nl500593j

274. Liakakos N, Gatel C, Blon T, et al (2014) Co–Fe Nanodumbbells: Synthesis, Structure, and Magnetic Properties. Nano Lett 14:2747–2754. https://doi.org/10.1021/nl500734k

275. Zanaga D, Altantzis T, Polavarapu L, et al (2016) A New Method for Quantitative XEDS Tomography of Complex Heteronanostructures. Part Part Syst Charact 33:396–403. https://doi.org/https://doi.org/10.1002/ppsc.201600021

276. Radermacher M (1988) Three-Dimensional reconstruction of single particles from random and nonrandom tilt series. J Electron Microsc Tech 9:359–394. https://doi.org/https://doi.org/10.1002/jemt.1060090405

277. Arslan I, Tong JR, Midgley PA (2006) Reducing the missing wedge: High-resolution dual axis tomography of inorganic materials. Ultramicroscopy 106:994–1000. https://doi.org/https://doi.org/10.1016/j.ultramic.2006.05.010

278. Kawase N, Kato M, Nishioka H, Jinnai H (2007) Transmission electron microtomography without the “missing wedge” for quantitative structural analysis. Ultramicroscopy 107:8–

15. https://doi.org/https://doi.org/10.1016/j.ultramic.2006.04.007

279. Ke X, Bals S, Cott D, et al (2010) Three-Dimensional Analysis of Carbon Nanotube Networks in Interconnects by Electron Tomography without Missing Wedge Artifacts. Microsc Microanal 16:210–217. https://doi.org/10.1017/S1431927609991371

280. Jarausch K, Leonard DN (2009) Three-dimensional electron microscopy of individual nanoparticles. J Electron Microsc (Tokyo) 58:175–183. https://doi.org/10.1093/jmicro/dfn028

281. Vanrompay H, Bladt E, Albrecht W, et al (2018) 3D characterization of heat-induced morphological changes of Au nanostars by fast in situ electron tomography. Nanoscale 10:22792–22801. https://doi.org/10.1039/C8NR08376B

282. Vanrompay H, Skorikov A, Bladt E, et al (2021) Fast versus conventional HAADF-STEM tomography of nanoparticles: advantages and challenges. Ultramicroscopy 221:113191. https://doi.org/https://doi.org/10.1016/j.ultramic.2020.113191

283. Zheng SQ, Keszthelyi B, Branlund E, et al (2007) UCSF tomography: An integrated software suite for real-time electron microscopic tomographic data collection, alignment, and reconstruction. J Struct Biol 157:138–147. https://doi.org/https://doi.org/10.1016/j.jsb.2006.06.005

284. Kremer JR, Mastronarde DN, McIntosh JR (1996) Computer Visualization of Three-Dimensional Image Data Using IMOD. J Struct Biol 116:71–76. https://doi.org/https://doi.org/10.1006/jsbi.1996.0013

285. Wolf D, Lubk A, Lichte H, Friedrich H (2010) Towards automated electron holographic tomography for 3D mapping of electrostatic potentials. Ultramicroscopy 110:390–399. https://doi.org/https://doi.org/10.1016/j.ultramic.2009.12.015

286. Radon J (1986) On the determination of functions from their integral values along certain manifolds. IEEE Trans Med Imaging 5:170–176. https://doi.org/10.1109/TMI.1986.4307775

287. Gilbert P (1972) Iterative methods for the three-dimensional reconstruction of an object from projections. J Theor Biol 36:105–117. https://doi.org/https://doi.org/10.1016/0022-5193(72)90180-4

288. P R Smith, T M Peters, R H T Bates (1973) Image reconstruction from finite numbers of projections. J Phys A Math Nucl Gen 6:361. https://doi.org/10.1088/0305-4470/6/3/011

289. Bladt E (2017) Two- and three-dimensional transmission electron microscopy of colloidal nanoparticles: from structure to composition. PhD Diss Univ Antwerp

290. Radermacher M (1992) Weighted Back-Projection Methods BT - Electron Tomography: Three-Dimensional Imaging with the Transmission Electron Microscope. In: Frank J (ed). Springer US, Boston, MA, pp 91–115

291. Goris B, Roelandts T, Batenburg KJ, et al (2013) Advanced reconstruction algorithms for electron tomography: From comparison to combination. Ultramicroscopy 127:40–47. https://doi.org/https://doi.org/10.1016/j.ultramic.2012.07.003

292. Moon TK (1996) The expectation-maximization algorithm. IEEE Signal Process Mag 13:47–60. https://doi.org/10.1109/79.543975

293. Heidari Mezerji H, Van den Broek W, Bals S (2011) A practical method to determine the

effective resolution in incoherent experimental electron tomography. Ultramicroscopy 111:330–336. https://doi.org/https://doi.org/10.1016/j.ultramic.2011.01.021

294. Batenburg KJ, Bals S, Sijbers J, et al (2009) 3D imaging of nanomaterials by discrete tomography. Ultramicroscopy 109:730–740. https://doi.org/https://doi.org/10.1016/j.ultramic.2009.01.009

295. Goris B, Van den Broek W, Batenburg KJ, et al (2012) Electron tomography based on a total variation minimization reconstruction technique. Ultramicroscopy 113:120–130. https://doi.org/https://doi.org/10.1016/j.ultramic.2011.11.004

296. Zhuge X, Jinnai H, Dunin-Borkowski RE, et al (2017) Automated discrete electron tomography – Towards routine high-fidelity reconstruction of nanomaterials. Ultramicroscopy 175:87–96. https://doi.org/https://doi.org/10.1016/j.ultramic.2017.01.009

297. Kavak S, Kadu AA, Claes N, et al (2023) Quantitative 3D Investigation of Nanoparticle Assemblies by Volumetric Segmentation of Electron Tomography Data Sets. J Phys Chem C 127:9725–9734. https://doi.org/10.1021/acs.jpcc.3c02017

298. Asapu R, Claes N, Ciocarlan R-G, et al (2019) Electron Transfer and Near-Field Mechanisms in Plasmonic Gold-Nanoparticle-Modified TiO2 Photocatalytic Systems. ACS Appl Nano Mater 2:4067–4074. https://doi.org/10.1021/acsanm.9b00485

299. Borah R, Smets J, Ninakanti R, et al (2022) Self-Assembled Ligand-Capped Plasmonic Au Nanoparticle Films in the Kretschmann Configuration for Sensing of Volatile Organic Compounds. ACS Appl Nano Mater 5:11494–11505. https://doi.org/10.1021/acsanm.2c02524

300. Shrivastav AM, Cvelbar U, Abdulhalim I (2021) A comprehensive review on plasmonic-based biosensors used in viral diagnostics. Commun Biol 4:70. https://doi.org/10.1038/s42003-020-01615-8

301. Mosquera J, Zhao Y, Jang H-J, et al (2020) Plasmonic Nanoparticles with Supramolecular Recognition. Adv Funct Mater 30:1902082. https://doi.org/https://doi.org/10.1002/adfm.201902082

302. Ni B, Mychinko M, Gómez-Graña S, et al (2023) Chiral Seeded Growth of Gold Nanorods Into Fourfold Twisted Nanoparticles with Plasmonic Optical Activity. Adv Mater 35:2208299. https://doi.org/https://doi.org/10.1002/adma.202208299

303. Arenas Esteban D, Pacquets L, Choukroun D, et al (2023) 3D Characterization of the Structural Transformation Undergone by Cu@Ag Core–Shell Nanoparticles Following CO2 Reduction Reaction. Chem Mater 35:6682–6691. https://doi.org/10.1021/acs.chemmater.3c00649

304. Claes N, Asapu R, Blommaerts N, et al (2018) Characterization of silver-polymer core–shell nanoparticles using electron microscopy. Nanoscale 10:9186–9191. https://doi.org/10.1039/C7NR09517A

305. Biran I, Houben L, Kossoy A, Rybtchinski B (2024) Transmission Electron Microscopy Methodology to Analyze Polymer Structure with Submolecular Resolution. J Phys Chem C 128:5988–5995. https://doi.org/10.1021/acs.jpcc.3c06977

306. Kuei B, Aplan MP, Litofsky JH, Gomez ED (2020) New opportunities in transmission

electron microscopy of polymers. Mater Sci Eng R Reports 139:100516. https://doi.org/https://doi.org/10.1016/j.mser.2019.100516

307. Hudry D, De Backer A, Popescu R, et al (2021) Interface Pattern Engineering in Core-Shell Upconverting Nanocrystals: Shedding Light on Critical Parameters and Consequences for the Photoluminescence Properties. Small 17:2104441. https://doi.org/https://doi.org/10.1002/smll.202104441

308. Sentosun K, Sanz Ortiz MN, Batenburg KJ, et al (2015) Combination of HAADF-STEM and ADF-STEM Tomography for Core–Shell Hybrid Materials. Part Part Syst Charact 32:1063–1067. https://doi.org/https://doi.org/10.1002/ppsc.201500097

309. Zhang Y-J, Radjenovic PM, Zhou X-S, et al (2021) Plasmonic Core–Shell Nanomaterials and their Applications in Spectroscopies. Adv Mater 33:2005900. https://doi.org/https://doi.org/10.1002/adma.202005900

310. Venditti I, Hassanein TF, Fratoddi I, et al (2015) Bioconjugation of gold-polymer core–shell nanoparticles with bovine serum amine oxidase for biomedical applications. Colloids Surfaces B Biointerfaces 134:314–321. https://doi.org/https://doi.org/10.1016/j.colsurfb.2015.06.052

311. Magnozzi M, Brasse Y, König TAF, et al (2020) Plasmonics of Au/Polymer Core/Shell Nanocomposites for Thermoresponsive Hybrid Metasurfaces. ACS Appl Nano Mater 3:1674–1682. https://doi.org/10.1021/acsanm.9b02403

312. Kim T, Kang H, Jeong S, et al (2014) Au@Polymer Core–Shell Nanoparticles for Simultaneously Enhancing Efficiency and Ambient Stability of Organic Optoelectronic Devices. ACS Appl Mater Interfaces 6:16956–16965. https://doi.org/10.1021/am504503q

313. Haubruge HG, Jonas AM, Legras R (2003) Staining of poly(ethylene terephthalate) by ruthenium tetroxide. Polymer (Guildf) 44:3229–3234. https://doi.org/https://doi.org/10.1016/S0032-3861(03)00255-6

314. Crassous JJ, Rochette CN, Wittemann A, et al (2009) Quantitative Analysis of Polymer Colloids by Cryo-Transmission Electron Microscopy. Langmuir 25:7862–7871. https://doi.org/10.1021/la900442x

315. Van den Hoek J, Daems N, Arnouts S, et al (2023) Improving Stability of CO_2 Electroreduction by Incorporating Ag NPs in N-Doped Ordered Mesoporous Carbon Structures. ACS Appl Mater Interfaces. https://doi.org/10.1021/acsami.3c12261

316. Manzaneda-González V, Jenkinson K, Peña-Rodríguez O, et al (2023) From Multi- to Single-Hollow Trimetallic Nanocrystals by Ultrafast Heating. Chem Mater 35:9603–9612. https://doi.org/10.1021/acs.chemmater.3c01698

317. Peeters H, Keulemans M, Nuyts G, et al (2020) Plasmonic gold-embedded TiO_2 thin films as photocatalytic self-cleaning coatings. Appl Catal B Environ 267:118654. https://doi.org/https://doi.org/10.1016/j.apcatb.2020.118654

318. Ristau R, Tiruvalam R, Clasen PL, et al (2009) Electron microscopy studies of the thermal stability of gold nanoparticle arrays. Gold Bull 42:133–143. https://doi.org/10.1007/BF03214923

319. Dutta A, Reid C, Heinrich H (2013) Simulation of Incoherent Scattering in High-Angle Annular Dark-Field Scanning Electron Microscopy. Microsc Microanal 19:852–853.

https://doi.org/10.1017/S1431927613006259

320. Coutts MJ, Cortie MB, Ford MJ, McDonagh AM (2009) Rapid and Controllable Sintering of Gold Nanoparticle Inks at Room Temperature Using a Chemical Agent. J Phys Chem C 113:1325–1328. https://doi.org/10.1021/jp808927t

321. Zhang S, Wu Y (2023) Investigating the crystallization behavior of TiO_2 during annealing: Molecular dynamics simulations. AIP Adv 13:85226. https://doi.org/10.1063/5.0165728

322. Martinez GT, Jones L, De Backer A, et al (2015) Quantitative STEM normalisation: The importance of the electron flux. Ultramicroscopy 159:46–58. https://doi.org/https://doi.org/10.1016/j.ultramic.2015.07.010

323. Batenburg KJ, Sijbers J (2011) DART: A Practical Reconstruction Algorithm for Discrete Tomography. IEEE Trans Image Process 20:2542–2553. https://doi.org/10.1109/TIP.2011.2131661

324. Schlücker S (2014) Surface-Enhanced Raman Spectroscopy: Concepts and Chemical Applications. Angew Chemie Int Ed 53:4756–4795. https://doi.org/https://doi.org/10.1002/anie.201205748

325. Li JF, Huang YF, Ding Y, et al (2010) Shell-isolated nanoparticle-enhanced Raman spectroscopy. Nature 464:392–395. https://doi.org/10.1038/nature08907

326. Galloway TA, Hardwick LJ (2016) Utilizing in Situ Electrochemical SHINERS for Oxygen Reduction Reaction Studies in Aprotic Electrolytes. J Phys Chem Lett 7:2119–2124. https://doi.org/10.1021/acs.jpclett.6b00730

327. Hartman T, Wondergem CS, Weckhuysen BM (2018) Practical Guidelines for Shell-Isolated Nanoparticle-Enhanced Raman Spectroscopy of Heterogeneous Catalysts. ChemPhysChem 19:2461–2467. https://doi.org/https://doi.org/10.1002/cphc.201800509

328. Rogolino A, Claes N, Cizaurre J, et al (2022) Metal–Polymer Heterojunction in Colloidal-Phase Plasmonic Catalysis. J Phys Chem Lett 13:2264–2272. https://doi.org/10.1021/acs.jpclett.1c04242

329. Lolla D, Gorse J, Kisielowski C, et al (2016) Polyvinylidene fluoride molecules in nanofibers, imaged at atomic scale by aberration corrected electron microscopy. Nanoscale 8:120–128. https://doi.org/10.1039/C5NR01619C

330. Chen F-R, Kisielowski C, Van Dyck D (2017) Prospects for atomic resolution in-line holography for a 3D determination of atomic structures from single projections. Adv Struct Chem Imaging 3:8. https://doi.org/10.1186/s40679-017-0041-6

331. R. Meyer R, Kirkland A (1998) The effects of electron and photon scattering on signal and noise transfer properties of scintillators in CCD cameras used for electron detection. Ultramicroscopy 75:23–33. https://doi.org/https://doi.org/10.1016/S0304-3991(98)00051-5

332. Thust A, Overwijk MHF, Coene WMJ, Lentzen M (1996) Numerical correction of lens aberrations in phase-retrieval HRTEM. Ultramicroscopy 64:249–264. https://doi.org/https://doi.org/10.1016/0304-3991(96)00022-8

333. MacTempas, Software for high resolution electron microscopy. http://www.totalresolution.com/index.html.

334. W. GR (1972) A practical algorithm for the determination of plane from image and diffraction pictures. Optik (Stuttg) 35:237–246

335. C. Kübel and A. Thust (2005) A Software Package for Focal-Series Reconstruction in HRTEM

336. Coene WMJ, Thust A, Op de Beeck M, Van Dyck D (1996) Maximum-likelihood method for focus-variation image reconstruction in high resolution transmission electron microscopy. Ultramicroscopy 64:109–135. https://doi.org/https://doi.org/10.1016/0304-3991(96)00010-1

337. Allen LJ, McBride W, O'Leary NL, Oxley MP (2004) Exit wave reconstruction at atomic resolution. Ultramicroscopy 100:91–104. https://doi.org/https://doi.org/10.1016/j.ultramic.2004.01.012

338. Meyer RR, Kirkland AI, Saxton WO (2002) A new method for the determination of the wave aberration function for high resolution TEM: 1. Measurement of the symmetric aberrations. Ultramicroscopy 92:89–109. https://doi.org/https://doi.org/10.1016/S0304-3991(02)00071-2

339. C. B. Carter and D. B. Williams (2016) Transmission Electron Microscopy. Springer

340. Van den Broek W, Rosenauer A, Goris B, et al (2012) Correction of non-linear thickness effects in HAADF STEM electron tomography. Ultramicroscopy 116:8–12. https://doi.org/https://doi.org/10.1016/j.ultramic.2012.03.005

341. Rahman S, Rahman MM, Abdullah-Al-Wadud M, et al (2016) An adaptive gamma correction for image enhancement. EURASIP J Image Video Process 2016:35. https://doi.org/10.1186/s13640-016-0138-1

342. Tan L, Jiang J (2019) Chapter 13 - Image Processing Basics. In: Tan L, Jiang J (eds) Digital Signal Processing (Third Edition), Third Edit. Academic Press, pp 649–726

343. Guo Q, Zhou C, Ma Z, Yang X (2019) Fundamentals of TiO_2 Photocatalysis: Concepts, Mechanisms, and Challenges. Adv Mater 31:1901997. https://doi.org/https://doi.org/10.1002/adma.201901997

344. Schneider J, Matsuoka M, Takeuchi M, et al (2014) Understanding TiO_2 Photocatalysis: Mechanisms and Materials. Chem Rev 114:9919–9986. https://doi.org/10.1021/cr5001892

345. Martínez Molina P, Meulendijks N, Xu M, et al (2021) Low Temperature Sunlight-Powered Reduction of CO_2 to CO Using a Plasmonic Au/TiO2 Nanocatalyst. ChemCatChem 13:4507–4513. https://doi.org/https://doi.org/10.1002/cctc.202100699

346. Kumar A, Choudhary P, Kumar A, et al (2022) Recent Advances in Plasmonic Photocatalysis Based on TiO_2 and Noble Metal Nanoparticles for Energy Conversion, Environmental Remediation, and Organic Synthesis. Small 18:2101638. https://doi.org/https://doi.org/10.1002/smll.202101638

347. Linic S, Christopher P, Ingram DB (2011) Plasmonic-metal nanostructures for efficient conversion of solar to chemical energy. Nat Mater 10:911

348. Kim M, Lin M, Son J, et al (2017) Hot-Electron-Mediated Photochemical Reactions: Principles, Recent Advances, and Challenges. Adv Opt Mater 5:1700004. https://doi.org/https://doi.org/10.1002/adom.201700004

349. Li K, Hogan NJ, Kale MJ, et al (2017) Balancing Near-Field Enhancement, Absorption, and

Scattering for Effective Antenna–Reactor Plasmonic Photocatalysis. Nano Lett 17:3710–3717. https://doi.org/10.1021/acs.nanolett.7b00992

350. Brongersma ML, Halas NJ, Nordlander P (2015) Plasmon-induced hot carrier science and technology. Nat Nanotechnol 10:25–34. https://doi.org/10.1038/nnano.2014.311

351. Panayotov DA, Frenkel AI, Morris JR (2017) Catalysis and Photocatalysis by Nanoscale Au/TiO_2: Perspectives for Renewable Energy. ACS Energy Lett 2:1223–1231. https://doi.org/10.1021/acsenergylett.7b00189

352. Murdoch M, Waterhouse GIN, Nadeem MA, et al (2011) The effect of gold loading and particle size on photocatalytic hydrogen production from ethanol over Au/TiO_2 nanoparticles. Nat Chem 3:489–492. https://doi.org/10.1038/nchem.1048

353. Wang K, Yoshiiri K, Rosa L, et al (2022) TiO2/Au/TiO_2 plasmonic photocatalyst with enhanced photocatalytic activity and stability under visible-light irradiation. Catal Today 397–399:257–264. https://doi.org/https://doi.org/10.1016/j.cattod.2021.09.023

354. Campbell CT, Parker SC, Starr DE (2002) The Effect of Size-Dependent Nanoparticle Energetics on Catalyst Sintering. Science (80-) 298:811–814. https://doi.org/10.1126/science.1075094

355. Parker SC, Campbell CT (2007) Reactivity and sintering kinetics of Au/TiO_2(110) model catalysts: particle size effects. Top Catal 44:3–13. https://doi.org/10.1007/s11244-007-0274-z

356. Li G, Fang K, Chen Y, et al (2020) Unveiling the gas-dependent sintering behavior of Au-TiO_2 catalysts via environmental transmission electron microscopy. J Catal 388:84–90. https://doi.org/https://doi.org/10.1016/j.jcat.2020.05.003

357. Guo R, Wang J, Bi Z, et al (2022) Recent Advances and Perspectives of Core-Shell Nanostructured Materials for Photocatalytic CO_2 Reduction. Small n/a:2206314. https://doi.org/https://doi.org/10.1002/smll.202206314

358. Chen T-M, Xu G-Y, Ren H, et al (2019) Synthesis of Au@TiO_2 core–shell nanoparticles with tunable structures for plasmon-enhanced photocatalysis. Nanoscale Adv 1:4522–4528. https://doi.org/10.1039/C9NA00548J

359. Bayles A, Tian S, Zhou J, et al (2022) Al@TiO_2 Core–Shell Nanoparticles for Plasmonic Photocatalysis. ACS Nano 16:5839–5850. https://doi.org/10.1021/acsnano.1c10995

360. Dai Y, Lu P, Cao Z, et al (2018) The physical chemistry and materials science behind sinter-resistant catalysts. Chem Soc Rev 47:4314–4331. https://doi.org/10.1039/C7CS00650K

361. Bigelow NW, Vaschillo A, Iberi V, et al (2012) Characterization of the Electron- and Photon-Driven Plasmonic Excitations of Metal Nanorods. ACS Nano 6:7497–7504. https://doi.org/10.1021/nn302980u

362. Dingenen F, Borah R, Ninakanti R, Verbruggen SW (2022) Probing oxygen activation on plasmonic photocatalysts . Front. Chem. 10

363. Žerjav G, Albreht A, Vovk I, Pintar A (2020) Revisiting terephthalic acid and coumarin as probes for photoluminescent determination of hydroxyl radical formation rate in heterogeneous photocatalysis. Appl Catal A Gen 598:117566. https://doi.org/https://doi.org/10.1016/j.apcata.2020.117566

364. Binkowski F, Wu T, Lalanne P, et al (2021) Hot Electron Generation through Near-Field Excitation of Plasmonic Nanoresonators. ACS Photonics 8:1243–1250. https://doi.org/10.1021/acsphotonics.1c00231

365. Bosomtwi D, Osiński M, Babicheva VE (2021) Lattice effect for enhanced hot-electron generation in nanoelectrodes. Opt Mater Express 11:3232–3244. https://doi.org/10.1364/OME.430577

366. Khurgin JB (2019) Hot carriers generated by plasmons: where are they generated and where do they go from there? Faraday Discuss 214:35–58. https://doi.org/10.1039/C8FD00200B

367. Hartland G V, Besteiro L V, Johns P, Govorov AO (2017) What's so Hot about Electrons in Metal Nanoparticles? ACS Energy Lett 2:1641–1653. https://doi.org/10.1021/acsenergylett.7b00333

368. Oh S, Kim J-H, Hwang HM, et al (2021) Band restructuring of ordered/disordered blue TiO_2 for visible light photocatalysis. J Mater Chem A 9:4822–4830. https://doi.org/10.1039/D0TA11505C

369. Paz Y, Luo Z, Rabenberg L, Heller A (1995) Photooxidative self-cleaning transparent titanium dioxide films on glass. J Mater Res 10:2842–2848. https://doi.org/10.1557/JMR.1995.2842

370. Frank J, McEwen BF (1992) Alignment by Cross-Correlation BT - Electron Tomography: Three-Dimensional Imaging with the Transmission Electron Microscope. In: Frank J (ed). Springer US, Boston, MA, pp 205–213

371. van Aarle W, Palenstijn WJ, De Beenhouwer J, et al (2015) The ASTRA Toolbox: A platform for advanced algorithm development in electron tomography. Ultramicroscopy 157:35–47. https://doi.org/https://doi.org/10.1016/j.ultramic.2015.05.002

372. Verbeeck J, Van Aert S (2004) Model based quantification of EELS spectra. Ultramicroscopy 101:207–224. https://doi.org/https://doi.org/10.1016/j.ultramic.2004.06.004

373. Johnson PB, Christy RW (1972) Optical Constants of the Noble Metals. Phys Rev B 6:4370–4379. https://doi.org/10.1103/PhysRevB.6.4370

374. Mardare D, Hones P (1999) Optical dispersion analysis of TiO_2 thin films based on variable-angle spectroscopic ellipsometry measurements. Mater Sci Eng B 68:42–47. https://doi.org/https://doi.org/10.1016/S0921-5107(99)00335-9

375. Borah R, Verbruggen SW (2022) Effect of size distribution, skewness and roughness on the optical properties of colloidal plasmonic nanoparticles. Colloids Surfaces A Physicochem Eng Asp 640:128521. https://doi.org/https://doi.org/10.1016/j.colsurfa.2022.128521

376. Sun Y, Han L, Strasser P (2020) A comparative perspective of electrochemical and photochemical approaches for catalytic H_2O_2 production. Chem Soc Rev 49:6605–6631. https://doi.org/10.1039/D0CS00458H

377. Chen L, Wang L, Wan Y, et al (2020) Acetylene and Diacetylene Functionalized Covalent Triazine Frameworks as Metal-Free Photocatalysts for Hydrogen Peroxide Production: A New Two-Electron Water Oxidation Pathway. Adv Mater 32:1904433. https://doi.org/https://doi.org/10.1002/adma.201904433

378. Tada H, Teranishi M, Naya S (2023) Hydrogen Peroxide Production by Inorganic

Photocatalysts Consisting of Gold Nanoparticle and Metal Oxide toward Oxygen Cycle Chemistry. J Phys Chem C 127:5199–5209. https://doi.org/10.1021/acs.jpcc.2c09066

379. Ezendam S, Herran M, Nan L, et al (2022) Hybrid Plasmonic Nanomaterials for Hydrogen Generation and Carbon Dioxide Reduction. ACS Energy Lett 7:778–815. https://doi.org/10.1021/acsenergylett.1c02241

380. Aslam U, Rao VG, Chavez S, Linic S (2018) Catalytic conversion of solar to chemical energy on plasmonic metal nanostructures. Nat Catal 1:656–665. https://doi.org/10.1038/s41929-018-0138-x

381. Yang K, Yao X, Liu B, Ren B (2021) Metallic Plasmonic Array Structures: Principles, Fabrications, Properties, and Applications. Adv Mater 33:2007988. https://doi.org/https://doi.org/10.1002/adma.202007988

382. Yu G, Qian J, Zhang P, et al (2019) Collective excitation of plasmon-coupled Au-nanochain boosts photocatalytic hydrogen evolution of semiconductor. Nat Commun 10:4912. https://doi.org/10.1038/s41467-019-12853-8

383. Bonin GO, Barrow SJ, Connell TU, et al (2020) Self-Assembly of Plasmonic Near-Perfect Absorbers of Light: The Effect of Particle Size. J Phys Chem Lett 11:8378–8385. https://doi.org/10.1021/acs.jpclett.0c02461

384. Krieger A, Zika A, Gröhn F (2022) Functional Nano-Objects by Electrostatic Self-Assembly: Structure, Switching, and Photocatalysis . Front. Chem. 9

385. Barrow SJ, Wei X, Baldauf JS, et al (2012) The surface plasmon modes of self-assembled gold nanocrystals. Nat Commun 3:1275. https://doi.org/10.1038/ncomms2289

386. Park S-G, Xiao X, Min J, et al (2019) Self-Assembly of Nanoparticle-Spiked Pillar Arrays for Plasmonic Biosensing. Adv Funct Mater 29:1904257. https://doi.org/https://doi.org/10.1002/adfm.201904257

387. Klinkova A, Choueiri RM, Kumacheva E (2014) Self-assembled plasmonic nanostructures. Chem Soc Rev 43:3976–3991. https://doi.org/10.1039/C3CS60341E

388. Verma R, Belgamwar R, Chatterjee P, et al (2023) Nickel-Laden Dendritic Plasmonic Colloidosomes of Black Gold: Forced Plasmon Mediated Photocatalytic CO_2 Hydrogenation. ACS Nano 17:4526–4538. https://doi.org/10.1021/acsnano.2c10470

389. Zhou L, Lei J, Wang F, et al (2021) Carbon nitride nanotubes with in situ grafted hydroxyl groups for highly efficient spontaneous H_2O_2 production. Appl Catal B Environ 288:119993. https://doi.org/https://doi.org/10.1016/j.apcatb.2021.119993

390. Zhou H, Li B, Liu J, et al (2024) Construction of novel tandem reaction system coupling H2O2 production with in situ bleaching over Au/TiO_2 photocatalyst with different metal-support interactions. Process Saf Environ Prot 183:355–364. https://doi.org/https://doi.org/10.1016/j.psep.2023.12.061

391. Ma J, Liu X, Wang R, et al (2022) Plasmon-induced near-field and resonance energy transfer enhancement of photodegradation activity by Au wrapped CuS dual-chain. Nano Res 15:5671–5677. https://doi.org/10.1007/s12274-022-4129-5

392. Hoeing D, Schulz F, Mueller NS, et al (2020) Dark plasmon modes for efficient hot electron generation in multilayers of gold nanoparticles. J Chem Phys 152:64710. https://doi.org/10.1063/1.5131696

393. Spies L, Schneider J, Curti M (2023) Time-resolved spectroscopy applied to heterogeneous photocatalytic materials (2019–2022). In: Crespi S, Protti S (eds) Photochemistry: Volume 51. Royal Society of Chemistry, p 0

394. Herring CJ, Montemore MM (2023) Recent Advances in Real-Time Time-Dependent Density Functional Theory Simulations of Plasmonic Nanostructures and Plasmonic Photocatalysis. ACS Nanosci Au 3:269–279. https://doi.org/10.1021/acsnanoscienceau.2c00061

395. Narang P, Sundararaman R, Atwater HA (2016) Plasmonic hot carrier dynamics in solid-state and chemical systems for energy conversion. 5:96–111. https://doi.org/doi:10.1515/nanoph-2016-0007

396. Klassen N V, Marchington D, McGowan HCE (1994) H_2O_2 Determination by the I3- Method and by KMnO4 Titration. Anal Chem 66:2921–2925. https://doi.org/10.1021/ac00090a020

397. Ong SW, Ong BL, Tok ES (2019) Optical and chemical stability of sputtered-Au nanoparticles and film in ambient environment. Appl Surf Sci 488:753–762. https://doi.org/https://doi.org/10.1016/j.apsusc.2019.05.233

398. Dabera GDMR, Walker M, Sanchez AM, et al (2017) Retarding oxidation of copper nanoparticles without electrical isolation and the size dependence of work function. Nat Commun 8:1894. https://doi.org/10.1038/s41467-017-01735-6

399. Song P, Wen D, Guo ZX, Korakianitis T (2008) Oxidation investigation of nickel nanoparticles. Phys Chem Chem Phys 10:5057–5065. https://doi.org/10.1039/B800672E

400. Genç A, Patarroyo J, Sancho-Parramon J, et al (2016) Tuning the Plasmonic Response up: Hollow Cuboid Metal Nanostructures. ACS Photonics 3:770–779. https://doi.org/10.1021/acsphotonics.5b00667

401. Zhang J, Chen H, Duan X, et al (2023) Photothermal catalysis: From fundamentals to practical applications. Mater Today 68:234–253. https://doi.org/https://doi.org/10.1016/j.mattod.2023.06.017

402. Zhou L, Swearer DF, Zhang C, et al (2018) Quantifying hot carrier and thermal contributions in plasmonic photocatalysis. Science (80-) 362:69 LP – 72. https://doi.org/10.1126/science.aat6967

403. Zhang Z-Q, Pei Y-C, Xiao M-J, et al (2021) In situ observation of the crystal structure transition of Pt–Sn intermetallic nanoparticles during deactivation and regeneration. Chem Commun 57:5454–5457. https://doi.org/10.1039/D1CC01181B

404. Qu J, Sui M, Li R (2023) Recent advances in in-situ transmission electron microscopy techniques for heterogeneous catalysis. iScience 26:107072. https://doi.org/https://doi.org/10.1016/j.isci.2023.107072

405. Lu Y, Yin W-J, Peng K-L, et al (2018) Self-hydrogenated shell promoting photocatalytic H2 evolution on anatase TiO2. Nat Commun 9:2752. https://doi.org/10.1038/s41467-018-05144-1

406. Zhou P, Navid IA, Xiao Y, et al (2022) Metal–Support Interaction-Promoted Photothermal Catalytic Methane Reforming into Liquid Fuels. J Phys Chem Lett 13:8122–8129. https://doi.org/10.1021/acs.jpclett.2c01459

407. Li Q, Wang H, Zhang M, et al (2023) Suppressive Strong Metal-Support Interactions on

Ruthenium/TiO_2 Promote Light-Driven Photothermal CO_2 Reduction with Methane. Angew Chemie Int Ed 62:e202300129. https://doi.org/https://doi.org/10.1002/anie.202300129

408. Huang Z, Cai X, Zang S, et al (2023) Strong Metal Support Effect of Pt/g-C_3N_4 Photocatalysts for Boosting Photothermal Synergistic Degradation of Benzene. Int. J. Mol. Sci. 24

409. Chen H, Yang Z, Wang X, et al (2021) Photoinduced Strong Metal–Support Interaction for Enhanced Catalysis. J Am Chem Soc 143:8521–8526. https://doi.org/10.1021/jacs.0c12817

410. Noval JJS, Gómez-Merchán R, Leñero-Bardallo JA, Gontard LC (2023) TEMAS: A Flexible Non-AI Algorithm for Metrology of Single-Core and Core-Shell Nanoparticles from TEM Images. Part Part Syst Charact 40:2200170. https://doi.org/https://doi.org/10.1002/ppsc.202200170

411. Gallusser B, Maltese G, Di Caprio G, et al (2022) Deep neural network automated segmentation of cellular structures in volume electron microscopy. J Cell Biol 222:e202208005. https://doi.org/10.1083/jcb.202208005

412. Urakubo H, Bullmann T, Kubota Y, et al (2019) UNI-EM: An Environment for Deep Neural Network-Based Automated Segmentation of Neuronal Electron Microscopic Images. Sci Rep 9:19413. https://doi.org/10.1038/s41598-019-55431-0